ALMA MATER STUDIORUM
UNIVERSITÀ DI BOLOGNA

DOTTORATO DI RICERCA IN

MECCANICA E SCIENZE AVANZATE DELL'INGEGNERIA

Ciclo 37

Settore Concorsuale: 09/B1 - TECNOLOGIE E SISTEMI DI LAVORAZIONE

Settore Scientifico Disciplinare: ING-IND/16 - TECNOLOGIE E SISTEMI DI LAVORAZIONE

TORSION TESTING FOR CHARACTERIZING THE PLASTIC BEHAVIOR IN METALS: DETERMINATION OF MATERIAL FLOW STRESS FOR FEM-BASED DESIGN AND OPTIMIZATION OF METAL FORMING PROCESSES

Presentata da: Sara Di Donato

Coordinatore Dottorato

Lorenzo Donati

Supervisore

Lorenzo Donati

Esame finale anno 2025

Acknowledgments

I wish to express my sincere gratitude to Prof. Lorenzo Donati and Prof. Barbara Reggiani. Thank you for all your teachings in the field of science and technology, but most importantly, thank you for your unwavering support. Thank you for being there for me not only as professors but also as individuals. I am grateful to you for being mentors who have fostered my passion and enjoyment for research.

A special acknowledgment also goes to my dear friends and colleagues, Dr. Riccardo Pelaccia, Dr. Marco Negozio, Dr. Luca Raimondi, and Dr. Lorenzo Cestone. Thank you, for without you, this journey would have been much more challenging and far less enjoyable.

With all my heart, I thank my family, my mother Luana, my father Gaspare, and my brother Davide. Your love and support are the foundation upon which I pursue my goals and dreams, always by my side.

Lastly, the greatest thanks go to Aleandro, my faithful partner in this journey and in life. Thank you for always being there for me, for supporting me with patience and love, for celebrating the joyful moments with me, and especially for helping me rise again during difficult times with your reassuring smile.

Abstract

This PhD thesis investigates the use of torsion testing as a method for characterizing the plastic behavior of metals, with particular emphasis on determining material flow stress, a critical parameter for finite element method (FEM) simulations. Accurate predictions of material behavior under various processing conditions are essential for optimizing metal forming processes. The study addresses limitations in traditional testing methods, such as tensile and compression tests, which fail to capture the full extent of material flow stress. In contrast, characterization via torsion test offers several advantages, including the ability to analyze materials for high values of strain, strain rate, and temperature, resembling conditions found in industrial manufacturing processes. The specimen in a torsion test undergoes shear deformation, and its geometry does not substantially evolve. This characteristic allows for accurate control of strain and strain rates and provides reliable data on the material's flow stress. Additionally, the integration of induction heating facilitates precise temperature management, essential for studying materials under hot working conditions.

The experimental work involves cold and hot torsion tests on various metals aimed at exploring material behavior across different strain rates and temperatures. A detailed comparison is initially conducted among the methods for characterizing the cold plastic behavior of ETP copper. The testing methods and the different analytical models for data processing are analyzed. The comparison reveals that the material exhibits different plastic behaviors under distinct stress states, due to the development of varying textures and differing hardening rates. Consequently, a new approach to processing cold torsion test data is proposed. This model is validated through a designed hybrid compression test, demonstrating its effectiveness in aligning torsion flow stress data with those obtained from tensile and compression tests. Moreover, the entire analysis is supported by FEM simulations of the tests, providing further insights into material behavior under various loading conditions.

Subsequently, the results from torsion copper characterization are applied to the study, modeling, and optimization of the wire drawing process for electrical cable production. In multi-pass industrial machines, deformation is continuously applied across multiple dies. Between two consecutive dies, rotating capstans pull the wire, thus generating both a drawing force and a back force. A theoretical multi-pass drawing model is developed, considering the entire process and focusing on the relationship

between drawing and back-stresses. The model is implemented by incorporating the material's plastic behavior as process conditions varied, obtained via cold torsion tests conducted on copper wire rods from four different suppliers. A numerical model is then proposed for simulating the drawing process in individual passes. Drawing tests were carried out, measuring the force applied to the wire by varying speed values in both lubricated and non-lubricated conditions. Experimental drawing force values are compared with values calculated from various analytical and numerical models. The analysis of deviations among the various methods highlights the importance of evaluating friction coefficient values in each model to prevent errors in estimating drawing forces. The aim of providing a reliable numerical model for predicting wire stress during the multi-pass drawing process will be achieved by accurately characterizing material flow stress and appropriately assessing the friction model.

In hot torsion testing, the induction heating process is influenced by numerous parameters, resulting in highly complex underlying physics that is challenging to model analytically. In addition to electromagnetic effects, thermal phenomena also play a critical role in induction heating, and one of the key factors affecting the heating process is solenoid geometry. To ensure an accurate evaluation of the heating cycle and to achieve the required temperature uniformly across the gauge length of the specimen, an experimental procedure was implemented on aluminum specimens. Different heating cycles were tested by varying the heating ramp and holding time, finding the optimal parameters to achieve homogeneous temperatures across the sample. The material plastic behavior characterization performed via hot torsion tests on various AA6082 aluminum alloys is then presented and compared. The influence of material flow stress modeling on numerical simulation results is examined, with comparisons between predicted results and experimental values obtained during an industrial extrusion process.

Numerical simulations using flow stress data from torsion tests effectively predicted material behavior during these processes, reinforcing the need for precise material characterization at high strain levels and elevated temperatures to improve product quality. In conclusion, the thesis establishes that torsion testing is a suitable technique for comprehensive material characterization in metal forming. The obtained data enhance the accuracy of FEM simulations, allowing for better control over manufacturing processes.

Table of contents

Chapter 1

TORSION TEST FOR MATERIAL FLOW STRESS CHARACTERIZATION

1.1. CHAPTER OVERVIEW

This chapter introduces torsion testing as a method to characterize material flow stress in metal forming processes. The chapter begins with a general description of metal forming and the mechanisms underlying the plastic deformation of metals in bulk-forming processes. The fundamental concepts of stress and strain state of a material subjected to deformation processes are recalled, and the importance of characterizing the elastic-plastic behavior of the material is emphasized. The limitations of traditional tensile and compression tests, namely necking, barreling, and limited strain levels, are discussed, which motivate the need for alternative methods.

The chapter then presents torsion testing as a solution to overcome the limitations of conventional methods. The advantages of the torsion test, including the maintenance of a relatively stable specimen shape and the possibility of controlled high deformation conditions and strain rates at controlled elevated temperatures, will be extensively detailed. The geometry of torsion specimens, along with considerations for temperature control via induction heating and the role of PID control systems in maintaining uniform temperatures, will be discussed. Additionally, an overview of the key components of a torsion testing machine will be provided.

Finally, the chapter will delve into data analysis and modeling. It explores various methods for converting torque-twist data into stress-strain curves, focusing on the Saint-Venant model for elastic deformation and the Nadai and Fields-Backofen models for plastic deformation. The chapter will conclude by introducing constitutive models, in particular the strain hardening, hyperbolic sine, and Hansel-Spittel models, which are used to represent the flow stress of material in finite element method (FEM) simulations of metal forming processes.

1.2. TORSION TEST

1.2.1. Introduction

Metal forming refers to the processes that significantly change the shape and size of a material through plastic deformation, primarily under the influence of external forces. This process is categorized into two main types: bulk forming and sheet forming. Bulk-forming processes involve the deformation of large volumes of material and are often considered three-dimensional processes due to the significant changes in shape and size that occur in all dimensions. The initial material used in these processes typically comes in the form of slabs, ingots, billets, or similar shapes, which are produced through methods such as casting into stationary molds or continuous casting techniques. In contrast, sheet forming refers to deformation processes applied to thin metal sheets, where volume change is minimal and tensile forces dominate, including techniques like stamping, deep drawing, and bending, with deformation primarily occurring under tensile stresses, often leading to risks such as local instability or necking.

Plastic deformation is a critical aspect of shaping metals in industrial applications because it allows materials to undergo permanent shape changes without cracking or fracturing, provided the correct conditions are met. At the atomic level, plastic deformation occurs when external stresses induce a shift in the arrangement of atoms within a metal. Unlike elastic deformation, where materials return to their original shape upon removing the load, plastic deformation results in permanent shape changes [1–3]. The theory of plasticity was developed to explain the behavior of ductile metals, which are typically polycrystalline, composed of numerous grains, each having a simple crystal structure. Experimental studies show that plastic deformation results from slip along specific crystallographic planes due to shear stress. These slip planes are usually parallel to the planes of closest atomic packing, as this arrangement requires the least force to initiate slip. A combination of a slip plane and a slip direction forms a slip system. While this general relationship between ductility and lattice type holds true, real metal crystals contain imperfections such as grain boundaries, geometric defects, and impurity atoms. These imperfections are critical in determining a metal's plastic behavior, making ductility a structure-sensitive property. In single crystals, Schmid's law states that slip begins when the resolved shear stress on a slip

system reaches a critical value known as the critical resolved shear stress. Discrepancies between theoretical and observed shear strength led to the conclusion that slip involves dislocations, which are defects in the crystal lattice, rather than the uniform movement of atomic planes. Dislocations, proposed by G.I. Taylor and E. Orowan, are essential to plastic deformation [4,5]. These line defects move along slip planes, and their interactions with grain boundaries and other dislocations lead to strain hardening. In polycrystalline metals, grain boundaries act as barriers, causing dislocations to accumulate, further increasing the strength of the material during deformation. When metals are strain-hardened, raising the temperature can reverse this effect through annealing, a process where the material returns to its unstrained state once the recrystallization temperature is reached. New strain-free grains replace the cold-worked structure, and the amount of cold work influences both the recrystallization temperature and the resulting grain size [5].

In metalworking, ductile metals can undergo extensive plastic deformation without fracturing, a key aspect of many industrial processes. These processes involve large plastic strains, making plasticity theory essential for predicting how metals respond under applied forces. Plasticity, unlike elasticity, depends on the full history of loading, with the material's final deformation being the sum of incremental distortions [1,4]. Plastic deformation also causes metals to transition from an isotropic to an anisotropic state as grains rotate toward preferred orientations, altering mechanical properties. Although this anisotropy and strain hardening complicate the material’s behavior, the theory of plasticity typically assumes the material remains isotropic during deformation [5]. Understanding basic stress-strain behavior under simple loading conditions is crucial before extending the theory to more complex stress states.

It is worth recalling some fundamental concepts and definitions that are essential for analyzing material behavior during deformation processes. The foundation of material behavior under deformation lies in understanding stress and strain. Stress (σ) quantifies the internal forces within a material resulting from externally applied forces. It's expressed as force per unit area and has units of Pascals (Pa) or megapascals (MPa). Essentially, stress is a tensor quantity, meaning it has both magnitude and direction, fully described by a 3x3 stress tensor. This tensor contains normal stresses ($\sigma_x, \sigma_y, \sigma_z$) acting perpendicular to the faces of a small cubic element within the material and shear stresses ($\tau_{xy}, \tau_{yz}, \tau_{xz}$) acting parallel to the faces. Normal stress represents

the force acting perpendicular to the surface. Tensile stress is positive (pulling force), while compressive stress is negative (pushing force). Shear stress represents the force acting parallel to the surface, causing a tendency for layers to slide past each other. The stress tensor can be diagonalized to find the principal stresses $(\sigma_1, \sigma_2, \sigma_3)$, which represent the maximum and minimum normal stresses at a point. These principal stresses act on planes where shear stresses are zero. Strain (ε) describes the deformation of the material in response to stress. Like stress, it's a tensor quantity, fully represented by a 3x3 strain tensor. It's dimensionless, representing the change in length, area, or volume relative to the original dimensions. Shear strain (γ) represents the change in angle between two initially perpendicular lines within the material.

The engineering stress-strain curve, obtained from a uniaxial tensile test, is a fundamental material characterization tool. The curve, shown in Fig. 1.1 a) and b), typically exhibits:

- Elastic Region: Linear relationship between stress and strain, governed by Young's modulus (E), which represents the material's stiffness. Upon unloading, the material returns to its original shape.
- Yield Point: The stress level beyond which plastic deformation (permanent deformation) begins. This is often identified by the 0.2% offset method.
- Plastic Region: Nonlinear relationship between stress and strain. Strain hardening (work hardening) occurs, where increasing stress is required to produce further plastic deformation.
- Ultimate Tensile Strength: The maximum stress reached before necking (localized reduction in cross-sectional area) initiates.
- Fracture: The point at which the specimen fails.

The engineering stress-strain curve (Fig. 1.1a) is misleading for large plastic deformations because it's based on the original cross-sectional area, which changes during necking. The true stress-true strain curve (Fig. 1.1b) provides a more accurate representation of the material's constitutive behavior, particularly in the plastic region.

Many engineering applications involve complex stress states. Effective stress $(\bar{\sigma})$ and effective strain $(\bar{\varepsilon})$ are scalar quantities that represent the equivalent uniaxial stress and strain that would produce the same amount of plastic deformation as the multiaxial state. Different yield criteria (e.g., Von Mises, Tresca illustrated in Fig. 1.1c)

provide different formulas for calculating effective stress and strain, each with its own assumptions and applications. The Von Mises criterion is commonly used and considers the distortion energy of the stress state.

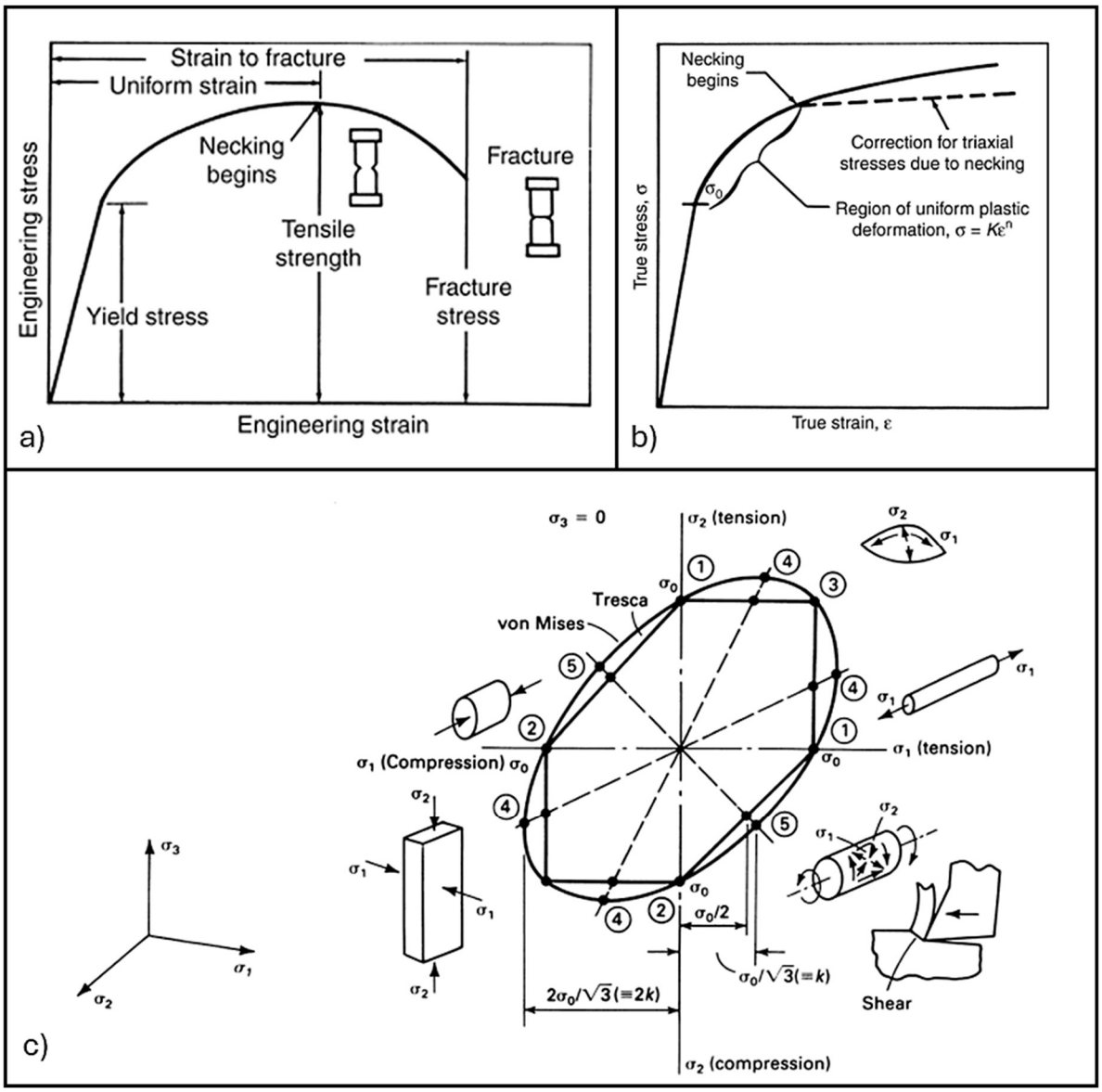

Fig. 1.1 a) Tensile Engineering stress-strain curve; b) Tensile true-stress/true-strain curve (flow curve); c) Von Mises and Tresca Yield criteria comparison with some typical stress states. [1]

1.2.2. Torsion testing for metal-forming behavior characterization

Several industrial processes rely on the principles of plastic deformation to shape metals. The most common bulk deformation processes include forging, rolling, extrusion, and wire drawing. Each process involves different mechanisms of deformation but shares the same fundamental goal of transforming metal workpieces into desired shapes through controlled plastic deformation:

- Forging involves compressing a metal workpiece between two dies to shape it. This process can be carried out at high temperatures (hot forging) or at room temperature (cold forging). The workpiece undergoes significant plastic deformation as it is compressed, leading to changes in both shape and mechanical properties. Hot forging is preferred for large deformations because the metal's ductility is enhanced at high temperatures, reducing the risk of cracking. In contrast, cold forging results in better surface finishes and higher strength due to strain hardening [1,2].
- In Rolling, a metal slab is passed through a series of rollers that progressively reduce its thickness. Rolling can be done at elevated temperatures (hot rolling), which allows for large reductions in thickness without significant strain hardening, or at lower temperatures (cold rolling), which increases the material's strength through work hardening. The majority of ingots are first processed through hot rolling to form intermediate products like blooms, slabs, and billets. These are then further rolled into various final products, including plates, sheets, bars, structural sections, rods (which can be drawn into wire), and rounds used for producing seamless tubing [1,2].
- During Extrusion, a metal billet is forced through a die to produce a long, continuous product of uniform cross-sectional shape. The high compressive forces applied during extrusion cause significant plastic deformation. Hot extrusion is typically used for metals with low ductility at room temperature, while in cold extrusion the initial material is shaped at room temperature. However, as the material deforms, heat is generated due to the conversion of mechanical work into thermal energy, raising the temperature to several hundred degrees [1,2,6].

- Wire Drawing involves pulling a metal workpiece through a die to reduce its diameter. The process is often used to produce wires, rods, and tubes. As the material is pulled through the die, it undergoes triaxial state deformation, which reduces its cross-sectional area while increasing its length [1,2,6].

The effectiveness of plastic deformation processes depends on several factors, including the material's flow stress, strain, strain rate, temperature, and workpiece geometry. Each of these factors plays a critical role in determining how much deformation a metal can undergo before fracture or other failure modes occur.

- *Flow Stress*: flow stress is the stress required to continue deforming a material plastically, as introduced in paragraph 1.2.1. It depends on the material's composition, grain structure, and temperature.
- *Strain*: strain refers to the amount of deformation a material undergoes relative to its original dimensions, as explained in paragraph 1.2.1. In bulk deformation processes, large strains are typically required to achieve the desired shape changes.
- *Strain Rate*: the strain rate, or the speed at which deformation occurs, also affects material behavior. Higher strain rates generally lead to higher flow stresses, especially in strain-rate-sensitive materials, as dislocations have less time to move and rearrange.
- *Temperature*: temperature plays a significant role in plastic deformation, especially in hot working processes. At elevated temperatures, metals exhibit increased ductility and reduced flow stress, making them easier to deform. This is because thermal energy allows atoms to overcome barriers to dislocation movement, facilitating slip.

The term "workability" refers to the ease with which a metal can be shaped without causing defects. It is influenced by the material's ductility, flow stress, and resistance to fracture. Workability limits are defined by the point at which undesirable conditions such as cracking, surface defects, or buckling occur. In processes like forging and rolling, excessive deformation can lead to laps, where the metal folds over itself, creating internal voids or surface defects. Similarly, in extrusion and drawing, excessive tensile stresses can lead to necking or fracture. To maximize workability, careful control of process parameters is essential. Preheating the workpiece,

optimizing strain rates, and selecting appropriate lubrication techniques can help reduce the risk of failure. Additionally, understanding the metallurgical changes that occur during deformation, such as grain refinement or recrystallization, is crucial for improving the mechanical properties of the final product [1].

In general, the flow stress of a material can be described as a function of temperature, strain rate, and strain:

$$\sigma = f(\varepsilon, \dot{\varepsilon}, T) \qquad (1.1)$$

This relationship highlights how the material's resistance to deformation evolves under varying conditions, where higher temperatures tend to reduce flow stress, while increasing strain and strain rates typically raise it. This dependency is crucial for accurately modeling material behavior during metal forming processes, especially under conditions of large deformations and high temperatures.

In this context, the need arises for a mechanical test capable of accurately characterizing the behavior of materials under conditions of high strain, strain rate, and temperature. Such a test must generate results that are broadly applicable across various metalworking operations. The ideal test should meet the following criteria [7,8]:

1 The results should be presented as stress-strain curves that have fundamental significance, meaning they provide a clear and scientific understanding of material behavior under load. Additionally, any test-specific characteristics should be correctable.

2 The test conditions should be consistent and not dependent on the material being tested.

3 The test should allow deformation to very high strain levels, reflective of industrial conditions.

4 It should be possible to measure the strain at fracture, and the test must cover the full range of temperatures encountered in practical applications.

5 The test should accommodate the full range of stress rates, which are common in metalworking.

Among the most commonly used material characterization methods are tensile, compression tests, and the Ford test. However, these methods face limitations in meeting the criteria outlined above, as illustrated in Fig. 1.2. In all the tests, the strain

levels reached are far lower than those typically encountered in industrial processes. In tensile tests, material characterization only reaches strain levels between 0.1 and 0.3 due to the onset of necking. Moreover, post-necking data becomes challenging to analyze. Compression tests avoid necking but are hindered by barreling, which results from friction between the plates and the sample. This leads to non-uniform deformation, and the maximum strain typically falls between 0.9 and 1.1. Additionally, during the tests, the changing geometry of the specimen leads to variations in strain rate, making it difficult to maintain constant conditions. High-temperature testing introduces further limitations. Elevated temperatures reduce the maximum achievable strain and increase problems related to friction and non-uniform stress distribution across the specimen. In these tests, furnace heating is commonly used, rather than induction heating, which offers more precise control. However, because the sample's geometry changes during testing, and due to the test setup, using induction heating is challenging. Furnace heating provides less control over temperature and is slower, making it difficult to regulate temperature directly through a PID system during the test.

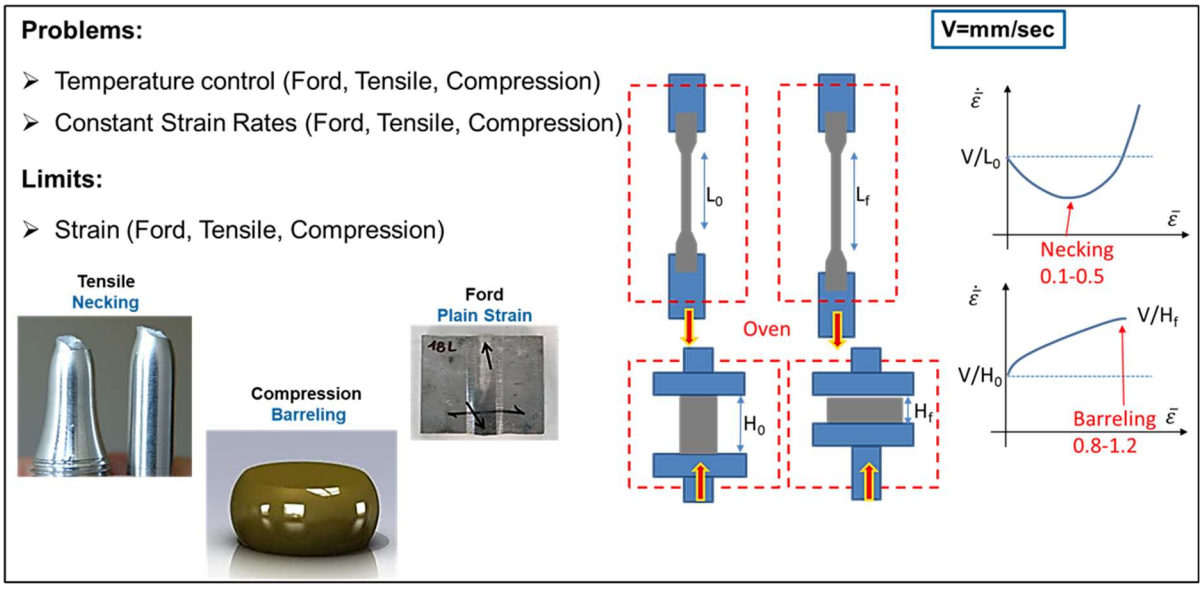

Fig. 1.2 Main problems and limits of Tensile, Compression, and Ford tests.

Therefore, to overcome these limitations, the torsion test is generally considered the most effective test method, allowing the characterization of materials at high strain and strain rates under controlled high-temperature conditions. It involves applying a twisting force (torque) to the specimen, which is clamped at both ends, while one end is rotated at a constant speed. The test provides the relationship between the angular deformation applied to the sample and the torque required to obtain it. During the test,

the machine outputs are the torque M expressed in N·m and the angle of twist θ in radians.

The torsion test has been investigated by researchers over the years as a means of workability assessment in metals and alloys. From the initial theoretical studies and investigations into its effectiveness in material characterization [9–13], to the design and development of specialized torsion testing machines and specimen geometries [7,8,14,15], and more recently, on applying the torsion test for characterizing the mechanical behavior of various metals [16–23].

The primary advantage of the torsion test lies in its ability to maintain a relatively stable shape in the test specimens during deformation, as long as the gauge section is kept at a fixed length. This characteristic is particularly valuable because it allows for a more controlled assessment of material properties. Additionally, the torsion test enables the application of a constant true strain rate to a specified annular region of the specimen by twisting it at a constant angular velocity.

About the geometry of the sample used during the torsion test, there are still no standards for the design. Various researchers have opted for different specimen geometries, including solid-bar specimens with reduced gauge sections and transition fillets, as well as tubular specimens. Solid-bar geometries facilitate easier temperature management across the cross-section of the sample and are capable of enduring higher torque levels without the risk of failure, achieving greater strain at fracture compared to thin-walled tubular specimens. Additionally, they are also generally easier to fabricate than tubular specimens. Conversely, tubular specimens offer significant advantages regarding stress and strain analysis. Key design considerations include the geometry of the gauge section, the fillet radius, the length of the shoulder, and the design of the grips.

The design specifications for the shoulders and grips of torsion specimens are heavily influenced by the heating method and the type of torsion machine being utilized. In general, the shoulder diameter should be at least 1.5 times the diameter of the gauge section, and ideally, it should be two to three times larger. This design approach helps prevent plastic deformation and minimizes elastic distortion.

The geometry of the gauge section plays a crucial role in determining the level of deformation and the corresponding strain rate for a specific twist amount and twist rate, as described by Eqs. (1.2) and (1.3).

$$\gamma = \frac{r\theta}{L} \tag{1.2}$$

$$\dot{\gamma} = \frac{r\dot{\theta}}{L} \tag{1.3}$$

Where γ is the shear strain, θ is the twist angle in radians, $\dot{\gamma}$ and $\dot{\theta}$ are respectively the shear strain rate and the twist rate, L is the gage length and r is the radial position, as indicated in Fig. 1.3. For a given twist, larger values of the radius r and smaller values of the length L facilitate higher shear strain γ. Likewise, large r and small L yield elevated values of the strain rate for a set twist rate. It is important to note that, during the torsion test, the specimen is subjected to a pure shear stress state, with strain and strain rate varying across the radius, their maximum values occurring at the surface and decreasing to zero at the center. For these reasons, the most significant limitation of the test is the conversion of output data from the machine, the torque (M) and torsion angle (θ), into values of tangential stress (τ) and strain (γ), and subsequently into equivalent stress $(\bar{\sigma})$ and strain $(\bar{\varepsilon})$ values. Over the years, different theories have been developed for data processing, which will be explained in the following paragraphs.

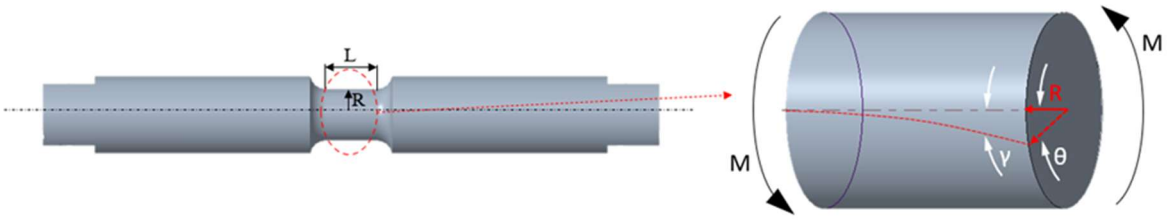

Fig. 1.3 Scheme of the shear strain occurring within specimen's gauge length during torsion test.

Another significant advantage of the torsion test is the effective temperature control made possible by heating the specimen via induction. Unlike tensile or compression tests, where the specimen undergoes significant changes in shape, resulting in challenges for uniform heating, the torsion test setup allows for precise heating management. The solenoid used for heating remains accurately centered on the specimen's gauge section, ensuring that the heating is localized to the desired area. Furthermore, the integration of a thermocouple, inserted into the specimen to reach

the beginning of the gauge section, as indicated in Fig. 1.4, combined with a PID control system, enables the maintenance of a stable and uniform temperature throughout the duration of the test. This temperature stability is critical for accurately assessing the material's behavior under controlled thermal conditions.

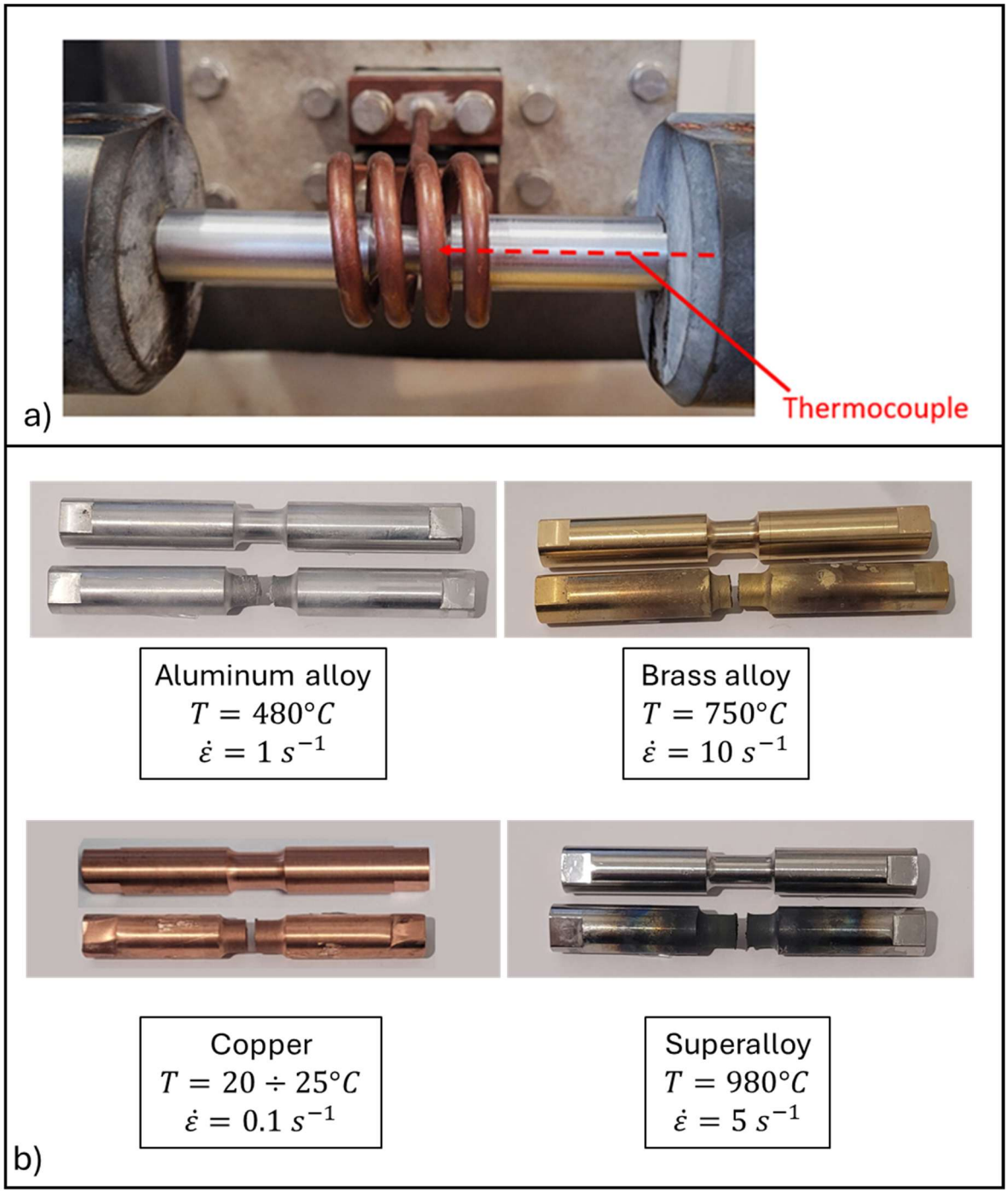

Fig. 1.4 a) Image of an Aluminum specimen subjected to induction heating by means of copper solenoid during hot torsion test; b) Different materials samples subjected to torsion test under different conditions.

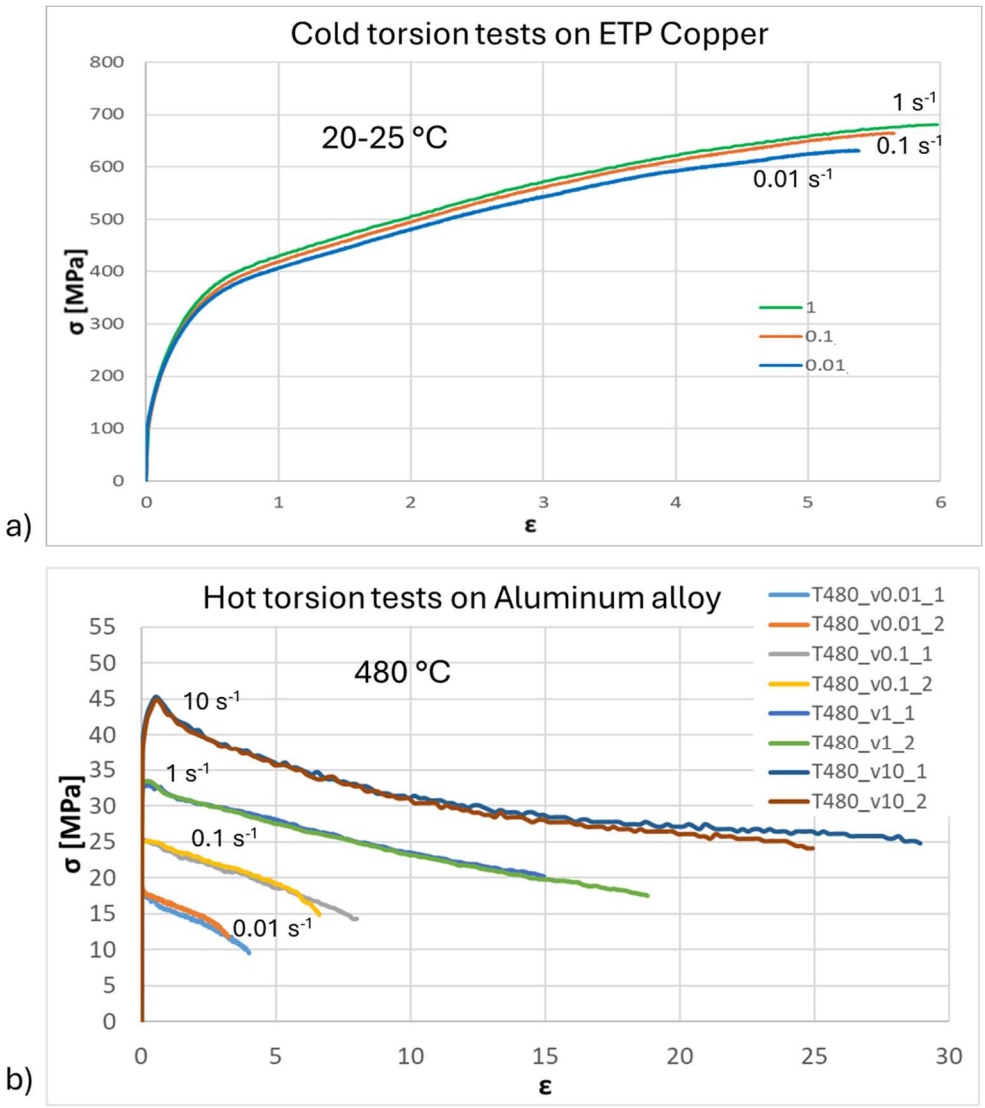

Fig. 1.5 Examples of flow stress curves obtained from cold and hot torsion tests on different materials.

Regarding the flow stress curves, to accurately comprehend how the material behaves during the torsion test, it is essential to take into account the temperature at which the test is conducted and the rate at which the material is deformed. Flow stress curves for materials tested at high temperatures typically display an initial peak followed by a period of softening before reaching a steady-state flow, as shown in the graph in Fig. 1.5b. This behavior is due to dynamic recrystallization and recovery mechanisms, which are activated at elevated temperatures. The peak in the flow stress corresponds to the initial work hardening of the material, while the subsequent softening reflects the material's microstructural changes, such as grain boundary migration and dislocation annihilation. In contrast, at lower temperatures, flow stress

curves often exhibit continuous strain hardening, as the microstructural recovery processes are less active, assuming the typical shapes of the curves shown in the graphs in Fig. 1.5a. Additionally, strain rate plays a significant role in determining the shape of the flow curves. At higher strain rates, flow stresses tend to increase, especially at elevated temperatures, due to the limited time available for dynamic recovery processes to occur.

1.2.3. Torsion test Machine

The torsional mode of mechanical testing is less commonly employed compared to tensile testing, resulting in a limited number of commercially available machines. Consequently, the apparatus is often custom-designed to meet the specific requirements of individual researchers. The torsion machine used at DIN - Department of Industrial Engineering of the University of Bologna is shown in *Fig. 1.6*.

Fig. 1.6 Photos of the Torsion Machine at the DIN-Department of Industrial Engineering of the University of Bologna.

As shown in the diagram in *Fig. 1.7*, the main components of the torsion machine are:

- Rotary motor
- Hydraulic cylinder
- Inductive heating generator
- PID control via thermocouple
- Cooling system
- Rotary encoder
- Load cell
- Control panel

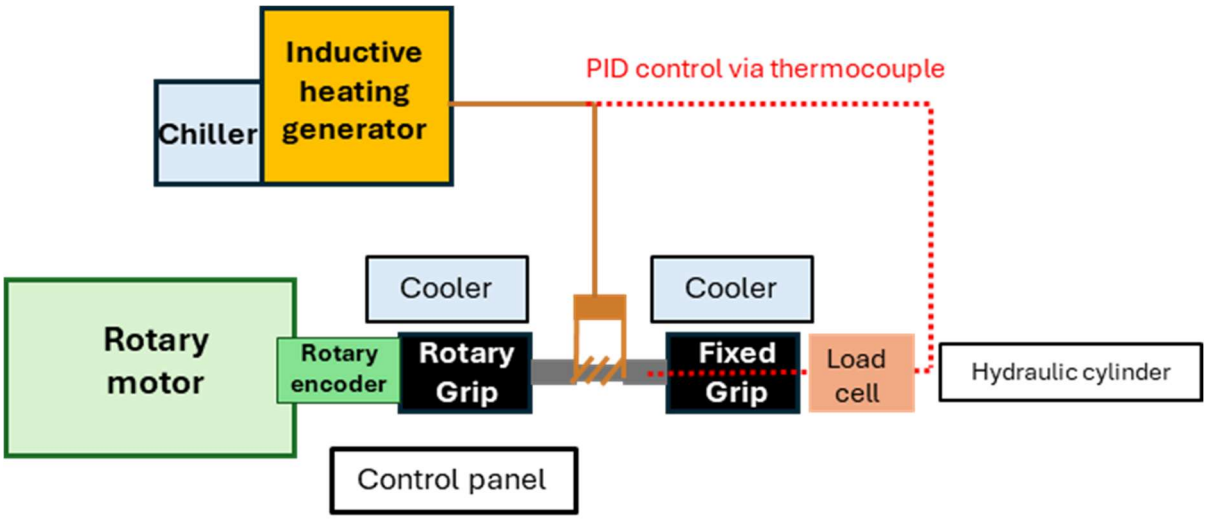

Fig. 1.7 Schematic of the Main Components of the Torsion Machine.

Rotary motor

The rotary motor is a crucial component of the torsion machine, responsible for generating the rotational motion required to apply torsional stress to the specimen under investigation. In addition to producing high torque, the rotary motor must maintain a constant rotational speed throughout the test. The motor is designed to achieve steady-state conditions as quickly as possible, reducing transient response time. To facilitate precise control over the rotational speed and torque output, the rotary motor is often integrated with a feedback system, such as a rotary encoder, which

continuously monitors its performance. This data can be fed back to the control system, allowing for real-time adjustments to maintain the desired testing parameters. The specifications of the rotary motor mounted on the torsion machine of the DIN are listed in Table 1.1.

Table 1.1 Rotary Motor technical specifications.

Three-Phase Synchronous Motor	Technical specification
Polar Torque	3
Rated Speed	2000 rpm
Maximum Speed	3500 rpm
Continuous Torque	133 Nm
Maximum Torque	231 Nm
Continuous Current	63 A
Maximum Current	144.5 A
Moment of Inertia	0.0138 kgm^2

Hydraulic cylinder

The hydraulic cylinder in the torsion machine plays a pivotal role in providing controlled linear motion to the specimen. This component utilizes hydraulic fluid under pressure to generate force, allowing for precise adjustments in the positioning of the specimen during torsion tests. As the specimen experiences torsional stress, it may undergo slight changes in length due to thermal expansion or deformation. The hydraulic cylinder compensates for these variations, ensuring that the specimen remains securely held in place throughout the test. This ability to adjust the position dynamically is essential for maintaining accurate torsional measurements and preventing mechanical failures or inaccuracies.

Inductive heating generator

The inductive heating generator, shown in Fig. 1.8 is a sophisticated device that heats the specimen to the required temperatures for hot torsion testing using the principle of electromagnetic induction. This generator operates by producing an alternating current, which flows through an inductor coil. The resulting electromagnetic field induces eddy currents within the conductive material of the specimen, generating heat due to the material's electrical resistance (known as the Joule effect). This method of heating offers several advantages over conventional heating techniques, including

rapid and uniform heating, precise temperature control, and high efficiency. The generator can heat materials such as aluminum, magnesium, titanium, bronze, steel, and their alloys to temperatures ranging from 100°C to 1200°C. Integrated temperature monitoring, typically through a thermocouple connected to the generator, allows for real-time feedback to the PID control system. This feedback ensures that the specimen reaches and maintains the desired temperature throughout the duration of the test, facilitating accurate characterization of material behavior under different thermal conditions.

Fig. 1.8 Photo of the Inductive Generator of the Torsion Machine at the DIN-Department of Industrial Engineering of the University of Bologna.

As shown by the parameters in Table 1.2, the inductive generator of the torsion test machine of the DIN is capable of delivering a maximum output power of 15 kW. When fully loaded, it consumes 21 kW of real power (with additional apparent power losses) and draws 42 amps of current from the electrical supply. The frequency range of 80 to 400 kHz.

Table 1.2 Inductive generator technical specifications.

Inductive generator	Parameter value
Maximum Output Power	15 kW
Input Power at No Load	1.3 kVA
Input Power at Load	28.6 kVA – 21 kW
Input Current at Load	42 A
Operating Frequencies	80 – 400 kHz

PID Control via Thermocouple

The PID (Proportional-Integral-Derivative) control system is integral to maintaining the desired temperature of the specimen during testing. This control mechanism utilizes feedback from a thermocouple, which measures the temperature of the specimen in real time. The PID controller processes the temperature data and calculates the necessary adjustments to the heating output of the inductive generator to minimize the error between the actual temperature and the setpoint temperature. Each component of the PID controller contributes to its overall performance:

- Proportional Control: This component provides a control output that is proportional to the current error value. It reacts to the magnitude of the error, allowing for rapid adjustments.
- Integral Control: This aspect addresses any accumulated past errors, ensuring that the system can eliminate residual steady-state error by adjusting the control output over time.
- Derivative Control: This part predicts future error based on its rate of change, providing a damping effect that helps stabilize the system and reduce overshoot.

Together, these components create a robust feedback loop that allows the PID controller to respond dynamically to fluctuations in temperature.

Cooling system

The cooling system is a critical component designed to manage the thermal stress encountered by both the specimen and the gripping apparatus during high-temperature torsion testing. Elevated temperatures can lead to significant thermal expansion and potential damage to the equipment, necessitating effective cooling solutions. In the

torsion machine, the cooling system typically includes water-cooling mechanisms for the grips, which are subject to considerable thermal stress as they hold the specimen during testing. By circulating cool water through these grips, the system helps maintain their temperature within safe operating limits, preventing thermal deformation and ensuring consistent performance. Additionally, the cooling system offers flexibility for the specimen itself. Depending on the requirements of the test, the specimen can be cooled using air, water, or a combination of both. This adaptability allows for customized cooling strategies, which can be critical for specific material properties or testing conditions. A dedicated chiller is also integrated into the system to provide direct cooling for the inductive heating generator and the solenoid. This chiller employs a closed-loop circuit design, where water circulates through the solenoid made of copper tube. It is essential for the solenoid to remain cool during current flow, as its primary function is to heat the specimen efficiently without losing heat to the surrounding components. By ensuring efficient cooling of the generator and solenoid, the chiller enhances the overall thermal management of the torsion machine.

Rotary Encoder

The rotary encoder is an essential feedback device integrated into the torsion machine, providing accurate measurements of the angular position and rotation of the rotary motor. This device plays a vital role in the overall control and monitoring of the torsion test. The encoder operates by converting rotational motion into an electrical signal, which can be processed by the control system. In the context of the torsion machine, the rotary encoder continuously tracks the rotational angle and speed of the specimen during testing. This real-time data is crucial for maintaining consistent torque application and for analyzing the material's response to torsional stress.

Load Cell

The piezoelectric axial/rotary load cell is a vital component of the torsion machine, responsible for accurately measuring the forces and torques applied to the specimen during torsion tests. Technical specifications of the load cell mounted on the torsion machine at DIN are listed in Table 1.3. This sensor operates based on the piezoelectric effect, wherein certain materials generate an electrical charge in response to mechanical stress. This property allows the load cell to convert mechanical load into an electrical signal, enabling precise measurement of force and torque. The load cell

is specifically designed to measure both axial forces (F_Z) and torsional moments (M_Z) acting along the axis of the sensor. It is equipped with sensitive quartz discs that respond to applied pressures and shear forces. The integration of these discs within the load cell allows it to capture minute changes in force and torque with high resolution, making it suitable for testing materials under dynamic conditions.

Table 1.3 Load cell technical specifications.

Load Cell	**Measurement range**.
Angular Torque Range	-200 Nm - +200 Nm
Axial Load Range	-20 kN - +20 kN

Key features of the piezoelectric load cell include:

- High Sensitivity: The load cell's design enables it to detect even the smallest changes in force and torque, ensuring accurate and reliable measurements throughout the testing process. This sensitivity is critical for assessing the mechanical properties of materials under varying stress conditions.
- Robust Design: Constructed to withstand the high pressures and temperatures associated with hot torsion testing, the load cell features a durable design that ensures longevity and reliability. Its resistance to environmental factors contributes to its overall performance.
- Coaxial Coupling: The load cell is designed with centering seats on both sides, allowing for very precise coaxial alignment during installation. This alignment minimizes measurement errors and ensures that the applied forces are accurately detected without introducing additional variables.
- Charge Output: The piezoelectric load cell produces an electrical charge proportional to the applied force and torque. This charge is detected by electrodes within the cell and transmitted via a shielded cable to a charge amplifier. The amplifier converts the charge signal into proportional output voltages that can be recorded and analyzed.
- Real-Time Data Acquisition: By integrating the load cell into the torsion machine's feedback loop, real-time data acquisition allows for continuous monitoring of applied forces and torques. This data is crucial for interpreting

material behavior during testing and enables adjustments to the testing parameters as necessary.

Control Panel

The control panel serves as the central interface for operators to interact with the torsion machine. It is designed to provide a user-friendly environment, as shown in Fig. 1.9, for configuring test parameters, initiating testing procedures, and monitoring system performance in real-time. Through the control panel, users can set up torsion tests by defining various parameters such as temperature, rotational speed, and the specific duration of the test. The interface also allows for calibration of the system, including adjustments to the PID controller's gain settings and other control parameters. In addition to setup and configuration, the control panel provides visual displays of real-time data, including temperature readings from the thermocouple, rotational speed from the rotary encoder, and overall system status indicators. This information allows operators to monitor the performance of the torsion machine throughout the testing process. Furthermore, the control panel integrates safety features, including alarms and shutdown mechanisms, to protect both the equipment and the operator during high-temperature testing. By consolidating all control, monitoring, and safety functions into a single interface, the control panel enhances operational efficiency and reduces the complexity of managing the torsion machine. Overall, the control panel represents the hub of the torsion machine's operation, facilitating seamless interaction between the user and the testing system while ensuring accurate and reliable material characterization.

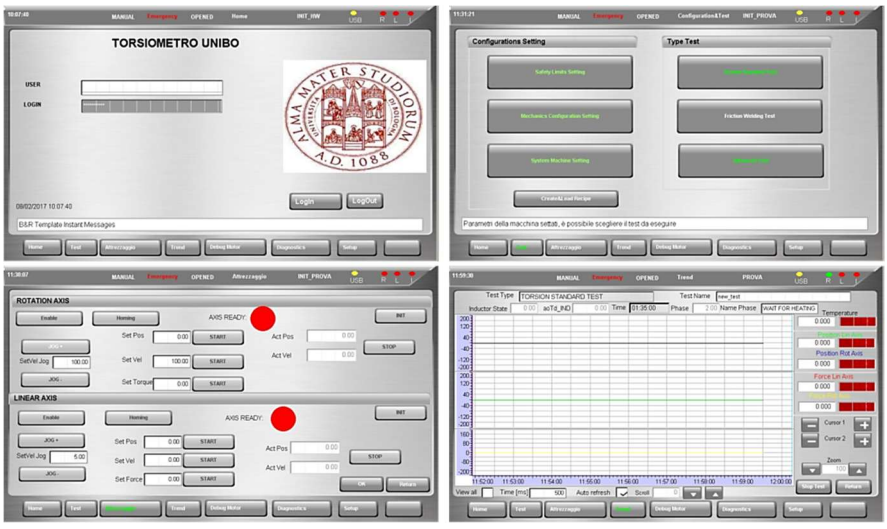

Fig. 1.9 Torsion Machine Control Panel Interface.

1.2.4. Models for elaboration of Torque-Twist data to Stress-Strain data

To analyze and predict the constitutive equation representing the flow behavior of materials, it is essential to transform raw data into flow curves. The most prevalent methods for converting torque-twist measurements, into shear stress-shear strain curves include the De Saint Venant [24] approach for the elastic region and the Nadai [9], or Fields and Backofen [10] methods for the plastic region.

De Saint Venant model

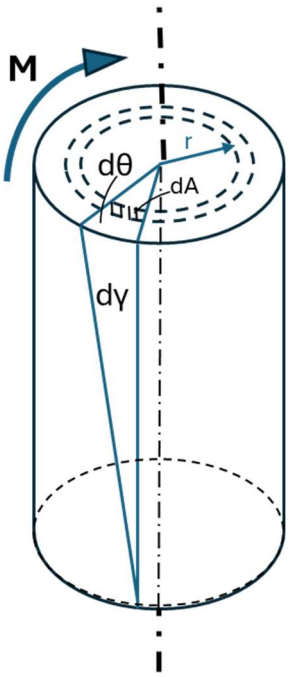

Fig. 1.10 Scheme of a solid cylindrical specimen under applied torsional moment.

Saint-Venant's theory, introduced in 1856, provides a detailed framework for understanding the elastic behavior of prismatic bars under torsion. His two key works on the subject, "Mémoire sur la torsion des prismes" [24] and "Mémoire sur la flexion des prismes" [25] focus on the elastic deformation and distribution of stresses within solids subjected to torsional and flexural loads. Saint-Venant assumes that the material remains within the elastic regime, where stress and strain are linearly related, and the internal stress distribution is governed by equilibrium conditions, resulting in well-defined formulas for the calculation of shear stress and strain.

In the elastic range, according to Hooke's Law, the shear stress τ is linearly proportional to the shear strain γ, through the shear modulus (or modulus of rigidity) G and this is expressed as:

$$\tau = G\gamma \tag{1.4}$$

When a cylindrical solid is subjected to a torque, it twists about its longitudinal axis, generating a distribution of shear strain along the radial direction. The shear strain γ at a point located at a radial distance r from the center of the shaft is given by:

$$\gamma = \frac{R\theta}{L} \tag{1.5}$$

This equation shows that the shear strain is linearly proportional to the radial position r; strain is zero at the center and maximum at the outer surface.

To relate shear stress to the applied torque, consider an infinitesimal element of the specimen at a radial distance r from the axis, as indicated in the scheme in Fig. 1.10. The elemental torque dM acting on an infinitesimal area dA of the cross-section is:

$$dM = \tau r\, dA = \tau r\, dr d\theta \tag{1.6}$$

To find the total torque M applied to the specimen, the differential torque is integrated over the entire cross-sectional area A:

$$M = \int_A \tau r\, dA \tag{1.7}$$

Substituting Eqs. (1.4) and (1.5) gives:

$$M = \frac{G\theta}{L} \int_A r^2\, dA \tag{1.8}$$

The integral $\int_A r^2\, dA$ is the polar moment of inertia J for the cross-section of the specimen, which characterizes the resistance of the section to torsion. For a solid circular cross-section, it is given by:

$$J = \frac{\pi R^4}{2} \tag{1.9}$$

Thus, the total torque becomes:

$$M = G\frac{\theta}{L}J \tag{1.10}$$

The shear stress τ at any radial distance r from the center of the cilinder can now be found by combining Eqs. (1.4) and (1.5):

$$\tau = \frac{r\theta}{L} \tag{1.11}$$

Using the relationship between torque and angle of twist from Eq. (1.10), $\frac{\theta}{L}$ can be substituted to give shear stress directly in terms of torque:

$$\tau = \frac{Mr}{J} \tag{1.12}$$

This expression shows that the shear stress varies linearly with the radial distance r, reaching its maximum value at the outer surface. Substituting into Eq. (1.12) the maximum radius $r = R$:

$$\tau_{max} = \frac{2M}{\pi R^3} \tag{1.13}$$

Saint-Venant's theory is based on key assumptions that limit its application to elastic deformations:

- Linear material behavior: Saint-Venant's theory relies on Hooke's Law, which applies only when the material deforms elastically. This assumption fails when a material enters the plastic regime, where stress-strain relationships become nonlinear and plastic flow needs to be considered.
- Small deformations: The theory assumes small strains, which is valid for elastic deformation. In plastic deformation, the strains can become large, and the distribution of stresses changes significantly, especially near points of stress concentration or yielding zones.

In contrast, plastic deformation introduces complexities such as strain hardening, large deformations, and non-uniform stress distributions, which invalidate the assumptions of Saint-Venant's theory. When a test specimen is subjected to continued deformation, it eventually enters the plastic region as the shear stresses τ surpass the yield strength of the specimen. This transition signifies that the stress distribution within the cross-section will no longer remain linear. Instead, starting from the outer regions, the stresses begin to follow a non-linear distribution. This distribution corresponds to a specific function related to the flow stress of the material. *Fig. 1.11* illustrates an example of a specimen exhibiting elastic-perfectly plastic behavior under a torsional moment. In the elastic region, the material follows Hooke's Law, maintaining a linear relationship between stress and strain. However, as the yield point is exceeded, the material enters the plastic deformation zone, characterized in this simplified case by a constant stress value, in general by a non-linear stress-strain relationship, reflecting the material's inherent flow characteristics.

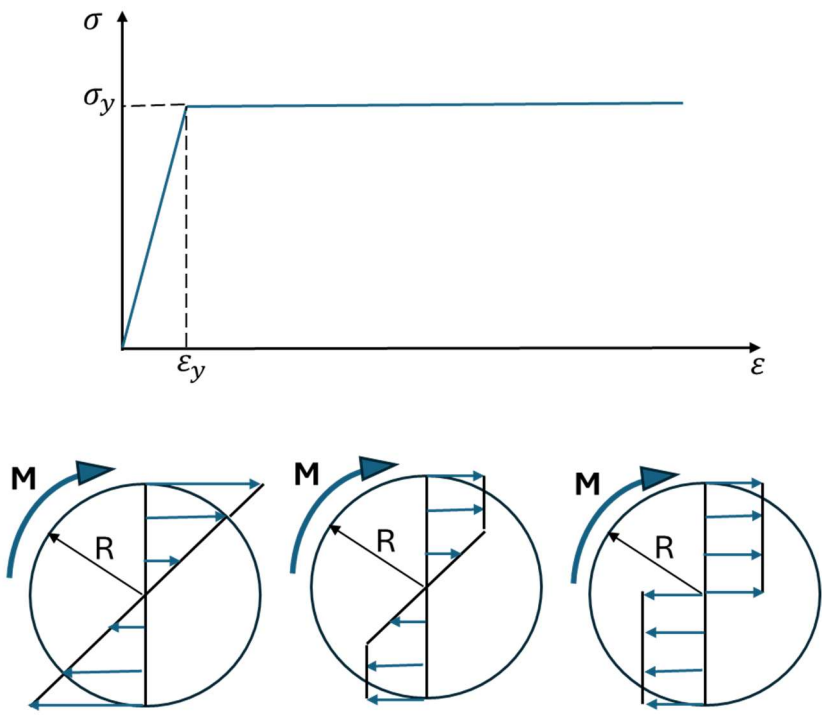

Fig. 1.11 Example of a solid cylindrical specimen of a material exhibiting elastic-perfectly plastic behavior under applied torsional moment.

Nadai model

Nadai [9], in 1950, formally extended the elastic analysis of a torsion bar to the case of plastic deformation. The theory is based on the hypothesis that the distortions produced in an isotropic cylinder by small angles of relative torsion can be considered as simple shear deformations proportional to the distance r, assuming that all radii remain straight during the deformation.

When a cylinder of length L is subjected to a torque, the twist angle per unit length can be defined as:

$$\theta' = \frac{\theta}{L} \quad \Rightarrow \quad \gamma = \theta' \cdot r \tag{1.14}$$

The torque acting on the infinitesimal area dA is given by:

$$dM = \tau r \, dA = \tau r \, dr d\theta \tag{1.15}$$

Considering the entire cross-section of the specimen with an external radius a, the total torque becomes:

$$M = 2\pi \int_0^a \tau r^2 dr \tag{1.16}$$

Now, considering that the shear stress is only a function of deformation, thus substituting in Eq. (1.16) the unknown stress curve $\tau = f(\gamma)$ and changing the variables, yields:

$$M = 2\pi \int_0^{\gamma_a} f(\gamma) \left(\frac{\gamma}{\theta'}\right)^2 \frac{d\gamma}{\theta'}, \quad \text{with} \quad \gamma_a = a\theta', \qquad r = \frac{\gamma}{\theta'}, \tag{1.17}$$

$$\text{and} \quad \frac{dr}{d\gamma} = \frac{1}{\theta'}$$

This can be rearranged as:

$$M\theta'^3 = 2\pi \int_0^{\gamma_a} f(\gamma)\gamma^2 d\gamma \tag{1.18}$$

Thus, by differentiating Eq. (1.18) with respect to θ', on the specimen's surface, where $\gamma = \gamma_a$, Eq. (1.19) is obtained:

$$\frac{dM\theta'^3}{d\theta'} = 2\pi f(\gamma_a)\gamma_a{}^2 d\gamma_a \qquad (1.19)$$

Substituting $f(\gamma_a) = t_a$ at the maximum radius of the specimen:

$$3M\theta'^2 + \theta'^3\frac{dM}{d\theta'} = 2\pi a^3\theta'^2\tau_a \qquad (1.20)$$

This rearrangement allows the tangential stress acting on the outer surface of the specimen to be expressed as in Eq (1.21):

$$\tau_a = \frac{1}{2\pi a^3}\left(3M + \theta'\frac{dM}{d\theta'}\right) \qquad (1.21)$$

At this point, Nadai proposed a graphical method to solve the equation. By observing the graph in *Fig. 1.12*, which shows a generic curve of the applied torque versus the angular rotation per unit length, it is clear that $\frac{dM}{d\theta'} = \frac{BC}{AB}$ and $\theta' = AB$. Therefore, Eq. (1.21) can be rewritten in graphical form as

$$\tau_a = \frac{1}{2\pi a^3}(3CD + BC) \qquad (1.22)$$

It is worth noting that if the curve $M = f(\theta')$ can be approximated by an exponential function, where n is the strain-hardening coefficient, it takes the form $M = C\theta'^n$, which differentiating with respect to θ' gives:

$$\frac{dM}{d\theta'} = Cn\theta'^{(n-1)} \quad \Rightarrow \quad Cn\theta'^{(n-1)} = n\frac{M}{\theta'} \quad \Rightarrow \quad \frac{dM}{d\theta'} = n\frac{M}{\theta'} \qquad (1.23)$$

Substituting into Eq. (1.21), it becomes:

$$\tau_a = \frac{M}{2\pi a^3}(3 + n) \qquad (1.24)$$

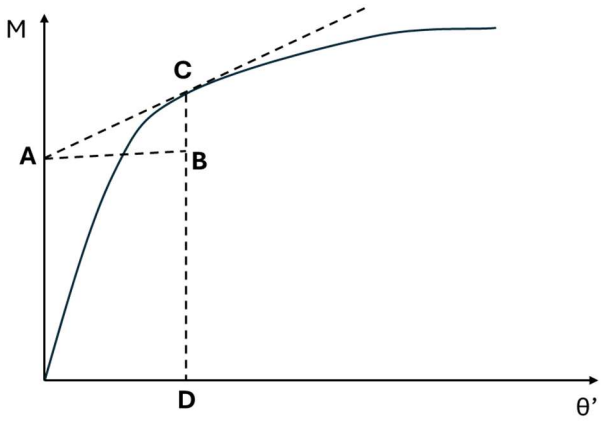

Fig. 1.12 Graphical determination of shear stress from torque-twist curve.

Nadai's method, however, suffers from two major limitations: firstly, it does not take into account the sensitivity to the rate of deformation (shear strain rate), meaning it cannot be applied at high temperatures, where sensitivity to the strain rate is significant. Secondly, the accuracy with which the surface shear stress is determined depends critically on the precision with which the slope of the torque-torsion displacement curve is known.

Fields and Backofen model

Fields and Backofen [10] expanded Nadai's method to strain rate-sensitive materials, allowing the model to be applied at high temperatures, where the strain rate significantly affects the material's flow stress.

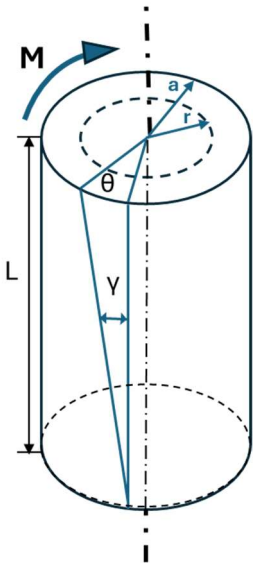

Fig. 1.13 Scheme of a cylindrical specimen with external radius (a) under applied torsional moment.

Referring to Equations (1.14), (1.17), and (1.18), it can be stated that, considering a cylindrical specimen with a maximum radius a and length L, as shown in the scheme in Fig. 1.13, in order to apply an angular twist equal to θ'_a at a rate of $\dot{\theta}'_a$, a total moment must be applied as expressed in Eq. (1.25):

$$M_a = \frac{2\pi}{{\theta'_a}^3}\int_0^{\gamma_a} \tau\gamma^2 d\gamma \qquad (1.25)$$

Considering a generic radius r of the specimen, smaller than the maximum radius, the equation can be written as:

$$M_a = \frac{2\pi}{{\theta'_a}^3}\left(\int_0^{\gamma_r} \tau\gamma^2 d\gamma + \int_{\gamma_r}^{\gamma_a} \tau\gamma^2 d\gamma\right) \qquad (1.26)$$

At this point, a second identical specimen with radius a is subjected to a moment M_b resulting in an angular rotation θ_b at a rate $\dot{\theta}_b$. This values are selected to ensure that the strain and strain rate on the specimen's external surface are equivalent to those observed at the arbitrary internal radius r of the first specimen, thereby satisfying the conditions outlined in Eqs.(1.27) and (1.28).

$$\gamma_b = a\theta'_b = r\theta'_a = \gamma_r \quad \text{with} \quad \theta'_b < \theta'_a \qquad (1.27)$$

$$\dot{\gamma}_b = a\dot{\theta}'_b = r\dot{\theta}'_a = \dot{\gamma}_r \quad \text{with} \quad \dot{\theta}'_b < \dot{\theta}'_a \qquad (1.28)$$

The moment M_b is therefore given by:

$$M_b = \frac{2\pi}{{\theta'_b}^3}\int_0^{\gamma_r} \tau\gamma^2 d\gamma \qquad (1.29)$$

Where the integral is identical to that in Eq. (1.43), thus, by substituting, M_a becomes:

$$M_a = \frac{{\theta'_b}^3}{{\theta'_a}^3} M_b + \frac{2\pi}{{\theta'_a}^3}\int_{\gamma_r}^{\gamma_a} \tau\gamma^2 d\gamma \qquad (1.30)$$

The difference between the two moments acting on the specimens is:

$$M_a - M_b = \left(\frac{{\theta'_b}^3 - {\theta'_a}^3}{{\theta'_a}^3}\right) M_b + \frac{2\pi}{{\theta'_a}^3} \int_{\gamma_r}^{\gamma_a} \tau \gamma^2 d\gamma \qquad (1.31)$$

Now, considering the first specimen, as the radius r approaches a, the difference $M_a - M_b$ tends to dM, and the other quantities tend to:

$$M_b \to M_a, \qquad \left(\frac{{\theta'_b}^3 - {\theta'_a}^3}{{\theta'_a}^3}\right) \to -3\frac{d\theta'}{\theta'}, \qquad \tau\gamma^2 d\gamma \to \tau a^3 {\theta'}^2 d\theta' \qquad (1.32)$$

Substituting into Eq. (1.31), it becomes:

$$dM = -\frac{3M\, d\theta'}{\theta'} + \frac{2\pi\tau a^3 d\theta'}{\theta'} \qquad (1.33)$$

Rearranging:

$$\tau = \frac{1}{2\pi a^3}\left(3M + \theta' \frac{dM}{d\theta'}\right) \qquad (1.34)$$

At this point, it can be observed that the Eq. (1.34) is identical to Nadai's Eq. (1.21), but the difference lies in the fact that it is not limited to materials insensitive to strain rate, provided that dM is obtained from a torque-twist curve that satisfies the conditions under which the derivation was made, that are:

$$a{\theta'}_b = r{\theta'}_a, \quad {\dot{\theta}'}_b = r{\dot{\theta}'}_a \quad \Rightarrow \quad \frac{\theta_b}{\dot{\theta}_b} = \frac{\theta_a}{\dot{\theta}_a} \qquad (1.35)$$

Such a condition necessitates that, if shear stress values are to be derived from a single torque-twist record, the twist rate must vary in proportion to the amount of twist:

$$\dot{\theta} = \theta \frac{\dot{\theta}_a}{\theta_a} \qquad (1.36)$$

where $\dot{\theta}_a$ represents the twist rate at a specific reference value of twist θ_a.

Since $\gamma_a = a\theta_a$ and $\dot{\gamma}_a = a\dot{\theta}_a$, the shear stress values determined through the application of Eq. (1.34) to this type of torque-twist record would correspond to a different $\dot{\gamma}$ for each value of γ. The utilization of such records necessitates the assumption that τ depends solely upon γ and the instantaneous value of $\dot{\gamma}$. However, this assumption is generally invalid, as the shear stress is also influenced by the strain-rate history.

Consequently, the desired torque-twist curve must be constructed through tests conducted at constant strain rate. A composite curve relating to the "constructed" torque, may be established by selecting the torque level for any given value of θ at the twist rate, $\dot{\theta}$, required to satisfy Eq. (1.36). Using the constructed curve, values of τ can be computed from Eq. (1.34). However, the effort could be considerable, as the resulting stress- strain curve relates τ and γ for $\dot{\gamma}$ increasing in proportion to γ. A group of constructed torque-twist curves would be required, each representing a different, constant value of $\dot{\theta}/\theta$, and the corresponding group of τ-γ curves derived from such data could then be cross-plotted to yield curves for constant $\dot{\gamma}$, as shown in *Fig. 1.14.*

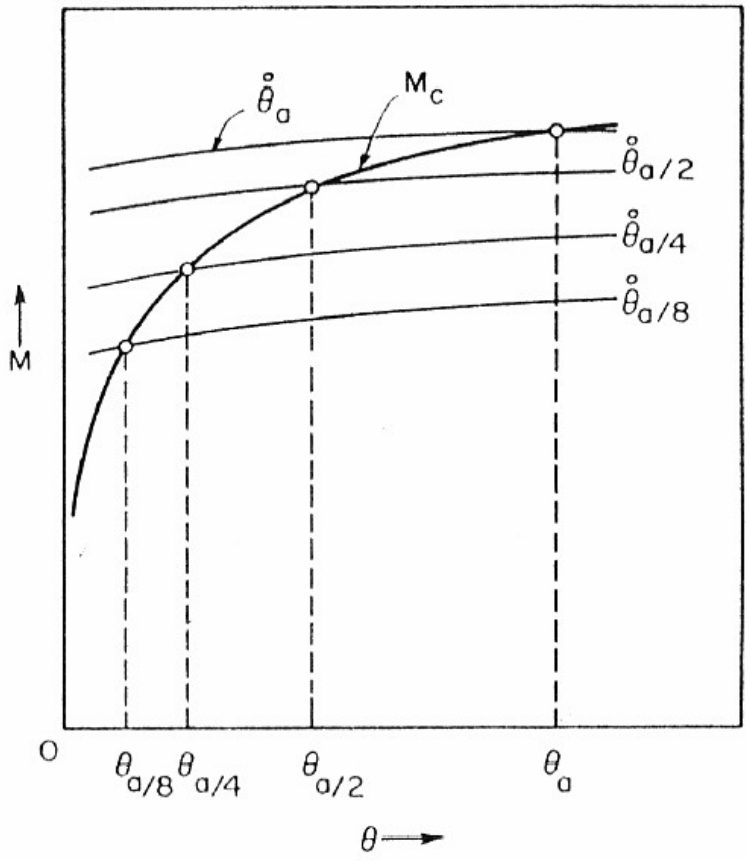

Fig. 1.14 Construction of a torque-twist curve where $\frac{\dot{\theta}}{\theta} = \frac{\dot{\theta}_a}{\theta_a}$, derived from torque-twist records at constant twist rates [10].

An alternative method could involve conducting differential tests. It is indeed possible to obtain a sufficient number of values of τ by taking advantage of the fact that plots in logarithmic coordinates of M-θ at constant $\dot{\theta}$ and of M-$\dot{\theta}$ at constant θ often coincide with straight lines. Considering a constant temperature during torsion tests at various constant rates of twist, the change in torque due to infinitesimal twisting is:

$$\frac{dM}{d\theta} = \left(\frac{\partial M}{\partial \theta}\right)_{\dot{\theta}} + \left(\frac{\partial M}{\partial \dot{\theta}}\right)_{\theta} \frac{d\dot{\theta}}{d\theta} \qquad (1.37)$$

If $\frac{d\dot{\theta}}{d\theta}$ is consistent with Eq. (1.36), it is possible write:

$$\frac{d\dot{\theta}}{d\theta} = \frac{\dot{\theta}_a}{\theta_a} = \frac{\dot{\theta}}{\theta} \qquad (1.38)$$

And substituting into Eq. (1.37):

$$\frac{dM}{d\theta} = \left(\frac{\partial M}{\partial \theta}\right)_{\dot{\theta}} + \left(\frac{\partial M}{\partial \dot{\theta}}\right)_{\theta} \frac{\dot{\theta}}{\theta} \qquad (1.39)$$

Now, since $d \ln x = \frac{dx}{x}$:

$$\frac{dM}{d\theta} = \frac{M}{\theta}\left(\frac{\partial \ln M}{\partial \ln \theta}\right)_{\dot{\theta}} + \frac{M}{\dot{\theta}}\left(\frac{\partial \ln M}{\partial \ln \dot{\theta}}\right)_{\theta} \frac{\dot{\theta}}{\theta} \qquad (1.40)$$

Denoting with n the slop of the curve M-θ at constant $\dot{\theta}$ and with m the slop of the curve M-$\dot{\theta}$ at constant θ and substituting into Eq. (1.34), the value of the stress on the surface of the specimen can be calculated as:

$$\tau = \frac{M}{2\pi a^3}(3 + n + m) \qquad (1.41)$$

1.3. FLOW STRESS DATA FOR FEM SIMULATION OF METAL FORMING PROCESSES

1.3.1. Introduction to the theory of finite element simulation

The finite element method (FEM) is a powerful numerical technique widely used to solve complex engineering and scientific problems that can be modeled by partial differential equations (PDEs). Initially developed in the late 1950s and early 1960s, FEM emerged from the need to address the complexities of structural engineering, where elasticity and stress analysis equations required efficient computational solutions. Over the years, FEM has evolved into a versatile tool applied in various fields such as fluid dynamics, heat transfer, electromagnetics, and metal forming processes [6,26].

The key concept behind FEM is to discretize a continuous problem (involving infinite degrees of freedom) into a system with a finite number of unknowns, which can be solved using computers. The finite elements that form the mesh, are connected at discrete points known as nodes, and a system of equations is generated to approximate the behavior of the entire structure or material. The ability of finite element codes to manage complex geometries, varying material properties, and boundary conditions has established FEM as a leading tool in computational mechanics.

A typical finite element analysis consists of three main stages:

- *Preprocessing*: where a model is created, a mesh of finite elements is overlaid on the geometry, and the boundary conditions of the problem are set;
- *Analysis:* where the system of equations is solved using the finite element code;
- *Postprocessing:* which interprets and visualizes the results (such as displacements and stresses) typically presented visually through graphical representations.

In metal forming, FEM plays a crucial role due to the highly nonlinear nature of these processes, which involve large deformations, nonlinear material behavior, and contact with friction. Traditional analytical methods fall short in predicting the complex interaction of stresses, strains, and temperatures that occur during metal forming.

FEM, however, can accommodate these factors by solving the governing equations numerically for the entire material undergoing deformation [27–29]. The ability to use FEM in metal forming processes has revolutionized how industries approach manufacturing. The design and optimization of processes are made possible through the use of the codes, enabling the simulation of plastic deformation, stress distribution, and temperature variations under different conditions. This eliminates the need for costly and time-consuming experimental setups, thereby accelerating development and significantly reducing production costs. Fig. 1.15 shows some applications of FEM simulation applied to metal forming processes

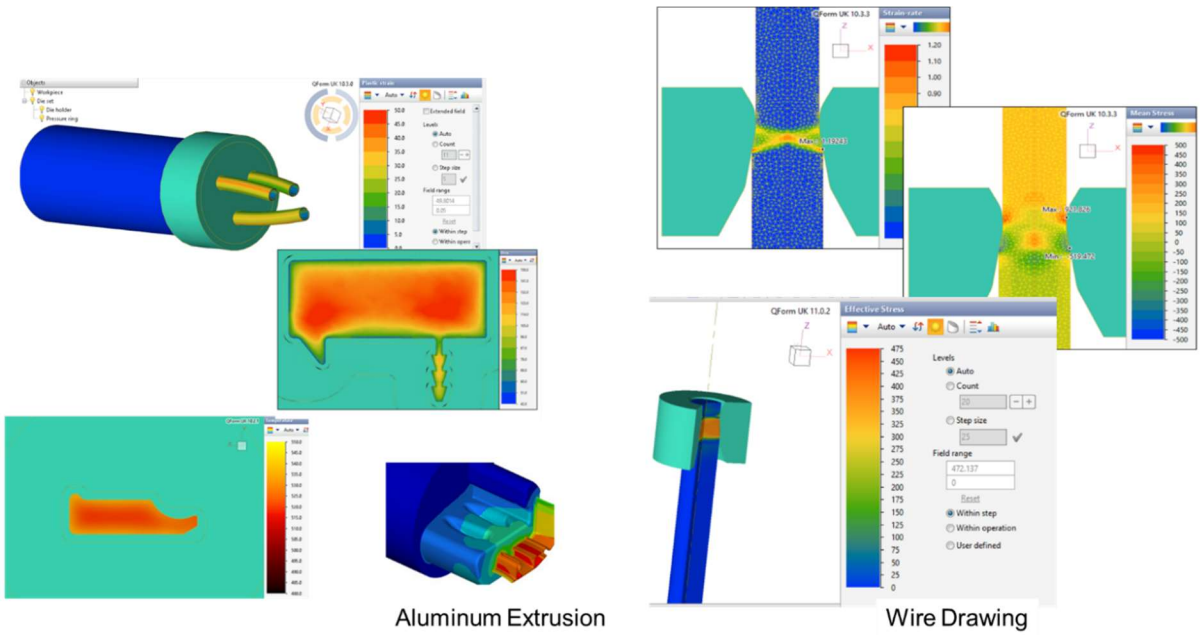

Fig. 1.15 Examples of numerical simulations of metal forming processes.

Currently, several commercial numerical codes are available on the market, each of which employs different simulation methodologies and approaches. The two dominant methodologies are the Lagrangian and Eulerian approaches [30,31]:

- *Lagrangian Approach*: in this method, the computational mesh follows the material particles, meaning that as the material deforms, the mesh deforms with it. This approach is highly accurate for simulations of material deformation but can become computationally expensive when large deformations occur. Severe mesh distortion necessitates remeshing, a process that increases computational time. However, it remains widely used in metal forming

simulations due to its precision in tracking material movement during processes like forging and stamping (Fig. 1.16).

- *Eulerian Approach*: Unlike the Lagrangian approach, the Eulerian method keeps the mesh fixed in space while the material flows through it. This approach is particularly useful in situations where the final geometry is known, but the material undergoes significant deformations. The Eulerian method simplifies the problem by avoiding mesh distortion, but it requires a priori knowledge of the final product's shape, making it less flexible in some applications (Fig. 1.16).
- *Arbitrary Lagrangian-Eulerian Approach (ALE)*: The ALE method combines the benefits of both Lagrangian and Eulerian approaches by allowing the mesh to move with the material in some regions and remain fixed in others. This offers a balance between accuracy and computational efficiency, making it suitable for simulations that involve complex material flows and boundary conditions.

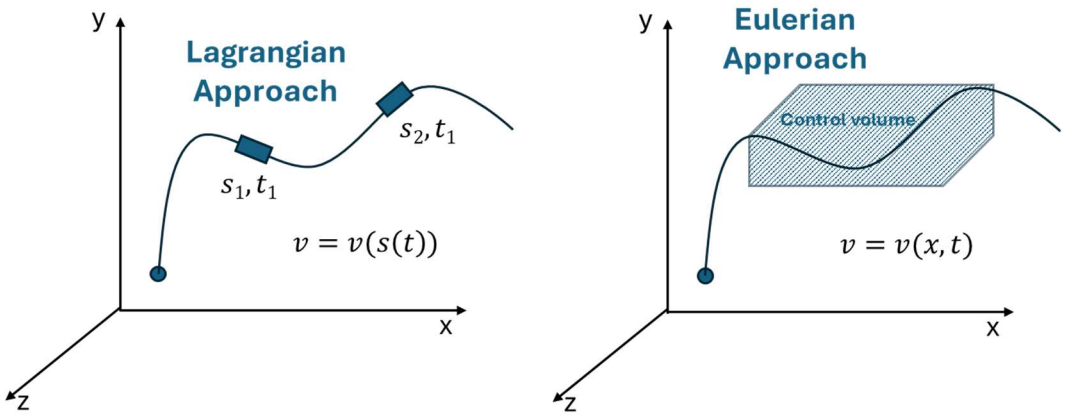

Fig. 1.16 Schematization of the Lagrangian and the Eulerian Approaches.

One of the most critical aspects of FEM simulations is the accurate characterization of the material's mechanical properties. In metal forming simulation, to produce reliable and predictive results, it is essential to input the correct flow stress data for the material being modeled. Without accurate material characterization, the simulation may yield inaccurate predictions of stress distribution, deformation, and failure modes. Since metal forming processes often involve materials undergoing large plastic deformations at elevated temperatures, the temperature-dependent behavior of materials must also

be accounted for. Incorrect assumptions about the material's stress-strain relationship can lead to unreliable simulations, potentially causing costly errors in the manufacturing process.

1.3.2. Constitutive models for material flow stress

For a given material, the relationships between stress and strain components can be expressed through constitutive equations, which describe how the material responds to applied loads. These constitutive laws form the basis for modeling the material's mechanical behavior under various conditions. In most finite element method (FEM) software, it is possible to input the material's flow stress behavior in one of two ways: either by directly providing tabulated experimental data obtained from characterization tests, or by using a constitutive law based on known material coefficients (Fig. 1.17).

When experimental data from material characterization tests is available, using tabular input is often the simpler and quicker approach. However, it is essential to pay close attention to the range of temperature and strain rate conditions under which the material was characterized. If, during the simulated process, the material undergoes conditions beyond the characterized range, the FEM code extrapolates the stress-strain values. This extrapolation can introduce errors, leading to unreliable results and inaccurate predictions in the simulation. Thus, care must be taken to ensure that the material remains within its tested range during the simulation.

On the other hand, when using a constitutive equation, the material's behavior under varying conditions of strain rate and temperature is known in advance, even outside the characterized range. This approach ensures a more robust and predictive model, provided that the correct constitutive law is chosen. It is, therefore, critical to select the appropriate constitutive model based on the specific process being simulated to ensure accuracy and reliability. The most commonly used constitutive models in FEM are employed to simulate plastic deformation, which is inherently nonlinear due to strain hardening or softening, strain-rate sensitivity, and the material's response to temperature changes.

Over the years, numerous constitutive equations have been developed and integrated into FEM codes to model material behavior. Among the most widely used are the exponential (strain hardening) model for its simplicity [1], the hyperbolic sine model proposed by Garofalo [32], and the more complex Hansel-Spittel model [33].

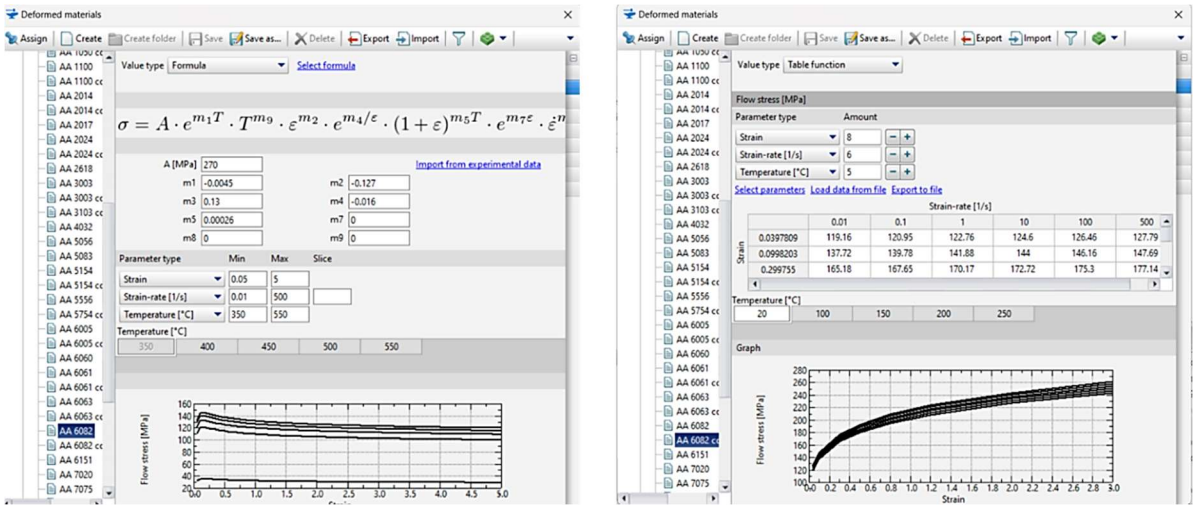

Fig. 1.17 Input of material flow stress in QForm UK®: example using the Hansel-Spittel model and tabular form.

Strain hardening Model

The exponential model, also known as the strain hardening model, is one of the simplest and most widely used constitutive equations for modeling material flow stress. The general form of this model is:

$$\bar{\sigma} = K\bar{\varepsilon}^{n} \tag{1.42}$$

Where n represents the strain-hardening exponent, while K is the strength coefficient. When plotting equivalent stress versus equivalent strain on a log-log scale, the resulting graph will form a straight line. The slope of this line corresponds to the value of n, and K is the stress value when the strain is 1.0. The strain-hardening exponent can range from $n = 0$ for a perfectly plastic material to $n = 1$ for an ideal elastic material.

Deviations from Eq. (1.42) are frequently observed, particularly at low or high strain levels. In some cases, data, that deviate from the expected behavior, can fit the modified relationship in Eq. (1.43):

$$\bar{\sigma} = K(\varepsilon_0 + \bar{\varepsilon})^{n} \tag{1.43}$$

Where ε_0 represents the pre-existing strain in the material prior to the characterization test.

Another commonly applied variation is Eq. (1.44) (Ludwik) [1]:

$$\bar{\sigma} = \sigma_0 + K\bar{\varepsilon}^n \tag{1.44}$$

Where σ_0 is the yield stress. The Ludwik equation is often preferred because it accounts for the fact that Eq. (1.43) implies zero stress at zero strain, which is not physically accurate. The value of σ_0 can be obtained by extrapolating the strain-hardening portion of the stress-strain curve to intersect with the elastic modulus line, providing a more realistic representation of material behavior at low strains.

Finally, another variation is obtained by also considering the effect of the strain rate on material flow stress, as represented in Eq. (1.45).

$$\bar{\sigma} = K\bar{\varepsilon}^n\dot{\bar{\varepsilon}}^m \tag{1.45}$$

Where m is the strain-rate sensitivity exponent.

This equation reflects how the material hardens as strain increases (strain hardening) and how strain rate affects the flow stress. Strain hardening is important in cold-forming processes, where materials become stronger as they are deformed, making it harder to continue the deformation. However, one limitation of this model is that it does not account for the effect of temperature on the flow stress. As a result, different sets of parameters must be determined for each temperature, making it less efficient for processes where temperature varies significantly.

Hyperbolic Sine Model

A more sophisticated constitutive model that addresses some of the limitations of the exponential model is the hyperbolic sine model. This model, proposed by Garofalo [32] and commonly used in conjunction with the Zener-Hollomon parameter, provides a more accurate prediction of material flow stress over a wide range of deformation conditions, particularly where high temperatures are involved. The Zener-Hollomon parameter (Z) is a temperature-compensated strain rate that is used extensively in creep studies to relate the deformation behavior of materials to stress and temperature conditions. The flow stress of a material can be correlated with Z in different forms depending on the stress range. At relatively low stresses, the flow follows a power law

(exponential form), while at higher stresses it transitions to a hyperbolic sine law, as shown in Eq. (1.46) [18]:

$$Z = \dot{\varepsilon}\, e^{\left(\frac{Q}{RT}\right)} = \begin{cases} B\bar{\sigma}^{n'} \\ A' e^{(\beta\bar{\sigma})} \\ A[\sinh(\alpha\bar{\sigma})]^{n} \end{cases} \qquad (1.46)$$

Where T is the absolute temperature, R is the universal gas constant, $B, A', A, n, n', \beta,$ and α are material constants. The stress multiplier α is an adjustable constant that allows scaling of the hyperbolic sine term to ensure that straight parallel lines appear in a plot of $ln(\dot{\varepsilon})$ versus $ln[sinh(\alpha\bar{\sigma})]$. While the deformation activation energy Q is found as in Eq. (1.47) [17]:

$$Q = -R \left.\frac{\partial \ln \dot{\varepsilon}}{\partial (1/T)}\right|_{\bar{\sigma}} \qquad (1.47)$$

A significant limitation of this model is that it is strain-independent. This means that while it accurately predicts stress as a function of temperature and strain rate, it does not account for changes in stress due to increasing strain during deformation. Consequently, for processes where large strains are involved, such as bulk metal forming, the model may lead to inaccuracies because it assumes that the stress remains constant as strain increases [34].

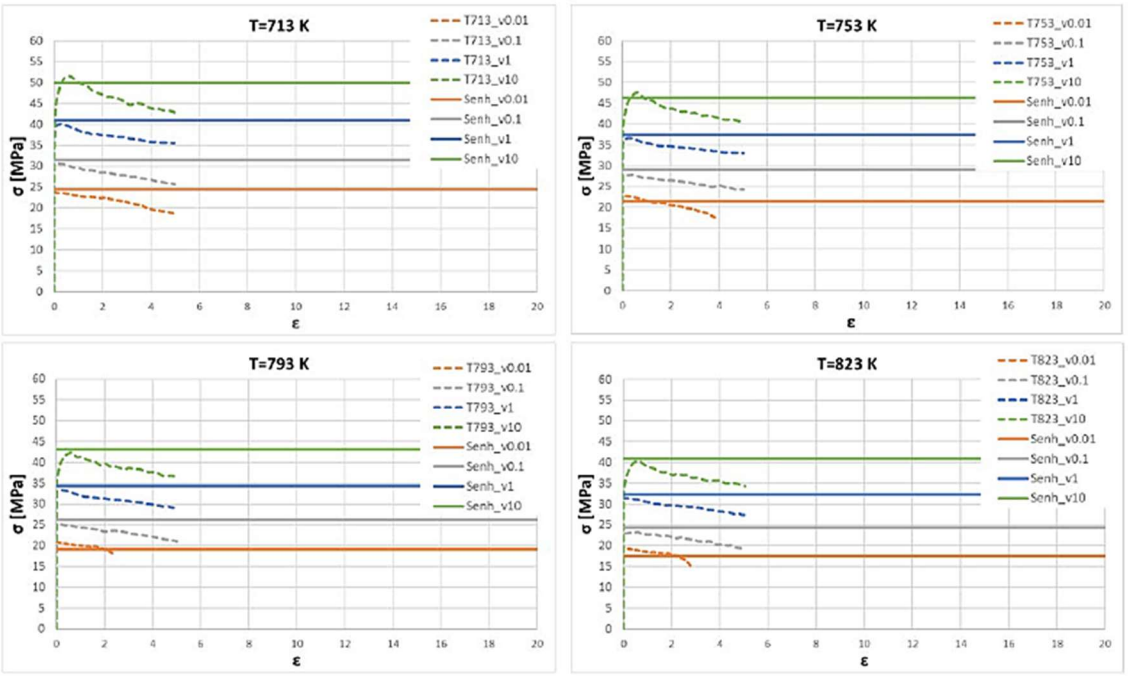

Fig. 1.18 Example of comparison between the torsion test experimental σ-ε curves (dashed lines) and the stress values predicted by Sinh law (solid lines) [35].

Fig. 1.18 presents a comparison between the experimental flow stress curves obtained from torsion tests on an aluminum alloy under various temperature and strain rate conditions, indicated with dashed lines, and the predicted flow stress curves based on the Hyperbolic Sine model, represented with solid lines. It is evident that the flow stress curves derived from the hyperbolic sine model do not change with varying strain.

Hansel Spittel Model

A more accurate model for predicting the flow stress behavior of materials is the Hansel-Spittel model [33], which incorporates nine material parameters to describe the flow stress as a function of temperature, strain rate, and strain. This model offers improved accuracy in capturing the material's response under varying conditions. However, one major limitation of the Hansel-Spittel law is the difficulty in regressing the constitutive parameters, which makes the process challenging. Moreover, the availability of comprehensive literature on this method remains limited [18,34,36–38].

The complexity of regression methods required to determine these constants makes the model difficult to implement, especially when reliable data for large strains, strain rates, and temperatures are not available. Additionally, the accuracy of this model is highly sensitive to the quality of experimental data, which can introduce errors if the material is not well-characterized. To accurately perform the regression of the coefficients then it is necessary to conduct numerous tests, varying the temperature under constant strain rate conditions and, conversely, varying the strain rate at constant temperature. For this reason, a comprehensive characterization through the torsion test, which allows trials maintaining constant temperature and strain rate, reaching large strain values, is essential.

The general form of the Hansel-Spittel equation is:

$$\bar{\sigma} = Ae^{m_1 T}\bar{\varepsilon}^{m_2}\dot{\bar{\varepsilon}}^{m_3}e^{\frac{m_4}{\bar{\varepsilon}}}(1+\bar{\varepsilon})^{m_5 T}e^{m_7\bar{\varepsilon}}\dot{\bar{\varepsilon}}^{m_8 T}T^{m_9} \qquad (1.48)$$

The H-S law can be used in a simplified form, using only 5 material coefficients, or getting all 9 of them, and they assume different values depending on whether the temperature is expressed in °C or K. The coefficients m_1 and m_9 define the material's sensitivity to temperature, m_5 defines the coupling temperature and strain, the term m_8

couple temperature and strain rate, m_2, m_4, and m_7 coefficients define the material's sensitivity to strain and m_3 depends on the material's sensitivity to strain rate.

This model offers a more accurate prediction of flow stress by considering the coupled effects of strain, strain rate, and temperature, as shown in the graph in Fig. 1.19, where the comparison between the experimental aluminum flow stress curves, indicated with dashed lines, and the predicted flow stress curves based on the Hansel-Spittel model, represented with solid lines, are reported. It is particularly useful in processes where all three variables vary dynamically, such as hot metal forming or forging.

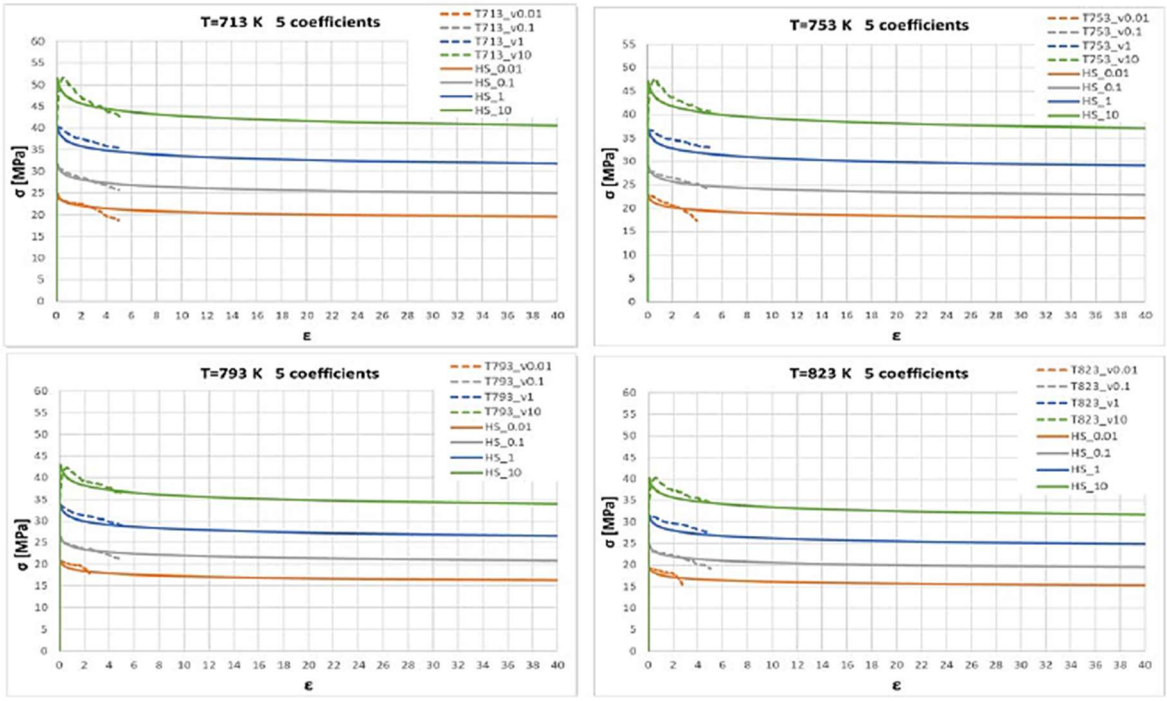

Fig. 1.19 Example of comparison between the torsion test experimental σ-ε curves (dashed lines) and the stress values predicted by Hansel-Spittel law (solid lines). [35]

1.4. CONCLUSIONS

This chapter has highlighted the crucial role of accurately characterizing plastic behavior of material in the design and optimization of metal forming processes. The discussion emphasized the importance of understanding the complex interactions of stress, strain, strain rate, and temperature in determining the material flow stress under plastic deformation. Accurately predicting flow stress is essential to avoid costly errors in process design and to maximize material utilization efficiency.

Traditional methods of material characterization, such as tensile and compression testing, although readily available, have significant limitations for metal forming applications. As outlined in this chapter, tensile tests suffer from necking, leading to nonuniform deformation and making it difficult to obtain accurate stress-strain data beyond the yield point. While compression tests avoid necking, they introduce barreling, another source of nonuniform deformation that compromises measurement accuracy. Furthermore, both methods typically provide data at strain levels significantly lower than those encountered in industrial metal forming processes, necessitating extrapolation that can be unreliable. Therefore, this chapter has underscored the critical need for alternative test methods capable of operating under high strain and strain rate conditions.

Torsion testing, discussed in detail in this chapter, has emerged as a suitable method for overcoming the limitations of tensile and compression testing. The primary advantages of the torsion test lie in the fact that the specimen maintains a relatively stable geometry during testing. This stability allows for the maintenance of a constant strain rate throughout the experiment, enables the achievement of large deformation values, and permits testing across a wide range of temperatures. The efficient use of induction heating, with the solenoid precisely centered on the gauge section, ensures uniform heating. Additionally, temperature control is optimized through a PID system and a thermocouple inserted in the specimen, providing accurate regulation of the testing conditions. However, analyzing and interpreting data from torsion tests present certain challenges. Converting torque and twist angle data into stress-strain curve requires the application of appropriate models, each with its own assumptions and limitations. This chapter discussed the Saint-Venant model, appropriate for elastic deformation, and the Nadai and Fields-Backofen models, which are more applicable

to plastic deformation. The limitations of these models were highlighted, particularly the limited applicability of the Saint-Venant model to plastic deformation and the insensitivity of the Nadai model to strain rate, along with its reliance on precise torque-twist curves. The Fields-Backofen model, which accounts for strain rate sensitivity, was presented as a more versatile option, although it requires a more complex experimental setup and analysis. Therefore, the choice of the appropriate model critically depends on the specific material being characterized and the range of deformation conditions.

Finally, the chapter highlighted the important role that FEM simulation play in the metal forming industry and how precise material characterization is an essential input into the numerical code to perform accurate simulations. Flow stress data can be inserted, either directly as tabulated experimental data or through constitutive models. The chapter described the use of constitutive models, including the strain hardening, hyperbolic sine, and Hansel-Spittel models, in representing the flow stress of materials in FEM simulations. Each model offers varying degrees of complexity and accuracy. Tabulated data provide the highest accuracy but are constrained by the experimental conditions and require significant experimental effort for full data coverage. Constitutive models offer broader applicability but require careful model selection and accurate parameter determination. The choice between these approaches depends on balancing accuracy, computational efficiency, and the extent of available experimental data.

In the next chapters, detailed experimental activities involving cold and hot torsion tests performed on different metals will be described to thoroughly characterize the material flow stress. These activities will also explore the application of the acquired data in the optimization of industrial processes such as extrusion and drawing, using both analytical models and FEM simulations.

REFERENCES

[1] Dieter GE, Kuhn HA, Semiatin SL, editors. Handbook of workability and process design. Materials Park, Ohio: ASM International; 2003.

[2] Semiatin SL, editor. Metalworking: Bulk Forming. ASM International; 2005. https://doi.org/10.31399/asm.hb.v14a.9781627081856.

[3] P C S. Multi directional forging: an advanced deforming technique for severe plastic deformation. Advanced Welding and Deforming, Elsevier; 2021, p. 529–56. https://doi.org/10.1016/B978-0-12-822049-8.00017-7.

[4] Jacob Lubliner. PLASTICITY THEORY. Revised Edition (PDF). University of California at Berkeley: 1990.

[5] Chakrabarty J. Theory of plasticity. 3rd ed. Amsterdam: Elsevier; 2006.

[6] Donati L, Reggiani B, Pelaccia R, Negozio M, Di Donato S. Advancements in extrusion and drawing: a review of the contributes by the ESAFORM community. Int J Mater Form 2022;15:41. https://doi.org/10.1007/s12289-022-01664-w.

[7] Hodierne FA. A torsion Test for Use in Metalworking Studies. JOURNAL OF THE INSTITUTE OF METALS 1962;91.

[8] Verlinden B. THE STUDY OF HOT WORKABILITY BY HOT TORSION. ATB METALLURGIE XXIX 1989;3–4:39–48.

[9] Nadai A. Theory of Flow and Fracture. vol. 1. 2nd ed. McGraw-Hill; 1950.

[10] Fields Jr, Backofen WA. Determination of strain-hardening characteristics by torsion testing. Proc Am Soc Test Mater 1957;57:1259–72.

[11] Shrivastava SC, Jonas JJ, Canova G. Equivalent strain in large deformation torsion testing : Theoretical and practical considerations. Journal of the Mechanics and Physics of Solids 1982;30:75–90. https://doi.org/10.1016/0022-5096(82)90014-X.

[12] Canova GR, Kocks UF, Jonas JJ. Theory of torsion texture development. Acta Metallurgica 1984;32:211–26. https://doi.org/10.1016/0001-6160(84)90050-6.

[13] Gräber A, Pöhlandt K. State of the art of the torsion test for determining flow curves. Steel Research 1990;61:212–8. https://doi.org/10.1002/srin.199000334.

[14] Khoddam S, Lam YC, Thomson PF. The effect of specimen geometry on the accuracy of the constitutive equation derived from the hot torsion test. Steel Research 1995;66:45–9. https://doi.org/10.1002/srin.199501086.

[15] Bressan JD, Unfer RK. Construction and validation tests of a torsion test machine. Journal of Materials Processing Technology 2006;179:23–9. https://doi.org/10.1016/j.jmatprotec.2006.03.099.

[16] Spigarelli S. Study of hot workability of a heat treated AA6082 aluminum alloy. Scripta Materialia 2003;49:179–83. https://doi.org/10.1016/S1359-6462(03)00206-9.

[17] Donati L, El Mehtedi M. Characterization Of Flow Stress Of Different AA6082 Alloys By Means Of Hot Torsion Test, Belfast, (United Kingdom): 2011, p. 455–60. https://doi.org/10.1063/1.3589557.

[18] El Mehtedi M, Spigarelli S, Gabrielli F, Donati L. Comparison Study of Constitutive Models in Predicting the Hot Deformation Behavior of AA6060 and AA6063 Aluminium Alloys. Materials Today: Proceedings 2015;2:4732–9. https://doi.org/10.1016/j.matpr.2015.10.006.

[19] Chattopadhyay S, Qu J, Nuri A, Hasan S, Kundu N. Torsion Tests to Study Plastic Deformation in Ductile Materials. 2017 ASEE Annual Conference & Exposition Proceedings, Columbus, Ohio: ASEE Conferences; 2017, p. 29032. https://doi.org/10.18260/1-2--29032.

[20] Zhang M, Deng L, Wang B, Xiang H. Effect of torsional rate on the gradient microstructure, texture evolutions and microhardness of pure copper. Materials Characterization 2020;161:110141. https://doi.org/10.1016/j.matchar.2020.110141.

[21] Chen X, Du Y, Du K, Lian T, Liu B, Li Z, et al. Identification of the Constitutive Model Parameters by Inverse Optimization Method and Characterization of Hot Deformation Behavior for Ultra-Supercritical Rotor Steel. Materials 2021;14:1958. https://doi.org/10.3390/ma14081958.

[22] Niu L, Zhang Q, Wang B, Han B, Li H, Mei T. A modified Hansel-Spittel constitutive equation of Ti-6Al-4V during cogging process. Journal of Alloys and Compounds 2022;894:162387. https://doi.org/10.1016/j.jallcom.2021.162387.

[23] Wang J, Xiao G, Zhang J. A new constitutive model and hot processing map of 5A06 aluminum alloy based on high-temperature rheological behavior and higher-order gradients. Materials Today Communications 2023;36:106502. https://doi.org/10.1016/j.mtcomm.2023.106502.

[24] de A.J.C.B. Saint-Venant. Mémoire sur la torsion des prismes, avec des considérations sur leur flexion ainsi que sur l'équilibre intérieur des solides élastiques en général, et des formules pratiques pour le calcul de leur résistance à divers efforts s'exercant simultanément. vol. 14. 1856.

[25] de A.J.C.B. Saint-Venant. Mémoire sur la flexion des prismes, sur les glissements transversaux et longitudinaux qui l'accompagnent lorsqu'elle ne s'opére pas uniformément ou en arc de cercle, et sur la forme courbe affectée alors par leurs sections transversales primitivement planes. vol. 1. 1856.

[26] Claes Johnson. Numerical Solution of Partial Differential Equations by the Finite Element Method. Mineola, New York: DOVER PUBLICATIONS, INC; 2009.

[27] Dodds RH. Numerical techniques for plasticity computations in finite element analysis. Computers & Structures 1987;26:767–79. https://doi.org/10.1016/0045-7949(87)90026-5.

[28] Klocke F, Beck T, Hoppe S, Krieg T, Müller N, Nöthe T, et al. Examples of FEM application in manufacturing technology. Journal of Materials Processing Technology 2002;120:450–7. https://doi.org/10.1016/S0924-0136(01)01210-9.

[29] Chenot J-L, Massoni E. Finite element modelling and control of new metal forming processes. International Journal of Machine Tools and Manufacture 2006;46:1194–200. https://doi.org/10.1016/j.ijmachtools.2006.01.031.

[30] Donea J, Giuliani S, Halleux JP. AN ARBITRARY LAGRANGIAN-EULERIAN FINITE ELEMENT FOOD FOR ~NSIENT DYNAMIC ~U~~U~T~ ERECTIONS n.d.

[31] Hughes TJR, Liu WK, Zimmermann TK. Lagrangian-Eulerian finite element formulation for incompressible viscous flows. Computer Methods in Applied Mechanics and Engineering 1981;29:329–49. https://doi.org/10.1016/0045-7825(81)90049-9.

[32] Garofalo F. An empirical relation defining the stress dependence of minimum creep rate in metals. Transactions of the Metallurgical Society of Aime 1963;227:351–6.

[33] Hansel A, Spittel T. Kraft-und Arbeitsbedarf Bildsamer Formgebungsverfahren. Leipzig, Germany: Deutscher Verlag für Grundstoffindustrie; 1978.

[34] El Mehtedi M, Musharavati F, Spigarelli S. Modelling of the flow behaviour of wrought aluminium alloys at elevated temperatures by a new constitutive equation. Materials & Design (1980-2015) 2014;54:869–73. https://doi.org/10.1016/j.matdes.2013.09.013.

[35] Di Donato S, Pelaccia R, Negozio M, Mehtedi ME, Reggiani B, Donati L. Hot Torsion Tests of AA6082 Alloy. Key Engineering Materials 2024;988:21–9. https://doi.org/10.4028/p-5c0LIi.

[36] Chen X, Du Y, Du K, Lian T, Liu B, Li Z, et al. Identification of the Constitutive Model Parameters by Inverse Optimization Method and Characterization of Hot Deformation Behavior for Ultra-Supercritical Rotor Steel. Materials 2021;14:1958. https://doi.org/10.3390/ma14081958.

[37] Wang H, Wang W, Zhai R, Ma R, Zhao J, Mu Z. Constitutive Equations for Describing the Warm and Hot Deformation Behavior of 20Cr2Ni4A Alloy Steel. Metals 2020;10:1169. https://doi.org/10.3390/met10091169.

[38] Niu L, Zhang Q, Wang B, Han B, Li H, Mei T. A modified Hansel-Spittel constitutive equation of Ti-6Al-4V during cogging process. Journal of Alloys and Compounds 2022;894:162387. https://doi.org/10.1016/j.jallcom.2021.162387.

Chapter 2

COLD TORSION TEST ON ETP COPPER: APPLICATION IN THE WIRE DRAWING INDUSTRIAL PROCESS

2.1. CHAPTER OVERVIEW

This chapter explores the plastic behavior of ETP copper under various loading conditions, specifically focusing on tensile, compression, and torsion tests. The chapter starts by introducing the material and the experimental procedures used, including the specimen geometry and the testing setup. Methods for processing the data from the different tests are investigated, outlining the steps to accurately determine the flow stress of the material. The results from the tensile, compression, and torsion tests will be compared and evaluated. Special emphasis will be placed on the characterization of the material up to large strains, a crucial requirement for industrial cold working processes such as wire drawing. The discrepancies between the flow stress values obtained from the different tests will be discussed, and a new model for processing cold torsion test data will be proposed. The model will be validated through a designed hybrid compression test, demonstrating its effectiveness in aligning the torsion flow stress data with those obtained from tensile and compression tests. Additionally, the entire analysis is supported by FEM simulations of the tests, providing further insights into the material's behavior under various loading conditions.

The material flow stress obtained from the cold torsion tests will be then applied in an industrial case study focused on the multi-pass wire drawing process for the production of electrical cables. Experimental, analytical, and numerical analysis of the process will be performed, and a theoretical model for the calculation of the stresses acting on the wire will be developed, focusing on the entire multi-pass process.

2.2. COMPARISON BETWEEN TENSILE, COMPRESSION, AND TORSION TESTS PERFORMED ON ETP COPPER

2.2.1. Introduction

The term "cold-working" refers to the process of plastic deformation of a metal carried out at temperatures below its recrystallization temperature. This temperature is typically defined as 35% to 50% of the metal's absolute melting point. Unlike the melting point, the recrystallization temperature is not sharply defined, but it represents the threshold below which the metal retains its work-hardened structure without significant recovery or recrystallization occurring [4,5]. In cold deformation processes, accurately characterizing the workability of a material is critical for understanding its behavior under different forming operations. At lower temperatures, the material's intrinsic workability can be influenced by various factors such as stress state, strain rate, metallurgical structure, and processing variables [1].

Therefore, correct material characterization is essential to optimize deformation processes such as wire drawing or forging which are based on cold plastic deformation. There are several mechanical tests used to characterize the elastoplastic behavior and, thus, the flow stress of the material, with the most widely used and common being the tensile and compression tests. As explained in paragraph 1.2.2, the tensile test is a commonly used method for evaluating mechanical properties such as strength and ductility. However, its utility is limited in cold work applications by the onset of necking, which leads to strain localization and an inhomogeneous stress state that complicates the interpretation of results beyond moderate deformations. On the other hand, the compression test provides valuable information on material flow under compressive stresses, without the complications of necking. This test allows for larger deformations than tensile tests, but barreling effects and friction between the specimen and tools introduce complexities in interpreting the stress-strain data, especially when aiming to simulate cold deformation processes over extended ranges of strain. When it comes to characterizing materials for cold deformation processes that demand large strain accumulation, the torsion test emerges as the most suitable method. The specimen under torsion provides extended strain values, and it allows for the characterization of

the material under a constant strain rate since the geometry of the specimen does not change substantially during the test.

In the following paragraphs, a comparative evaluation of tensile, compression, and torsion tests, performed on ETP Copper (Electrolytic Tough Pitch Copper) is explored, with a focus on their relevance to cold plastic deformation and their effectiveness in characterizing material behavior at large strains. The principal physical and mechanical properties of ETP copper are reported in Table 2.1, while Fig. 2.1 displays a photograph of the specimens used in the various tests.

Table 2.1 ETP Copper basic properties.

MATERIAL BASIC PROPERTIES	**ETP Copper (Pure 99.95% in weight)**
Density	8940 [kg/m^3]
Thermal conductivity	390 [W/m·K]
Specific heat	390 [J/kg·K]
Young module	121000 [MPa]
Poisson	0.35
Thermal expansion	1.60635e-5 [1/°C]

Initially, the results from the compression and tensile tests were compared revealing that the flow stress curves are in good agreement, showing similar behavior up to a strain value of 0.33. After this point, the flow stress curve from the tensile test deviated significantly from the compression test curve. This discrepancy is attributed to the influence of necking, which affects the flow stress behavior in tensile test. In the past, several researchers have addressed the issue of processing tensile test data beyond the necking point. Ling [39] emphasized the complexities involved in accurately characterizing true stress-strain behavior after necking, underscoring the need for precise measurements to predict material failure. La Rosa et al. [40] numerically validated the Bridgman model, confirming its utility for both notched and unnotched specimens in describing stress distributions. They demonstrated the model's effectiveness in predicting material behavior under various loading conditions. Further investigations by La Rosa et al. [41] evaluated the limitations of the Bridgman method, particularly regarding the flow-stress to true-stress ratio, emphasizing that careful parameter selection is essential for accurate material characterization. Celentano et

al. [42] also validated the Bridgman method through both experimental and simulation approaches, reinforcing its significance in tensile behavior characterization. Kajberg and Lindkvist [43] introduced an inverse modeling technique using in-plane displacement fields for large-strain material characterization, addressing the limitations of traditional approaches. Additionally, Wang et al. [44] and Paul et al. [45] employed digital image correlation (DIC) techniques to refine strain measurement and analyze post-necking behavior, further contributing to the understanding of material behavior under complex deformation conditions.

Subsequently, the experimental data from the torsion tests were compared with those from tensile and compression tests, revealing that the flow stress values obtained from the torsion test are consistently lower than those derived from the other tests. The discrepancy between the flow stress of materials obtained from tensile and torsion tests has been highlighted in various studies in the past. Nadai et al. [46] and Davis [47] pointed out that materials exhibit different behaviors under tensile and torsional loading, with the latter often resulting in lower flow stress values. The foundational work by Bishop and Hill [48] established that these differences are likely attributed to variations in crystallographic anisotropy and the structural changes induced by torsional stresses compared to those produced by tensile loading. Canova et al. [49] and Shrivastava et al. [50] proposed several explanations for the observed discrepancies in flow stress values between torsion and tensile tests. One key factor they highlighted is the choice of yield criterion: using the von Mises yield criterion, which is common in torsion, may underestimate the equivalent stress compared to more precise models like the Bishop and Hill formulation. Additionally, the development of different textures during deformation plays a role, as torsion leads to distinct texture evolution compared to tension or compression, affecting the anisotropic material properties. Furthermore, they emphasized that differing rates of work hardening between torsion and tension contribute to the variation in flow curves. Ultimately, they suggest that the lower flow stresses observed in torsion tests likely result from a combination of these factors, making it critical to select an appropriate yield criterion and account for texture and work hardening influences.

Finally, the chapter presents a novel approach to processing torsion test data by incorporating a correction factor based on the Taylor factors, which account for the material's anisotropic behavior. The results indicated that the corrected flow stress

values from the torsion test were more in line with those from the tensile and compression tests. To validate the proposed model for processing torsion test data, a hybrid compression test was conducted. The hybrid test was designed to eliminate the effects of indeterminate friction between the specimen and the plates and to provide a more accurate representation of the material's true stress-strain curve. The numerical simulations for the hybrid compression test were performed using the QForm UK® software and the results were compared to the experimental data. The simulations provided a good match to the experimental data, validating the proposed model's accuracy. The results also demonstrated the model's robustness and reliability across various strain rates.

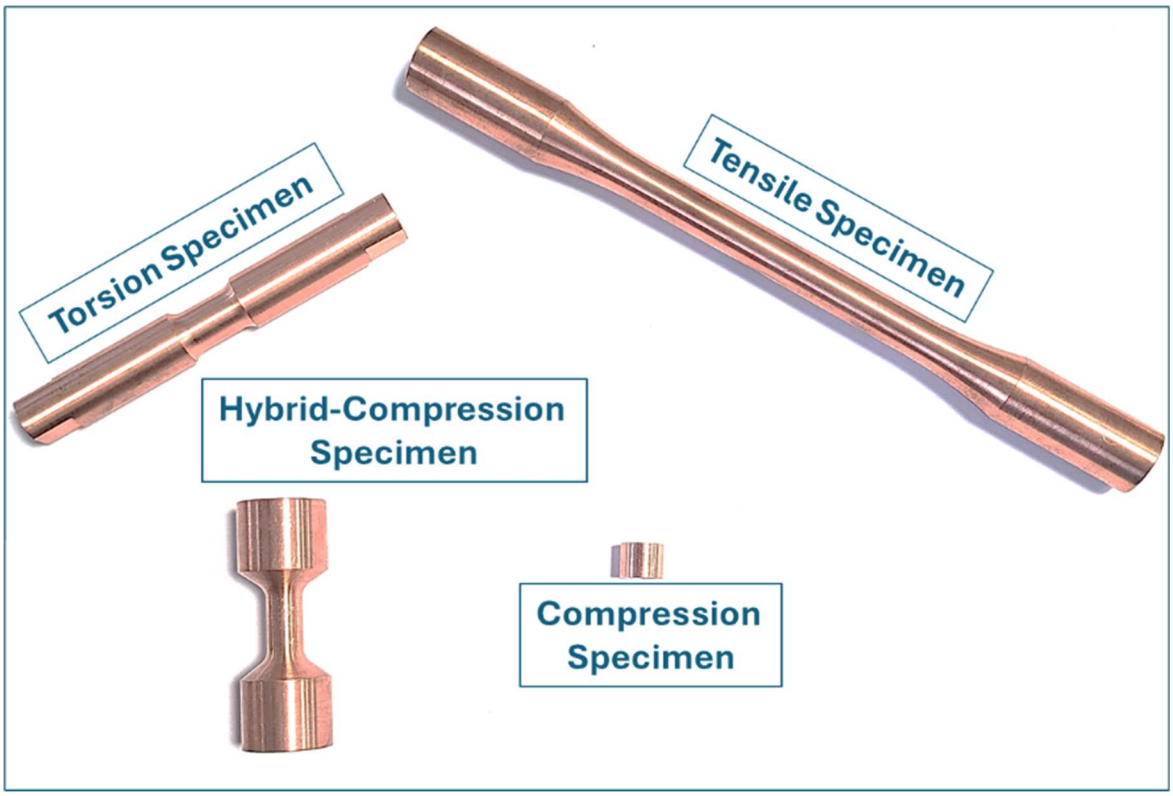

Fig. 2.1 Pictures of the ETP copper specimens used in the tests.

2.2.2. Experimental procedure

Tensile test

Fig. 2.2 Tensile specimen before and after the test.

Tensile tests were performed under displacement-controlled conditions using a servo-hydraulic INSTRON 8033 universal testing machine equipped with a 25 kN load cell. In *Fig. 2.2* a tensile specimen before and after the test is shown. During the test, a strain gauge was used to control the elongation of the specimen, while the cross-head rate was set to 0.8 mm/s, ensuring an average strain rate of 0.01 s^{-1}, as shown in *Table 2.2*, where the strain rate was calculated as in Eq.(2.1), in which V_p is the press cross-head speed, and L is the length of the specimen at each instant of time.

$$\dot{\varepsilon} = \frac{V_p}{L} \qquad (2.1)$$

The specimen was designed following the indications of the standard UNI EN ISO 6892-1, with a diameter of 10 mm and a length of 70 mm as shown in *Fig*. 2.3.

Table 2.2 Velocity parameters for the tensile and compression tests.

TENSILE				COMPRESSION			
Specimen length *[mm]*	Strain	Press cross-head speed *[mm/s]*	Strain rate *[s^{-1}]*	Specimen length *[mm]*	Strain	Press cross-head speed *[mm/s]*	Strain rate *[s^{-1}]*
70	0.00	0.8	0.011	8	0.0	0.07	0.009
74	0.06	0.8	0.011	7	0.1	0.07	0.010
80	0.13	0.8	0.010	6	0.3	0.07	0.012
86	0.21	0.8	0.009	5	0.5	0.07	0.014
95	0.31	0.8	0.008	3	1.0	0.07	0.023

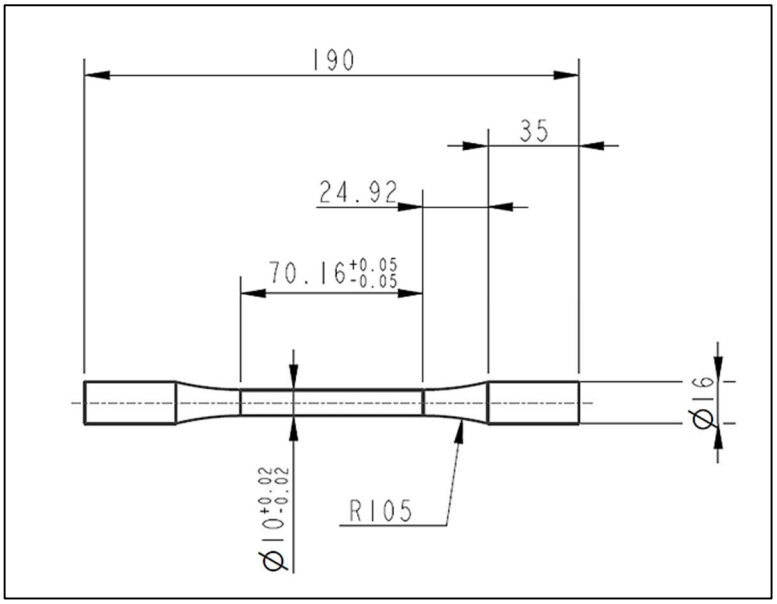

Fig. 2.3 Tensile specimen geometry.

Three tensile tests were repeated maintaining the same conditions, demonstrating excellent repeatability of the test, as shown in *Fig. 2.4* where the results are presented in the form of Engineering Stress [MPa] and Strain [%] calculated according to Eq (2.2) and Eq (2.3).

$$e\% = \frac{L_i - L_0}{L_0} \times 100 \qquad (2.2)$$

$$s = \frac{F}{A_0} \qquad (2.3)$$

With L_i and L_0, respectively, the length of the specimen at each instant of time and the initial length in [mm], F the tensile load in [N], and A_0 the initial specimen cross-section.

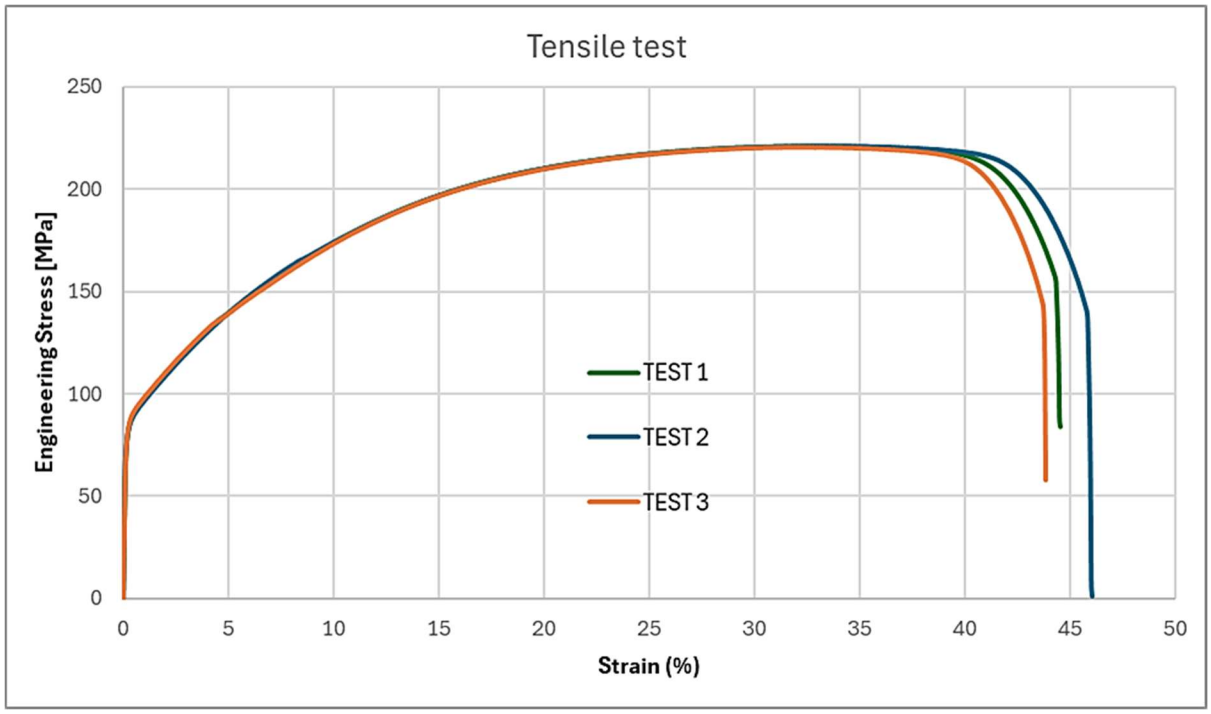

Fig. 2.4 Engineering Stress-Strain curves from tensile tests. Three repetitions of the test maintaining the same condition.

Furthermore, during the tests, the specimen was framed by a camera, allowing the measurement of the diameter of gauge length at each deformation step and, therefore, the monitoring of the necking zone. This allowed data conversion from the press output force-displacement to the true stress-strain curve. The scanned images were processed using custom software written in Matlab R2023b, which performs a series of image manipulation and cleaning techniques to remove noise and detect, by counting the image pixels, the measurement of the specimen diameter and radius of curvature in the necking area, as shown in *Fig. 2.5.*

Fig. 2.6 shows the specimen's cross-section variation measured via Matlab script processing camera images. In the graph, in addition to the engineering stress curve in green, the measurements in mm of the maximum diameter of the specimen indicated in blue, of the minimum diameter indicated in fuchsia, and of the radius of curvature indicated in red are reported. It can be observed that up to a strain value of approximately 0.33, the specimen elongates homogeneously, with the values of the maximum and minimum diameter coinciding; then, the necking of the specimen begins, recording a sudden decrease in the minimum diameter and the appearance of a radius of curvature in the necking zone which from an infinite value reaches a minimum value of approximately 7 mm before the specimen breaks.

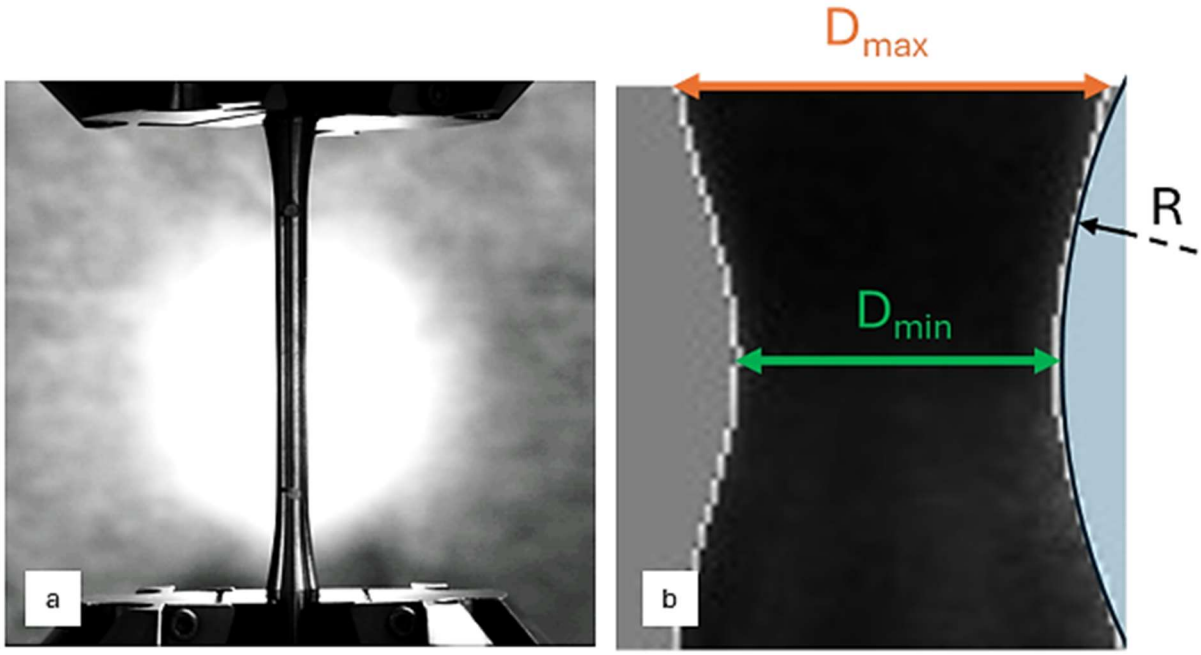

Fig. 2.5 a)Photo of the ETP Copper tensile test performed at the DIN-Department of Industrial Engineering of the University of Bologna; b) picture from Matlab script for image processing and measurement of geometric variation of the specimen.

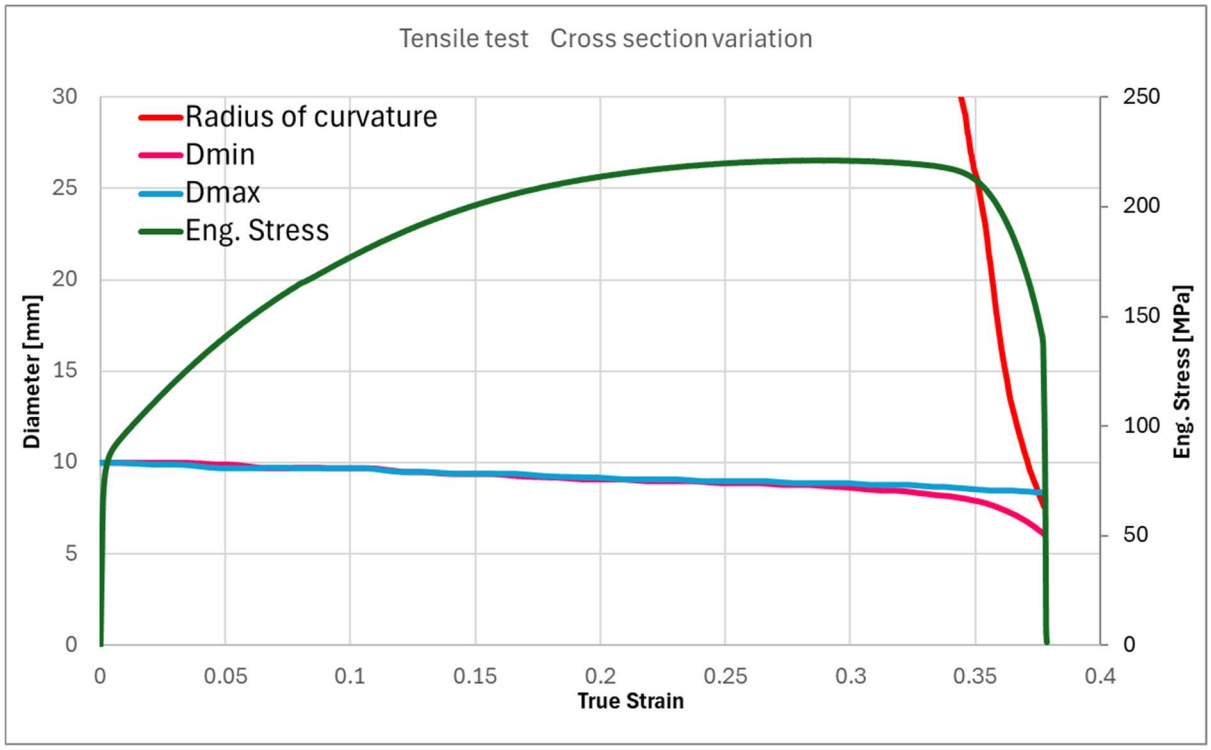

Fig. 2.6 Sample geometric variation during tensile test.

Finally, in *Fig. 2.7* the flow stress curve of ETP copper obtained from the tensile test is shown. The blue curve in the graph represents the true stress and strain values calculated as in Eq.(2.4) and (2.5), where A_i is the instantaneous specimen cross-section value. The orange curve instead shows the flow stress of the material by applying the Bridgman correction.

$$\sigma_t = \frac{F}{A_i} \tag{2.4}$$

$$\varepsilon = \ln \frac{L_i}{L_0} \tag{2.5}$$

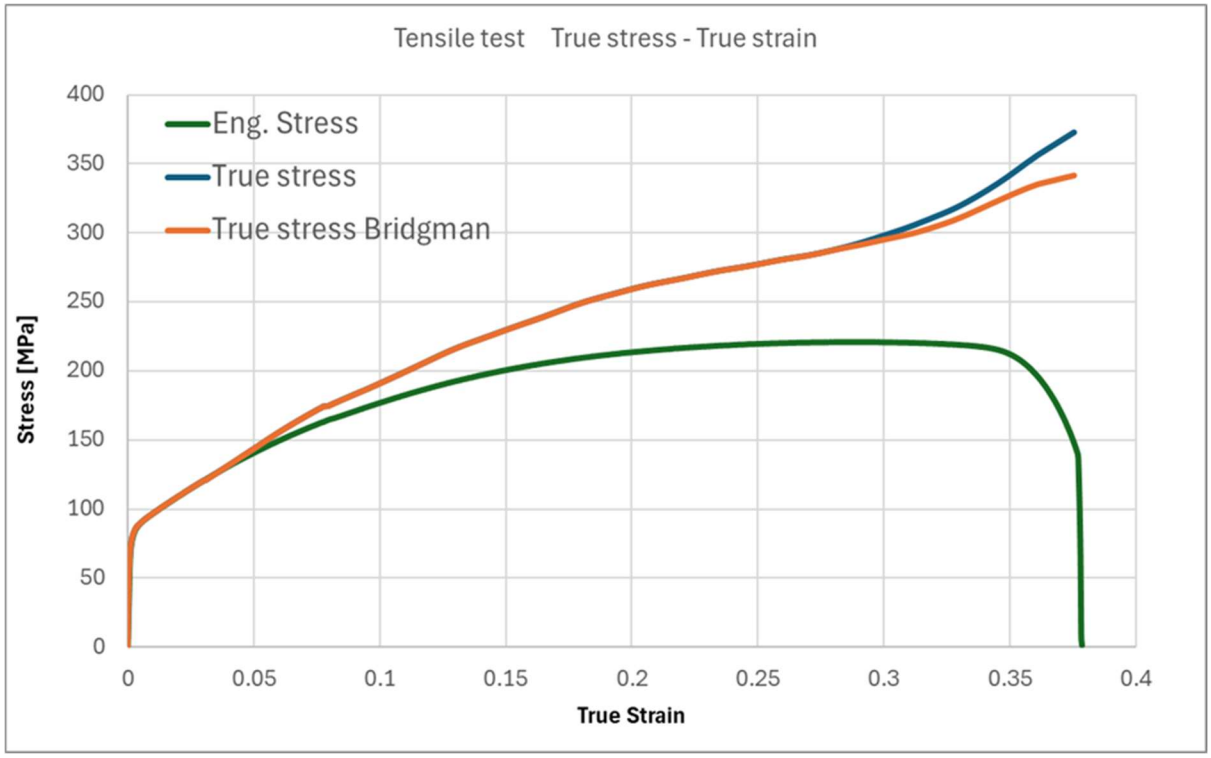

Fig. 2.7 ETP Copper stress-strain curve from tensile test. Engineering stress values, true stress values, and true stress values corrected by Bridgman theory.

The theory, developed in the 1940s by Bridgman [51,52] addresses the effects of triaxial stresses that affect the specimen after the onset of necking, causing a transition from the uniaxial stress state typical of the tensile test to a triaxial stress state. The theory provides a mathematical analysis to adjust the axial stress to reflect the true stress state, taking into account geometric changes in the specimen, particularly the radius of curvature at the neck, allowing for a more accurate representation of the material flow behavior under uniaxial conditions. According to Bridgman's theory, the

stress values were calculated as in Eq (2.6), where *R* is the radius of curvature and *r* is the minimum radius of the specimen in the necking zone.

$$\sigma_B = \frac{\sigma_t}{\left(\frac{1+2R}{r}\right)\left[\ln\left(1+\frac{r}{2R}\right)\right]} \qquad (2.6)$$

It is evident that true stress values exceed engineering stress values. Furthermore, from the onset of necking - approximately after a strain of 0.33 - incorporating the Bridgman correction yields lower true stress values.

Compression test

Fig. 2.8 Compression specimen before and after the test.

The compression tests were carried out on cylindrical specimens, shown in *Fig. 2.8*, with a diameter of 10 mm and a height of 8 mm according to the ASTM-E9 standard, using the INSTRON 8033 universal testing machine equipped with a 25 kN load cell (*Fig. 2.9*). The speed of the crossbar was set at 0.07 mm/s guaranteeing an average strain rate of 0.01 s^{-1}, as shown in *Table 2.2.*

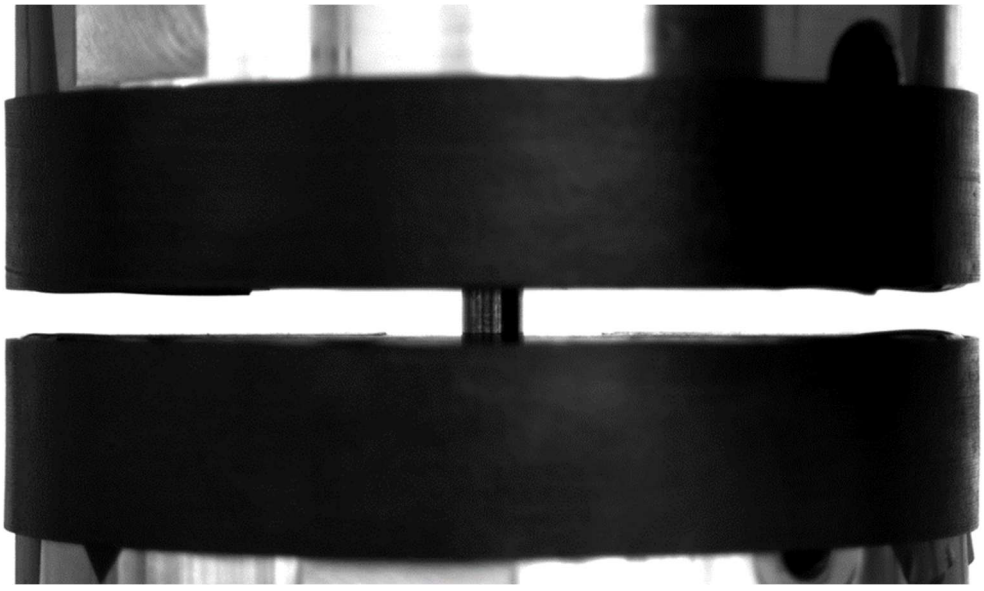

Fig. 2.9 Photo of the ETP Copper compression test performed at the DIN-Department of Industrial Engineering of the University of Bologna.

To process the data from the force-displacement output curves to the true stress-strain curves, it wasn't possible in this case to use the camera due to the presence of lubricant. The volume constancy method was therefore used to measure the real cross-section of the specimen as the deformation increased, according to Eqs. (2.7),(2.8) and (2.9).

$$A_0 L_0 = A_i L_i \tag{2.7}$$

$$\sigma_t = \frac{F}{A_i} \tag{2.8}$$

$$\varepsilon = \ln \frac{L_0}{L_i} \tag{2.9}$$

To prevent measurement errors, a correction was applied to the test data to account for the compliance of the press. This adjustment allowed the analysis to focus exclusively on the elastoplastic behavior of the sample, excluding the elastic response of the testing equipment. Initially, the stiffness of the press's load train was determined, as illustrated in *Fig. 2.10a*, by loading the press without a specimen between the plates up to the maximum available force. The actual displacement of the sample during the compression test was then calculated as shown in Eq. (2.10).

$$s = s_p - \frac{F}{K} \tag{2.10}$$

Where s_p [mm] is the measured displacement of the specimen measured during the test, F is the compression load in [N], and K is the measured stiffness of the press with a value of 334087 [N/mm]. As indicated in the graph in *Fig. 2.10b*, where the yellow line indicates the output data tests and the green one the corrected data, this correction compensated for the displacement error in the test data, which reached approximately 0.68 mm at maximum load.

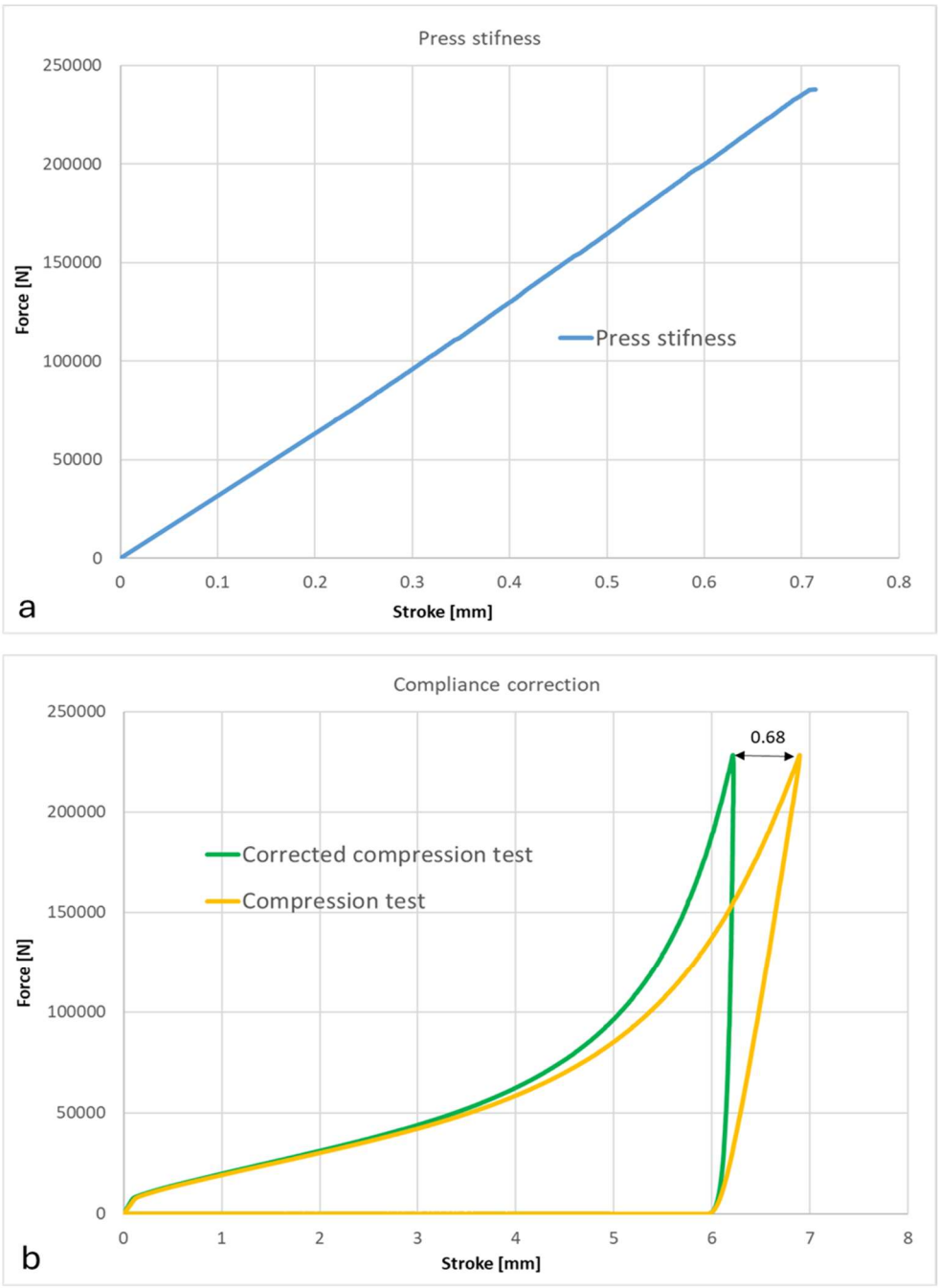

Fig. 2.10 a) Stiffness of the press's load train; b) Load-stroke curve corrected considering press compliance in the compression test.

To assess the effect of the friction coefficient between the specimen and plates on the characterization of the material flow stress, 3 different lubrication conditions were tested, using TADAL CU 1350 N industrial oil: unlubricated, lubricated only at the beginning of the test, and multiple lubrication carried out by interrupting the test after every 1 mm stroke. *Fig. 2.11* shows the comparison between the 3 lubrication conditions. The test results are presented in the form of true stress and strain: the red

dashed curve indicates the test performed without lubrication, the blue line represents the test performed by placing the lubricant between the specimen and the plates only at the beginning of the test, and finally the green line indicates the test performed by interrupting the trial every 1 mm of stroke to replenish new lubricant (the curve shows the loading and unloading of the specimen at each interruption). It can be noted that at low strain values, approximately up to a value of 0.4, there is no difference between the curves obtained under different conditions; while increasing the strain values, the effect of friction begins to be relevant causing an increase in stress values both in the non-lubricated and in the initially lubricated test, due to the loss of lubricant during the test. A similar effect can be seen in every section of the curve with interrupted lubrication: at the beginning of the stroke, the stress values are not influenced by the effect of the friction, while, as the stroke increases, the stress values increase due to the lack of lubrication.

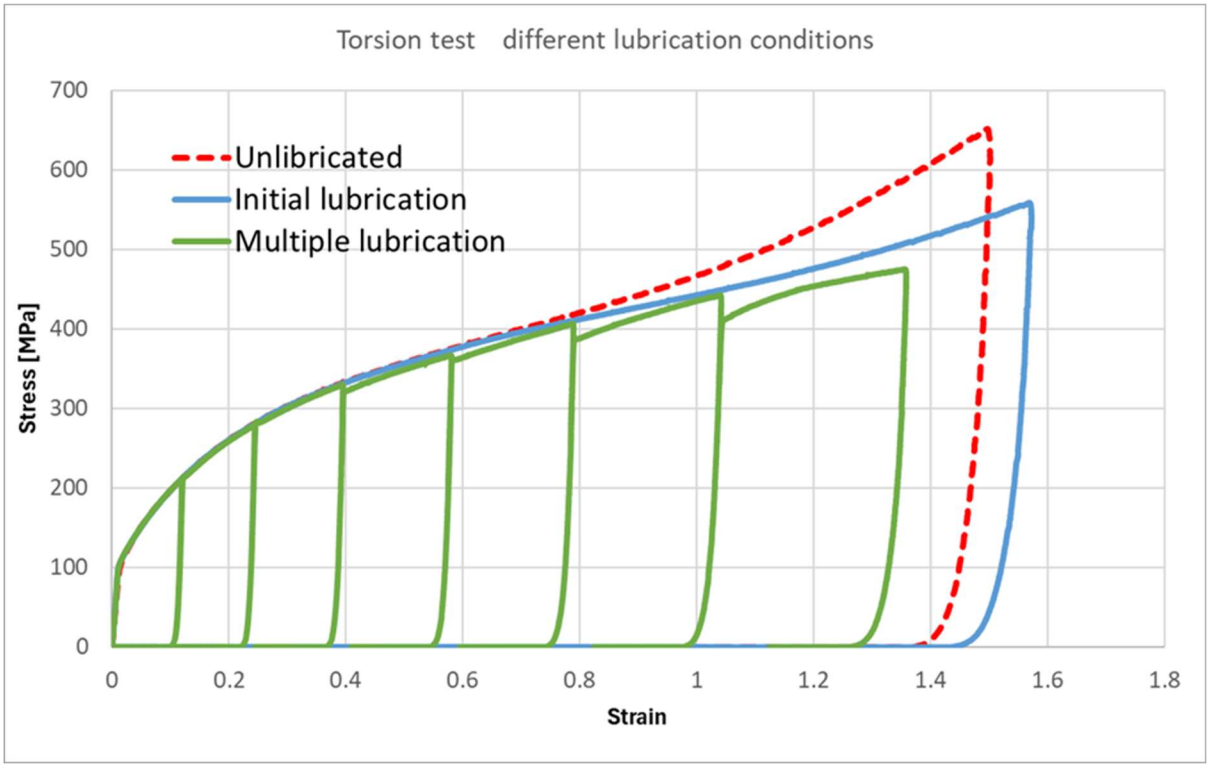

Fig. 2.11 Stress-strain compression curves with three different lubrication conditions.

It was therefore decided to take as true values of the material flow stress only the first points of each 1 mm stroke in the intermediate lubrication test. By interpolating the first points, the flow stress curve was therefore found, as can be observed in *Fig. 2.12* and

in *Fig. 2.13* where the 3 curves obtained from 3 repetitions of the intermediate lubrication test are shown, with excellent repeatability of the test.

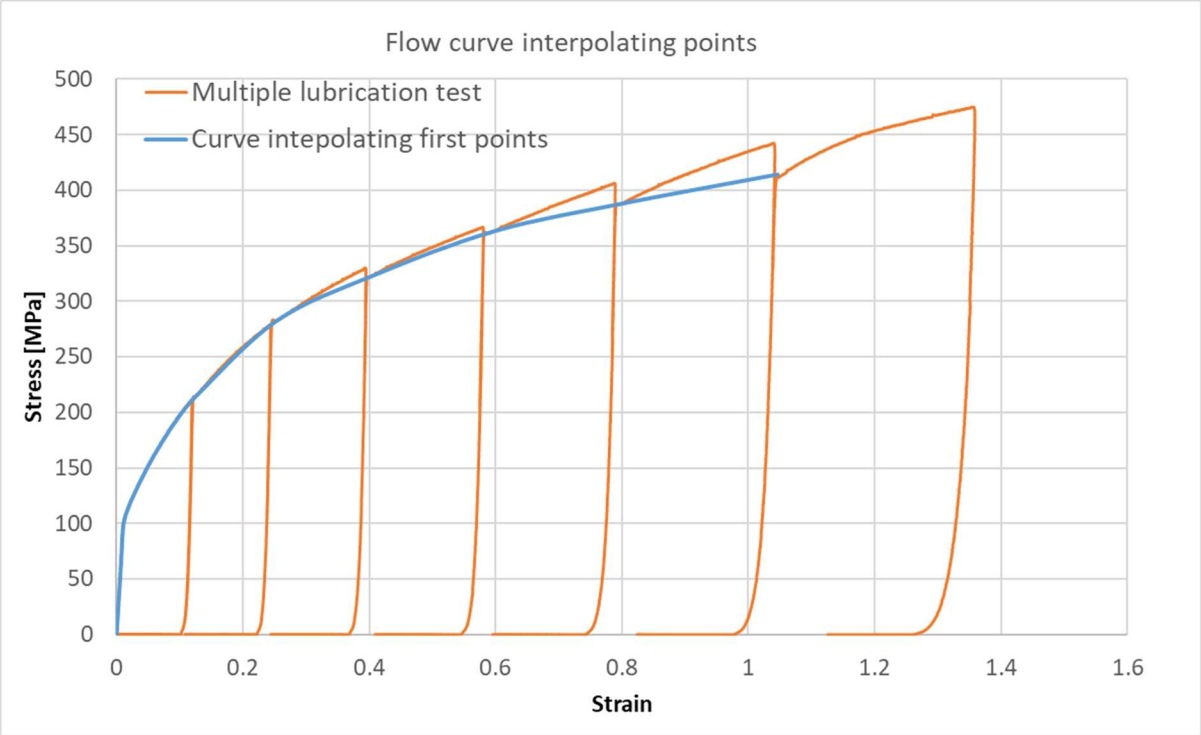

Fig. 2.12 Stress-strain compression curve obtained by interpolating first points from the interrupted multiple lubrication test.

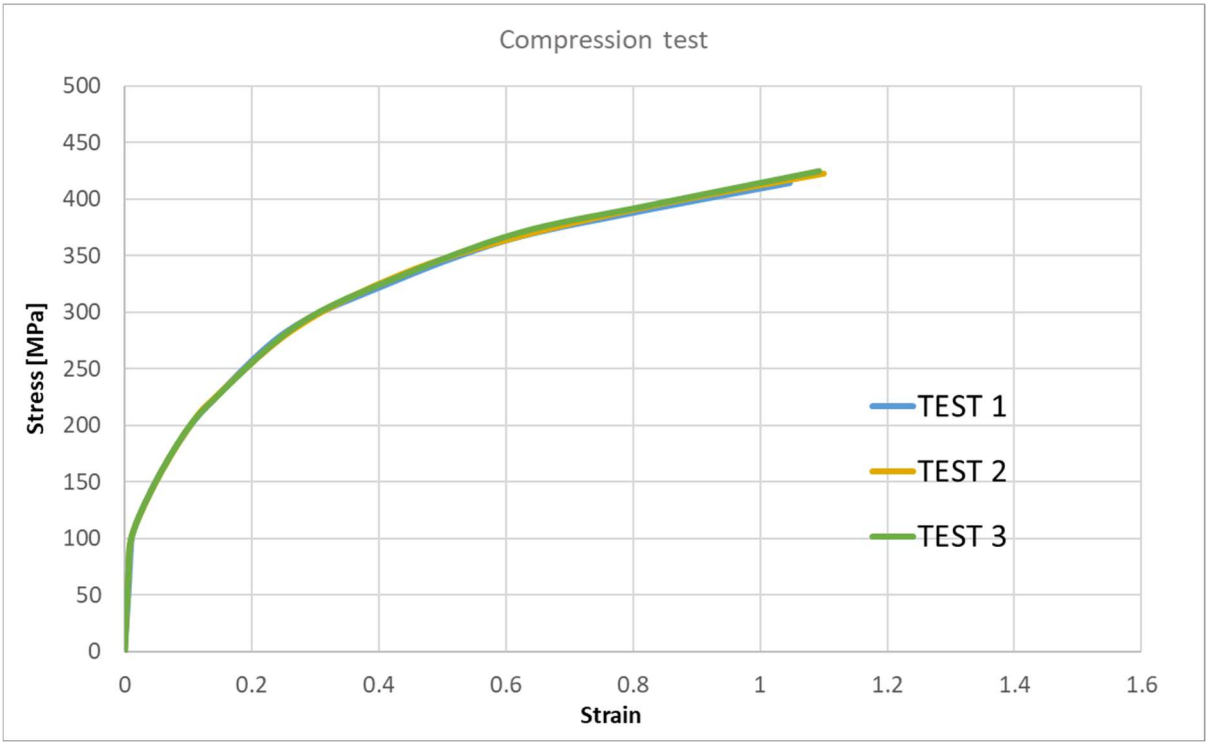

Fig. 2.13 ETP Copper stress-strain curve from compression test.

Torsion test

The torsion tests were performed on solid-bar specimens, as shown in *Fig. 2.14* and *Fig. 2.15*. Although the torsion test has been used for many years, any standard doesn't exist for specimen design, and researchers all over the years tried to use different geometries for the specimens with a gauge-length-to-radius ratio approximately from 0.63:1 to 17:1 [12,13,17,18,53]. For the torsion test on the ETP Copper, a solid bar specimen with a gauge length of 10 mm and a diameter of 8 mm was used, as shown in *Fig. 2.16*.

Fig. 2.14 Torsion specimen before and after the test.

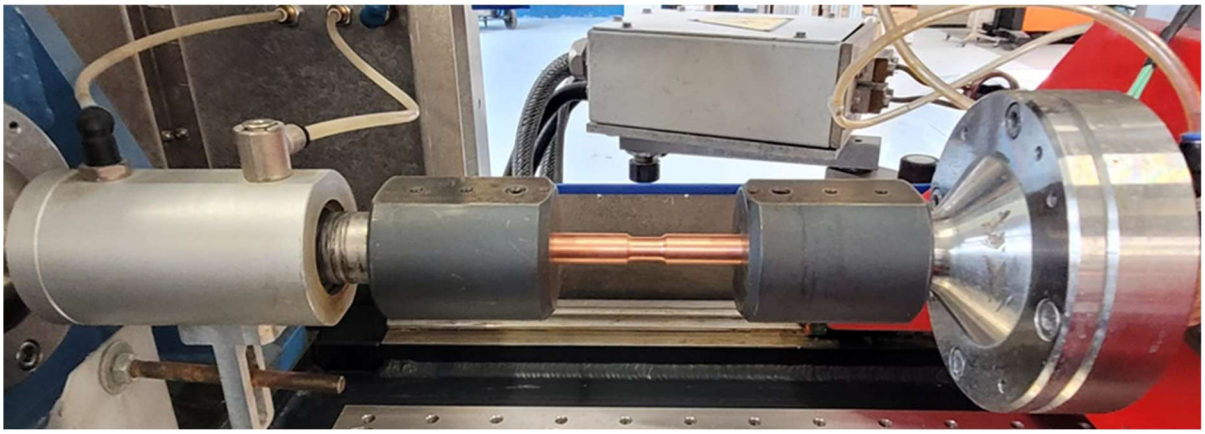

Fig. 2.15 Photo of the ETP Copper torsion test performed at the DIN-Department of Industrial Engineering of the University of Bologna

The tests were conducted at room temperature - 20-25 °C - with three strain rate values 0.01, 0.1, and 1 s^{-1}. For each condition, a minimum of three repetitions was performed, demonstrating good repeatability of the test, as shown in *Fig. 2.17,* where the results are represented as Torque (M) [Nm] vs Rotation angle (θ) [rad]; the green lines correspond to tests conducted at a strain rate of 0.01 s^{-1}, the red/orange lines to 0.1 s^{-1}, and the blue lines to 1 s^{-1}.

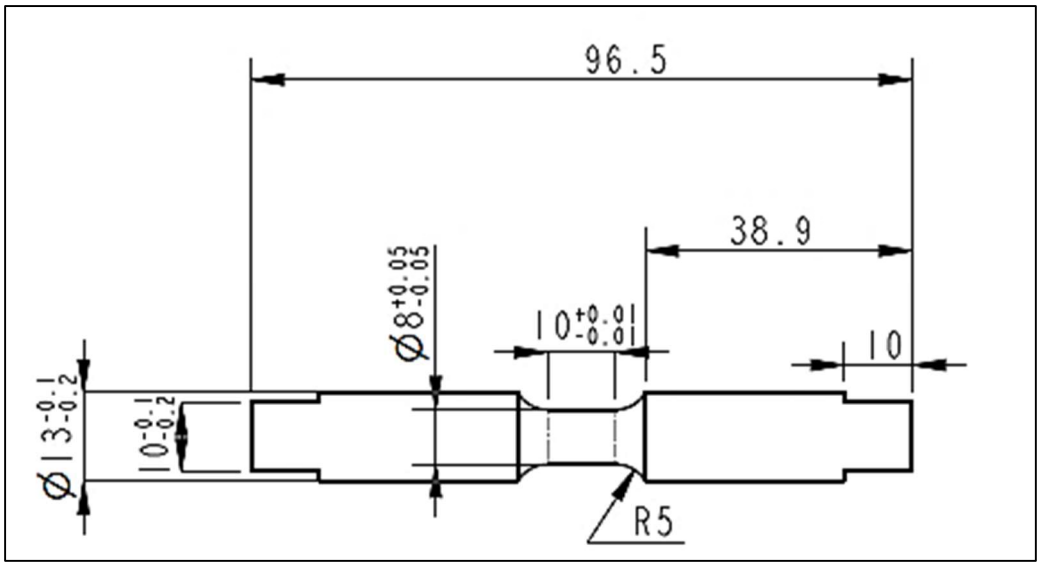

Fig. 2.16 Torsion specimen geometry.

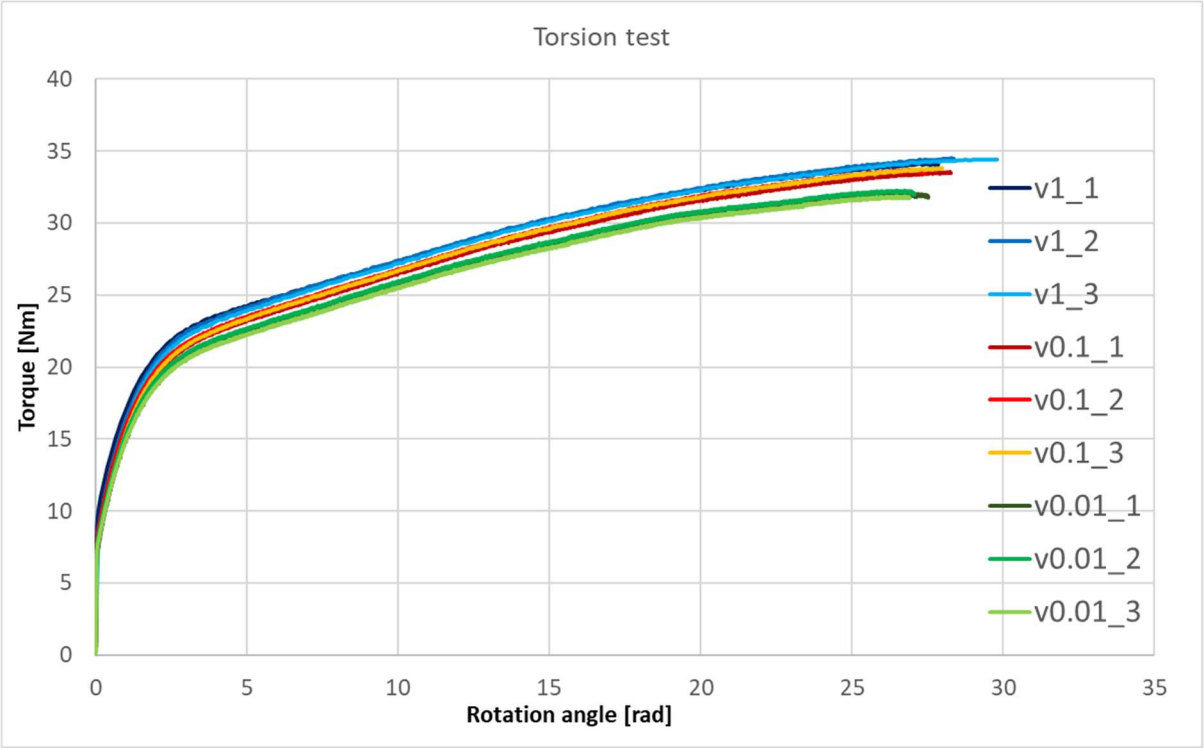

Fig. 2.17 Torque-Rotation angle curves from torsion tests at different strain rates.

The torsion test provides the relationship between the angular deformation applied to the sample and the torque required to obtain it. During the test, the machine outputs are the torque M expressed in N·m and the angle of twist θ in radians. To calculate the shear strain γ and the corresponding shear stress τ, the Fields-Backofen solution [10], illustrated in section 1.2.4 was applied. Using this method, the strain and stress in the

relation τ- γ and the shear strain rate are considered to be those corresponding to the outside diameter of the solid bar sample, as expressed in Eqs. (2.11), (2.12), and (2.13).

$$\gamma = \frac{R\theta}{L} \tag{2.11}$$

$$\dot{\gamma} = \frac{R\dot{\theta}}{L} \tag{2.12}$$

$$\tau = \frac{M}{2\pi R^3}(3 + n + m) \tag{2.13}$$

Where R is the value of the external radius of the specimen expressed in mm, L is the value of the gauge length in mm, θ is the rotational deformation angle in radians, $\dot{\theta}$ is the rate of angular deformation expressed as radians for seconds, M is the torsional torque applied to the specimen in N·mm. The strain hardening coefficient n is the instantaneous slope of $\ln M$ versus $\ln \theta$, calculated as in Eq. (2.14), while the strain rate sensitivity coefficient m is the slope of $\ln M$ versus $\ln \dot{\theta}$ at fixed values of θ, as in Eq. (2.15).

$$n = \left.\frac{\partial \ln M}{\partial \ln \theta}\right|_{\dot{\theta}} \tag{2.14}$$

$$m = \left.\frac{\partial \ln M}{\partial \ln \dot{\theta}}\right|_{\theta} \tag{2.15}$$

Finally, to obtain the material flow stress in the form of equivalent stress $\bar{\sigma}$ and the equivalent strain $\bar{\varepsilon}$, the Von Mises model was applied as in Eqs. (2.16) and (2.17).

$$\bar{\sigma} = \tau\sqrt{3} \tag{2.16}$$

$$\bar{\varepsilon} = \frac{\gamma}{\sqrt{3}} \tag{2.17}$$

Fig. 2.18 shows the results of the torsion test performed with a strain rate of 0.01 s^{-1}. In a first approximation, the coefficients n and m were neglected, as shown by the pink curve. Moreover, a further torsion test was performed stopping the trial at regulated strain intervals measuring the diameter and gage length. It was found that the

specimen's geometry experienced slight variations during the test, with an increase in length and a decrease in diameter. In this case, the material flow stress was calculated by applying Eqs. (2.11), (2.12), and (2.13), but using the values of the specimen diameter and length measured at each test stop, as shown by the purple curve in the graph. The variation of diameter and length as a function of the rotation angle was then computed by applying a nonlinear regression model to interpolate the curve's data points, utilizing MATLAB's fitting tool with the Levenberg-Marquardt algorithm, as shown in *Fig. 2.19* and *Fig. 2.20*. The torsion test data were then processed considering also the sample's geometric variation as a function of angular deformation according to Eqs. (2.18) - (2.21), and indicated by the light green curve in *Fig. 2.18*.

$$R(\theta) = (0.1684e^{-1.0571\theta} + 7.8817e^{2.6734\theta})/2 \quad (2.18)$$

$$L(\theta) = (11.3102e^{7.0255\theta} - 1.0609e^{-1.0233\theta}) \quad (2.19)$$

$$\gamma = \frac{R(\theta) \cdot \theta}{L(\theta)} \quad (2.20)$$

$$\tau = \frac{M}{2\pi[R(\theta)]^3}(3 + n + m) \quad (2.21)$$

Finally, the coefficients n and m were calculated according to Eqs. (2.14) and (2.15). As shown in *Fig. 2.21*, for the coefficient n the average value of the curves slope of the tests conducted at three different speeds was calculated, indicated by the dashed lines; while for the value of m, as shown in *Fig. 2.22*, the average value of the slope of the curves at constant strain values indicated by the different colors was considered. The values of the coefficients thus calculated are: $n = 0.246; m = 0.0109$.

In *Fig. 2.18,* the resulting curve of the torsion data processed according to the Fields and Backofen theory, taking into account the variation of the specimen geometry and the coefficients n and m, are indicated by the dark green curve. It is evident that the flow stress values of the material calculated by considering these factors attain higher values compared to the initial application of the Fields and Backofen theory, assuming that the specimen geometry remained constant during testing and neglecting the coefficients n and m. This demonstrates that, in the characterization tests of cold-

worked ETP copper, it is essential not to neglect these effects that influence the material's flow stress.

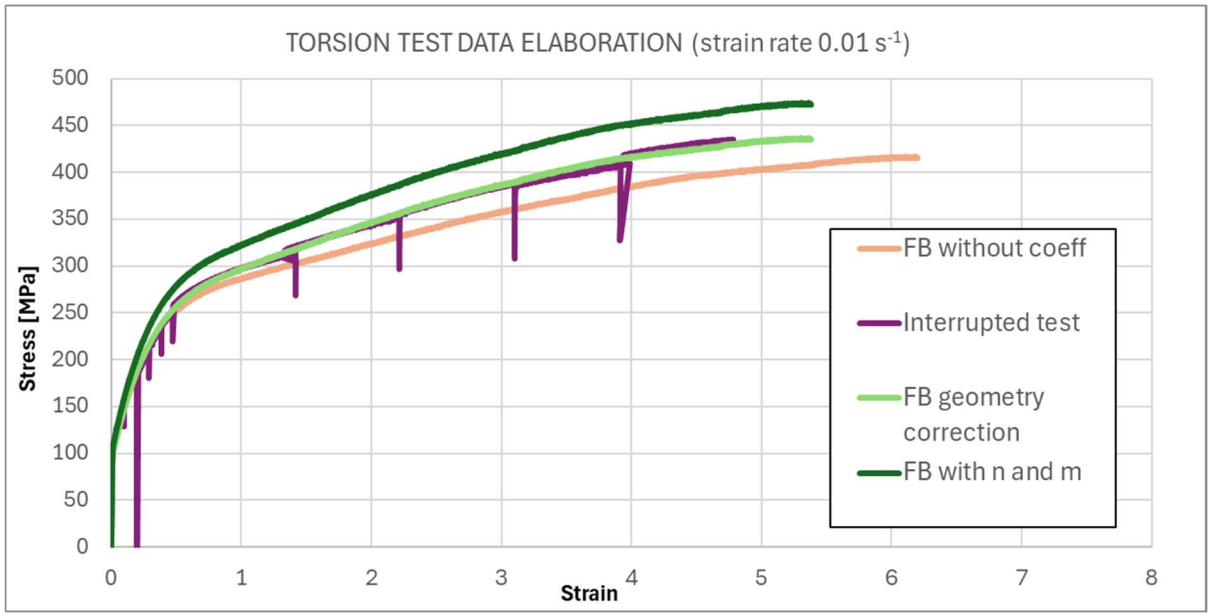

Fig. 2.18 ETP Copper stress-strain curve from torsion test elaborated according to Field and Backofen theory, considering n and m coefficient and the sample geometry variation.

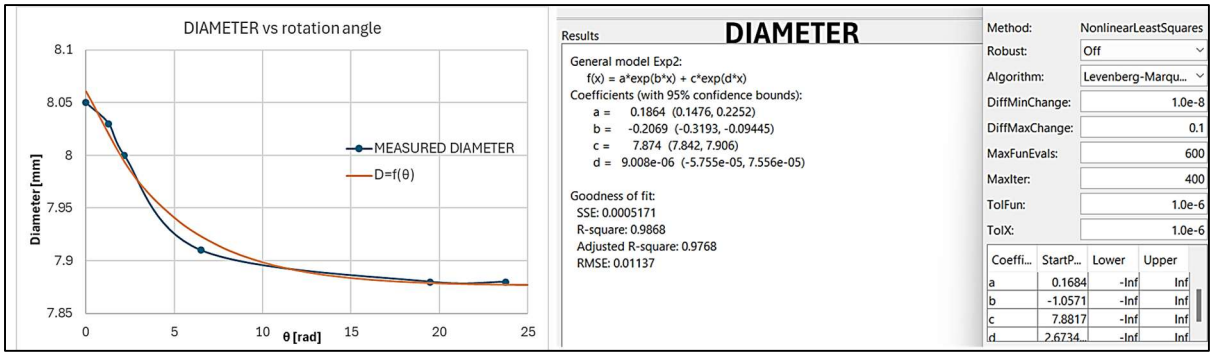

Fig. 2.19 Sample diameter variation during the torsion test.

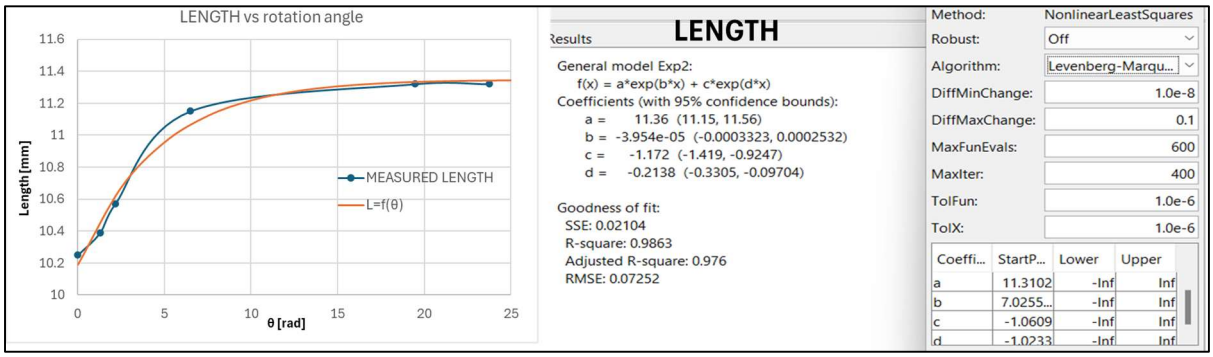

Fig. 2.20 Length diameter variation during the torsion test.

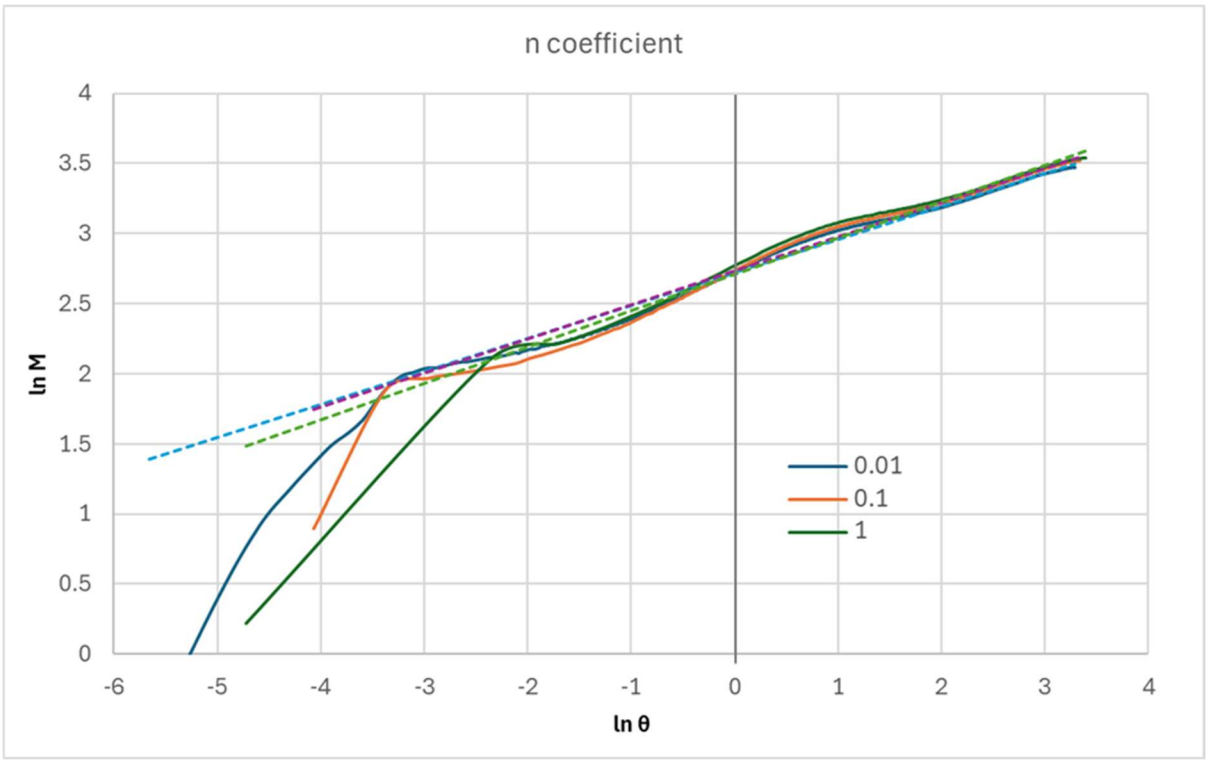

Fig. 2.21 The strain hardening coefficient n calculation.

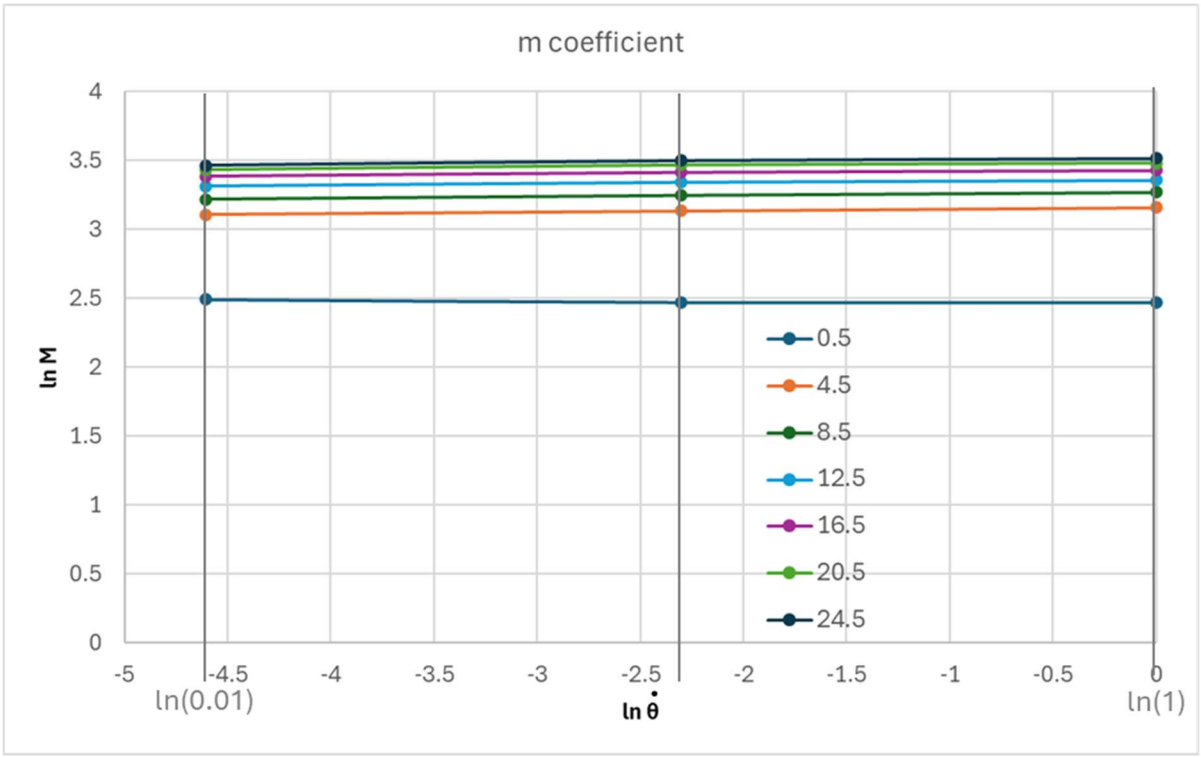

Fig. 2.22 The strain rate sensitivity coefficient m calculation.

2.2.3. Flow stress curves comparison

Tensile and Compression tests

The tensile and compression test results were compared, as shown in *Fig. 2.23*, in the form of equivalent stress vs equivalent strain. The flow stress of the material obtained from the tensile test is indicated by the red continuous curve, while the compression test by the blue curve. It can be observed that the two curves are perfectly coincident up to a strain value of about 0.33, and then the necking of the specimen occurs in the tensile test. Young's modulus of 121000 MPa and yield stress of 85 MPa were found. From the strain value of 0.3 onwards, the flow stress values obtained from the tensile test are greater than those of the compression test, even though the Bridgman correction [51,52] was applied in the data processing, as explained in section 2.2.2.

The cause of this discrepancy may arise from several factors. Primarily, the application of Bridgman correction requires precise measurements of the specimen during testing, which are challenging to implement, and the method employed in this work, utilizing a high-definition camera, was insufficiently precise to completely eliminate measurement errors related to variations in the specimen's geometry. Furthermore, Bridgman's theory is based on the following assumptions: i) the arc of a circle approximates the contour of the neck; ii) the cross-section of the necked region remains circular during the test; iii) the von Mises criterion for yielding applies; iv) the strains are constant over the cross-section of the neck. These simplifications lead to an overestimation of the stress values in the tensile test compared to the compression test, as already shown in the literature by numerous studies [39–42]. Some other techniques have been proposed to process the data of the tensile tests, attempting to overcome the limitations of the Bridgman theory, but these techniques are time-consuming and require sophisticated equipment [43–45].

In this case, it was therefore worthwhile to consider the tensile test only up to a strain of 0.33 and counting a perfect overlap with the compression test, which allowed to characterize the material up to a strain value of 1.1.

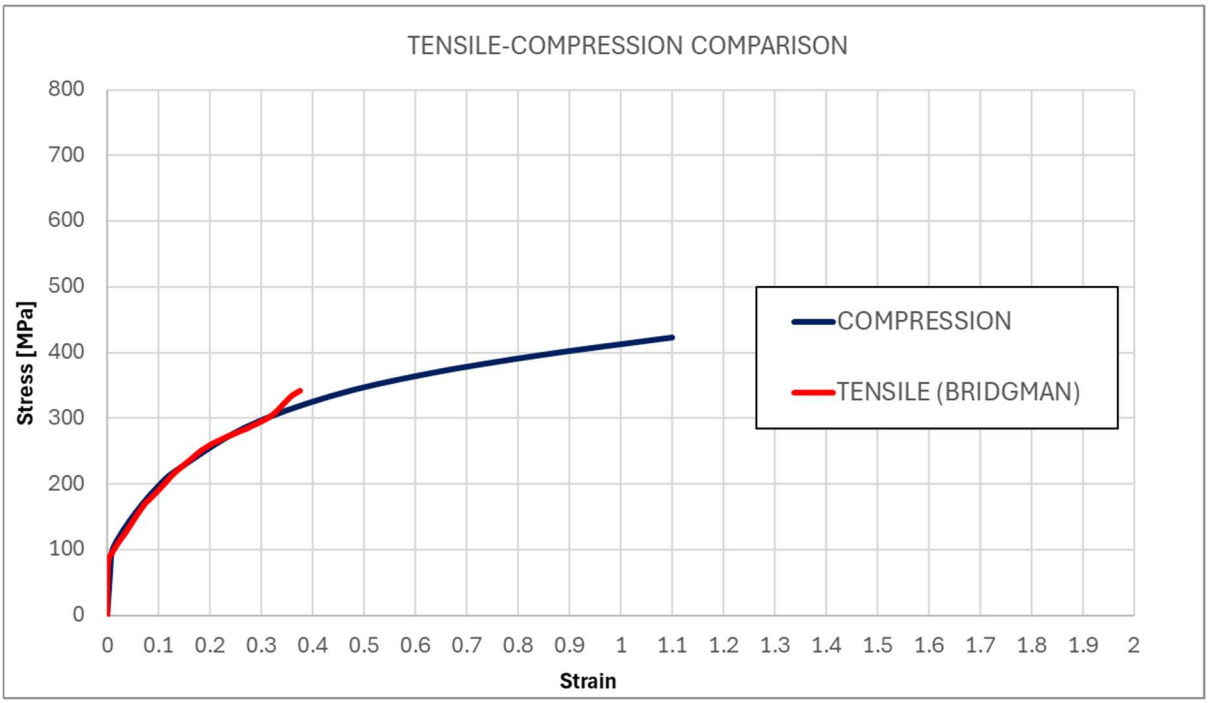

Fig. 2.23 Comparison between ETP Copper flow stress curves obtained from Tensile and Compression tests.

Torsion test vs Tensile and Compression tests

The tensile, compression, and torsion test results were compared, as shown in *Fig. 2.24*, in the form of equivalent stress vs equivalent strain. It can be observed that with the torsion test, larger strain values are reached compared to the tensile and compression tests. However, it is evident that the equivalent stress values measured in torsion are significantly lower than those determined in the uniaxial tensile and torsion tests. This discrepancy persists despite the corrections made during the processing of torsion test data using the Field and Backofen method, which considers the coefficients n and m as well as the specimen's geometric changes, which resulted in flow stress values that are slightly higher than the initial approximation, as illustrated by the dark green curve in the graph.

Furthermore, at this stage, a new approach to processing torsion data was tested using De Saint-Venant's theory [24,25]. The shear stress and shear strain values were calculated according to Eqs. (2.22) and (2.23), and the Von Mises criterion was applied to determine the equivalent stress values, as outlined in Eqs. (2.16) and (2.17).

$$\gamma = \frac{R(\theta) \cdot \theta}{L(\theta)} \qquad (2.22)$$

$$\tau = \frac{2M}{\pi[R(\theta)]^3} \qquad (2.23)$$

The flow stress values obtained using De Saint-Venant's model are represented in the graph in *Fig. 2.24* by the solid yellow line. It is evident that these values are much closer to the results obtained from tensile and compression tests up to a strain of 0.5. Beyond this point, even with De Saint-Venant, the stress values begin to show a significant deviation from the tensile and compression results, particularly under higher strain levels.

Although De Saint-Venant's theory yields results much closer to those from tensile and compression tests, it cannot be applied to torsion data processing beyond a certain level of strain because the assumptions underlying the theory, which are rooted in elastic deformation, no longer hold true as the material enters the plastic deformation regime. In fact, as explained in paragraph 1.2.4, De Saint Venant's model is based on the following key assumptions: i) Linear material behavior: the theory relies on Hooke's Law, which applies only when the material deforms elastically. This assumption fails when a material enters the plastic regime, where stress-strain relationships become nonlinear and plastic flow needs to be considered; ii) Small deformations: the theory assumes small strains, which is valid for elastic deformation. In plastic deformation, the strains can become large, and the distribution of stresses changes significantly, especially near points of stress concentration or yielding zones. In contrast, once strain exceeds a certain threshold, the material's response is governed by more complex mechanisms, such as yielding and plastic flow, which require models that account for non-linear material behavior. Consequently, while De Saint-Venant's theory is an effective tool for analyzing elastic deformation, as explained by several past studies [54–56], it becomes unsuitable for torsion data processing beyond a certain strain because it fails to incorporate the material's plastic response and non-linear behavior under large deformations.

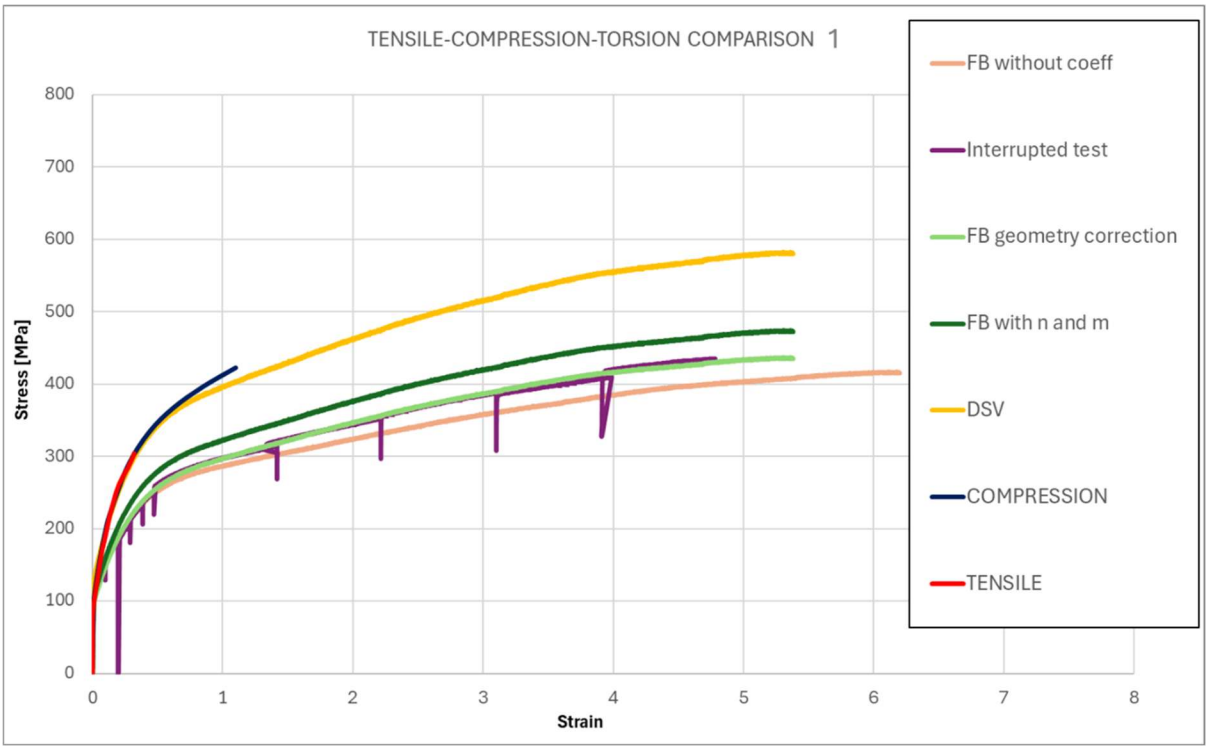

Fig. 2.24 Comparison between ETP Copper flow stress curves obtained from tensile test, compression test, and torsion test.

The discrepancy between the flow stress of the material obtained from tensile and torsional tests has already been observed in studies present in the literature [46–50] and the most widely accepted theory is the one proposed by Bishop and Hill [48] and further developed by Canova [49], according to which the effect is probably due to the differences in the crystallographic anisotropy or in the structure produced by the torsional stress, as opposed to the tensile and compression stress. In particular, in both tension and torsion, the evolution of stress and strain is influenced by changes in texture and work-hardening. For torsion of FCC materials, the Taylor factors (σ_{23}/τ_c) evolve with strain from an initial value of 1.65, gradually decreasing towards about 1.38, reflecting changes in texture. Concurrently, the critical resolved shear stress τ_c increases due to work hardening. This evolution leads to a reduction in the Von Mises equivalent stress from $\sqrt{3} \cdot 1.65\tau_c = 2.86\tau_c$ towards $\sqrt{3} \cdot 1.38\tau_c = 2.39\tau_c$ at large strains. In contrast, during tension, due to the fiber texture development, the Taylor factor (σ_{33}/τ_c) increases from 3.06 to 3.67, leading to an increase in equivalent stress from $3.06\tau_c$ to $3.67\tau_c$. Here, the difference between the two testing methods is emphasized: increases (σ_{23}/τ_c) with strain in tension, whereas (σ_{33}/τ_c) decreases

with strain in torsion. Moreover, tension activates more slip systems than torsion, leading to greater dislocation interaction and higher work-hardening.

Then, correction factors based on this approach were calculated to compare the flow stress curve obtained in the torsion test with that obtained in the tensile and compression tests. In the first attempt, a coefficient was calculated considering the Taylor values for tensile and torsion at low strains, as in Eq. (2.24):

$$C_1 = \frac{3.06}{1.65\sqrt{3}} = 1.06993 \qquad (2.24)$$

However, by correcting the torsion test with this factor, the equivalent stress values in the torsion test remain lower than those of the compression test, as shown by the dashed green curves in *Fig. 2.25*, where the correction was applied to the torsion data elaborated with Fields and Backofen without coefficient (pink line), as well as at the data elaborated with geometry correction factor (light green line), and with Field and Backofen accounting geometry changing and coefficients (dark green line).

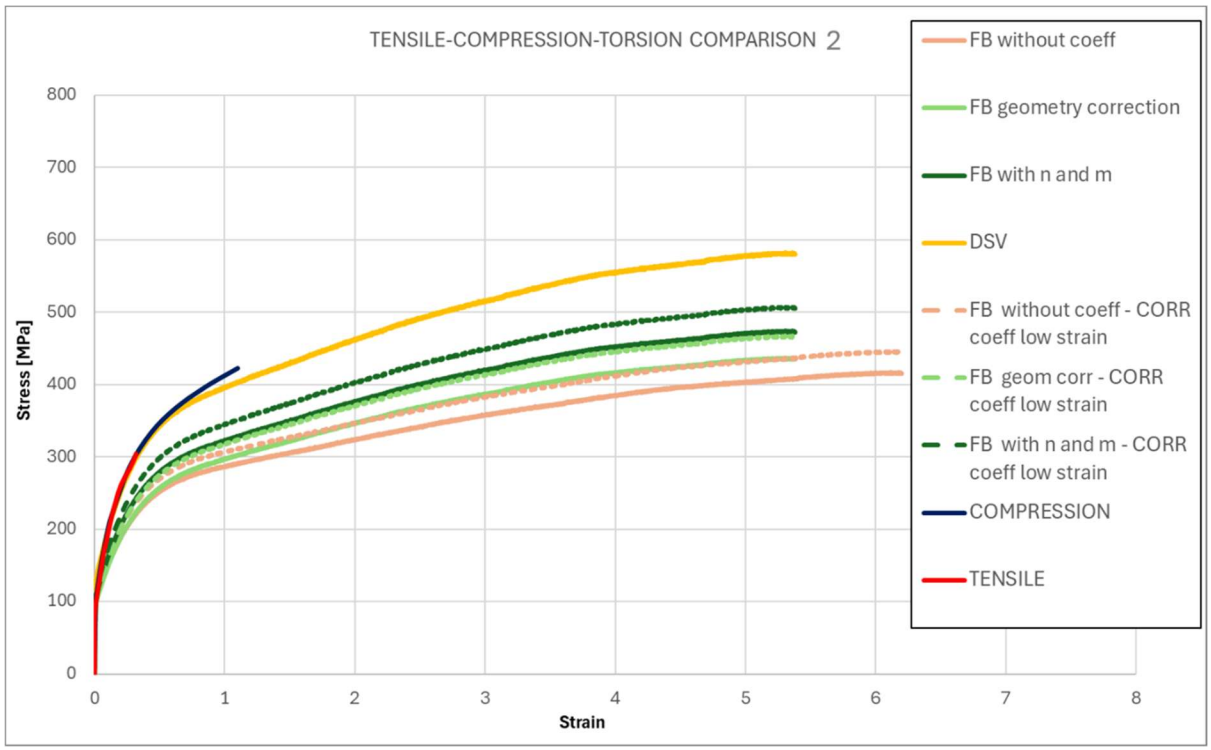

Fig. 2.25 Comparison between flow stress curves from the torsion test corrected using the coefficient calculated from the Taylor values at low strains.

In the second attempt, a correction factor was calculated, taking into account the Taylor values at large strains such as in Eq. (2.25), but this time, the torsion corrected stress values are higher than those of the compression test, as shown by the dashed curves in *Fig. 2.26*.

$$C_2 = \frac{3.67}{1.38\sqrt{3}} = 1.5354 \qquad (2.25)$$

Furthermore, it should be noted that it is difficult to define the specific strain values for which the different Taylor coefficients can be considered valid.

Consequently, from the comparison between the compression test and the torsion test, a new correction function was modeled, interpolating through a nonlinear regression the values of the correction coefficient as a function of the deformation as expressed in Eq.(2.26):

$$C(\varepsilon) = \frac{\sigma_{compr}}{\bar{\sigma}_{tors}} = 1.284e^{-0.0008\varepsilon} - 0.4286e^{-20.4102\varepsilon} \qquad (2.26)$$

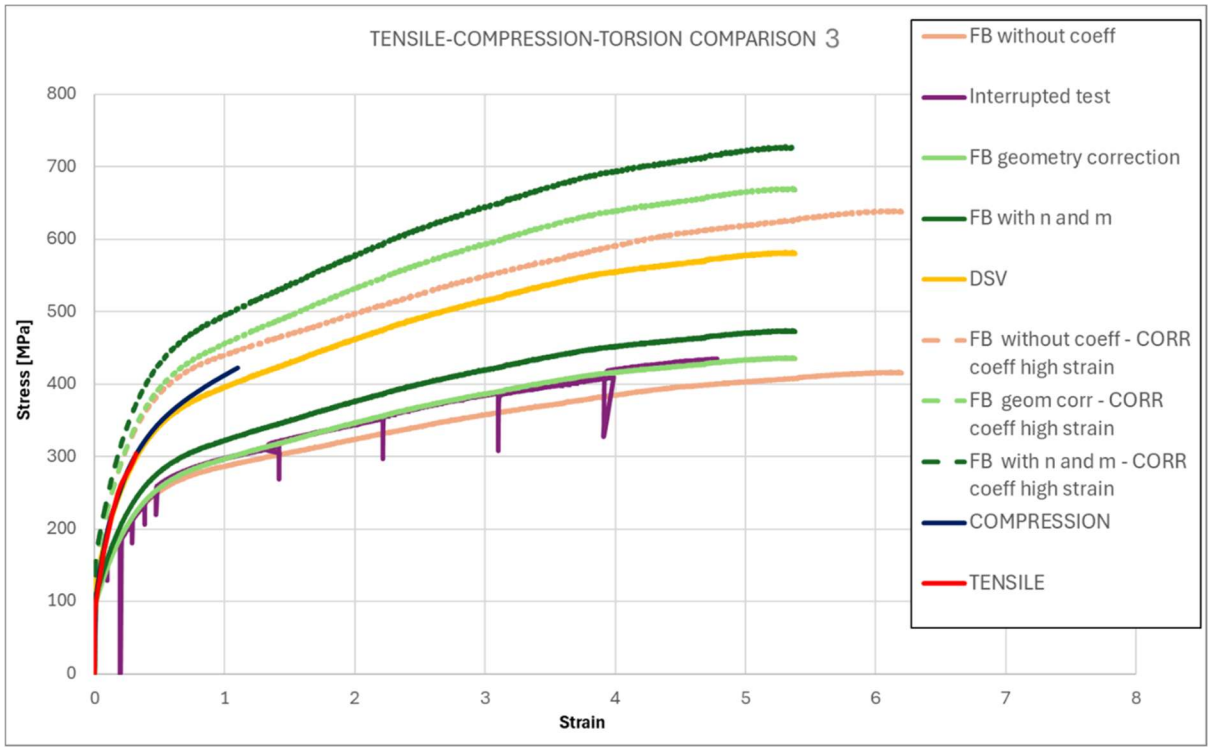

Fig. 2.26 Comparison between flow stress curves from the torsion test corrected using the coefficient calculated from the Taylor values at large strains.

The correction coefficient was computed by applying a nonlinear regression model to interpolate the curve's data points, utilizing MATLAB's fitting tool with the Levenberg-Marquardt algorithm., as shown in *Fig. 2.27*. In the graph in part *a)* the blue curve indicates the torsion test flow stress, the green curve the compression flow stress, the purple curve indicates the ratio between the values of stress from compression and torsion tests, as indicated in the secondary y-axis on the right, and finally, the red dashed line indicates the values of the stress obtained by applying the correction coefficient to the torsion flow stress data.

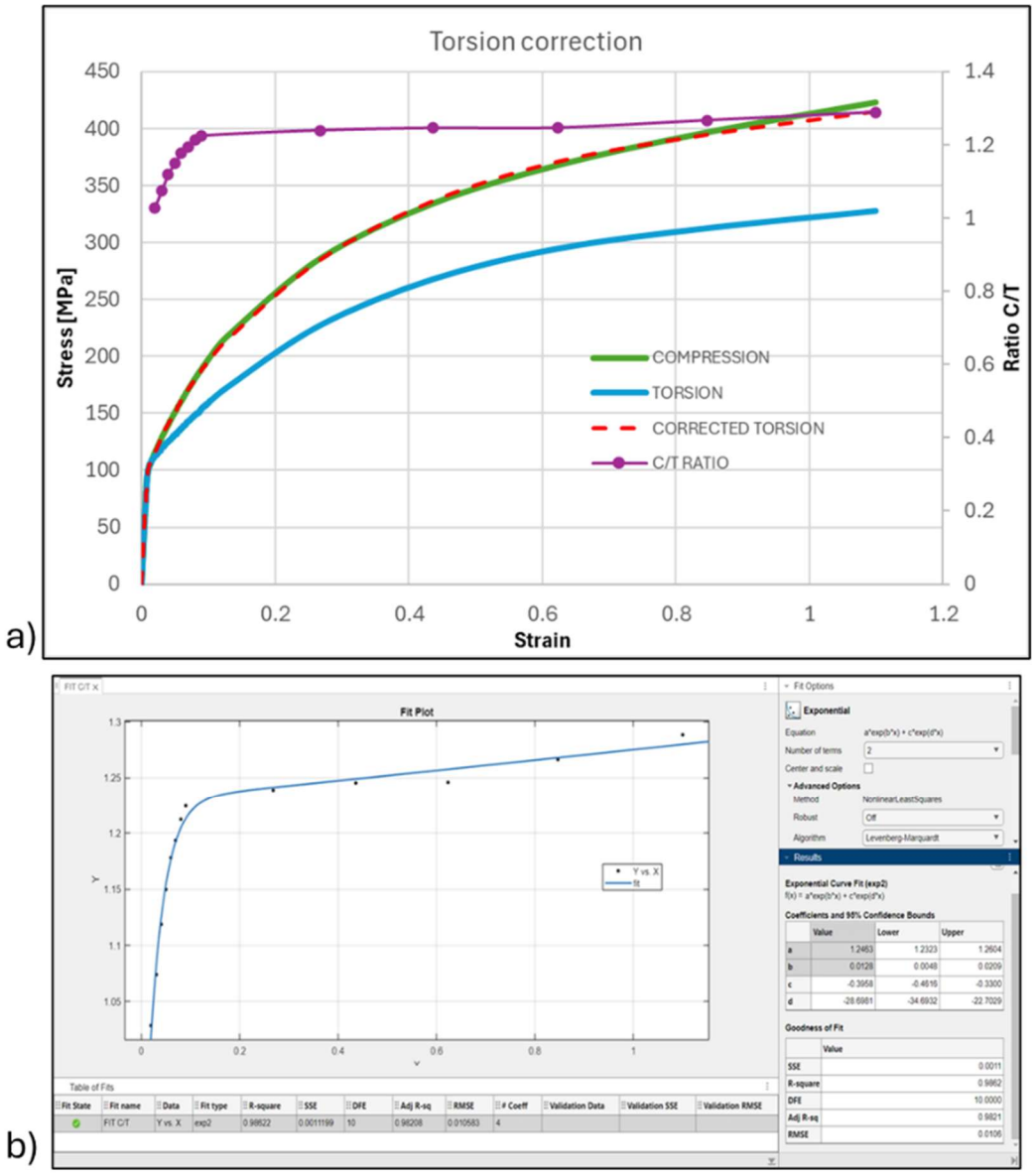

Fig. 2.27 a) Proposed correction function for torsion data elaboration obtained by comparison between torsion and compression tests; b) Nonlinear regression model.

Finally, in *Fig. 2.28*, the flow stress curve of the material is presented in light blue derived from the application of the new model formulated for processing torsion data. This model incorporates the correction coefficient as specified in Eq. (2.26), developed from comparative analyses with compression test data. It can be noted how this modeling, unlike that of De Saint Venant expressed in yellow or those obtained by calculating the correction coefficients according to the Taylor factors at low and high deformations indicated respectively by the short-dashed and long-dashed green lines, aligns precisely with the tensile test and therefore with the compression test up to the strain value of 1.1 but at the same time allows for a characterization of the material up to higher deformation values. Since the new model was obtained from the comparison between the same compression and torsion tests, a new test was devised to validate its accuracy, which will be detailed in the subsequent section 2.2.4.

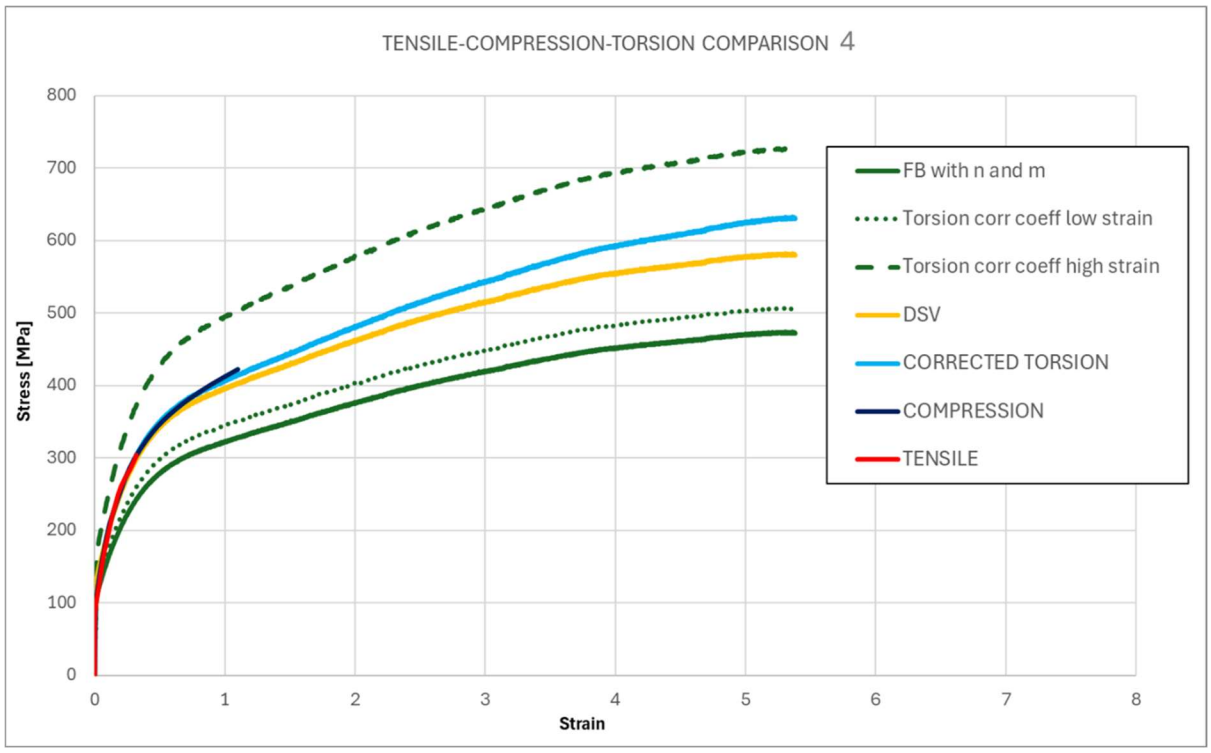

Fig. 2.28 Comparison between flow stress curves from the torsion test elaborated with the proposed model.

2.2.4. Proposed corrected torsion-compression model validation

Hybrid compression test

Fig. 2.29 Hybrid-compression specimen before and after the test.

In order to validate the proposed model for the processing of flow stress data from the cold torsion test, a hybrid compression test was designed (*Fig. 2.29* and *Fig. 2.30*) using a specimen with the geometry shown in *Fig. 2.31*. This design avoids lubrication between the specimen and plates, as the test conditions create a scenario similar to complete adhesion, thus overcoming the error due to the undetermined value of the friction coefficient in the numerical modeling.

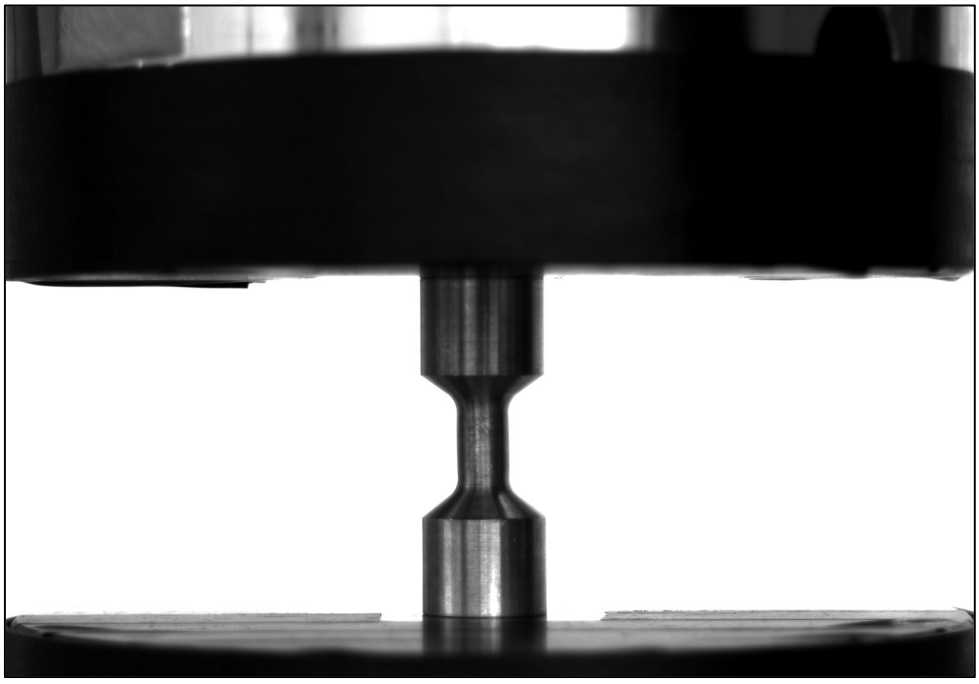

Fig. 2.30 Photo of the ETP Copper Hybrid-compression test performed at the DIN-Department of Industrial Engineering of the University of Bologna.

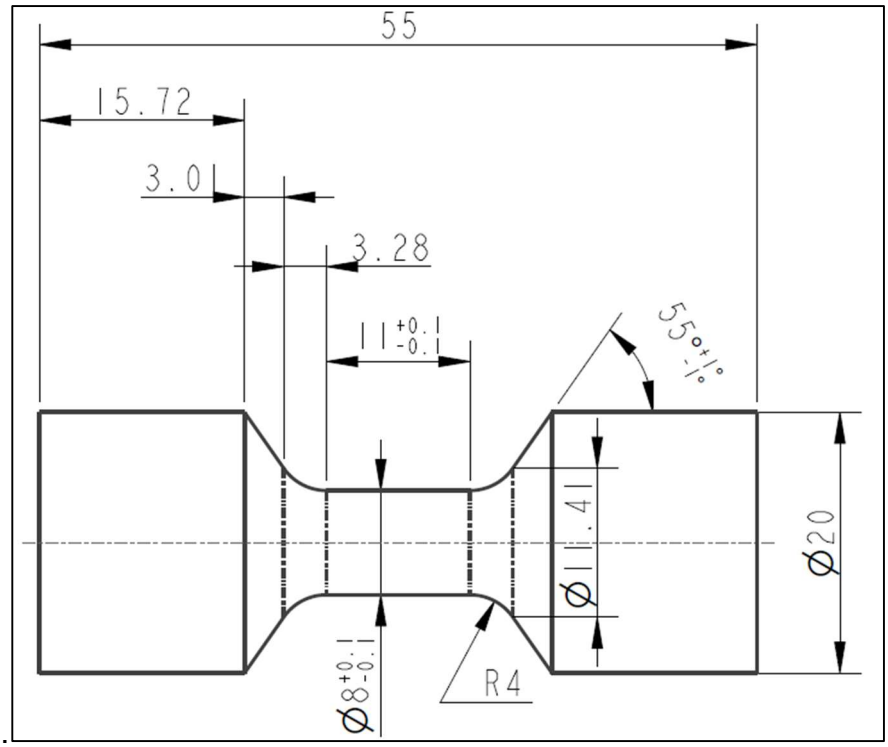

Fig. 2.31 Hybrid-compression test specimen geometry.

The specimen will be subjected to compression, but due to its designed geometry, only the gauge length will deform under a triaxial stress state. This test will allow a comparison of experimental and numerical results in terms of compressive load. The material flow stress, obtained under axisymmetric stress states from tensile and compressive tests or under pure shear from torsion tests, will be used as input values in the simulation, permitting validation of the most accurate model for processing flow stress data and determination of the most appropriate test for metal cold behavior characterization, as will be discussed in the following paragraph.

The experimental trial was performed using the INSTRON 8033 universal testing machine by varying the press crossbar's speed across three conditions: 0.1, 1, and 6 mm/s, aiming to maintain average strain rates of approximately 0.01, 0.1, and 1 s^{-1}, respectively, as shown in Table 2.3. Furthermore, also in these tests, to avoid measurement errors, a correction was applied to the test data to take into account the press compliance as indicated in Eq (2.10) in paragraph 2.2.2. The Load [kN] - Displacement [mm] curves obtained in the experimental tests are therefore shown in *Fig. 2.32* with the orange curve indicating the test carried out at a speed of 0.1 mm/s, the yellow one at a speed of 1 mm/s and the green one at a speed of 6 mm/s.

Table 2.3 Velocity parameters for the hybrid-compression tests.

HYBRID-COMPRESSION TEST								
Specimen length *[mm]*	Cross head speed *[mm/s]*	Strain rate *[s^{-1}]*	Specimen length *[mm]*	Cross head speed *[mm/s]*	Strain rate *[s^{-1}]*	Specimen length *[mm]*	Cross head speed *[mm/s]*	Strain rate *[s^{-1}]*
11	0.1	0.009	11	1	0.091	11	6	0.545
10	0.1	0.010	10	1	0.100	10	6	0.600
9	0.1	0.011	9	1	0.111	9	6	0.667
8	0.1	0.013	8	1	0.125	8	6	0.750
7	0.1	0.014	7	1	0.143	7	6	0.857
6	0.1	0.017	6	1	0.167	6	6	1.000
5	0.1	0.020	5	1	0.200	5	6	1.200
4	0.1	0.025	4	1	0.250	4	6	1.500

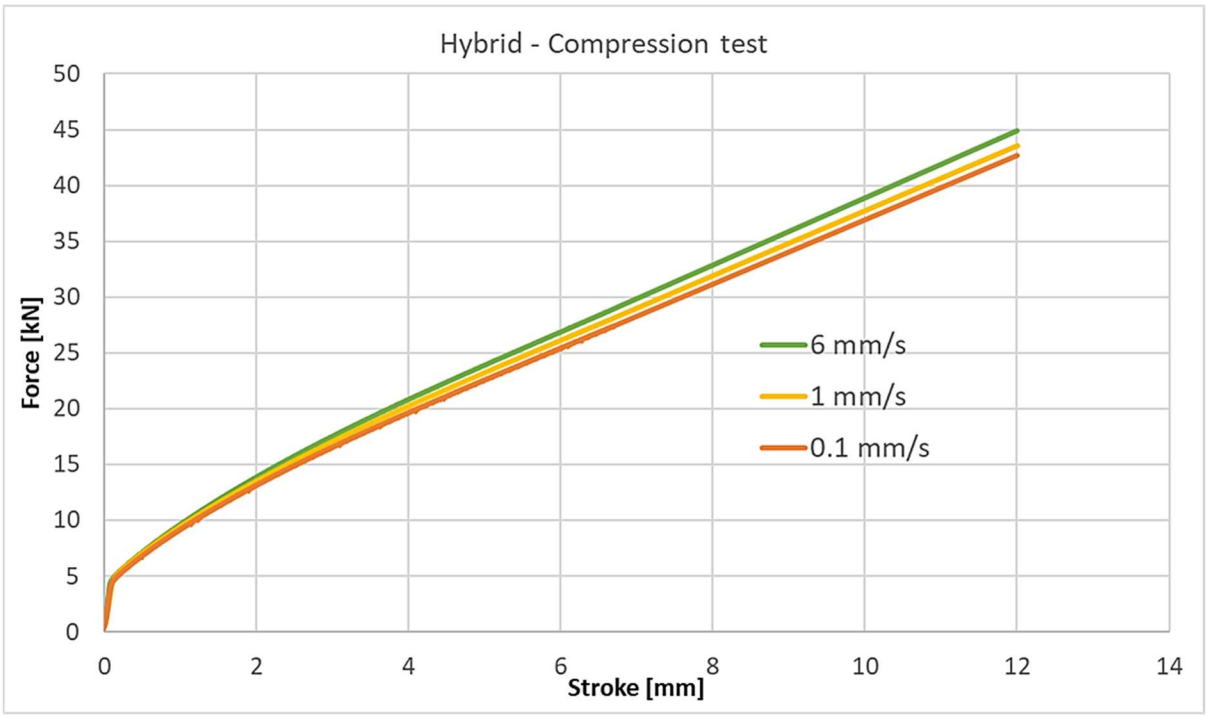

Fig. 2.32 Force-Stroke curve from hybrid-compression tests performed varying the press cross-head speed.

Qform UK® FEM simulation software

QForm UK® is an advanced finite element method (FEM) simulation software specifically developed for the modeling and analysis of metal forming processes, such as forging, rolling, extrusion, and ring rolling. It is designed to handle both hot and cold deformation processes with high computational efficiency and accuracy. The software supports both 2D and 3D simulations, as shown in *Fig. 2.33a)* and *b)*, and includes a wide range of material models, allowing precise predictions of material flow, stress-strain distribution, temperature evolution, and tool wear. One of its main strengths is its automatic adaptive meshing system, which dynamically refines the mesh in critical areas to ensure high accuracy without excessively increasing computational cost. This feature is particularly useful in large deformation processes, where maintaining element quality is essential for reliable results. A key advantage of the code is its efficient and robust computational algorithms. The software employs implicit time integration schemes combined with optimized solvers to achieve stable and fast convergence, even in highly non-linear problems.

QForm UK® includes a comprehensive database of materials, allowing users to select predefined properties or input experimental data for custom alloys. The software's thermal analysis module accounts for heat transfer between the workpiece, tools, and environment, which is crucial in hot forming applications. Additionally, QForm UK® provides specialized modules for grain structure evolution, phase transformations, and damage prediction, making it highly valuable for metallurgical process studies. The software employs a material card system, where users can specify the physical, thermal, and mechanical properties of the material. The code supports various formulations for flow stress characterization, including tabulated experimental data, and temperature and strain-rate dependent functions, as shown in *Fig. 2.33c)*. The software adopts the Von Mises yield criterion, which assumes that plastic deformation initiates when the second invariant of the deviatoric stress tensor reaches a critical value. By accurately defining the flow stress and yield behavior through the material card, QForm UK® ensures precise prediction of stress distribution, strain localization, and potential defect formation during metal forming processes, making it a powerful tool for both industrial applications and academic research.

In recent years, QForm UK® has seen substantial improvements in its numerical methods and solver efficiency, ensuring reliable predictions even in complex forming

operations [57–60]. It features a user-friendly and intuitive graphical interface, as shown in *Fig. 2.33d)*, which simplifies the setup of simulations, post-processing, and data analysis. This ease of use reduces the learning curve and allows researchers and engineers to focus on process optimization rather than software complexities.

Due to these advantages, QForm UK® has seen widespread adoption in the industrial sector, where it is extensively used for process optimization, defect reduction, and tool life improvement in metal forming applications.

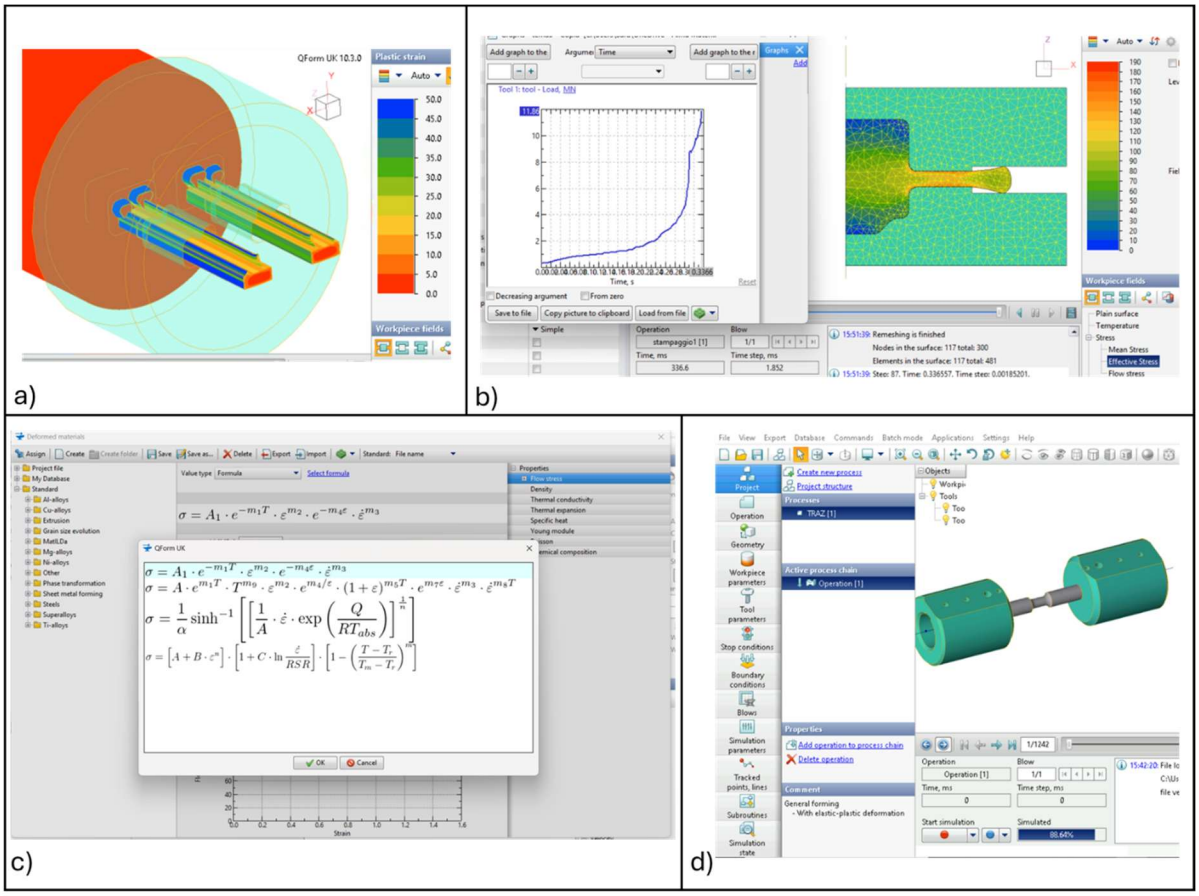

Fig. 2.33 Examples of Qform UK application: a) 3D Aluminum Extrusion process; b) 2D Fogrging process; c) Workpiece material card; d) Software user interface.

Numerical simulations of the tests

For the tensile test, torsion test, and hybrid compression test, Finite Element Method (FEM) simulations were prepared and executed using QForm UK® software. The simulations were modeled as 3D general forming processes, considering the elastic-plastic behavior of the material, while the tools were assumed to be rigid. The workpiece material was modeled with the basic properties listed in *Table 2.1*, while

about the material flow stress, for each type of test, four distinct simulations were run, with the flow stress of the material being varied for each case. The flow stress values used in the simulations were derived from the tensile test, compression test, torsion test, and from the torsion test with data processed according to the proposed model. Finally, for each simulation, a comparison was made between the experimentally and numerically obtained results. Specifically, the load-force and displacement were compared for the tensile and hybrid compression tests, while the torque and angular displacement were compared for the torsion test. These comparisons allowed for the validation of the FEM simulations against the experimental data, providing insights into the material's behavior under different loading conditions and assessing the effectiveness of the proposed model in predicting material responses.

In the simulation of the tensile test, the contact between the specimen and the tools was modeled as a fixed, rigid contact (simulating the clamping mechanism in reality). The mesh properties are reported in *Fig. 2.35*, and a velocity of 0.8 mm/s was applied to the upper tool in the z-direction, resulting in an average specimen strain rate of approximately 0.01 s^{-1}, as shown in *Fig. 2.34*.

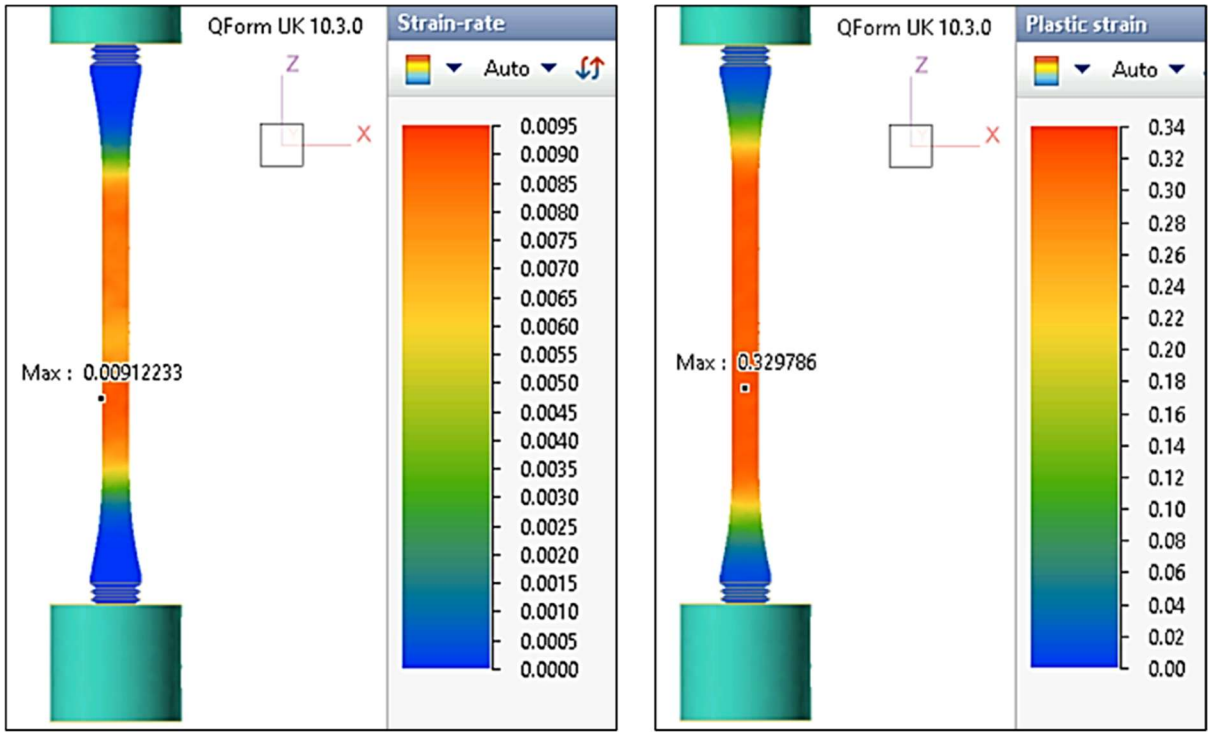

Fig. 2.34 Numerical simulation of the tensile test, on the left strain rate values, on the right strain values.

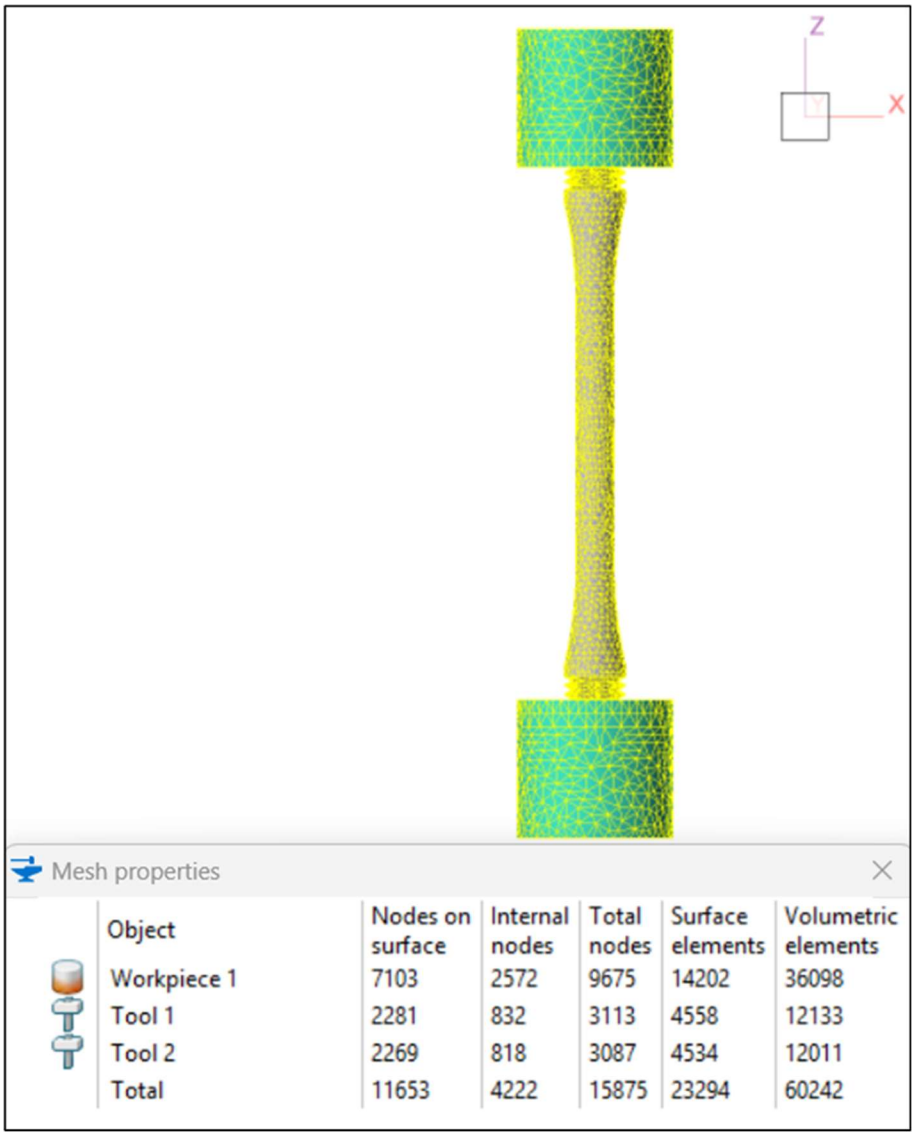

Object	Nodes on surface	Internal nodes	Total nodes	Surface elements	Volumetric elements
Workpiece 1	7103	2572	9675	14202	36098
Tool 1	2281	832	3113	4558	12133
Tool 2	2269	818	3087	4534	12011
Total	11653	4222	15875	23294	60242

Fig. 2.35 Mesh properties in the numerical simulation of the tensile test using QForm UK® software.

In *Fig. 2.36*, the results of the numerical-experimental comparison of the tensile test are illustrated. In graph a), the results are related to the simulation run using the flow stress of the material obtained from the actual tensile test; in graph b), the flow stress from the compression test was utilized; in graph c) the flow stress obtained from the torsion test; finally, in graph d), the flow stress from the torsion test with data processed according to the proposed model was used. The blue curves in the graphs indicate the load [kN] and displacement [mm] values as outputs from the press during the experimental trials, while the orange curves represent the results from the numerical simulations. From graph a) it is evident that the numerical and experimental results are perfectly aligned up to a stroke value of 0.34 mm, demonstrating that, in the actual

tensile test, valid material characterization results were only obtained up until the onset of necking. Beyond this point, the use of the tensile test-derived flow stress in the simulation leads to an overestimation of the force values. This overestimation persists despite attempts to apply Bridgman's correction to the data, as detailed in Section 2.2.2. From graph b), it is evident that by using the interrupted compression test, we achieved a perfect overlap between the numerical and experimental data even during the necking phase in the tensile test, resulting in an accurate material characterization up to a strain of approximately 0.45. Conversely, graph c) shows that using the torsion test data leads to a significant underestimation of the actual force values in the simulation. On the other end, in graph d), it is apparent that when the torsion data are processed according to the proposed model, there is a notable improvement in the agreement between the experimental and numerical results. It is worth noting that material characterization via tensile and compression tests yields a more accurate representation of the material's elastic behavior, while the torsion test tends to neglect the elastic region to some extent.

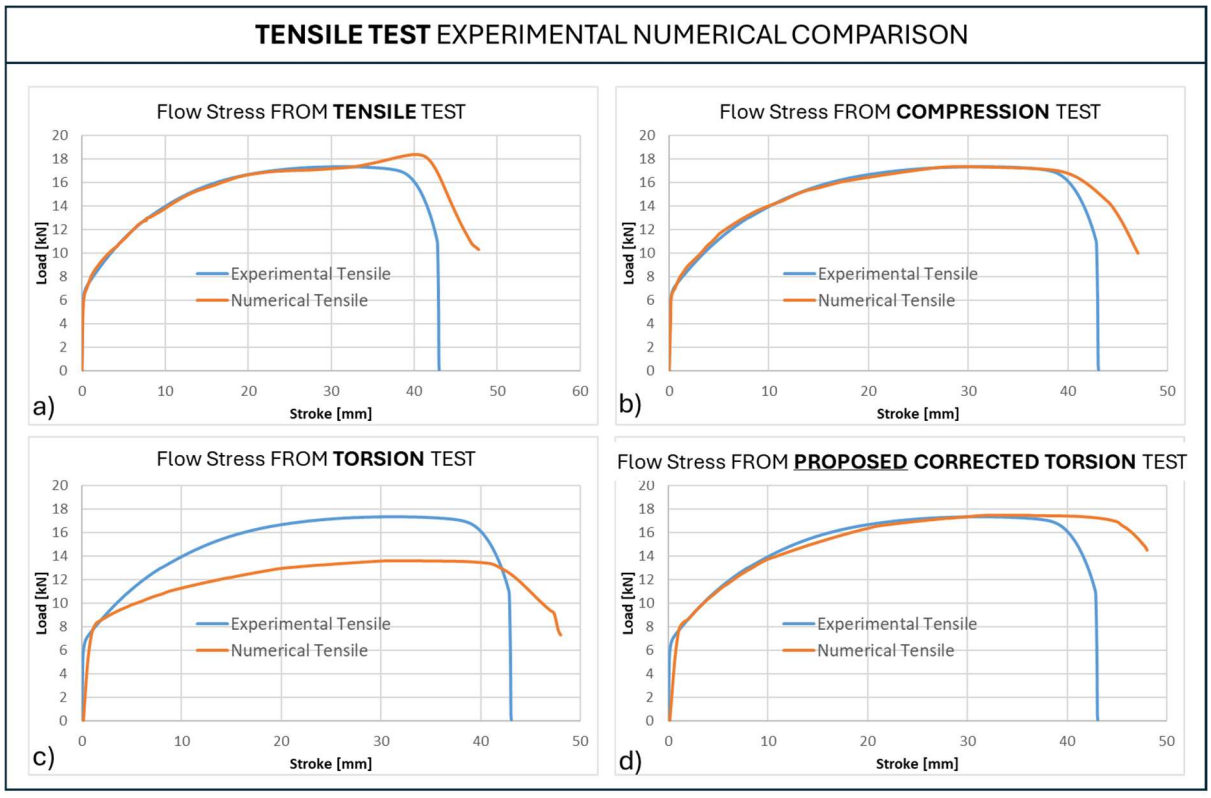

Fig. 2.36 Comparison between experimental tensile load-stroke curves and numerical results obtained using flow stress from different tests.

For the simulation of the torsion test, a rotational speed of 0.4 rpm was assigned to the rotating tool, which, given the specimen geometry, corresponds to a strain rate of 0.01 s^{-1}. The contact between the tools and the specimen was modeled as in reality, with a shape-interlocking constraint, and a Coulomb friction coefficient of 0.5 was set, considering that the area is not lubricated. The mesh parameters are reported in *Fig. 2.37*.

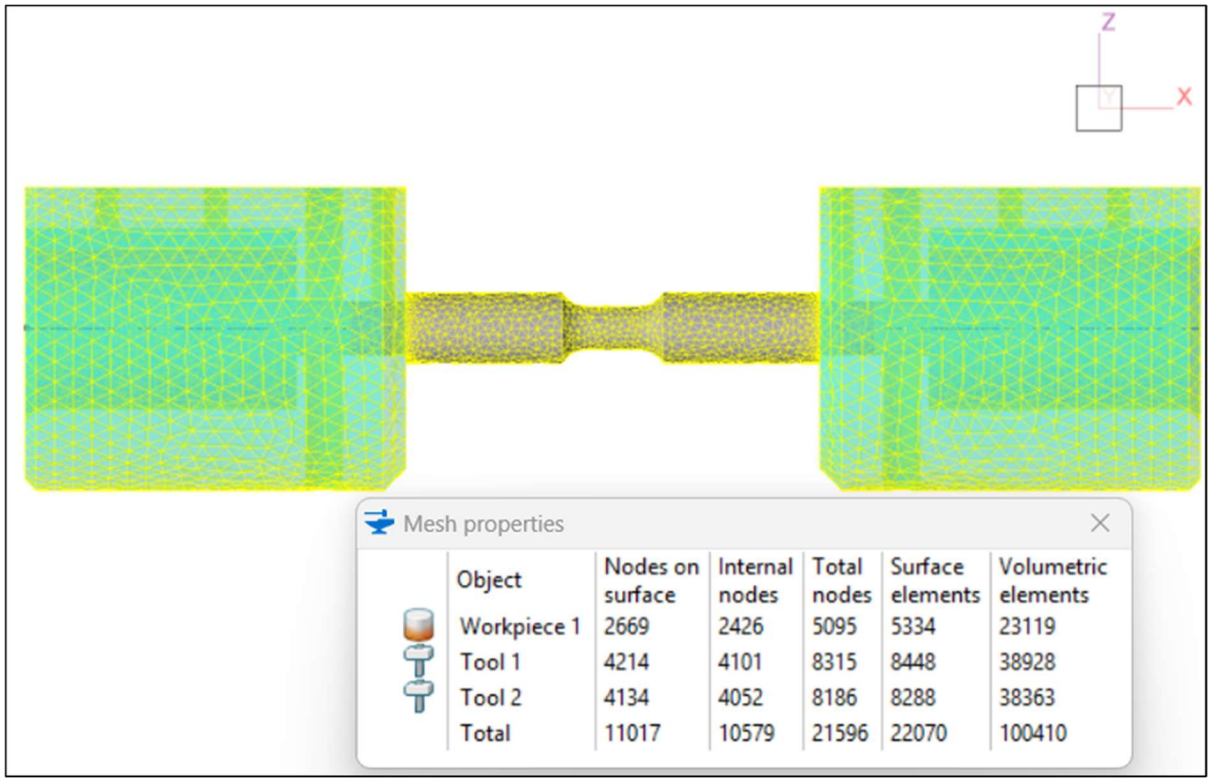

Object	Nodes on surface	Internal nodes	Total nodes	Surface elements	Volumetric elements
Workpiece 1	2669	2426	5095	5334	23119
Tool 1	4214	4101	8315	8448	38928
Tool 2	4134	4052	8186	8288	38363
Total	11017	10579	21596	22070	100410

Fig. 2.37 Mesh properties in the numerical simulation of the torsion test using QForm UK® software.

In *Fig. 2.39*, the results of the numerical-experimental comparison for the torsion test are presented in the form of torque [Nm] vs rotation angle [rad], following the same order and legend as the graphs from the tensile test. By observing graph a), it is clear that when simulating the torsion test using the flow stress of the material obtained from the tensile test, the torque is significantly overestimated up to a rotation angle of approximately 26 rad. At this point, the specimen reaches a strain of around 0.3, as shown in *Fig. 2.38a*. It can be seen that, as the FEM simulation progresses, the software extrapolates the results, calculating a torque that remains mostly constant. This result occurs because the software lacks information on the material's plastic behavior at higher strain values and then is unable to account for the progressive

hardening that occurs during torsional loading. Similarly, from graph b), it emerges that using the compression test, there is an overestimation of the torque up to an angular rotation value of about 35 rad, which corresponds to a strain value of approximately 1.1, as shown in *Fig. 2.38b*, and then the torque remains fairly constant as the rotation increases. At this point, by observing graphs c) and d), it can be observed that using the flow stress obtained from the torsion test results in an almost perfect agreement between the real and simulated torque values. However, when applying the proposed correction to the torsion test data, the simulation overestimates the real torque, as shown in graph d). This discrepancy arises because the software does not account for the fact that the material exhibits different crystallographic behavior when subjected to tensile versus torsional loading.

Initially, the calculations of Field and Backofen applied to process the torsion test data were consistent with the real torque values; however, once the proposed model is applied, the simulation fails to account for the material's inherent crystallographic differences between tension and torsion, leading to an overestimation of the torque. This difference in mechanical response is tied to the microstructural evolution of the material, where grain reorientation and texture development differ under various loading conditions. Torsional loading induces shear stresses that affect dislocation motion and crystallographic slip differently than tensile loading, leading to distinct hardening behaviors in the material, as discussed in paragraph 2.2.3. As a result, without specific modeling to account for these behaviors, the simulation cannot accurately capture the material's response in all conditions.

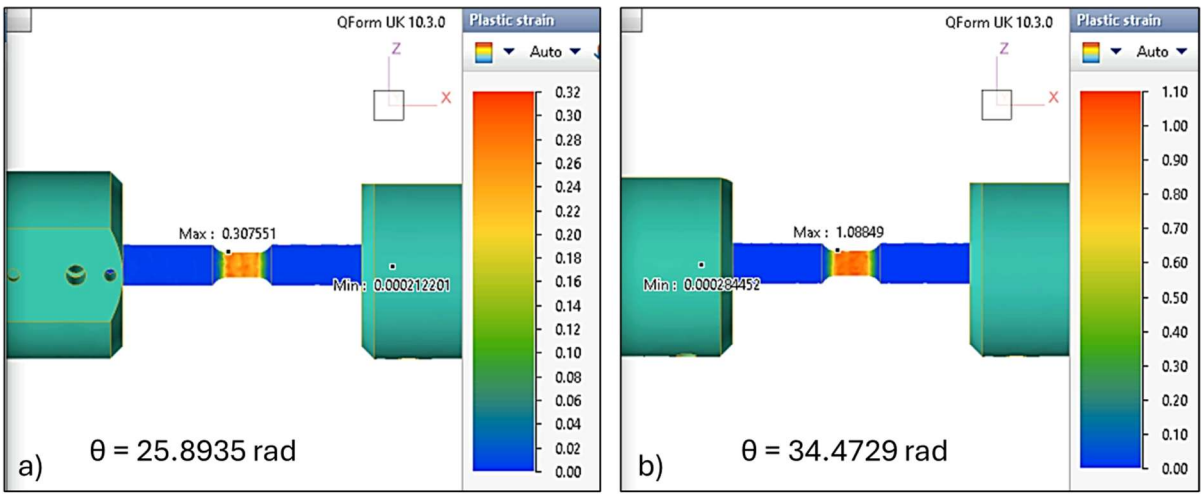

Fig. 2.38 Numerical simulation of the torsion test, strain values.

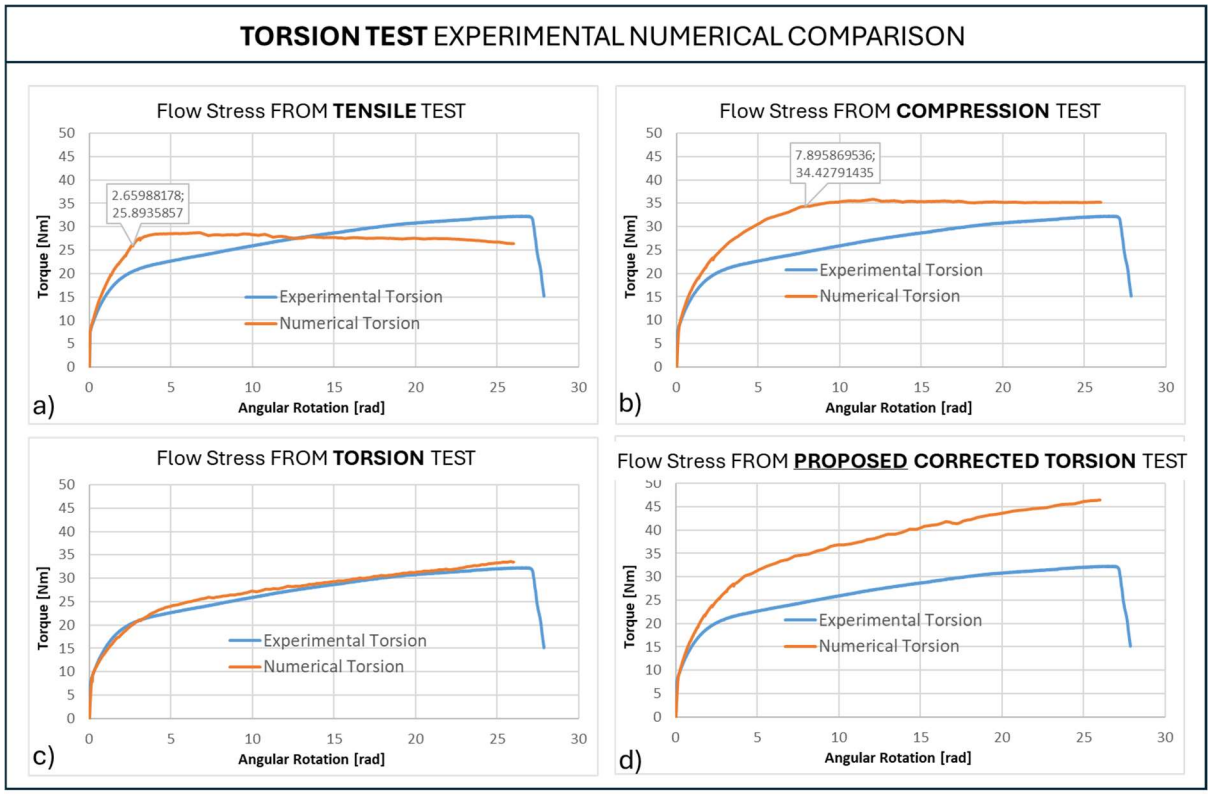

Fig. 2.39 Comparison between experimental torsion torque-angular rotation curves and numerical results obtained using flow stress from different tests.

To determine the most suitable test for characterizing the material's plastic behavior under cold deformation, particularly when subjected to triaxial stress states and large strain values, the hybrid compression test was simulated. The downward velocity of the upper tool was set to 0.1 mm/s to achieve an average strain rate of 0.01 s^{-1} during the simulation of the test, as shown in *Fig. 2.41.* Additionally, the tools were modeled as simple flat plates, and the contact between the tools and the specimen was defined using a Coulomb friction coefficient of 0.5 to simulate the absence of lubrication. Finally, the mesh parameters are reported in *Fig. 2.40.*

The results of the numerical-experimental comparison for the hybrid compression test are presented in *Fig. 2.42*. It can be observed from graphs a) and b) that using the flow stress derived from the tensile and compression tests yields an excellent agreement between the experimental and simulated data. Also in this case, as the strain increases, the software goes into extrapolation; however, this effect is not evident in the load-displacement curve of the test, due to the fact that, during the hybrid compression test, the specimen changes in geometry, leading to an increase in its cross-sectional area, which results in an increased load. Moreover, using the flow

stress from the compression test, as the strain increases, there is a slight overestimation of the force. On the other hand, from graphs c) and d), it is evident that when the simulation is run using the flow stress from the torsion tests, there is an underestimation of the actual loading force. However, when the torsion test data is processed using the proposed model, a perfect agreement between the numerical and experimental results is achieved.

This result validates the proposed model for processing cold torsion test data.

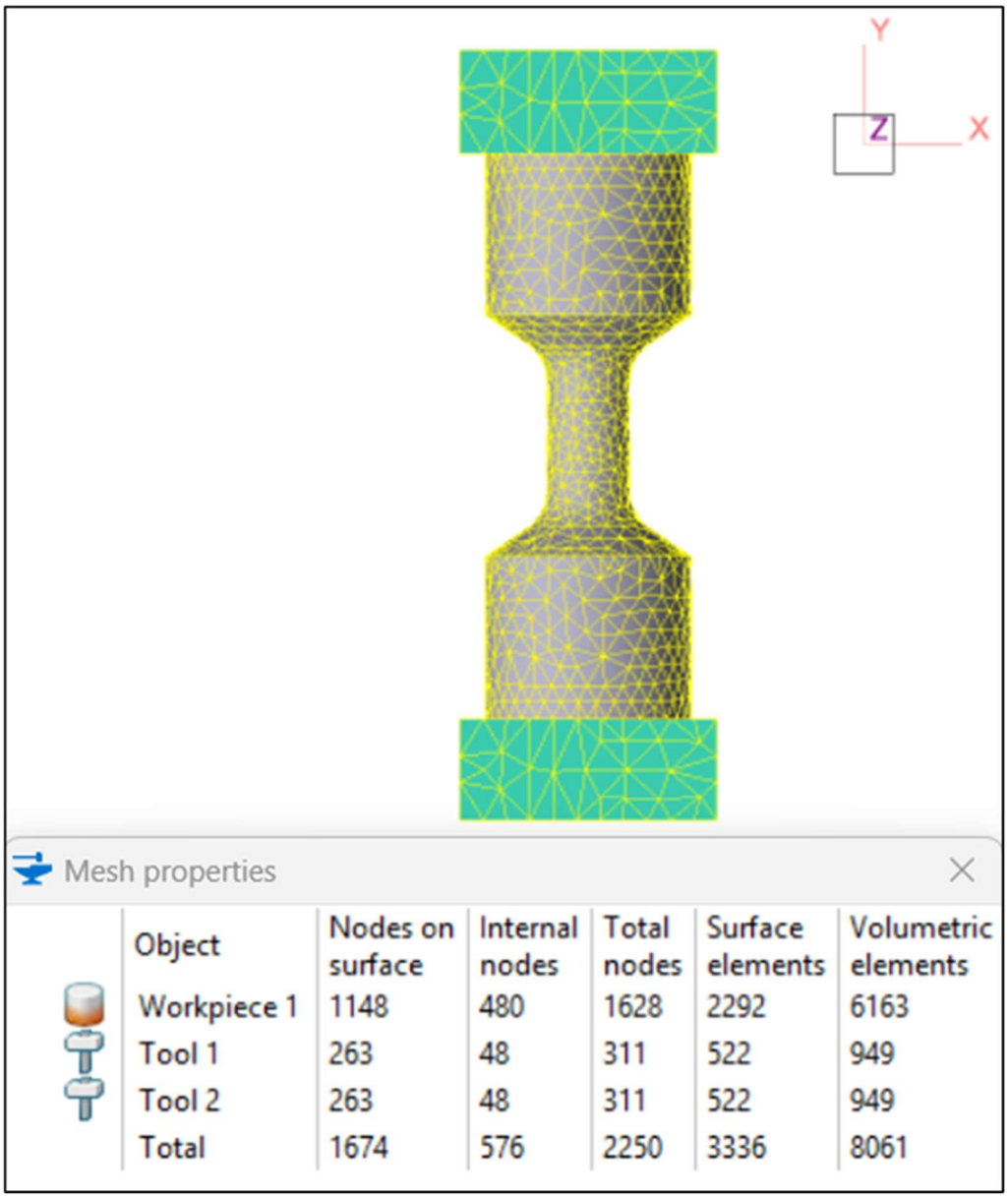

Object	Nodes on surface	Internal nodes	Total nodes	Surface elements	Volumetric elements
Workpiece 1	1148	480	1628	2292	6163
Tool 1	263	48	311	522	949
Tool 2	263	48	311	522	949
Total	1674	576	2250	3336	8061

Fig. 2.40 Mesh properties in the numerical simulation of the hybrid compression test using QForm UK® software.

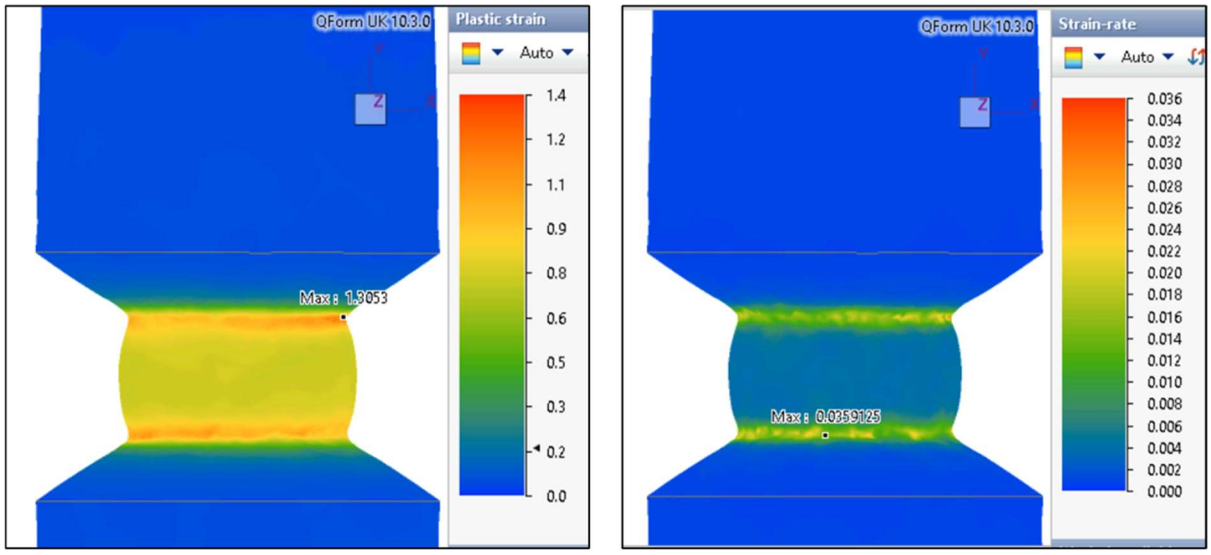

Fig. 2.41 Numerical simulation of the hybrid-compression test, on the left strain values, on the right strain rate values.

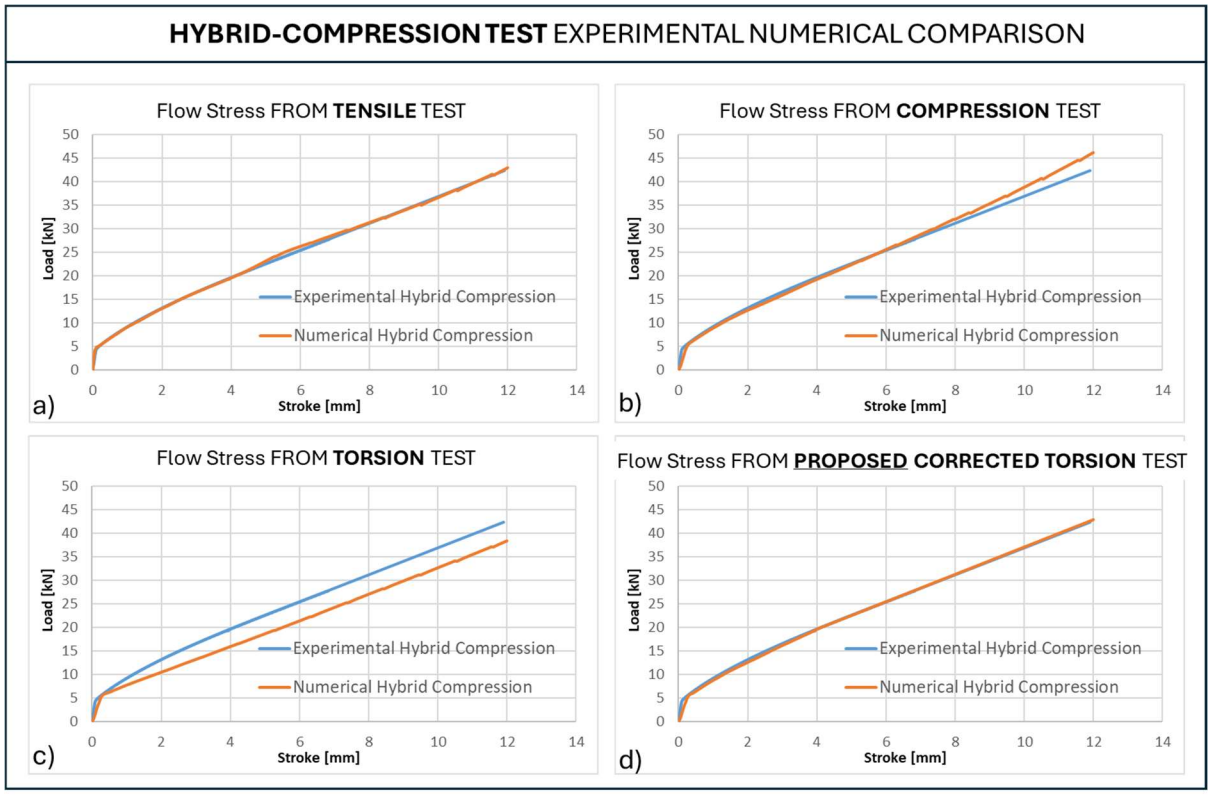

Fig. 2.42 Comparison between experimental hybrid-compression load-stroke curves and numerical results obtained using flow stress from different tests.

Furthermore, to validate the proposed model for processing the torsion test data including the effect of strain rate variation, the torsion tests performed at the speed of 0.1 and 1 s^{-1} were also processed, as shown in *Fig. 2.44a)*. In the graph, the blue curve

represents the flow stress of the material obtained from the torsion test at 0.01 s^{-1}, the orange curve at 0.1 s^{-1}, and the green curve at 1 s^{-1}. The solid lines indicate the flow stress values processed using the proposed model, while the dashed lines represent the flow stress calculated using the Fields and Backofen method. Subsequently, the complete material characterization of ETP copper, derived from the torsion tests processed using the proposed model across different strain rates, was inserted as material flow stress for the numerical model, and simulations of the hybrid compression test were run at the varied strain rates, as shown in *Fig. 2.43*.

Finally, in *Fig. 2.43* a), b), and c), the numerical-experimental comparison clearly demonstrates a perfect agreement between the experimental tests and the simulations of the hybrid compression test at different speeds, confirming that the proposed model, although developed based on tests at a strain rate of 0.01 s^{-1}, can be successfully applied to higher strain rates, ensuring its robustness and reliability for various testing conditions. The test simulation comparisons reveal that in cold deformation processes involving a triaxial stress state, such as the one represented by the hybrid compression test, using flow stress data obtained from cold torsion tests, processed through the Fields and Backofen model with the application of the Von Mises yield criterion, results in an underestimation of the actual forces involved in the deformation. This underestimation points to a crystallographic texture development and strain-hardening behavior in the material that is comparable to uniaxial tension and compression conditions, even when subjected to triaxial stress. Such behavior aligns with the observation that, under cold working conditions, the effects of texture and dislocation interactions become more pronounced, affecting the macroscopic mechanical response. Conversely, in hot deformation conditions, where the material is processed above its recrystallization temperature, these crystallographic and work-hardening effects are significantly minimized. This is due to the fact that the elevated temperatures enable restorative processes, such as dynamic recovery and recrystallization, which inhibit the formation of texture and reduce internal stress accumulation. As a result, the material exhibits a more uniform response to different loading conditions, without the marked discrepancies observed in cold working conditions, where texture development and slip systems play a more dominant role. [1,4]

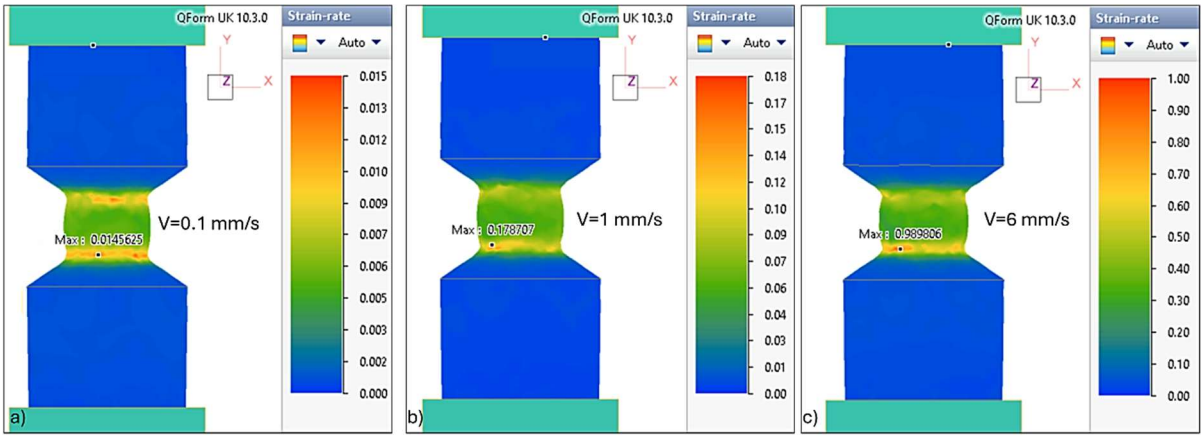

Fig. 2.43 Numerical simulation of the hybrid-compression test performed with press speed of a)0.1 mm/s, b) 1 mm/s, c) 6 mm/s.

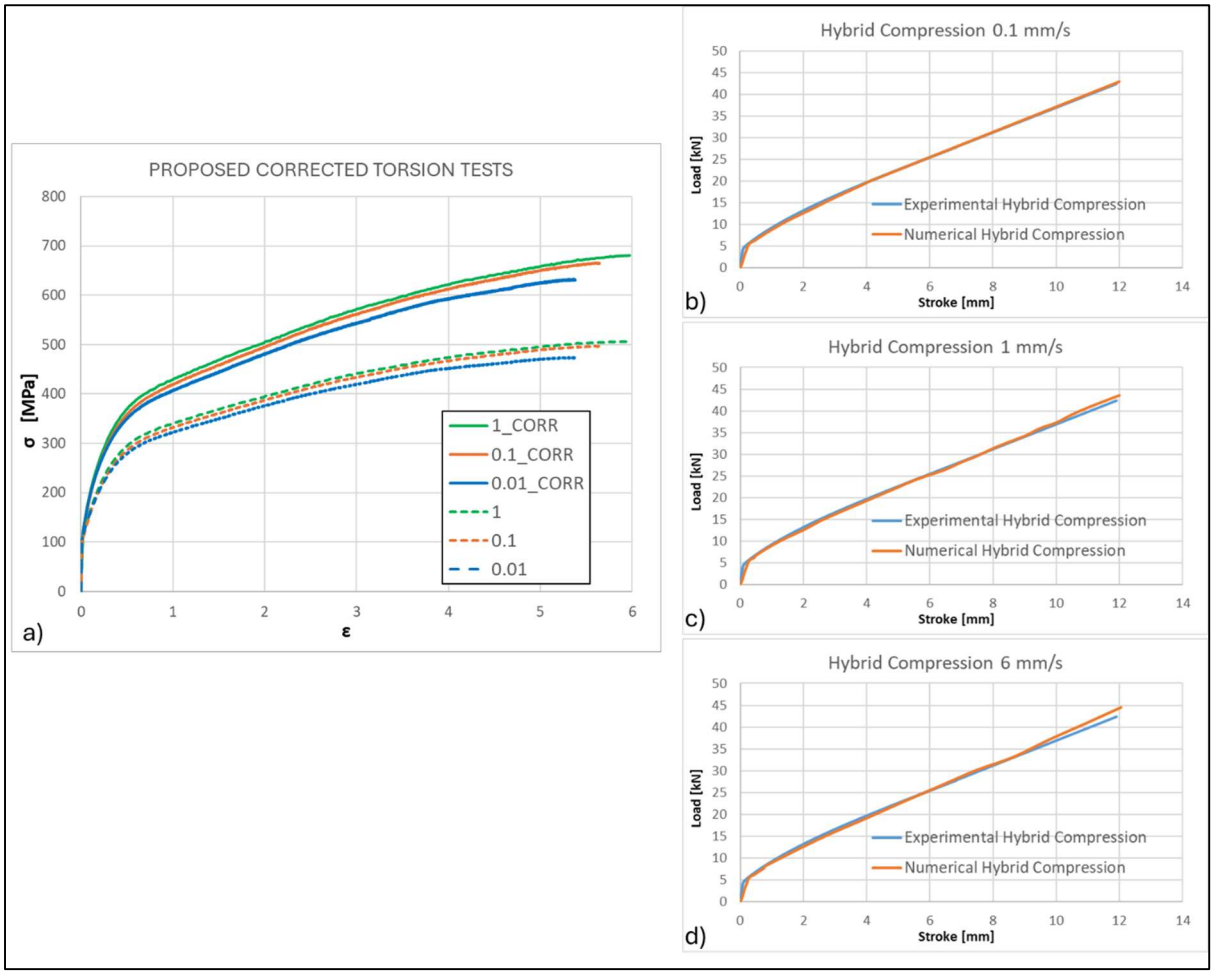

Fig. 2.44 a) Comparison between flow stress curves from torsion tests at different strain rates, elaborated with Fields and Backofen and the proposed model; b), c) d) Comparison between experimental hybrid-compression load-stroke curves and numerical results at different speeds.

2.3. INDUSTRIAL CASE STUDY: Experimental, analytical, and numerical analysis of the copper wire multi-pass drawing process

2.3.1. Copper Wire Multi-Pass Drawing: Process Modeling and Optimization

Introduction

In this section, the results from the characterization of ETP Copper, explained in the previous sections, will be applied to the study, modeling, and optimization of the copper drawing process for the production of electrical cables.

The drawing technology is a cold metal forming process that is mainly used for the production of wires, bars or tubes. In wire drawing technology, the process consists of reducing the cross-section of the starting rod through its deformation inside several dies with decreasing diameters. This deformation is produced by the application of a traction force at the exit of the die. Such pull force creates a triaxial stress state in the die able to permanently reduce the diameter of the wire and consequently strain hardened the material due to the large deformation in the cold working process. Therefore, one of the main limitations of the process is given by the need to keep the pull stress always below the yield stress of the material (strain hardening included), thus avoiding necking and wire breaks. This condition limits the wire reduction of a single pass, so that multi-passes are needed in order to achieve the requested final dimensions. Nowadays, the process is carried out continuously using complex industrial multi-step machines characterized by high deformation rates.

Several models have been proposed in the literature for the analytical computation of the material deformation process during wire drawing. The SLAB method, firstly proposed by Siebel [61,62], is one of the most widespread in relation to its simple application. It involves the definition of the equilibrium forces by dividing the whole section area of the wire into smaller parts (slab) and then integrating the equation in the drawing direction. The method employs the assumption of a homogenous deformation field along the slab height with the normal stress uniformly distributed on

the plane parallel to it; the integral equation's solution results from these simplified boundary conditions. Another analytical method was developed by Wistreich [63] and then applied by Wright [64]: it involves the evaluation of a ‘deformation zone shape parameter’ depending on the reduction ratio and the die's semi-angle; the contribution of the distortion and friction works are calculated by introducing a redundant work factor obtained with semi-empirical approaches from physical measurements and depending on the deformation zone shape parameter. In both theories (Wistreich and Siebel), the additional friction work due to the presence of the bearing length downstream of the drawing cone is omitted. One of the most notable models was proposed by Avitzur [65,66]: it involves the application of the Upper-Bound approach to the drawing problem, dividing the wire into three zones, in each of which the velocity field is assumed to be continuous. The inlet and exit zones of the die are characterized by the lack of deformation in the wire, and the axial component of the velocity is uniform, while in the central zone, the plastic flow occurs, and the velocity field is directed toward the cone's apex with axial cylindrical symmetry. Avitzur’s method involves friction work due to the presence of the bearing length.

It is known that the wire drawing process depends on three main parameters: the wire material properties, the die geometry (such as die angle and reduction ratio), and the process conditions (such as friction at the interface between the die and the wire). Over the years, several researchers focused their attention on investigating the influence of these parameters on the process. Dixit and Dixit [67] studied the effect of the reduction ratio, the die semi-angle, the friction coefficient, and the back tension on die pressures and on the pull stress. They found that an increase in the reduction, or a decrease in the die angle, or a decrease of the friction coefficient tends to homogenize the wire deformation over the cross section. Otherwise, with low reduction and large die-angle, the plastic zone near the axis of symmetry narrows down and may eventually disappear, causing the central bursting defect to occur. Vega et al. [68] applied the Avitzur's model and investigated the effects of the die angle, the friction coefficient, and the reduction ratio on the drawing force during the copper wire drawing process. They showed that the drawing force increases when the reduction ratio and the die angle increase, while the friction coefficient affects the optimum die angle value corresponding to the minimum value of the drawing force: the optimum die angle increases with increasing coefficient of friction. M. Tintelecan et al. [69] carried out an

experimental campaign to calculate the value of the drawing force using dies with different semi-angles and bearing lengths and to estimate their optimal values for steel wire drawing. They obtained the smallest values for experimental drawing force with the die semi-angle between 6° and 8° and the bearing length corresponding to 40% of the final diameter. G.A.S. Martinez et al. [70] carried out an investigation on the operational parameters to obtain the best combination that minimizes energy consumption during the process. The effects of the drawing speed, drawing force, temperature, and tension distribution on the wire drawing were investigated using an experimental and numerical approach. They found that the dies with die angle of 18° reach the minimal friction coefficients at the most significant speed (20.6-24.2 m/s); instead, those with die angles of 14° reach the minima at smaller speeds (14.4-18.7 m/s), due to the difference in dragging the lubricant associated with the different geometries of the dies. Compressive stresses on the surface and at the center of the wire are larger for dies with larger die angles; on the other hand, dies with a smaller die angle show a more homogenous as far as the distribution of radial stresses is concerned.

In the previously discussed papers, the efforts made in the research for the optimization of the process have always been focused on the single wire-drawing pass. In the multi-pass industrial machines, the deformation is achieved continuously and at the same time on several dies. Between two consecutive dies, rotating capstans pull the wire, thus generating the pull force but also a back force. Indeed, the capstan speed is greater than the speed of the wire wrapped around it, thus generating slip and, consequently, transmitting pull and back tension to the wire. In this contest, to the best of the author's knowledge, only J. Thimont et al. [71] introduced a model that considered pull forces by capstans and die pressure in the multi-pass drawing process. They investigated the wire drawing process performed by ArcelorMittal WireSolutions to produce high strength steel wire. After developing a constitutive law based on the wire microstructure evolution, they developed a multipass drawing theoretical model applied to an industrial machine consisting of 14 passes of wire reduction, considering the relation between drawing force and back-pull force.

In this thesis work, the wire drawing process was extensively studied from various perspectives, at first, a theoretical multi-pass wire drawing model was developed, considering the entire process and focusing on the relationship between drawing stress

and back-stress, following the Avitzur model. The drawing stresses acting on the material were investigated by analyzing the variation in process parameters such as the friction coefficient between the wire and die, between the wire and capstan, and the number of wire windings around the capstans. Subsequently, the model was implemented by incorporating the plastic behavior of the material as the process conditions varied, obtained by means of the cold torsion tests.

Industrial wire drawing

The wire drawing process was performed on ETP Pure Copper (99.9% in weight) at the ICEL s.c.p.a company of Lugo (Italy). The wire rod was subjected to a preliminary drawing process from a diameter of 8.00 mm to 1.83 mm (area reduction 94.77%). Subsequently, without any annealing treatment, 21 drawing passes were carried out up to a final diameter of 0.205 mm, which corresponds to a total strain of $\bar{\varepsilon} = 7.33$ (total area reduction 99.93%). This value was calculated according to (2.27) [62]:

$$\bar{\varepsilon} = 2ln\frac{D_i}{D_f} \qquad (2.27)$$

where D_i and D_f are the initial and final diameters.

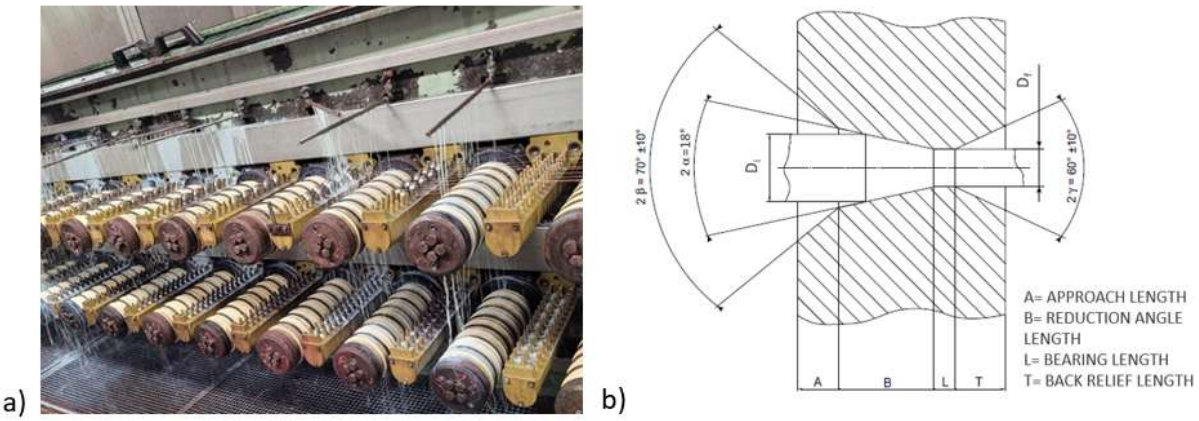

Fig. 2.45 a) Picture of industrial machine used in ICEL s.c.p.a. b) Diagram of the die (the profile of the die is not so sharp, as shown in the diagram, but the different areas are blended together with rounded edges). [72]

Two different industrial multi-pass wire drawing machines were considered, each featuring different mechanical elongation ratios, as summarized in *Table 2.4*. Both machines are equipped with 21 dies (representing the drawing passes) and 20 capstans *(Fig. 2.45a)*. Upon exiting the machines, the wire enters directly into the

annealer. Dies with semi-angle of 9° and bearing lengths of 25% of the final diameter are mounted on both machines, as schematically represented in *Fig. 2.45b.*

Machine and wire elongation at each pass of reduction are calculated as in Eqs. (2.28) and (2.29): [62,64]

$$E\%_{machine_i} = \left(\frac{S_{C_i}}{S_{C_{i-1}}} - 1\right) * 100 \qquad (2.28)$$

$$E\%_{wire_i} = \left[\left(\frac{D_{i_i}}{D_{f_i}}\right)^2 - 1\right] * 100 \qquad (2.29)$$

Where S_{C_i} is the tangential speed of the capstan, which is placed at the exit of the die, after the i_{-th} pass of reduction from the initial diameter D_{i_i} to the final D_{f_i}.

It has to be noted that the machine elongation, which depends on the transmission ratio of the gears' train moving the capstans, Eq (2.28), must be always lower than the wire elongation, Eq. (2.29) at each pass in order to work with a slip condition between the capstans and the wire.

Fig. 2.46 shows the data collected during the monitoring of the wire breaks that occurred within the two machines over a period of 60 days, divided into four time periods of 15 days each to carry out a statistical analysis of the failure rate of the machines. Machine 1 was found to have a higher failure rate than Machine 2, with a wire break occurring on average every 2.5 days compared with every 4 days on Machine 2.

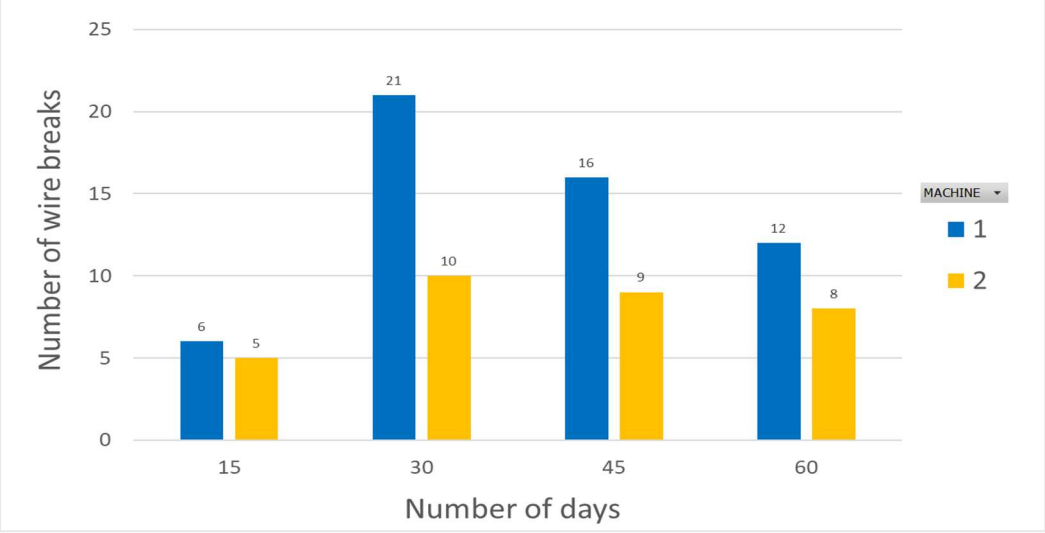

Fig. 2.46 Monitoring of the wire breaks that occurred on the two machines in 60 days, divided into four time periods of 15 days each. [72]

Table 2.4 Comparison between the mechanical characteristics of Machine 1 and Machine 2.

	MACHINE N°1					**MACHINE N°2**				
N° Pass	Diameter Initial [mm]	Diameter Final [mm]	Reduction Ratio [%]	Wire Elongation [%]	Machine Elongation [%]	Diameter Initial [mm]	Diameter Final [mm]	Reduction Ratio [%]	Wire Elongation [%]	Machine Elongation [%]
1	1.83	1.592	24.3	32.1	24.0	1.830	1.6144	22.2	28.5	25.0
2	1.592	1.417	20.8	26.2	24.0	1.6144	1.4382	20.6	26.0	25.0
3	1.417	1.261	20.8	26.3	24.0	1.4382	1.2813	20.6	26.0	25.0
4	1.261	1.122	20.8	26.3	24.0	1.2813	1.1415	20.6	26.0	25.0
5	1.122	0.998	20.9	26.4	24.0	1.1415	1.0169	20.6	26.0	25.0
6	0.998	0.888	20.8	26.3	24.0	1.0169	0.9059	20.6	26.0	25.0
7	0.888	0.790	20.9	26.3	24.0	0.9059	0.8071	20.6	26.0	25.0
8	0.790	0.703	20.8	26.3	24.0	0.8071	0.719	20.6	26.0	25.0
9	0.703	0.626	20.7	26.1	24.0	0.719	0.6405	20.6	26.0	25.0
10	0.626	0.557	20.8	26.3	24.0	0.6405	0.5706	20.6	26.0	25.0
11	0.557	0.495	21.0	26.6	24.0	0.5706	0.5187	17.4	21.0	19.2
12	0.495	0.441	20.6	26.0	24.0	0.5187	0.4716	17.3	21.0	19.2
13	0.441	0.392	21.0	26.6	24.0	0.4716	0.4287	17.4	21.0	19.2
14	0.392	0.359	16.1	19.2	17.2	0.4287	0.3897	17.4	21.0	19.2
15	0.359	0.329	16.0	19.1	17.2	0.3897	0.3543	17.3	21.0	19.2
16	0.329	0.301	16.3	19.5	17.2	0.3543	0.3221	17.4	21.0	19.2
17	0.301	0.276	15.9	18.9	17.2	0.3221	0.2928	17.4	21.0	19.2
18	0.276	0.253	16.0	19.0	17.2	0.2928	0.2662	17.3	21.0	19.2
19	0.253	0.232	15.9	18.9	17.2	0.2662	0.242	17.4	21.0	19.2
20	0.232	0.213	15.7	18.6	17.2	0.242	0.22	17.4	21.0	19.2
21	0.213	0.205	7.4	8.0	-	0.22	0.205	13.2	15.2	-

Wire drawing analytical models

Three analytical models for the calculation of the stress applied to the wire during the drawing process are the most widely referenced in the literature. The first is the SLAB method [61,62] which is based on the definition of an equilibrium of forces applied to a thin section of the wire (slab) and then integrated in the drawing direction. The method assumes that the deformation field is uniform across the height of the slab, with normal stress uniformly distributed on the plane parallel to it. The solution to the integral

equation is derived from these simplified boundary conditions, and it takes the form of (2.30).

$$\sigma_d = \frac{1+B}{B}\bar{\sigma}_m\left[1-\left(\frac{R_f}{R_i}\right)^{2B}\right]+\frac{2\alpha}{3\sqrt{3}}(\bar{\sigma}_{in}+\bar{\sigma}_{out}) \qquad \text{with} \qquad B=\mu\cot\alpha \qquad (2.30)$$

Where α is the semi-angle of the die, μ is the Coulomb's friction coefficient, $\bar{\sigma}_{in}$ and $\bar{\sigma}_{out}$ are the equivalent flow stress of the material at the inlet and the exit of the die, and $\bar{\sigma}_m$ is the mean flow stress. The second method is that proposed by Wistreich [63] and Wright [64] and reported in Eq. (2.31). They introduced a redundant work factor ϕ for the estimation of inhomogeneous deformation due to the distortion of the wire. The value of the redundant work factor was obtained with a semi-empirical approach and depends on the deformation zone shape Δ.

$$\sigma_d = \bar{\sigma}_m\phi\left[ln\left(\frac{1}{1-r}\right)+\frac{4\mu}{\Delta}\right] \quad \text{with} \quad \Delta=\frac{\alpha}{r}\left(1+\sqrt{1-r}\right)^2 \quad \text{and} \quad \phi=0.8+\frac{\Delta}{4.4} \qquad (2.31)$$

Where r is the reduction ratio.

The last method was proposed by Avitzur [65], applying the Upper-Bound approach to the drawing problem, and the formulation is shown in Eq. (2.32). It involved the assumption that the wire can be divided into three zones, in each of which the velocity field is assumed to be continuous: the inlet and exit zones of the die are characterized by the lack of deformation in the wire and the axial component of the velocity is uniform, while in the central zone, the plastic flow occurs and the velocity field is directed toward the cone's apex with axial cylindrical symmetry.

$$\sigma_d = \bar{\sigma}_m\frac{2f(\alpha)\,ln\left(\frac{R_i}{R_f}\right)+\frac{2}{\sqrt{3}}\left(\frac{\alpha}{sen^2(\alpha)}-cot(\alpha)\right)+2\mu\left[cot(\alpha)\left(1-ln\left(\frac{R_i}{R_f}\right)\right)ln\left(\frac{R_i}{R_f}\right)+\frac{L}{R_f}\right]}{\left(1+2\mu\frac{L}{R_f}\right)} \qquad (2.32)$$

Where $f(\alpha)$ is a function of the die's semi-angle calculated as in Eq. (2.33),

$$f(\alpha)=\frac{1}{sin^2(\alpha)}\left[1-cos(\alpha)\sqrt{1-\frac{11}{12}sin^2(\alpha)}+\frac{1}{\sqrt{11,12}}ln\left(\frac{1+\sqrt{\frac{11}{12}}}{\sqrt{\frac{11}{12}}cos(\alpha)+\sqrt{1-\frac{11}{12}sin^2(\alpha)}}\right)\right] \qquad (2.33)$$

All three analytical models involve the effects on the wire caused by uniform work due to the reduction ratio, non-uniform or redundant work due to the wire distortion,

and friction work modeled according to Coulomb model. However, the SLAB and Wistreich-Wright models don't account for the additional friction work due to the presence of the bearing length downstream of the drawing cone.

Multi-pass implemented analytical model

To develop the analytical model for calculating the stresses acting on the wire during the multi-pass wire drawing process, also considering the presence of the capstans, Avitzur's theory was employed for the modeling of the individual drawing steps, whereas the Capstan theorem (or theorem of Eytelwein) has been used to model the drive capstan between two consecutive passes of reduction [73,74]. As shown in the schemes in *Fig. 2.47a* and in *Fig. 2.48*, the relation between drawing stress σ_d and the back-stress at the next die σ_b is expressed as follows:

$$\sigma_{b_i} = \sigma_{d_{i-1}} e^{-2\pi N \mu_c} \qquad (2.34)$$

Where N is the number of windings of the wire around the capstan and μ_c is the friction coefficient between wire and capstan.

At the start of the drawing operation (step 1), σ_{d_1} is calculated without considering the contribution of the back-stress. From step 2 and for the next steps, σ_{b_i} is calculated considering the $\sigma_{d_{i-1}}$ contribution and then used to calculate σ_{d_i}.

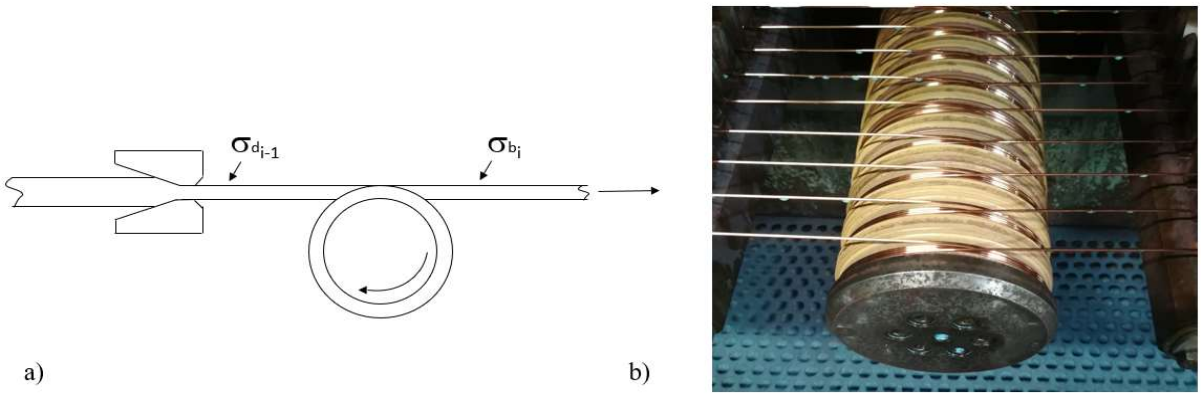

Fig. 2.47 a) Diagram of a capstan. Relation between drawing stress and back-stress; b) Picture of the capstan on industrial machine used in ICEL s.c.p.a. [72]

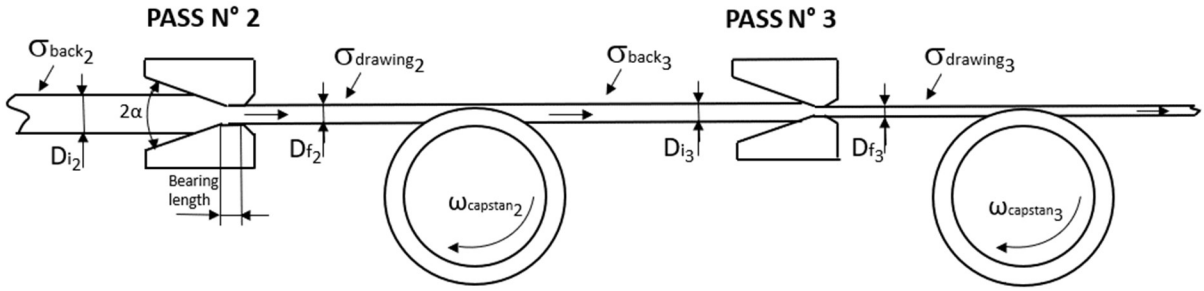

Fig. 2.48 Operation diagram of two consecutive drawing steps: pass number 2 and pass number 3. [72]

As a first approach in the study of the drawing process, the flow stress law for ETP copper in the form of Eq. (2.35), found in the literature [74] and obtained from tensile tests on the wire, was incorporated into the modeling of the drawing stress calculations.

$$\overline{\sigma} = C(\overline{\varepsilon})^n = 359(\overline{\varepsilon})^{0.149} \qquad (2.35)$$

The drawing and back-stresses were compared with the yield stress step by step when different processing conditions were applied for both Machine 1 and Machine 2. The results of the analytical analysis are shown in the graph in figures from *Fig. 2.49* to *Fig. 2.52.* In all the graphs, the drawing stress is represented with a regular line and the back-stress with a dashed line, with green lines corresponding to Machine 1 and red ones to Machine 2.

Fig. 2.49 shows the stresses when both friction coefficients between the wire and die, and between wire and capstan are μ=0.05 [64,68,75], and the number of windings of the wire around all the capstans is 3. Clearly, the drawing stresses and back-stresses are always safely lower compared with the material yield stress although the two machine configurations produce different maximum drawing stresses: 340 MPa for Machine 1 at step 13 and 325 MPa for Machine 2 at step 10. It is also observable that, in Machine 1, a decrease of stress occurs at pass 14 while, in Machine 2 it occurs at pass 11: these points correspond to the change of the machines' elongation ratio, which depends on the speed ratio of the gears' train moving the capstans, as previously described. In Machine 2, the wire is stressed more homogeneously along the steps while, in Machine 1, the wire is significantly stressed in the first steps (1-13), while in the last steps (14-21) stress is significantly reduced. Regardless, the wires should always be safely produced by both machines since drawing stresses are always

well below the wire yield stress. But it is also clear that, as the friction coefficient between wires and die increases (i.e. from 0.05 to 0.25), a considerable increase of the drawing stress acting on the wire may occur, as shown in *Fig. 2.50*. These friction coefficient values correspond to a lubrication regime that varies from an excellent lubrication with a thick film of lubricant to a limit lubrication with sticking between die and wire [64]. The changes in lubricant efficiency or in die wear may explain the different failure ratios of the two machines: in both machines these effects shift the drawing stress values close to the material resistance limit curve until pass n° 10; on Machine 1 the critical level is almost reached in steps from n° 11 to n° 13, making these steps the most critical, while on Machine 2 from pass n° 11 the stress values decrease to a safe level with respect to the material limit curves.

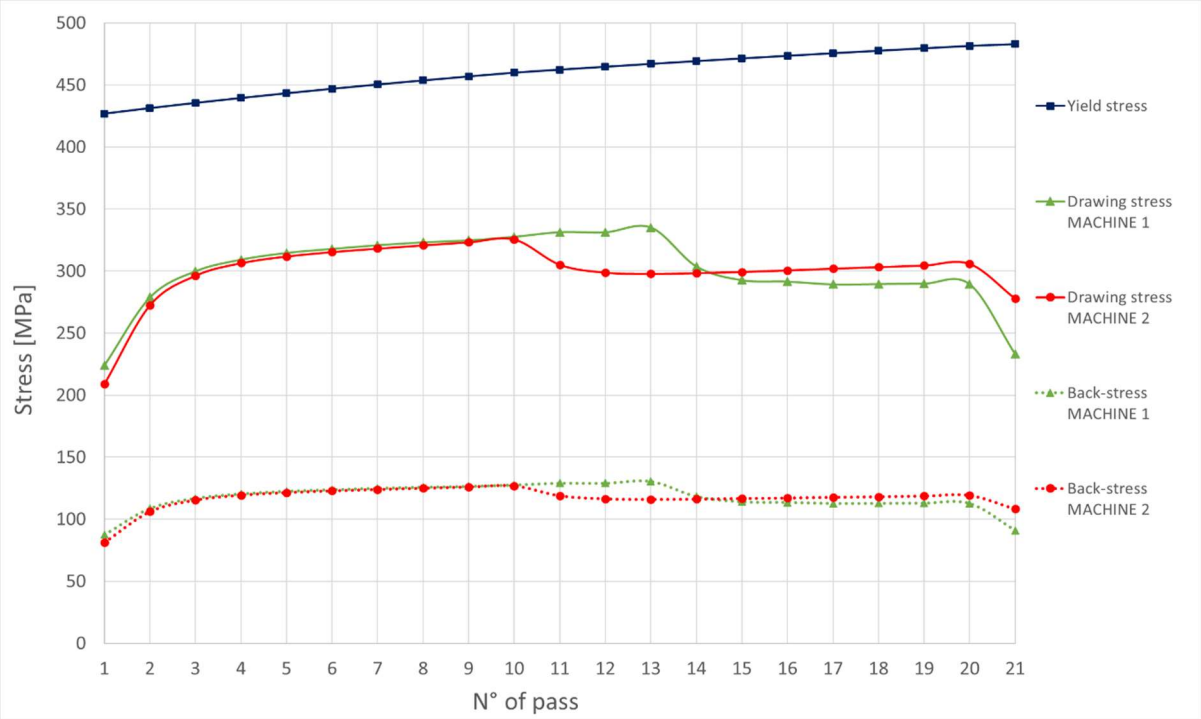

Fig. 2.49 Comparison between drawing stress and back-stress on Machine1 and Machine2 with coefficient of friction wire/dies and wire/capstans equal to μ=0.05 and the number of wire windings around each capstan equal to 3. [72]

In *Fig. 2.51* the value of the drawing stress is calculated considering different friction coefficients between capstans and wire under the same friction coefficient μ=0.05 between wire and die. It must be noted that the friction coefficient between capstans and wire has an opposite effect on all the stresses compared with the friction coefficient between the wire and die: an increase of the friction coefficient produces a relevant

decrease of the drawing stress and of the back-stress at the inlet of each die. Similar trends can be plotted for Machine 2 as well.

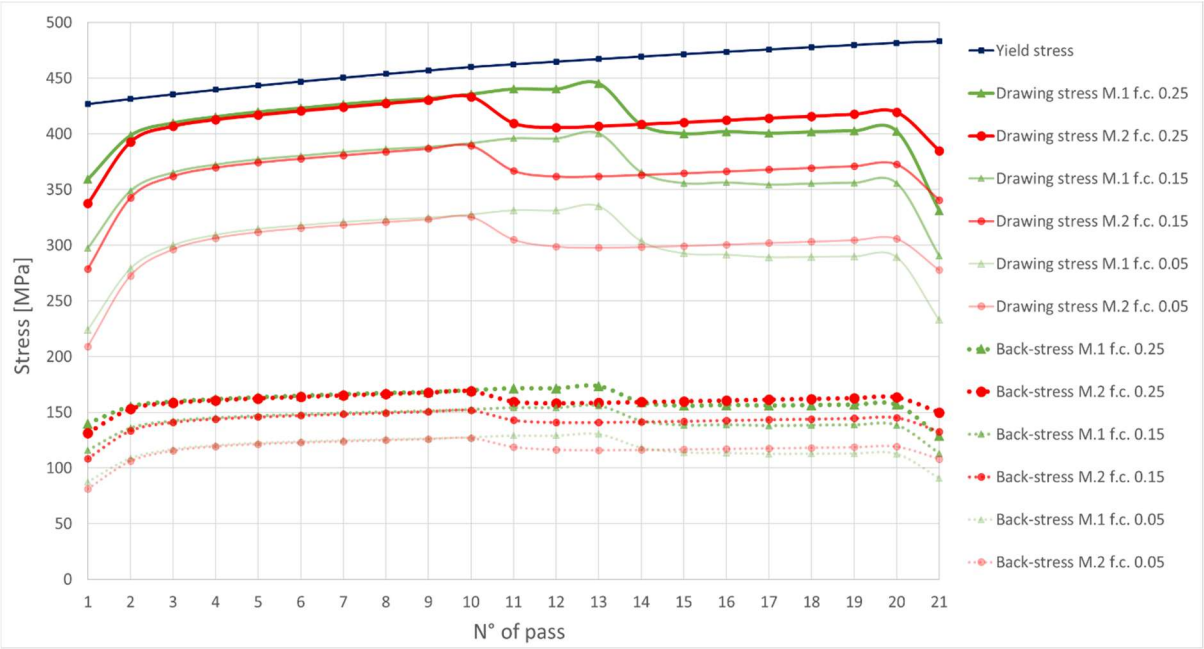

Fig. 2.50 Variation of the drawing stress and the back-stress with friction coefficient between wire and dies at each pass of reduction; friction between wire and capstan constant equal to μ_c=0.05; wire windings around capstan N=3. [72]

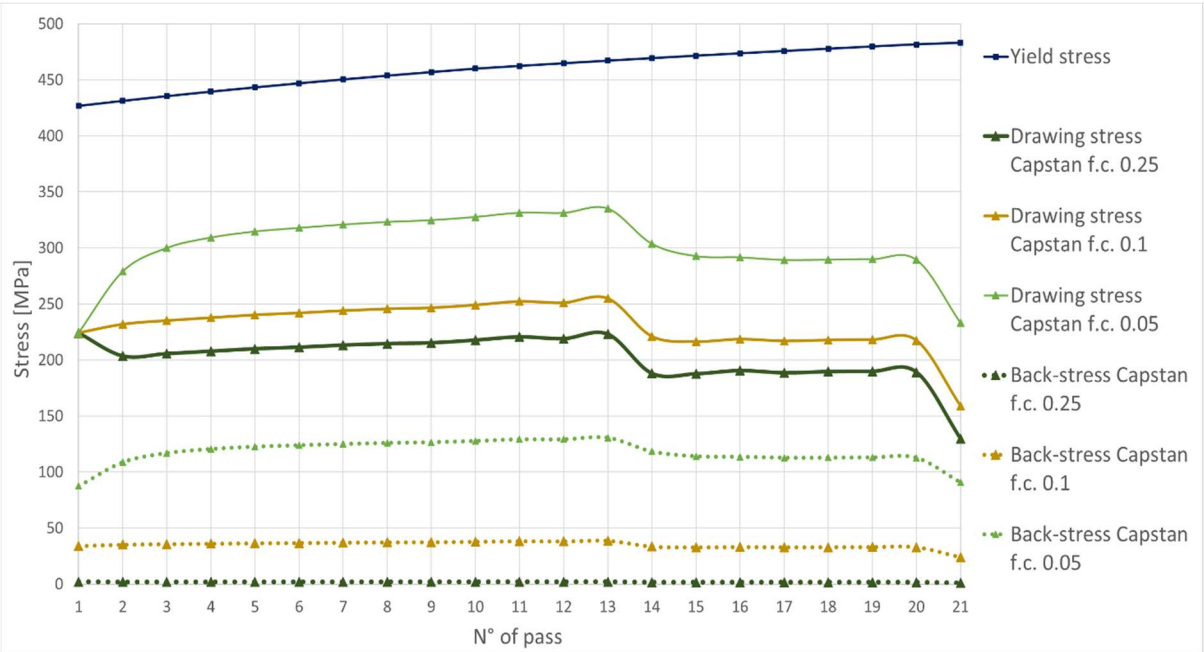

Fig. 2.51 Variation of the drawing stress and the back-stress with friction coefficient between wire and capstans at each pass of reduction on Machine1; friction between wire and die constant equal to μ=0.05; wire windings around capstan N=3. [72]

Fig. 2.52 shows the drawing and back-stress behaviors considering a different number of wire windings around the capstans. This parameter has a great impact on the management of process stresses. Increasing the number of windings from 2 to 3 and 4, the stresses decrease, because the back-stresses acting on the wire are reduced.

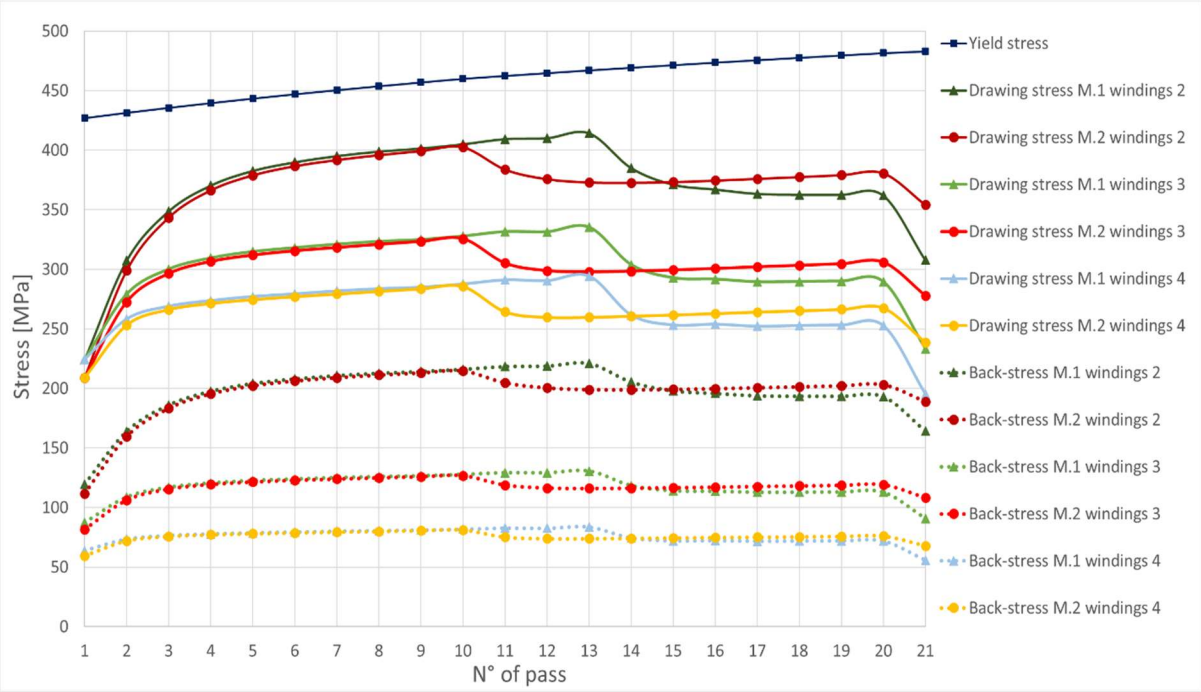

Fig. 2.52 Variation of the drawing stress and the back-stress with the number of windings of the wire around the capstans at each pass of reduction on Machine1 and Machine2; friction coefficient between wire/dies and wire/capstans equal to μ=0.05. [72]

Multi-pass analytical model implemented with the ETP Copper flow stress characterization

In the previous paragraph the graphs of the stresses acting on the wire during the drawing process as a function of the number of passes were shown. It is important to note that during the process, the material is subjected not only to high strain values exceeding 7 for the wire exiting the machine but also to high strain rates. As explained in the analytical modeling of the multi-pass drawing process, from the inlet to the outlet of the machine, the cross-section of the wire decreases while its length increases, resulting in an incremental increase in the drawing speed with each pass. In industrial

machines, the copper wire drawing process is performed at high production speeds, as can be seen in *Fig. 2.53*, where an example of the production speed trend at each step is reported for a copper wire that is drawn from an initial diameter of 1.83 mm to a final diameter of 0.2 mm through the reduction steps sequence of Machine 1. Considering that the final speed of the wire exiting the machine is 30 m/s, the average strain rate at each pass, calculated as in Eq. (2.36), varies from very low strain rate values on the first steps to values of about 86500-87000s^{-1} on the last steps. It is, therefore, essential to include in the process modeling an adequate material flow stress that takes into account not only the work hardening but also the strain rate and the high strain values to which the material is subjected.

$$\dot{\bar{\varepsilon}} = \bar{\varepsilon}\frac{V_{Tr}}{L_d} \quad \text{where} \quad L_d = \frac{D_0 - D_f}{2\tan\alpha} \qquad (2.36)$$

Where $V_{Tr}$is the wire drawing speed and L_d is the average deformation length, as shown in *Fig. 2.53*.

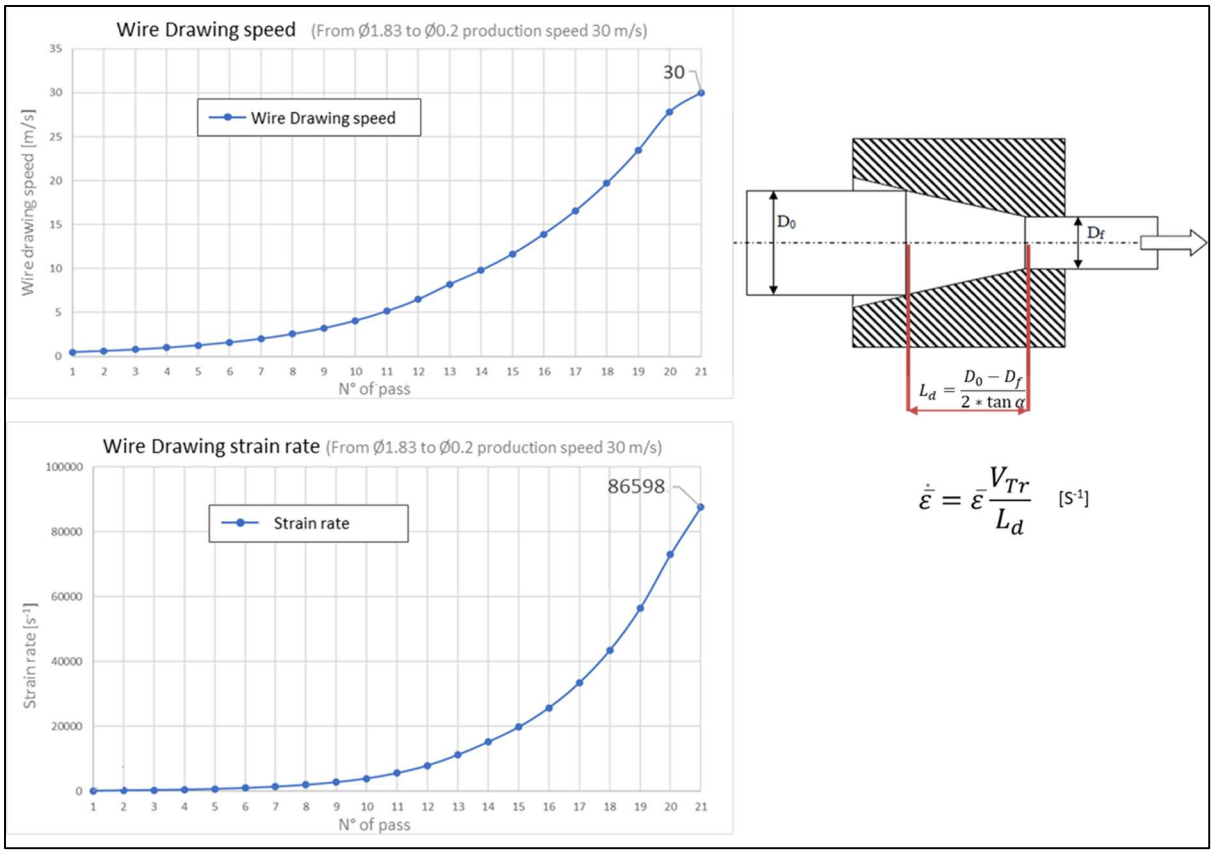

Fig. 2.53 Variation of wire strain rate at each step in a multi-pass wire drawing process with a production speed of 30 m/s.

At this point, cold torsion tests were performed on four copper wire rods purchased by ICEL s.c.p.a. from four different suppliers. The wire rod material was ETP copper (pure 99.95% in weight) and was labeled as C1, C2, and C3 coming respectively from the first 3 suppliers; in addition, an Oxygen Free copper rod (pure 99.99% pure in weight) called C4 was also characterized. The torsion tests were carried out using the procedure explained in detail in paragraph 2.2, varying three strain rates, 0.1, 1, and 5 s^{-1}, and the results in the form of stress vs strain are shown in the graphs in *Fig. 2.54*. Furthermore, for each copper, a flow stress law of the material was regressed, considering the influence of strain rate in the form given in Eq. (2.37) where n is the strain hardening coefficient and m is the strain rate sensitivity coefficient.

$$\overline{\sigma} = \mathrm{C} \cdot \bar{\varepsilon}^{n} \cdot \dot{\bar{\varepsilon}}^{m} \qquad (2.37)$$

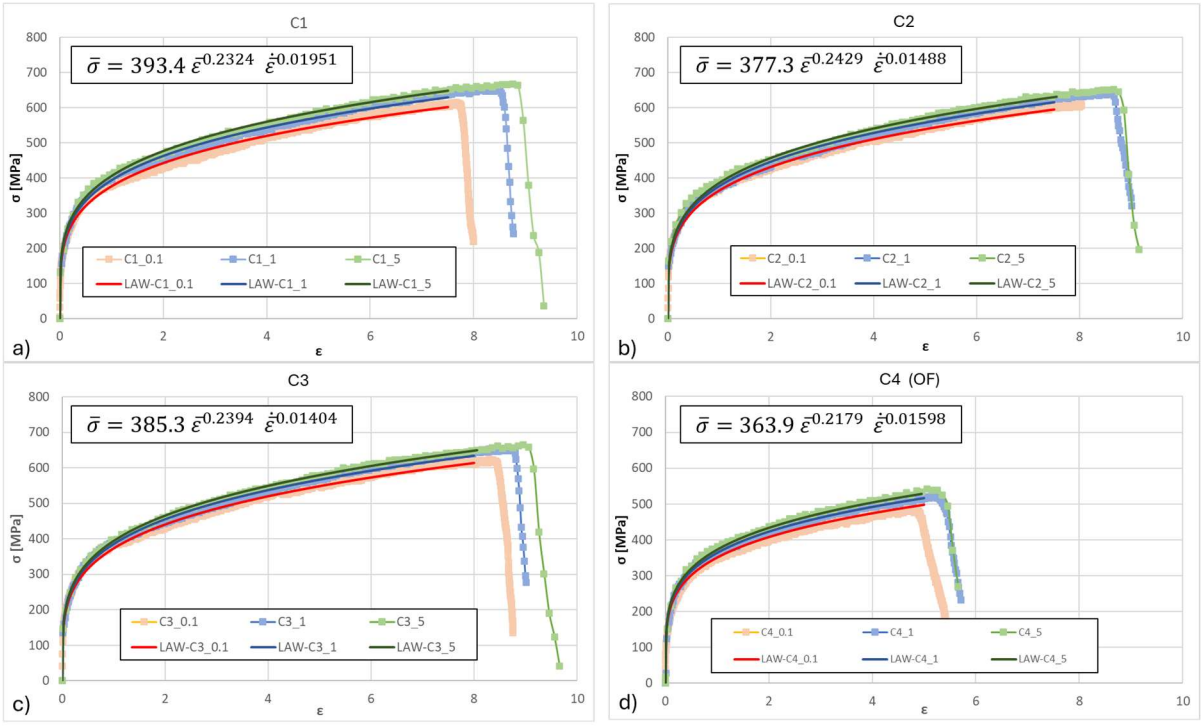

Fig. 2.54 Flow stress curves obtained from cold torsion tests on ETP Copper a)C1, b)C2 c)C3, and Oxygen-free Copper d) C4.

In the graphs of *Fig. 2.54*, the stress-strain values for the tests conducted at a strain rate of 0.1 s^{-1} are shown in red, those at a rate of 1 s^{-1} in blue, and those at 5 s^{-1} in green. The graphs feature lighter curves and markers for the experimental data and darker curves for the flow law-generated curves, respectively for copper C1 in graph

a), C2 in graph b), C3 in graph c), and C4 in graph d). Observing the graphs, it can be noted that the three ETP coppers, C1, C2, and C3, exhibit similar resistance and deformability behavior, with specimens breaking at strain values between 8-9. The oxygen-free copper C4, however, demonstrated to be significantly less resistant and deformable than the ETP copper, with lower stress and strain values.

The flow stress laws derived for the materials characterization were implemented into the multi-pass drawing model, explained in the previous paragraph, and the results are shown in the subsequent figures from *Fig. 2.55* to *Fig. 2.58*, corresponding to the four coppers. The graphs in the figures illustrate the stress acting on the wire during the drawing process on Machine 1 under ideal conditions, with friction coefficients of 0.05 and the number of wire windings around capstans equal to 3. Also, in these graphs, the drawing stress is indicated with solid lines, and the back-stress with dashed lines, and each point marker indicates a wire drawing step, while the x-axis denotes the strain values the wire achieves at each pass. Additionally, in each graph, a thick red curve represents the stress values from the torsion test performed on the material at a strain rate of 5 s^{-1}. It is worth noting that, as previously explained, the material is subjected to increasing strain rates from the inlet to the outlet of the machine, reaching very high strain rates, and this leads to variations in the wire's yield strength depending on the strain rate. In each graph, a red band is depicted to illustrate the range of deformation resistance, with the lower and upper boundaries representing the material's resistance at a strain rate of 5 s^{-1} and an elevated strain rate of 87000 s^{-1}, respectively. Furthermore, each graph compares the stress values obtained considering the material characterization with those from the previous analysis, shown in green.

From the analysis of the graphs, it is evident that when considering also the actual flow stress of the material and its dependence on strain rate, the wire undergoes higher stress levels at each pass during the industrial process compared to the ideal case. However, it is also observed that the yield strength of the wire increases with rising strain rates. Although the wire's yield strength increases, the margin between operational stress levels and critical values that could lead to wire failure is reduced. This narrowing margin elevates the risk of wire breaks happening, especially when process conditions change, for example, the friction coefficient increases due to die wear, the presence of copper residual powder, surface damage to the wire, etc. These factors can lead to critical stress levels that result in wire breakage, as demonstrated

in *Fig. 2.59*, where a friction coefficient of 0.25 was used between the wire and the dies.

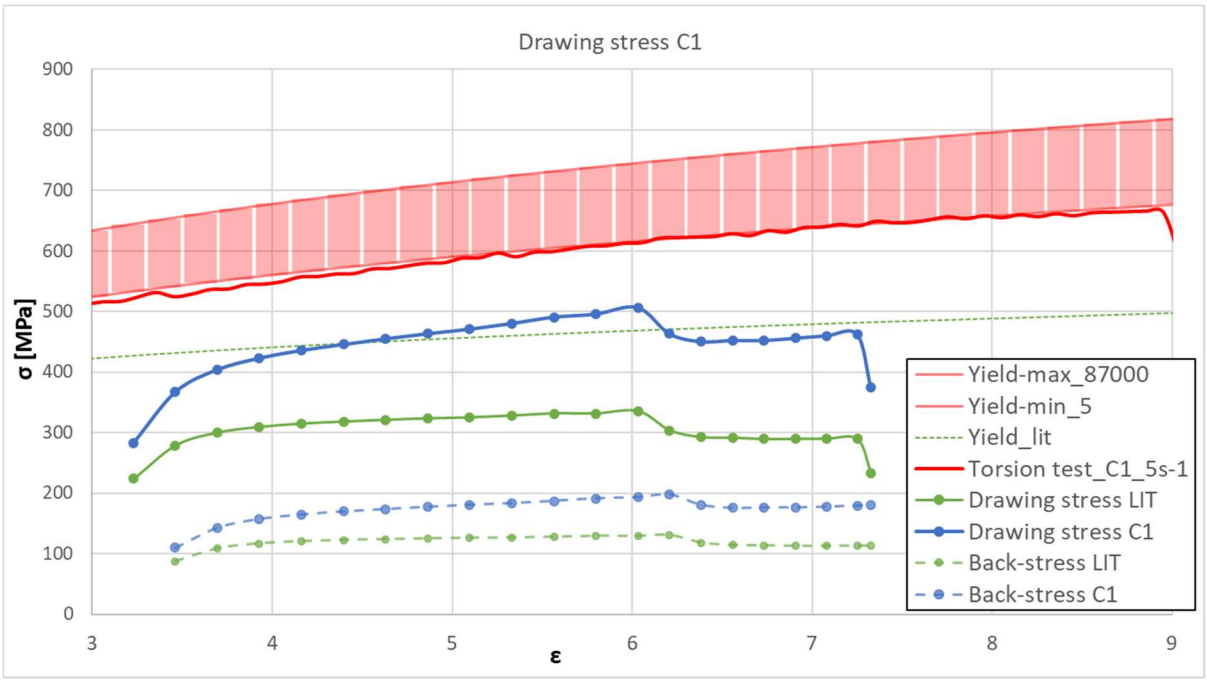

Fig. 2.55 Comparison between drawing stress and back-stress on Machine1, calculated considering the C1 copper flow stress and ideal conditions.

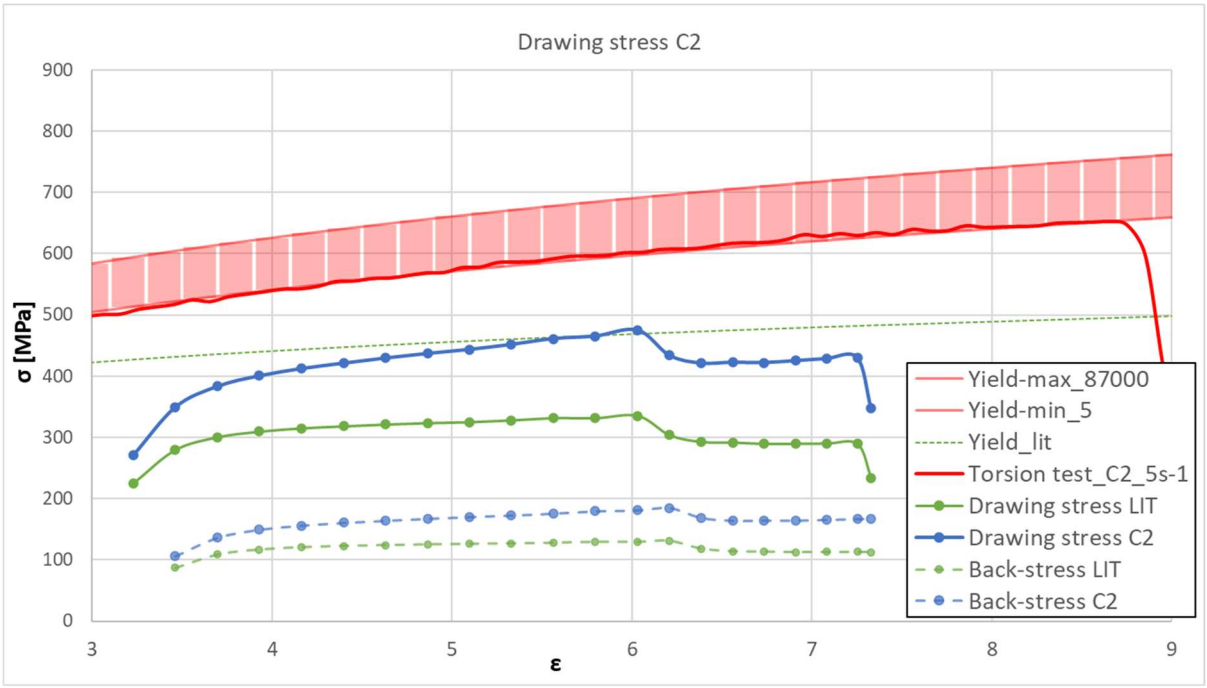

Fig. 2.56 Comparison between drawing stress and back-stress on Machine1, calculated considering the C2 copper flow stress and ideal conditions.

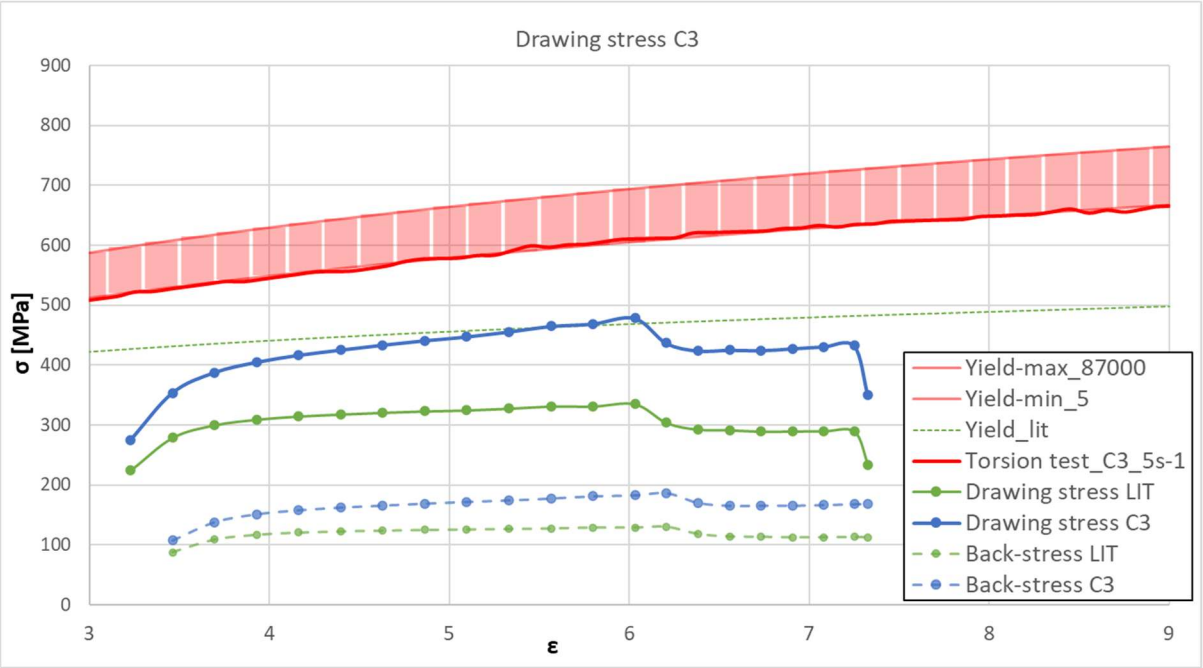

Fig. 2.57 Comparison between drawing stress and back-stress on Machine1, calculated considering the C3 copper flow stress and ideal conditions.

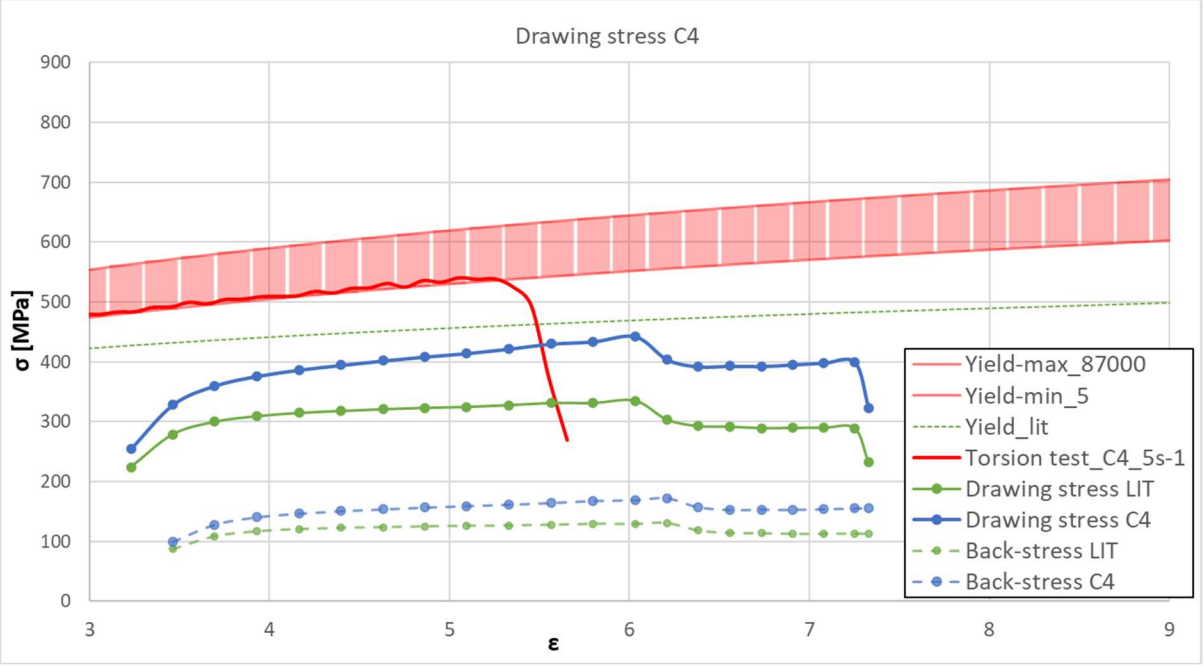

Fig. 2.58 Comparison between drawing stress and back-stress on Machine1, calculated considering the C4 copper flow stress and ideal conditions.

In relation to *Fig. 2.58*, which focuses on Oxygen-Free copper, the torsion test results reveal that this material exhibits notably reduced deformability compared to ETP copper, with a maximum strain value of about 5. Consequently, executing a complete

wire drawing sequence from a rod with an initial diameter of 8 mm to a wire with a final diameter of 0.20 mm without intermediate annealing becomes highly critical and challenging because of the material's inability to withstand such high deformation levels without succumbing to fracture.

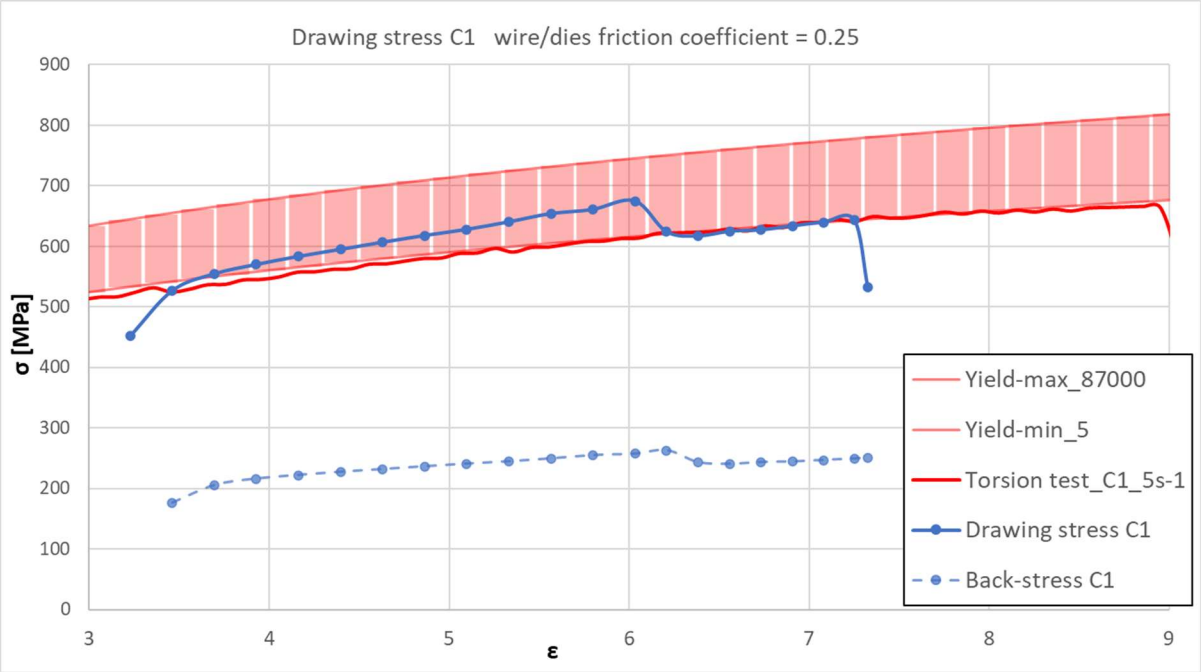

Fig. 2.59 Drawing stress and back-stress on Machine1, calculated considering the C1 copper flow stress and friction coefficient of 0.25 between wire and dies.

Finally, in *Fig. 2.60* an optimization of the process was proposed on Machine 1 by acting on the number of windings of the wire around each capstan. The parameters set are shown in *Table 2.5*: the number of wire windings around the capstan has been set to 4 from pass 1 to pass 12; from pass number 13, when the elongation ratio of the machine decreases, the number of wire windings has been set to 3; in the last two passes the number of windings has been set to 2. It should be noted that a greater number of windings tends to increase the wearing of the wire, especially on the last steps where it becomes thinner. For this reason, the common practice is to set a decreasing number of windings from the inlet to the outlet of the machine. The proposed threading was tested on the machine, with good results on the frequency of wire failures; nevertheless, when a wire break occurs, it causes longer machine downtimes due to longer times to re-insert the machine and start-up. For this reason, its advantage within the industrial process is still under evaluation

Table 2.5 Parameter values set on Machine1 to optimize the drawing stresses.

N° Pass	Diameter Initial [mm]	Diameter Final [mm]	Reduction ratio [%]	Die semi-angle [°]	Bearing length [mm]	Number of wire windings
1	1.83	1.592	24.3	9	0.398	**4**
2	1.592	1.417	20.8	9	0.354	**4**
3	1.417	1.261	20.8	9	0.315	**4**
4	1.261	1.122	20.8	9	0.281	**4**
5	1.122	0.998	20.9	9	0.250	**4**
6	0.998	0.888	20.8	9	0.222	**4**
7	0.888	0.790	20.9	9	0.198	**4**
8	0.790	0.703	20.8	9	0.176	**4**
9	0.703	0.626	20.7	9	0.157	**4**
10	0.626	0.557	20.8	9	0.139	**4**
11	0.557	0.495	21.0	9	0.124	**4**
12	0.495	0.441	20.6	9	0.110	**4**
13	0.441	0.392	21.0	9	0.098	**3**
14	0.392	0.359	16.1	9	0.090	**3**
15	0.359	0.329	16.0	9	0.082	**3**
16	0.329	0.301	16.3	9	0.075	**3**
17	0.301	0.276	15.9	9	0.069	**3**
18	0.276	0.253	16.0	9	0.063	**3**
19	0.253	0.232	15.9	9	0.058	**3**
20	0.232	0.213	15.7	9	0.053	**2**
21	0.213	0.205	7.4	9	0.051	**2**

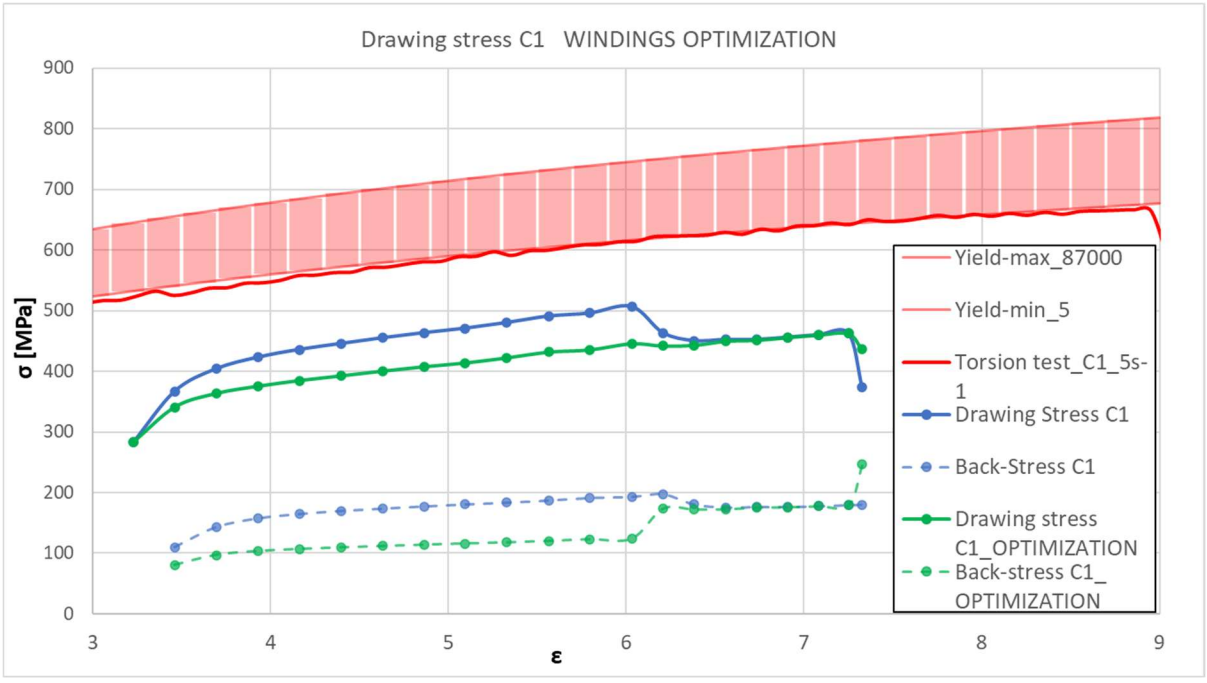

Fig. 2.60 Stress optimization by varying the number of the wire windings around the capstans in different passes of reduction on Machine1.

2.3.2. Experimental, analytical, and numerical analysis of the copper wire multi-pass drawing process

Introduction

From the analysis of the drawing process carried out in the previous paragraph, it has been demonstrated that an adequate characterization of the material's plastic behavior at large strain values is necessary. Furthermore, the analysis of the variability of process conditions revealed that, in addition to the number of wire windings around the capstans, one of the most significant parameters affecting the stresses on the wire is the coefficient of friction value. However, the values used in the analysis are theoretical, as it is difficult to provide an accurate estimate of the exact value coefficient of friction.

Moreover, the application of analytical methods requires a large calculation effort, and simplified boundary conditions are assumed in the models, such as an average distribution of the strain and the strain rate of the wire within the die. On the other hand, The Finite Element Method (FEM) has emerged as a prominent tool in contemporary times, playing a significant role in advancing the design and optimization of bulk-forming processes [6]. Several efforts have been made by researchers to apply the FEM method to the analysis of the wire drawing process [68,76–80], however further investigations are necessary to obtain reliable simulations.

In this section, a model is proposed for simulating the drawing process on individual passes, examining the first 4 steps of the process performed on Machine 1 using the copper previously referred to as C1. In this initial simplified model, the presence of the capstans is omitted; future developments of the work will include the introduction of capstans also into the numerical model.

About the experimental procedure, using an LD5 Lloyd press, drawing tests were carried out on the four steps of the process, from diameter 1.83 mm to 1.122 mm, measuring the force applied to the wire by varying two speed values (60, and 1200 mm/min) in lubricated and non-lubricated conditions. Initially, the experimental drawing force values were compared with the force values calculated with the different analytical models, finding different values for the Coulomb friction coefficient derived from each model. Furthermore, the numerical simulation model was applied to the

copper wire multi-pass drawing process using the commercial FE code Qform UK®, comparing the predicted drawing force values with the analytical and experimental data. The analysis of deviations among various analytical methods highlights the importance of evaluating friction coefficient values in each model to prevent errors in estimating drawing forces. The aim to provide a reliable numerical model for predicting wire stress during the multi-pass drawing process will be achieved by accurately characterizing material flow stress and assessing the friction model appropriately.

Experimental procedure

It is worth recalling that in the ICEL s.c.p.a company (Lugo IT), copper electrical cables are produced starting from a rod with an initial diameter of 8 mm. The rod was subjected to a preliminary multi-pass drawing process from a diameter of 8.00 mm to 1.83 mm (area reduction of 94.77%).

Subsequently, using an LD5 Lloyd press, shown in *Fig. 2.61a*, wire drawing tests were carried out on the four steps of the process, from diameter 1.83 mm to 1.122 mm, measuring the drawing force applied to the wire by varying speed values in lubricated and non-lubricated conditions. The speed was varied from a minimum value of 60 mm/min to a maximum value of 1200 mm/min achievable with the press equipment. The wire was not subjected to any annealing treatment between one drawing step and the next, as happens in the industrial process, and the parameters of the experimental procedure are recalled in *Table 2.6*.

Table 2.6 Experimental procedure Step schedule.

N° pass	Initial diameter [mm]	Final diameter [mm]	Reduction Ratio [%]	Equivalent strain	Total cumulated strain
Preliminary	8.000	1.830			2.9503
1	1.830	1.592	24.3	0.2786	3.2289
2	1.592	1.417	20.8	0.2329	3.4618
3	1.417	1.261	20.8	0.2333	3.6951
4	1.261	1.122	20.8	0.2336	3.9287

During each drawing pass, the wire was inserted into the die which was placed into a die holder fixed with the lower plate of the press. At the exit of the die, the wire was pulled by the grip fixed at the upper mobile crosshead with constant speed, and the drawing force was measured by the load cell.

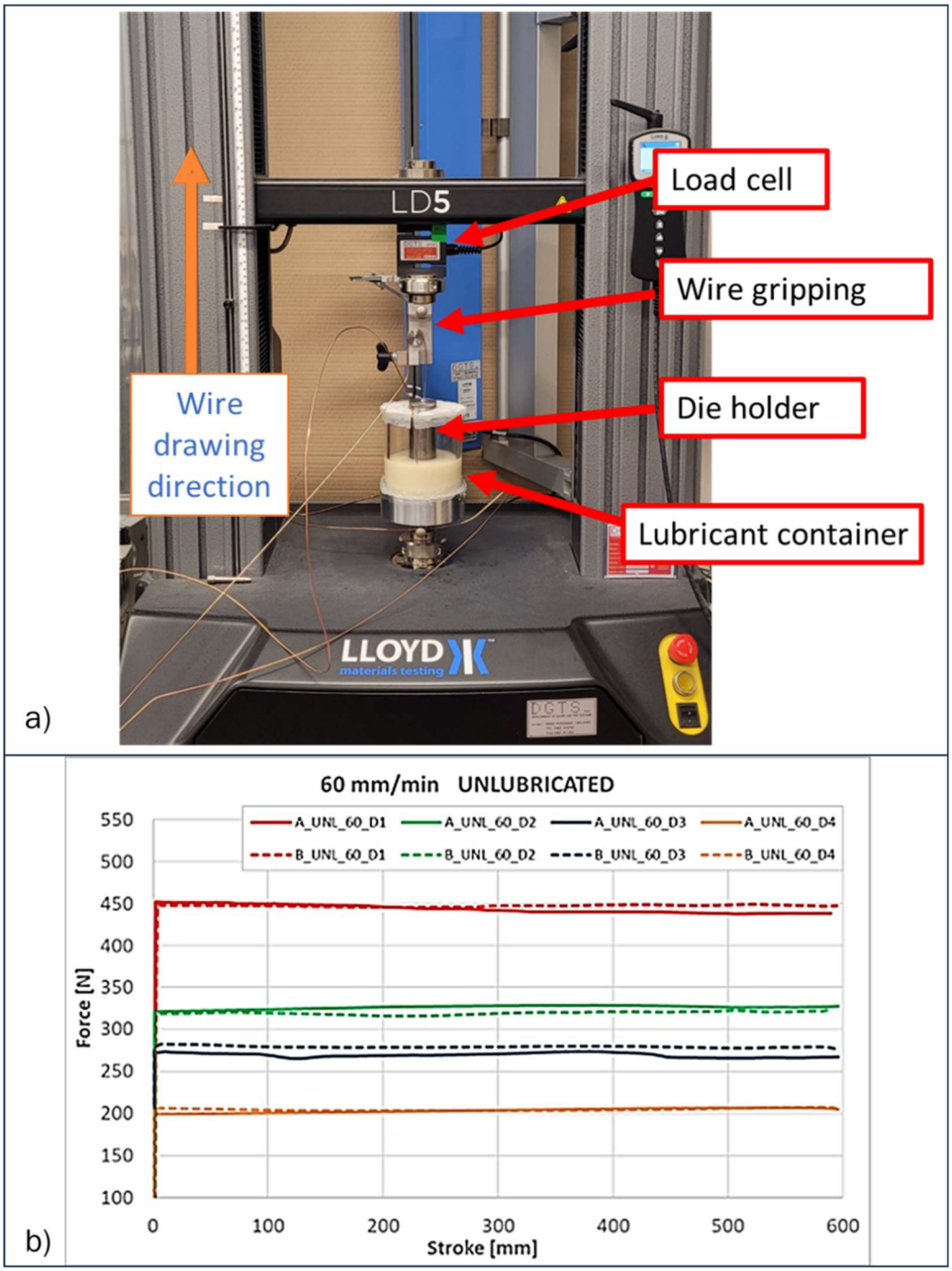

Fig. 2.61 a) Picture of the set-up for the wire drawing tests using the LD5 Lloyd press; b)Wire drawing tests in unlubricated condition conducted at the velocity of 60, two tests are shown for each condition. [81]

The dies used in the experimentation were the standards recommended for copper wire drawing, with a core in polycrystalline diamond (PCD), semi-angle of 9°, and bearing length of 25% of the final diameter. In the tests performed in lubricated condition, the die holder was placed inside a container filled with lubricating emulsion composed of industrial oil TADAL CU 1350 N and water, with a Brix concentration of

8%. The test was stopped after a stroke of 600 mm, and two trials were conducted for each condition to avoid possible error by a single repetition and a variability of about ±10 N was found, as shown in *Fig. 2.61b*. The curves refer to wire drawing tests in unlubricated condition conducted at passes 1 in red, 2 in green, 3 in blue, and 4 in orange, at the velocity of 60 mm/min, and the two tests are shown for each condition with solid and dashed lines.

Numerical model

The simulation of the wire drawing process was performed using the commercial FE code Qform UK® and was represented as an axisymmetric Lagrangian model, as shown in *Fig. 2.62*. Accordingly, the following boundary conditions were set: symmetry along the z-axis and a constant velocity applied at the wire's end.

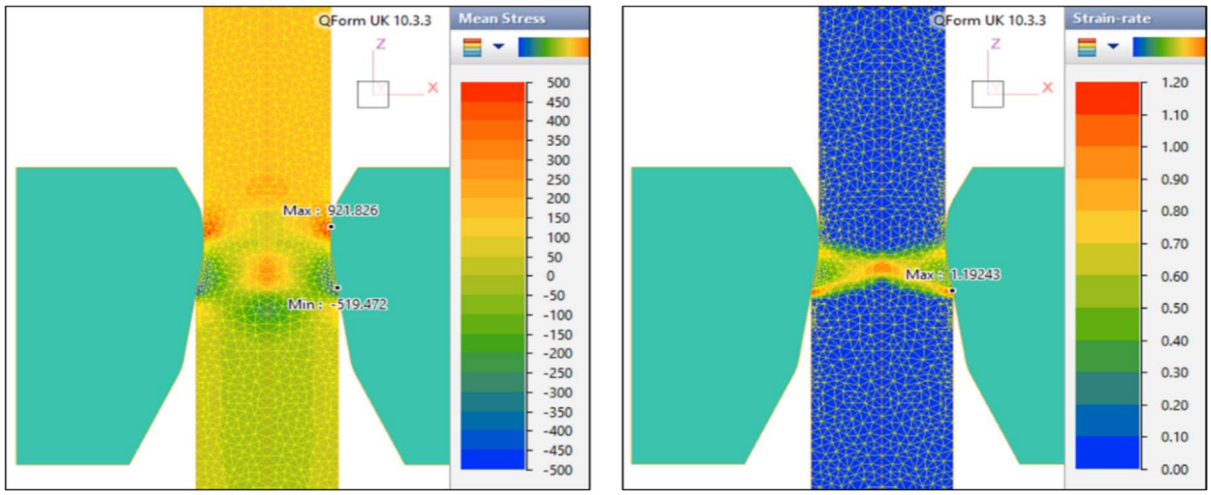

Fig. 2.62 Numerical simulation of the wire drawing process. Example of the simulation on the fourth drawing pass. On the left the distribution of stress on the wire [MPa]. On the right the strain rate field in the drawing die [1/s]. [81]

The geometry of the dies was modeled as described in the experimental procedures, and a wire length of 600 mm was simulated to be drawn in four consecutive operations corresponding to the four passes of the drawing experimentation. The flow stress of the material was modeled with the equation regressed from the torsion tests on ETP Copper C1, explained in paragraph 2.3.1 and reported in Eq. (2.38). The other material parameters were listed in *Table 2.7*, and the Coulomb model was used for friction.

$$\bar{\sigma} = 393.4 \cdot \bar{\varepsilon}^{0.2324} \cdot \dot{\bar{\varepsilon}}^{0.01951} \qquad (2.38)$$

Table 2.7 Material parameters for the ETP Copper and the polycrystalline diamond.

Material Properties	Wire ETP Copper	Die PCD
Density [Kg/m^3]	8940	4000
Specific heat [J/(kg·K)]	390	502
Thermal conductivity [W/(m·K)]	390	600
Thermal expansion [1/°C]	1.60635e-5	5.2e-7
Young's modulus [MPa]	121000	900000
Poisson's ratio	0.35	0.22
Yield stress [MPa]		6900

Results and discussion

The wire drawing forces were calculated by applying the analytical models of SLAB theory, by Wistreich-Wright, and by Avitzur, described in section 2.3.1, considering the drawing stress on the wire multiplied by the wire section at the exit of each die. The flow stress of the material deriving from the experimental tests was used in the calculation, considering the average equivalent strain as the natural logarithm of the ratio between inlet and outlet diameter at each step, and the average strain rate as the product of the strain and drawing speed divided by the length of the deformation zone. Then, by comparing the analytically calculated forces with the experimental results of the drawing tests, a range of friction coefficient values was calculated for the unlubricated and lubricated drawing conditions, for each model. The range of values in which the Coulomb friction coefficient can be included was estimated considering the maximum value and the minimum value calculated from all the tests in unlubricated conditions at speeds of 60 and 1200 mm/min and from all tests in the lubricated condition, considering that the average absolute relative error between experimental and calculated values was less than 2%.

Fig. 2.28 shows the comparison between the drawing forces calculated by the SLAB method and the experimental data. The experimental data are indicated with the solid thick lines, while the analytical values calculated with the mean coefficient friction are indicated with dashed lines, and the bar error represents the values calculated with the relative estimated range of friction coefficient. Moreover, the red lines represent the first pass of reduction ration, the green lines the second step, the blue ones the third

pass and the yellow the four step. For the SLAB method, it takes values between 0.1-0.16 for the unlubricated condition and between 0.055-0.1 for the lubricated condition, as indicated in *Fig. 2.68*.

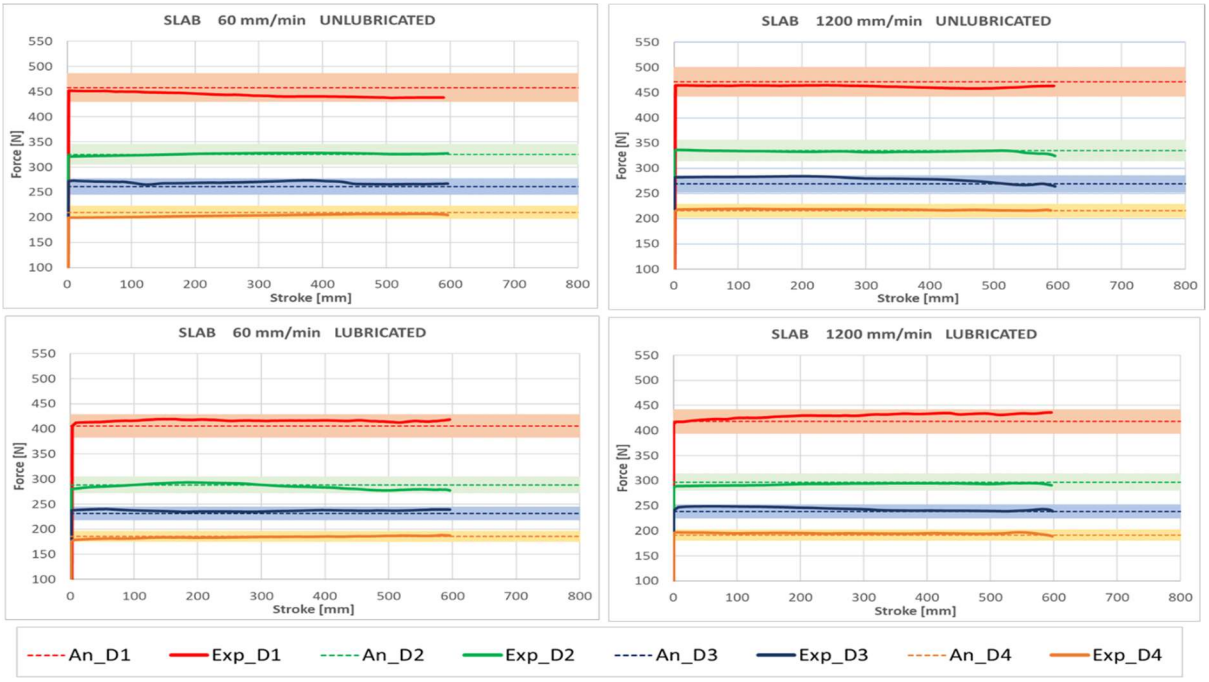

Fig. 2.63 Comparison between the drawing forces calculated by the SLAB method and the experimental data. [81]

In *Fig. 2.64* and *Fig. 2.65* the values of the wire drawing forces calculated using respectively the Wistreich-Wright model and the Avitzur model are shown. In the Wistreich-Wright the friction coefficient assumes the values between 0.07-0.1 for the unlubricated condition and between 0.048-0.75 for the lubricated condition. While it takes the values between 0.055-0.095 for the unlubricated condition and 0.02-0.052 for the lubricated condition in the Avitzur model. The comparison between the values assumed by the friction coefficient in the different analytical and numerical models is shown in *Fig. 2.68*. The same method used for calculating the friction coefficient in the analytical models was applied in the numerical simulation and it was found that the friction coefficient is within a range between 0.14-0.17 for the unlubricated condition and between 0.11 and 0.13 for the lubricated condition. The results are shown in *Fig. 2.66* and *Fig. 2.67* where the drawing force values obtained from the numerical simulations with the maximum value of the friction coefficient are shown with dashed lines and the values obtained with the minimum friction coefficient with dash-dot lines.

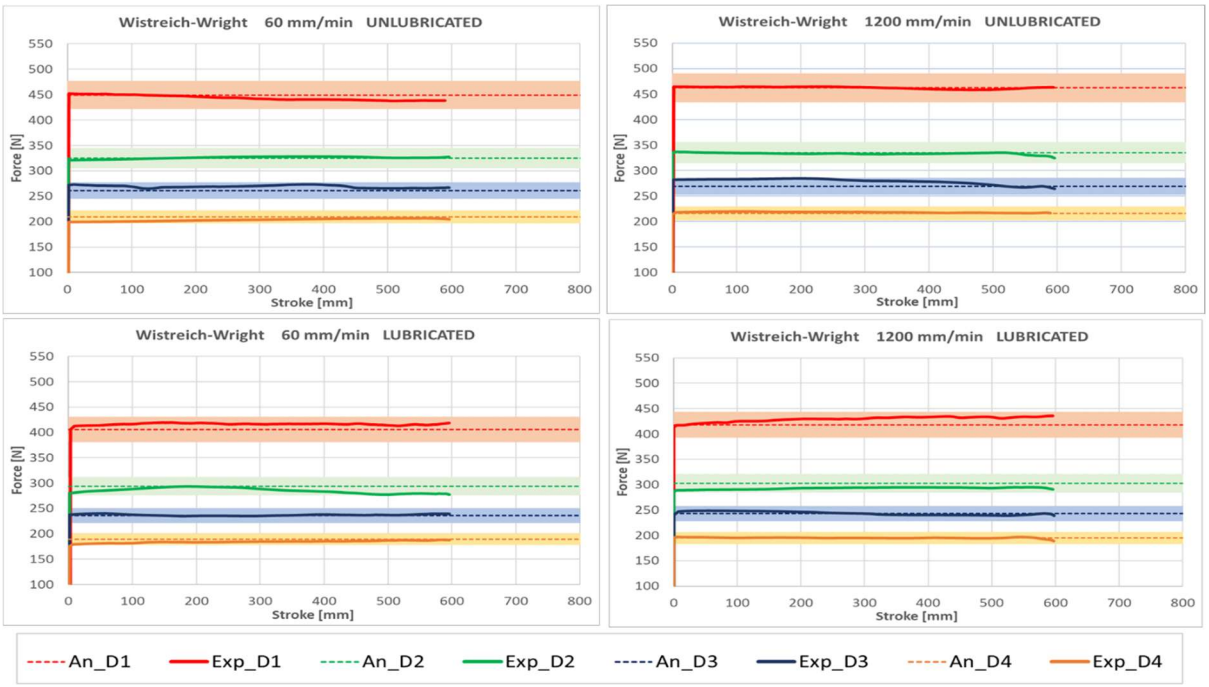

Fig. 2.64 Comparison between the drawing forces calculated by the Wistreich-Wright model and experimental data. [81]

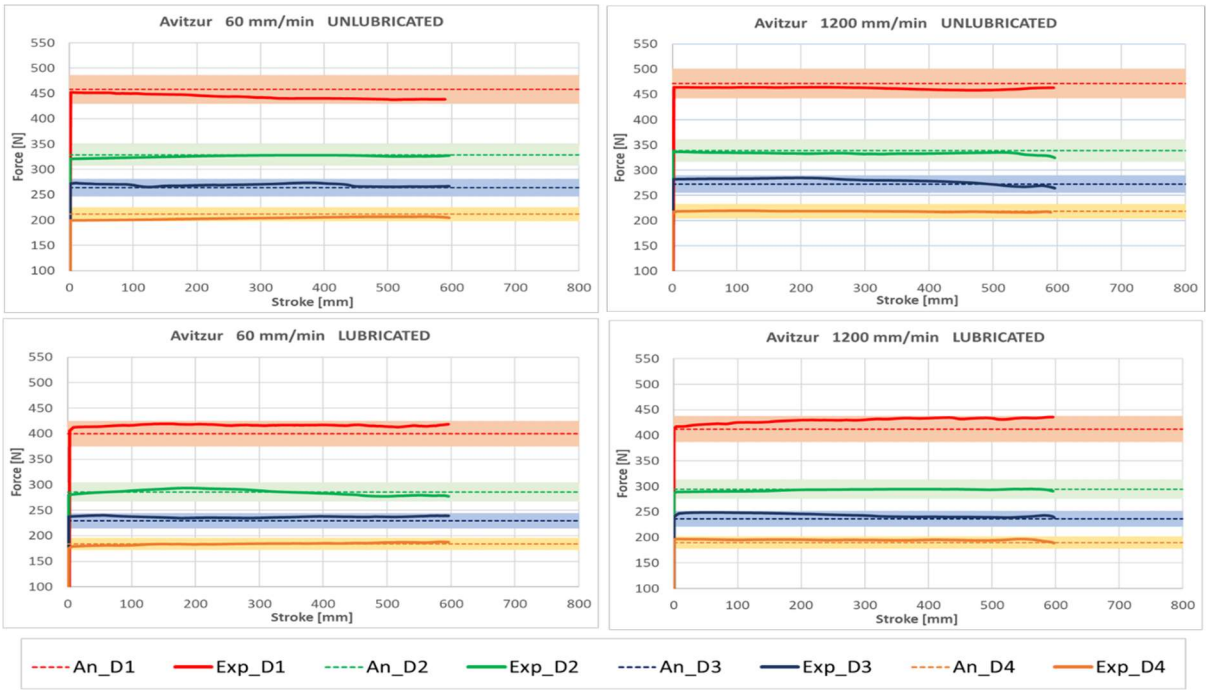

Fig. 2.65 Comparison between the drawing forces calculated by Avitzur model and the experimental data. [81]

It was found that in the Avitzur and Wistreich-Wright modeling the friction coefficient takes on low values, since the Avitzur model also involves the effect of the friction between the wire and the die in the bearing length, while in the Wright model, the

average pressure inside the die is calculated through the semi-empirical approximation of the redundant work factor. Therefore, in both models, increasing the friction coefficient value leads to an overestimation of the drawing forces. On the contrary, in the SLAB method the friction coefficient takes on higher values and its variation has less influence on the calculation of the forces, falling within a wider range of values. Finally, it was found that the friction coefficient assumes higher values in the numerical simulation and varies in small ranges. In conclusion, the numerical model provides good reliability, inserting values of the friction coefficient higher than those of the analytical models, since in the analytical models simplified conditions of average strain and strain rates in the die are considered. It is worth noting that further studies are necessary to achieve greater reliability, involving hydrodynamic effects due to high drawing speeds and temperature increases.

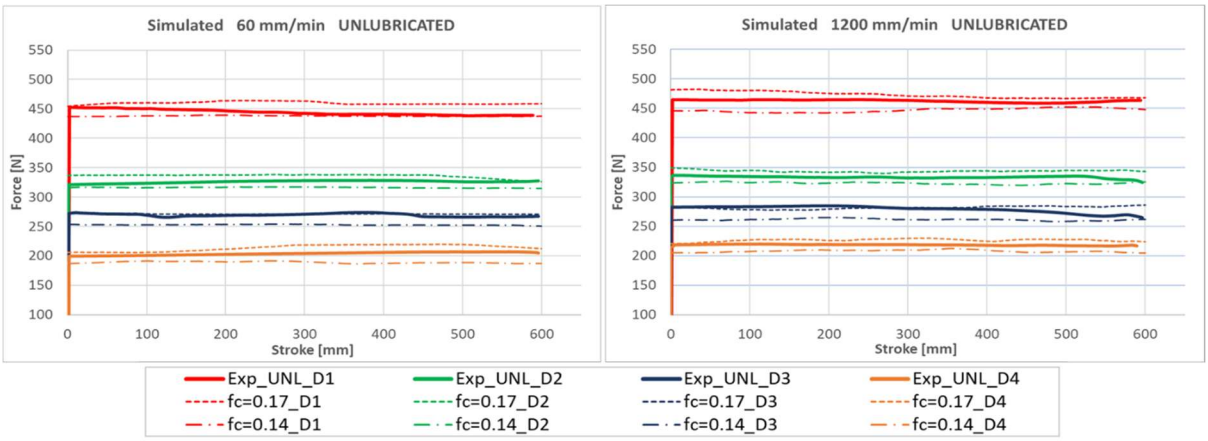

Fig. 2.66 Comparison between forces predicted by simulation and experimental data in unlubricated conditions. [81]

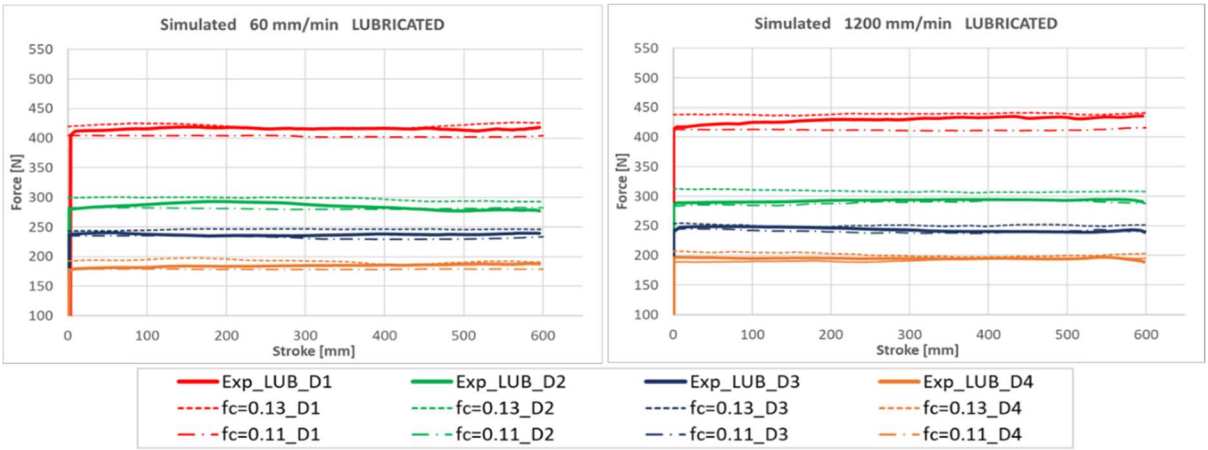

Fig. 2.67 Comparison between forces predicted by simulation and experimental data in lubricated conditions. [81]

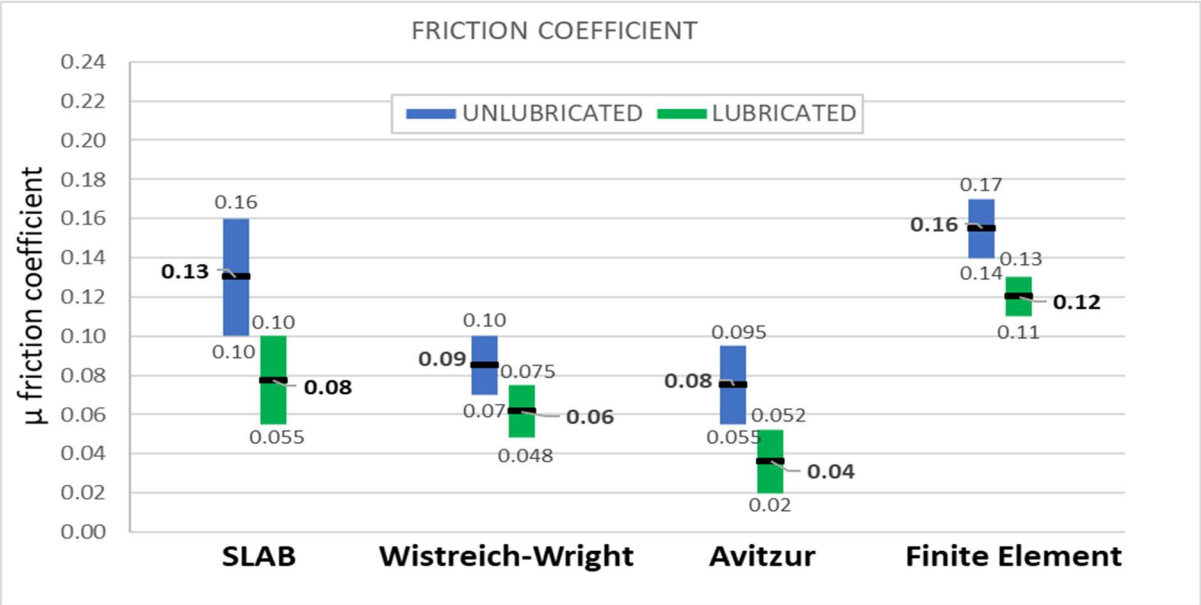

Fig. 2.68 Comparison between the range of the friction coefficient values calculated from the three analytical models and the numerical method, for the unlubricated and lubricated conditions. [81]

2.4. CONCLUSIONS

This chapter has provided a comparative analysis of the mechanical behavior of ETP copper under tensile, compression, and torsion loading conditions, with a particular focus on cold metal forming deformation processes. Through the detailed investigation of each test, several key conclusions have emerged.

The tensile test results demonstrated that while this method is effective for characterizing the material up to moderate strains, the onset of necking, which occurs around a strain value of 0.33, significantly complicates the interpretation of the data. Even with the application of Bridgman's correction, the flow stress values beyond this point deviate from the true material behavior due to the triaxial stress state that develops during necking. On the other hand, the compression test allowed for material characterization up to higher strain values of 1.1, making it a more reliable method for understanding the material's behavior at larger strains. However, challenges such as barreling and friction effects between the specimen and the test apparatus were encountered, particularly at higher strain levels. These effects introduced additional complexities in interpreting the flow stress data, although they were partially mitigated by implementing multiple lubrication strategies.

The torsion test emerged as the most effective method for characterizing ETP copper under large strain conditions, as it allowed for continuous deformation without significant geometric changes to the specimen. This provided a clearer representation of the material's true flow stress behavior. However, the equivalent stress values obtained from the torsion test were consistently lower than those from the tensile and compression tests. This discrepancy was attributed to factors such as crystallographic anisotropy and texture development during torsional loading. In both tensile and torsion, the evolution of stress and strain is influenced by changes in texture and work-hardening, moreover, tension activates more slip systems than torsion, leading to greater dislocation interaction and higher work-hardening.

The comparison between the compression and torsion tests led to the development of a new correction function, which interpolates the values of the correction coefficient as a function of deformation using nonlinear regression. A new model for processing cold torsion test data was proposed, which incorporates the correction coefficient derived from comparative analyses with compression test results. It was found that this modeling approach aligns closely with the results obtained from tensile and compression tests up to a strain value of 1.1, while also allowing for the characterization of the material at higher deformation levels. The model was validated through a hybrid compression test, which was specifically designed to eliminate the effects of friction. The hybrid test demonstrated that the corrected torsion flow stress data align more closely with the tensile and compression test results, particularly at higher strain levels. The results of the hybrid compression test, both experimental and numerical, confirmed the robustness and reliability of the proposed model across different strain rates. The torsion test, when processed with the proposed model, provided the most accurate characterization of the material up to large strains, making it the preferred method for cold working applications.

Subsequentially, material characterization was performed using cold torsion tests on different batches of copper sourced from various suppliers, and the resulting flow stress data were utilized for the modeling of the industrial wire drawing process for the production of electrical cables. An analytical, numerical, and experimental analysis of the multi-pass wire drawing process was conducted to assess the material's behavior and optimize the operational parameters. A prediction model of the stresses acting on the material during the wire drawing process on multi-pass industrial machines was

proposed and discussed. The drawing stresses acting on the material were investigated and compared, step by step, to the material yield stress when different processing conditions were applied. The study highlighted that among the process parameters, lubrication conditions and the effects of capstans significantly influence the stress behavior in wires [72].

Additionally, it was demonstrated that utilizing accurate material characterization in modeling can lead the wire into critical processing zones that may cause fractures, effects that typically do not lead to wire breaks under ideal modeling conditions. However, for the multi-pass process modeling, theoretical values for the friction coefficient were still employed due to the challenges in estimating it accurately. In a subsequent analysis, a comparative study was conducted, evaluating the calculated drawing force values obtained from analytical models and those from numerical simulations. By comparing experimental data with the calculated values, a range of friction coefficient values for both lubricated and unlubricated conditions was established for each analytical model, considering a maximum calculation error of 2%. A reliable model for the numerical simulation of the multi-pass wire drawing process was developed, and it was found that the analytical models tend to underestimate the value of the friction coefficient due to the simplified assumptions regarding the average strain and strain rate of the material within the die [81].

In summary, a good correlation was found between the experimental data and the predicted values of the drawing forces acting on the wire as the reduction ratio and speed varied. However, further studies are necessary to incorporate the hydrodynamic effects associated with high industrial drawing speeds into the model.

REFERENCES

[39] Ling Y. Uniaxial True Stress-Strain after Necking. AMP J Technol 1996;5:37–48.

[40] La Rosa G, Mirone G, Risitano A, Pine G. Numerical Verification Of The Bridgman ModelFor Notched And Unnotched Round Specimens. WIT Transactions on Engineering Sciences 26 2000.

[41] La Rosa G, Risitano A, Mirone G. Postnecking elastoplastic characterization: Degree of approximation in the bridgman method and properties of the flow-stress/true-stress ratio. Metall Mater Trans A 2003;34:615–24. https://doi.org/10.1007/s11661-003-0096-y.

[42] Celentano DJ, Cabezas And EE, Garcı´a CM. Analysis of the Bridgman Procedure to Characterize the Mechanical Behavior of Materials in the Tensile Test: Experiments and Simulation. Journal of Applied Mechanics 2005;72:149–52. https://doi.org/10.1115/1.1827243.

[43] Kajberg J, Lindkvist G. Characterisation of materials subjected to large strains by inverse modelling based on in-plane displacement fields. International Journal of Solids and Structures 2004;41:3439–59. https://doi.org/10.1016/j.ijsolstr.2004.02.021.

[44] Wang K, Carsley JE, He B, Li J, Zhang L. Measuring forming limit strains with digital image correlation analysis. Journal of Materials Processing Technology 2014;214:1120–30. https://doi.org/10.1016/j.jmatprotec.2014.01.001.

[45] Paul SK, Roy S, Sivaprasad S, Bar HN, Tarafder S. Identification of Post-necking Tensile Stress–Strain Behavior of Steel Sheet: An Experimental Investigation Using Digital Image Correlation Technique. J of Materi Eng and Perform 2018;27:5736–43. https://doi.org/10.1007/s11665-018-3701-3.

[46] Nadai A. Plastic Behavior of Metals in the Strain-Hardening Range. Part I. Journal of Applied Physics 1937;8:205–13. https://doi.org/10.1063/1.1710282.

[47] Davis EA. Plastic Behavior of Metals in the Strain-Hardening Range. Part II. Journal of Applied Physics 1937;8:213–7. https://doi.org/10.1063/1.1710283.

[48] Bishop JFW, Hill R. CXXVIII. A theoretical derivation of the plastic properties of a polycrystalline face-centred metal. The London, Edinburgh, and Dublin Philosophical Magazine and Journal of Science 1951;42:1298–307. https://doi.org/10.1080/14786444108561385.

[49] Canova G, Shrivastava S, Jonas J, G'Sell C. The Use of Torsion Testing to Assess Material Formability. Formability of Metallic Materials—2000 A.D., ASTM International100 Barr Harbor Drive, PO Box C700, West Conshohocken, PA 19428-2959; 1982, p. 189–210. https://doi.org/10.1520/STP28395S.

[50] Shrivastava SC, Jonas JJ, Canova G. Equivalent strain in large deformation torsion testing: theoretical and practical considerations. J Mech Phys Solids 1982;30:75–90.

[51] Bridgman PW. vol. 32. 1944.

[52] Bridgman PW. Studies in large flow and fracture. McGraw Hill; 1956.

[53] Dieter GE, Kuhn HA, Semiatin SL, editors. Handbook of workability and process design. Materials Park, Ohio: ASM International; 2003.

[54] Timoshenko S, Goodier JN. Theory of elasticity. McGraw Hill book company; 1951.

[55] Ecsedi I. Some analytical solutions for Saint-Venant torsion of non-homogeneous cylindrical bars. European Journal of Mechanics - A/Solids 2009;28:985–90. https://doi.org/10.1016/j.euromechsol.2009.03.010.

[56] Romano G, Barretta A, Barretta R. On torsion and shear of Saint-Venant beams. European Journal of Mechanics - A/Solids 2012;35:47–60. https://doi.org/10.1016/j.euromechsol.2012.01.007.

[57] Tretyakov D, Bylya O, Shitikov A, Gartivig A, Stebunov S, Biba N. The prospects of implementation of artificial intelligence for modelling of microstructural parameters in metal forming processes, 2024, p. 2164–73. https://doi.org/10.21741/9781644903131-238.

[58] Kniazkin I, Krylov V, Shitikov A, Kulakov I, Biba N. Investigation of heat transfer dependencies in quenching of extrusion profiles based on experiment and FEM simulation, 2024, p. 723–32. https://doi.org/10.21741/9781644903131-80.

[59] Kniazkin I, Biba N, Kulakov I, Duzhev A, Stebunov S. Automated Optimum Extrusion Die Design and Profile Quality Control Based on Simulation. KEM 2024;987:31–40. https://doi.org/10.4028/p-8ZRuLD.

[60] Kniazkin I, Pelaccia R, Negozio M, Di Donato S, Donati L, Reggiani B, et al. Investigation of the skin contamination predictability by means of QForm UK extrusion code, 2023, p. 543–52. https://doi.org/10.21741/9781644902479-59.

[61] Osakada K. History of plasticity and metal forming analysis. Journal of Materials Processing Technology 2010;210:1436–54. https://doi.org/10.1016/j.jmatprotec.2010.04.001.

[62] Kurt L. Handbook of Metal Forming. First. United States of America: Society of Manufacturing Engineers; 1985.

[63] Wistreich JG. THE FUNDAMENTALS OF WIRE DRAWING. Metallurgical Reviews 1958;3:97–142. https://doi.org/10.1179/mtlr.1958.3.1.97.

[64] Wright RN. Wire technology: process engineering and metallurgy. Second Edition. Amsterdam: Elsevier; 2016.

[65] Avitzur B, Narayan C, Chou YT. Upper-bound solutions for flow through conical converging dies. International Journal of Machine Tool Design and Research 1982;22:197–214. https://doi.org/10.1016/0020-7357(82)90026-9.

[66] Avitzur B, Choi JC. Compatibility of the upper-bound approach and the balance of forces for the treatment of metal-forming processes. Journal of Mechanical Working Technology 1986;13:141–50. https://doi.org/10.1016/0378-3804(86)90061-6.

[67] Dixit US, Dixit PM. An analysis of the steady-state wire drawing of strain-hardening materials. Journal of Materials Processing Technology 1995;47:201–29. https://doi.org/10.1016/0924-0136(95)85000-7.

[68] Vega G, Haddi A, Imad A. Investigation of process parameters effect on the copper-wire drawing. Materials & Design 2009;30:3308–12. https://doi.org/10.1016/j.matdes.2008.12.006.

[69] Tintelecan M, Sas-Boca IM, Iluţiu-Varvara D-A. The Influence of the Dies Geometry on the Drawing Force for Steel Wires. Procedia Engineering 2017;181:193–9. https://doi.org/10.1016/j.proeng.2017.02.369.

[70] Martinez GAS, Qian W-L, Kabayama LK, Prisco U. Effect of Process Parameters in Copper-Wire Drawing. Metals 2020;10:105. https://doi.org/10.3390/met10010105.

[71] Thimont J, Felder E, Bobadilla C, Buessler P, Persem N, Vaubourg Jp. Study Of The Wet Multipass Drawing Process Applied On High Strength Thin Steel Wires, Belfast, (United Kingdom): 2011, p. 467–72. https://doi.org/10.1063/1.3589559.

[72] Di Donato S, Donati L, Negozio M. Copper Wire Multi-Pass Drawing: Process Modeling and Optimization. KEM 2022;926:499–510. https://doi.org/10.4028/p-g4wbpz.

[73] Copper wire drawing production of round copper wires for the cable industry. Second edition. Aachen: 2020.

[74] Negroni FD, Thomsen EG, Kobayashi S. A Drawing Modulus for Multi-Pass Drawing. CIRP Annals 1986;35:181–3. https://doi.org/10.1016/S0007-8506(07)61866-6.

[75] Haddi A, Imad A, Vega G. Analysis of temperature and speed effects on the drawing stress for improving the wire drawing process. Materials & Design 2011;32:4310–5. https://doi.org/10.1016/j.matdes.2011.04.010.

[76] Rodríguez O, Santana GA, Del Rey JC, Guerrero G. Study and analysis of the wiredrawing of CuZn $_{37}$ wires via numerical simulations and slab method. IOP Conf Ser: Mater Sci Eng 2021;1193:012014. https://doi.org/10.1088/1757-899X/1193/1/012014.

[77] Lazzarotto L, Dubar L, Dubois A, Ravassard P, Oudin J. Identification of Coulomb's friction coefficient in real contact conditions applied to a wire drawing process. Wear 1997;211:54–63. https://doi.org/10.1016/S0043-1648(97)00080-X.

[78] Tang KK, Li ZX, Wang J. Numerical simulation of damage evolution in multi-pass wire drawing process and its applications. Materials & Design 2011;32:3299–311. https://doi.org/10.1016/j.matdes.2011.02.026.

[79] Panteghini A, Genna F. Effects of the strain-hardening law in the numerical simulation of wire drawing processes. Computational Materials Science 2010;49:236–42. https://doi.org/10.1016/j.commatsci.2010.05.002.

[80] Baek HM, Jin YG, Hwang SK, Im Y-T, Son I-H, Lee D-L. Numerical study on the evolution of surface defects in wire drawing. Journal of Materials Processing Technology 2012;212:776–85. https://doi.org/10.1016/j.jmatprotec.2011.10.028.

[81] Di Donato S, Negozio M, Pelaccia R, Reggiani B, Donati L. Experimental, analytical, and numerical analysis of the copper wire multi-pass drawing process, 2024, p. 742–52. https://doi.org/10.21741/9781644903131-82.

Chapter 3

HOT TORSION TEST: APPLICATION IN THE ALUMINUM EXTRUSION INDUSTRIAL PROCESS

3.1. CHAPTER OVERVIEW

This chapter investigates the thermomechanical behavior of aluminum alloys during hot extrusion, focusing on the impact of material characterization on the accuracy of Finite Element Method (FEM) simulations. The work starts describing the hot torsion test methodology employed to characterize the high-temperature flow behavior of the material. A detailed explanation of the experimental setup for precise temperature control during induction heating will be provided, emphasizing the crucial role of this precise control in obtaining reliable and reproducible test results.

Subsequently, material characterization through hot torsion tests performed on four nominally AA6082 alloys will be presented. These tests will cover a range of temperatures and strain rates, allowing for a critical comparison of flow stress behavior across the different samples and highlighting variations in ductility and strength. The results will then be used to select appropriate flow stress models for subsequent FEM simulations.

Next, a comprehensive industrial case study will be presented, detailing the experimental setup and parameters of a benchmark aluminum extrusion process. This case study will serve as the basis for comparing the results of FEM simulations against experimental data. The FEM simulations will be conducted using different aluminum flow stress, derived from the hot torsion test results, allowing us to assess the impact of material characterization accuracy on the simulation's predictions for key parameters such as extrusion load, profile velocity, and exit temperature.

3.1.1. Introduction

The differentiation between cold-working and hot-working of metals is generally based on the recrystallization temperature, which is typically about 50% of the material's absolute melting temperature. Hot working typically occurs at temperatures between 70% and 80% of its absolute melting point [1,4,5]. At these elevated temperatures, the material gains sufficient internal energy to activate additional deformation mechanisms beyond conventional slip. Hot working facilitates dynamic and static processes of recovery and recrystallization, which play critical roles in refining the material's microstructure. Dynamic recovery occurs during deformation, where dislocations annihilate or rearrange, reducing internal stress. Dynamic recrystallization, similarly, occurring during deformation, involves the nucleation of new grains that replace deformed ones, promoting grain refinement and increasing ductility. After deformation, static recovery and static recrystallization may occur while the material remains at high temperatures. The ability of a material to undergo these processes depends on factors such as its stacking fault energy (SFE), which determines the mobility of dislocations and influences the rate of work hardening. Materials with low SFE exhibit more rapid strain hardening due to restricted dislocation movement. On the other hand, metals with high SFE, such as aluminum alloys, have more mobile dislocations, leading to lower rates of strain hardening. These mechanisms restore the microstructure, reduce work hardening, and maintain low flow stresses, contributing to increased material workability. Both recovery and recrystallization are highly temperature-sensitive, as they are thermally activated processes. By increasing the temperature, the rate at which these mechanisms proceed increases, which allows hot working processes to achieve large deformations while maintaining low flow stresses. In summary, hot working involves a complex interplay between temperature, strain rate, and material-specific properties, such as stacking fault energy. Therefore, to develop effective manufacturing techniques for metals, accurate knowledge of their hot-working behavior is essential. This includes understanding how the material's ductility and flow stress change with temperature and strain rate.

In this context, the most suitable test is considered the hot torsion test since the solid specimen is deformed at a constant strain rate under torsion and provides extended strain values. Another significant advantage of the hot torsion test is the temperature

control compared to the tensile and compression tests. In the torsion test, the material can be effectively heated using induction due to the stationary nature of the specimen's geometry throughout the test. The solenoid used for heating remains accurately centered on the specimen's gauge section, ensuring that the heating is localized to the desired area. Furthermore, the integration of a thermocouple, inserted into the specimen to reach the beginning of the gauge section, combined with a PID control system, enables the maintenance of a stable and uniform temperature throughout the duration of the test. This temperature stability is critical for accurately assessing the material's behavior under controlled thermal conditions, making the hot torsion test particularly advantageous in studies of thermomechanical properties [1,17,18,82].

3.1.2. Introduction to the Induction heating

Induction heating is a process where heat is generated in a conductive material through electromagnetic induction. An alternating current (AC) is passed through a coil, called inductor (typically a solenoid), which produces a varying magnetic field around it. When a workpiece made of conductive material is placed within a magnetic field, eddy currents are induced in the material due to the changing magnetic field interacting with the conductor. These currents, in turn, generate heat due to the material's resistance, as described by the Joule effect.

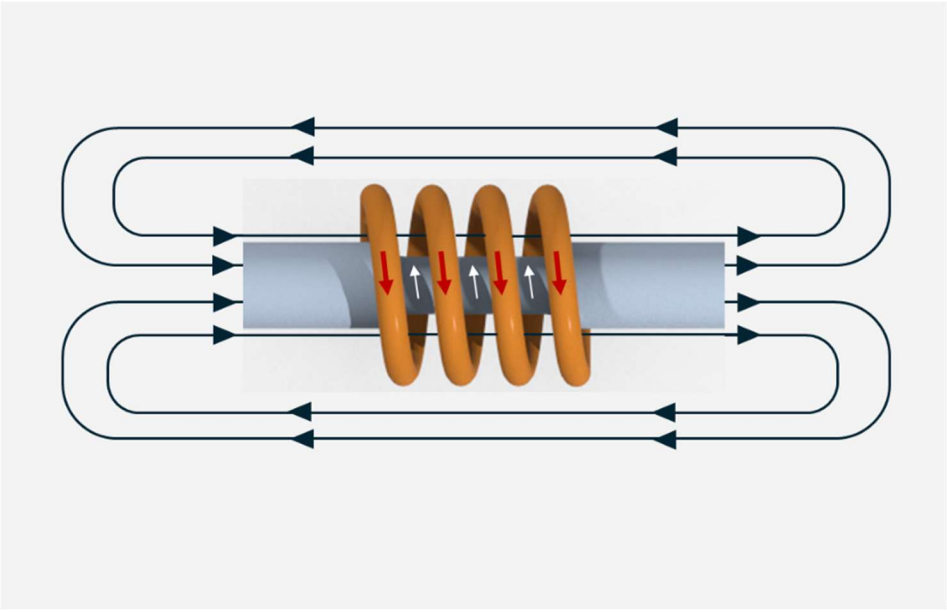

Fig. 3.1 Schematic representation of the induction heating process for a specimen during hot torsion test.

The intensity of the magnetic field is influenced by various factors, including the current in the inductor, the geometry of the inductor, and the proximity of the workpiece. The magnetic field oscillates at the same frequency as the current passing through the coil, and the eddy currents produced in the workpiece flow in a direction opposite to the inducing current, creating an opposing magnetic field as shown in the scheme in *Fig. 3.1*. This interaction causes the total magnetic field to be the sum of the fields generated by the inductor and the eddy currents within the workpiece. This heating process is highly efficient for several reasons. The heat is generated directly inside the material, rather than being applied from an external source, and it can be localized to specific regions, depending on the geometry of the inductor and the material.

The critical parameters that influence the efficiency and effectiveness of induction heating include the electrical conductivity and magnetic permeability of the workpiece, as well as the frequency of the alternating current. Electrical conductivity plays a crucial role in the induction heating process, influencing the depth of heating, the uniformity of temperature distribution, and the efficiency of energy transfer. Materials with higher conductivity will generally heat more efficiently. For metals, conductivity can change significantly with temperature, affecting the overall heating process. Magnetic permeability refers to the material's ability to support the formation of magnetic fields within it. In ferromagnetic materials, such as certain types of steel, the magnetic permeability is typically very high, but it decreases sharply above a critical temperature known as the Curie temperature. Above this point, the material becomes paramagnetic and its permeability becomes equal to that of free space, reducing its ability to concentrate the magnetic field and altering the heating efficiency [83,84].

The induction heating fundamental principles are governed by Faraday's Law of Electromagnetic Induction, which states that a changing magnetic field within a closed loop induces an electromotive force (EMF) in the conductor. This induced EMF drives eddy currents and the resistance of the material to these currents generates heat. The key equation governing the induction process is the Faraday Law on Induction expressed in Eq. (3.1).

$$\mathrm{EMF} = -\frac{\mathrm{d}\Phi_B}{\mathrm{dt}} \qquad (3.1)$$

Where Φ_B is the magnetic flux through the material, *t* is time, and the negative sign indicates that the induced EMF opposes the change in magnetic flux, a concept known

as Lenz's Law. The induced current density *J* (A/m²) is proportional to the rate of change of the magnetic field *E* (V/m), and the electrical conductivity of the material *k* (S/m), as in Eq. (3.2).

$$J = kE \tag{3.2}$$

The heat generated by these eddy currents in the material is described by Joule's Law, expressed in Eq (3.3).

$$Q = I^2R \qquad \text{for a volume element:} \quad q = J^2\rho \tag{3.3}$$

Where Q is the power loss or heat generated (W), I is the current (A), R is the resistance (Ω), q is the power density (W/m³), and ρ is the resistivity of the material (Ω·m).

The heating effect in induction heating is highly influenced by the skin effect, where eddy currents are concentrated near the surface of the material. The skin depth, denoted by δ, refers to the distance from the surface where the current density drops to $1/e$ (approximately 37%) of its original value at the surface, and is given by Eq. (3.4).

$$\delta = \sqrt{\frac{2\rho}{\mu\omega}} \qquad \text{with} \qquad \omega = 2\pi f \tag{3.4}$$

Where ρ is the material resistivity (Ω·m), μ is the magnetic permeability of the material (H/m), and f is the frequency of the AC current (Hz).

In addition to the skin effect, several other factors influence the distribution of eddy currents and the resultant heating patterns within the workpiece:

- Skin Effect: as mentioned, the skin effect causes the eddy currents to concentrate near the surface of the conductor. The skin depth determines the effective penetration of the current into the material and is influenced by the frequency of the applied current and the material's properties.
- Proximity Effect: the proximity effect describes the influence of neighboring conductors on the distribution of current within the material. In induction heating, the proximity of the workpiece to the inductor and the presence of

other conductive materials can distort the magnetic field, causing non-uniform current distribution. This effect is more pronounced at higher frequencies, where the skin depth is smaller, and can lead to uneven heating if not carefully controlled.

- Ring Effect: in a circular inductor coil, the magnetic field is more concentrated inside the coil than outside. This phenomenon, known as the ring effect, leads to more efficient heating near the inner surface of the coil, while the outer surface may receive less heat. The design of the inductor coil must account for this effect to ensure uniform heating across the workpiece.
- End and Edge Effects: at the ends or edges of the workpiece, the magnetic field distribution is often distorted, leading to localized regions of higher current density and increased heating. These end and edge effects are more significant at higher frequencies and in workpieces with sharp corners or irregular geometries. Special inductor designs, such as using coils with varying spacing or shapes, can mitigate these effects to achieve more uniform heating.

Therefore, the geometry of the inductor plays a crucial role in determining the heating patterns and overall efficiency of the process. Induction coils are typically made from copper tubing, and their shape and size are optimized based on the geometry of the workpiece and the desired heating profile. Factors such as the number of coil turns, the spacing between the turns, and the proximity of the coil to the workpiece all influence the magnetic field distribution and the effectiveness of the heating process. One of the challenges in designing induction heating systems is achieving uniform heating across workpiece geometries. The inductor must be designed to concentrate the magnetic field in the regions where heating is desired while minimizing losses due to leakage of the magnetic field into areas that do not require heating.

It is evident then that the efficiency of induction heating depends on a careful balance between several parameters, including the power input, frequency, and material properties. Furthermore, in addition to the electromagnetic effects, thermal phenomena also play a critical role in induction heating. The three main mechanisms of heat transfer are:

1. Conduction: it is the primary mode of heat transfer within the workpiece, where heat generated at the surface is transferred to the interior regions through conduction. The rate of heat conduction depends on the material's thermal

conductivity, which is also temperature-dependent. Materials with high thermal conductivity, such as metals, will transfer heat more rapidly.

2. Convection: heat is also transferred from the surface of the workpiece to the surrounding environment through convection. This process depends on the convective heat transfer coefficient, which varies with the material properties, the surrounding fluid (typically air), and the relative motion between the workpiece and the fluid.
3. Radiation: as the temperature of the workpiece increases, it also loses heat to the environment through radiation. The Stefan-Boltzmann law governs this process, where the heat loss is proportional to the fourth power of the surface temperature. The emissivity of the material's surface also affects the rate of radiative heat transfer.

In summary, induction heating is a highly efficient and versatile technology that combines complex electromagnetic and thermal phenomena. By carefully controlling factors such as power input, frequency, and material properties, it is possible to optimize the heating process. In practical terms, the design and optimization of induction heating systems often rely on a combination of empirical knowledge, computational modeling, and experimentation to account for the numerous variables that influence the process [85–87].

3.1.3. Heating cycle assessment

Temperature control experimental procedure

As introduced in the previous section, the process of induction heating for a workpiece is influenced by numerous parameters, making the underlying physics highly complex and challenging to model analytically. One of the key factors affecting the heating process is the geometry of the solenoid, which is often optimized based on the specialized knowledge and experimental experience of induction generator manufacturers.

The solenoid used on the torsion machine at the DIN - Department of Industrial Engineering at the University of Bologna has the geometry shown in *Fig. 3.2*. It consists of a copper tube with an outer diameter of 5 mm and a central bore of 3 mm to allow

for water cooling. The solenoid comprises four coils, with a spacing of 3 mm between them, resulting in a total length of approximately 35 mm and an inner diameter of 25 mm. The induction generator works with a frequency range between 80 ÷ 400 kHz with a maximum output power of 15 kV.

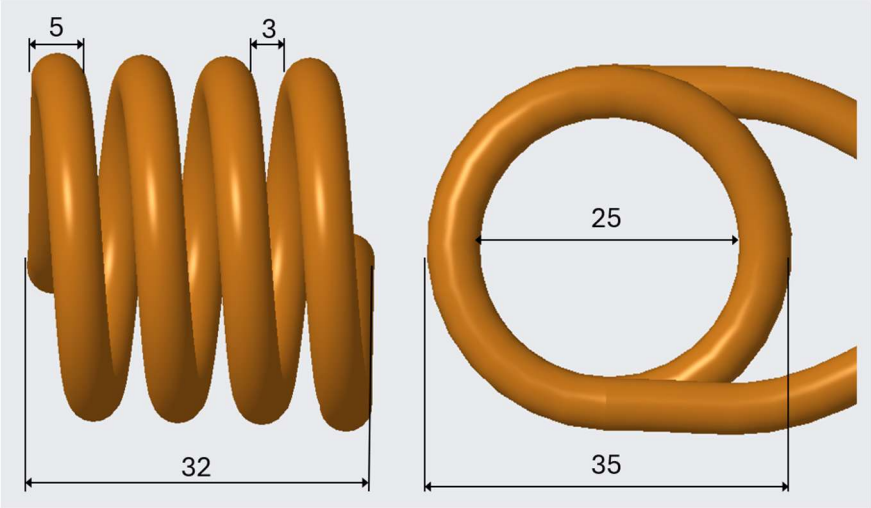

Fig. 3.2 Drawing of the copper tube solenoid used on the torsion machine at the DIN - Department of Industrial Engineering, University of Bologna.

To ensure an accurate evaluation of the heating cycle and to achieve the required temperature uniformly across the entire gauge length of the specimen, an experimental procedure was implemented. The test was performed using an Aluminum alloy specimen with a gauge length of 10 mm in length and diameter, as shown in *Fig. 3.3b*. External thermocouples were attached along the gauge section of the specimen and connected to an external data acquisition system, as shown in *Fig. 3.3*. The thermocouples, designated as T1, T2, and T3, were positioned on the outer surface of the gauge section respectively, moving along the longitudinal axis, at the beginning (just after the transition), the center, and the end (just before the transition) of the specimen. Additionally, a fourth thermocouple, T4, was inserted into a small hole drilled into the center of the gauge section, extending 5 mm inward from the external surface, to monitor the core temperature. In the schematic shown in *Fig. 3.3b*, the control thermocouple TC1, integrated into the PID control system of the torsion machine and inserted inside the specimen in the 3mm-diameter hole, is also shown. This setup allowed for a comprehensive and precise measurement of the temperature distribution across the specimen during the heating process.

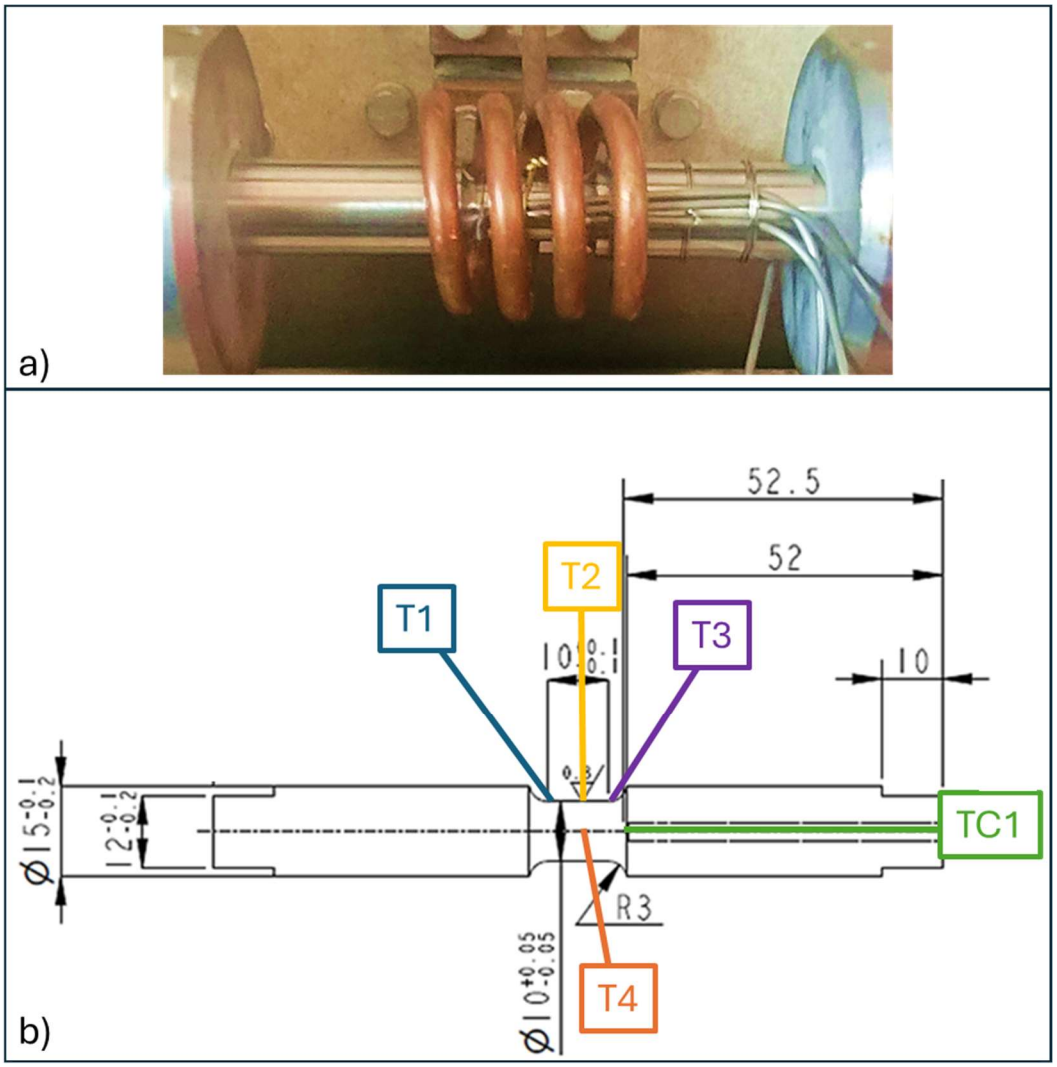

Fig. 3.3 a) Photo of the specimen during the experimental activity for temperature control during induction heating in the torsion test; b) Diagram of the thermocouple positioning on the specimen.

A first heating cycle of the specimen was tested, and the temperature trends monitored by the thermocouples are shown in the graph in *Fig. 3.4*. The green line represents the programmed heating cycle and corresponds to the temperature recorded by the torsion machine thermocouple TC1, while the blue, yellow, purple, and orange lines represent the temperatures recorded by thermocouples T1, T2, T3, and T4, respectively. The cycle involved heating the specimen up to a temperature of 500°C with a rate of 2°C/s, therefore setting a ramp of 250s, and then maintaining it at 500°C for 360s (6 min). The dashed lines on the secondary y-axis show the deviation between the actual temperature measured by each thermocouple and the desired reference temperature at every point in time. As can be observed from the graph, during the initial phase of heating at the rate of 2°C/s, there is a pronounced overshoot

in the surface temperature due to the "skin effect" caused by the rapid current flow, leading to a surface temperature difference of up to 100°C during the first 120 seconds. After this initial peak, the temperature begins to homogenize between the outer surface and the core of the specimen as heating continues, gradually approaching the target reference temperature. However, at the end of the heating phase, around 250 seconds, the outer surface temperature, particularly in the center of the specimen (as measured by thermocouple T2), reaches peaks of 550-560°C, exceeding the desired temperature by approximately 50°C. During the 6-minute holding phase aimed at homogenization, the temperature gradually stabilizes, and the surface temperature decreases. Nevertheless, by the end of the holding period, there remains a temperature difference of about ±25°C between the surface and the core of the specimen.

A second heating cycle was subsequently tested, in which the specimen was again heated to a temperature of 500°C, but this time using a slower heating rate of 1°C/s. The results of this cycle are illustrated in *Fig. 3.5*. This slower rate yielded significantly improved results, as it allowed for better homogenization of the temperature throughout the specimen, bringing it more closely in line with the desired target. As in the first cycle, there was an initial overshoot in surface temperature caused by the peak current at the beginning of the heating phase. However, due to the lower rate, the torsion machine delivered less current per second, leading to a much smaller temperature difference during the first 200 seconds, with a deviation of around 70°C. As heating progressed, the temperature between the outer surface and the core of the specimen began to equalize, converging towards the set temperature. After 500 seconds, the surface temperature was only about 10°C higher than the target value. During the 6-minute holding phase, the temperature distribution further stabilized, resulting in uniform heating across all regions of the specimen. By the end of the hold time, the temperature difference throughout the specimen was reduced to a range of just ±5°C. This demonstrates that using a reduced heating rate not only minimizes the initial temperature overshoot but also ensures that the target temperature is achieved with greater precision and uniformity across the entire specimen, making this cycle more effective for precise thermal control.

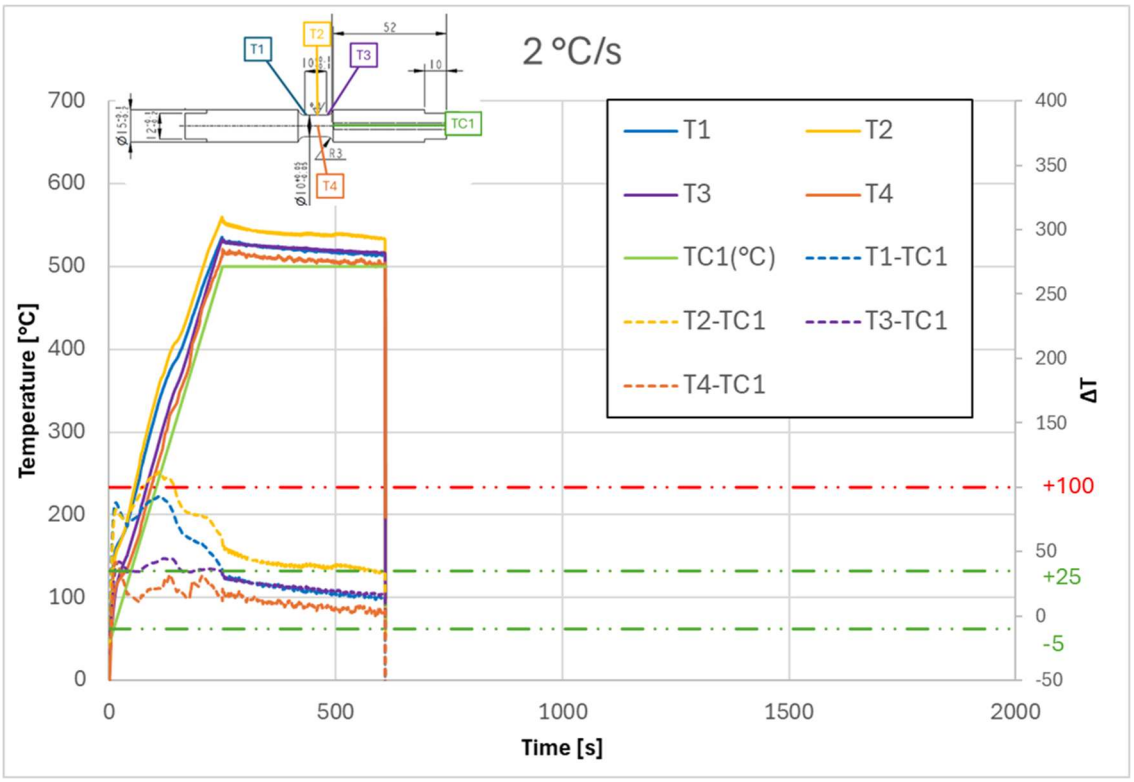

Fig. 3.4 Temperature trend of the specimen recorded by thermocouples overtime during the induction heating cycle at a temperature of 500°C, using a heating rate of 2 °C/s and a 6-minute holding period.

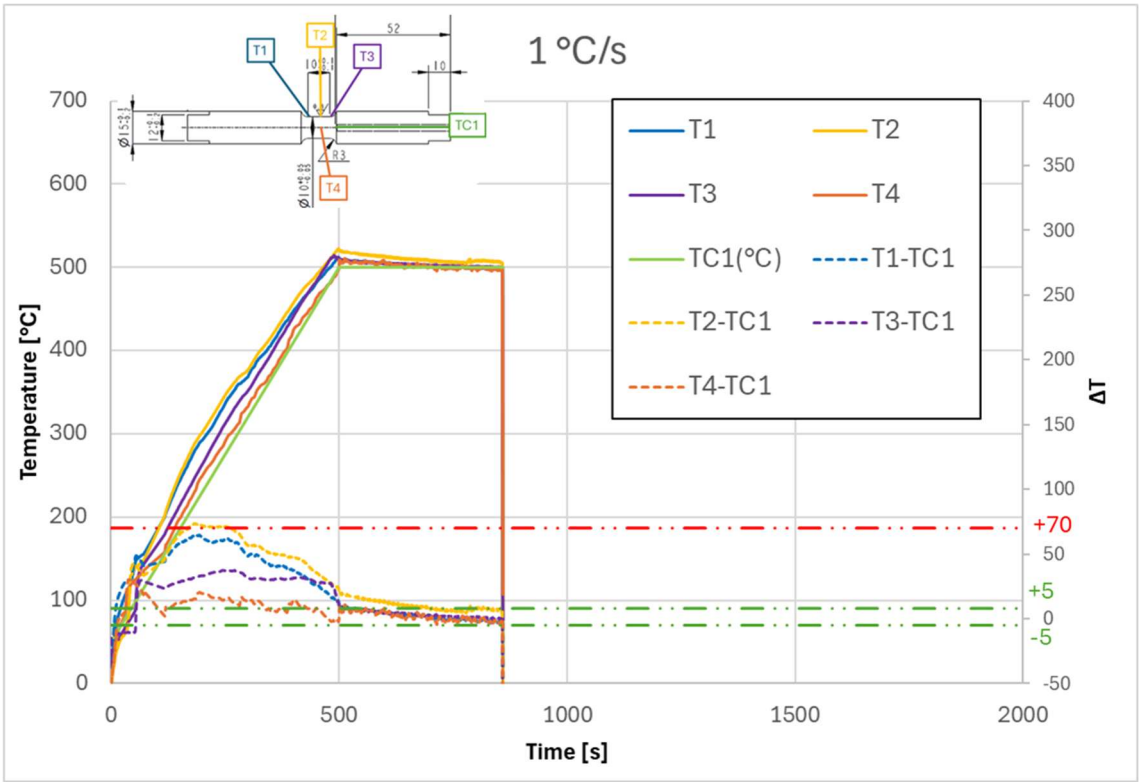

Fig. 3.5 Temperature trend of the specimen recorded by thermocouples overtime during the induction heating cycle at a temperature of 500°C, using a heating rate of 1 °C/s and a 6-minute holding period.

Finally, a third heating cycle was tested, also achieving a temperature of 500°C, as shown in *Fig. 3.6*, but this time using a reduced heating rate of 0.5°C/s. As observed from the graph, this cycle yielded only a slight improvement compared to the 1°C/s cycle during the initial phase, with the temperature difference peaking at around 50-60°C. As the heating progressed, the temperature profiles became comparable to those observed in the 1°C/s cycle, confirming the fine performance with a final temperature difference of approximately ±5°C from the target temperature. Both the 1°C/s and 0.5°C/s cycles allowed for excellent temperature homogenization throughout the gauge length of the specimen. However, the 0.5°C/s cycle required a total time of 1360 seconds (approximately 23 minutes), compared to 860 seconds (around 14 minutes) for the 1°C/s cycle. Therefore, the 1°C/s heating cycle was chosen for the hot torsion tests on aluminum, as it provided the optimal compromise between achieving perfect temperature uniformity in the specimen and minimizing the total cycle time. Additionally, it was considered that the initial surface temperature overshoot occurs at lower temperatures and lasts for only a few seconds. Thus, even with a 70°C difference, the temperature remains far from critical values that could induce thermal cycles or structural transformations in the aluminum alloy.

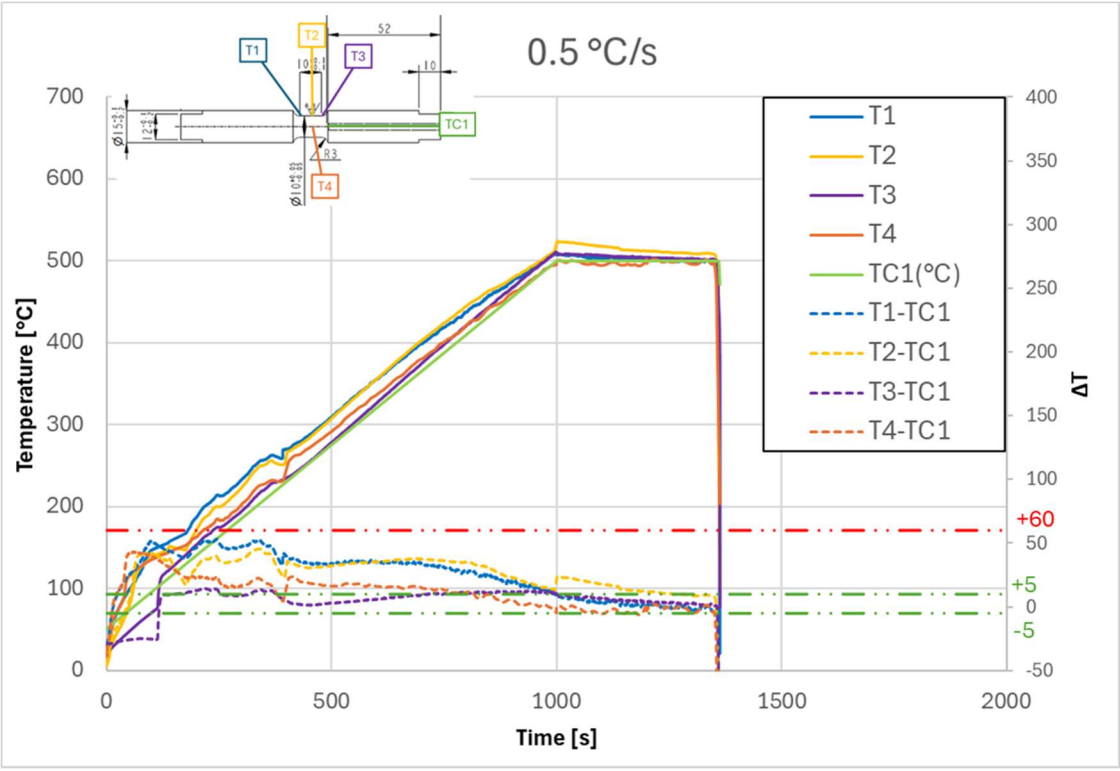

Fig. 3.6 Temperature trend of the specimen recorded by thermocouples overtime during the induction heating cycle at a temperature of 500°C, using a heating rate of 0.5 °C/s and a 6-minute holding period.

As a final validation, the heating cycles at rates of 1°C/s and 0.5°C/s were also tested at a final target temperature of 550°C, as shown in *Fig. 3.7* The results were similar to those observed at 500°C, reaffirming the initial observations and supporting the decision to use the heating cycle involving a heating phase (ramp) at a rate of 1°C/s and a holding phase of 6 minutes for the aluminum hot torsion tests.

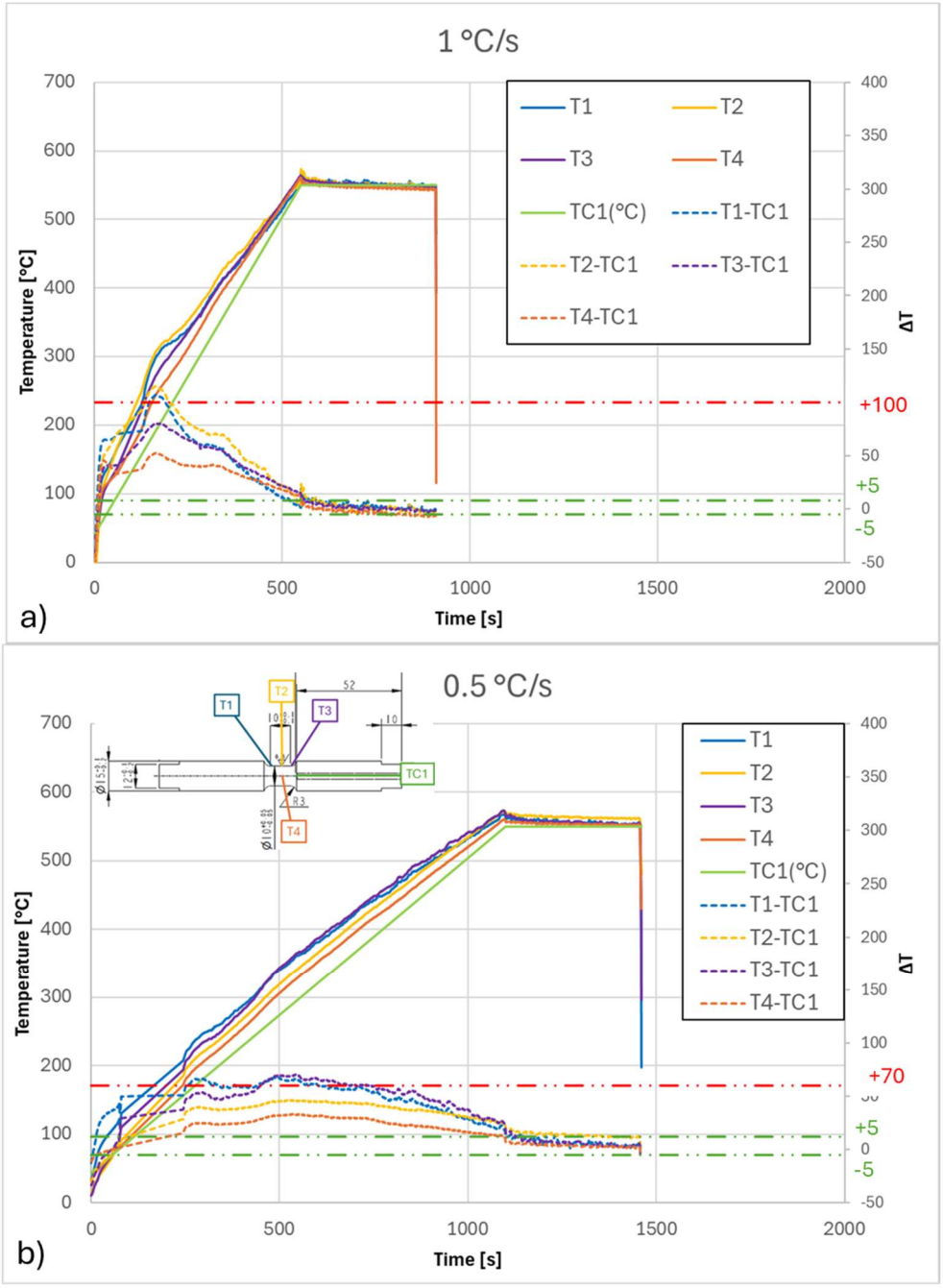

Fig. 3.7 Temperature trend of the specimen recorded by thermocouples overtime during the induction heating cycle at a temperature of 550°C, using: a) a heating rate of 1 °C/s, b) a heating rate of 0.5 °C/s and a 6-minute holding period.

3.2. INDUSTRIAL CASE STUDY: The Influence of Alloy Characterization Approaches on Extrusion Process FEM Simulation Reliability

3.2.1. Introduction

The extrusion of aluminum alloys is a manufacturing process used to produce profiles with a constant cross-section and complex geometries. In this process, a pre-heated billet is forced through a die opening, forming the desired profile. To control the hot extrusion process effectively, several key factors must be considered, such as the design of the tools, the main process parameters, and the thermodynamics of the extrusion process.

Extrusion can be classified as either direct or indirect. In direct extrusion, the billet is placed inside a container, and a hydraulic press applies pressure via a ram. Initially, the billet undergoes compression until its diameter matches the container. At this point, the material begins to flow through the die to form the profile. In indirect extrusion, however, the extruded profile moves in the opposite direction to the ram, reducing the friction between the billet and the container. This lowers the extrusion force and increases the process speed. However, indirect extrusion is limited by the geometry of the die, which must move within the container, limiting the complexity of achievable shapes.

The extrusion load is influenced by the material plastic deformation and the frictional opposing movement of the billet, and its trend differs between direct and indirect extrusion. At the beginning of the piston stroke, the force increases progressively until the extrusion chamber is fully filled. In direct extrusion, the force reaches a higher peak because the initial friction between the billet and the internal walls of the container must be overcome. In contrast, this frictional resistance is absent in indirect extrusion, resulting in a significantly lower and more consistent extrusion force throughout the piston stroke when compared to the direct extrusion process. The extrusion ratio (ER) is a key parameter defined by the ratio between the container area and the extruded profile area. A higher extrusion ratio indicates a greater amount of mechanical work required, leading to increased extrusion load.

Temperature also plays a critical role, as higher extrusion temperatures lower the billet material's flow stress, reducing the required extrusion load. Similarly, extrusion speed is important for controlling productivity. However, increasing the speed also raises the extrusion load due to higher strain rates, despite the accompanying temperature rise. Overall, strain rate has a more significant impact on the extrusion load than temperature does [51–54].

In sectors like aluminum extrusion, where on-site experiments are expensive and time-consuming due to the complexity of the process, the Finite Element Method (FEM) has become a crucial tool for improving design and process optimization. Over time, FE codes have advanced significantly, allowing for precise problem-solving in shorter computational times. This evolution has driven the widespread adoption of numerical simulations in the manufacturing industry, with the goal of improving product quality and minimizing material scraps [6]. In recent years, numerous researchers have explored various aspects of the extrusion process through the application of FEM codes, from process and tool optimization to microstructure prediction, proposing different methodologies and improving the accuracy of the simulation [55–65].

In this context, it has become increasingly clear that to perform reliable and accurate simulations, it is necessary to provide the FEM code with precise modeling of material flow stress. Therefore, appropriate characterization tests are required in order to achieve the high deformation values typical of the extrusion process and simultaneously maintaining constant temperature and strain rates inside the trial. The most suitable test is considered the hot torsion test since the solid specimen under torsion provides extended strain values, overcoming the limits of the high-temperature tensile and compression tests where the flow curves are usually limited respectively to 0.2 and 1 of true strain [3].

In the following sections, the characterization performed through hot torsion tests of different aluminum alloys belonging to the AA6082 class will be presented and compared. Furthermore, the influence of material flow stress modeling on numerical simulation results will be examined, with comparisons between the predicted results with experimental values obtained during an industrial extrusion process. The torsion tests were carried out on specimens extracted from four different casting batches, all within the AA6082 alloy class and industrially homogenized to an O condition. The trials were performed, in the following conditions: three levels of strain rate 0.1 s^{-1}, 1 s^{-}

^{1}, and 10 s^{-1}, and three temperatures 450°C, 500°C, and 550°C. Subsequently, the results of the torsion tests were inserted as input data for the numerical simulation of an industrial extrusion case properly monitored, and the outputs were compared to experimental data in order to check the effect on numerical simulation accuracy.

3.2.2. Methodology and experimental procedures

Hot torsion test

The hot torsion tests were carried out on homogenized solid-bar specimens of different AA6082 alloys, with a gauge length and a diameter of 10 mm, as shown in *Fig. 3.8*. This geometry allows for easier temperature control across the sample section; furthermore, the solid-bar specimen can withstand higher torque levels without risk of failure and higher strain at breaks compared to the thin-walled tubular specimen and is often easier to produce with respect to the tubular one.

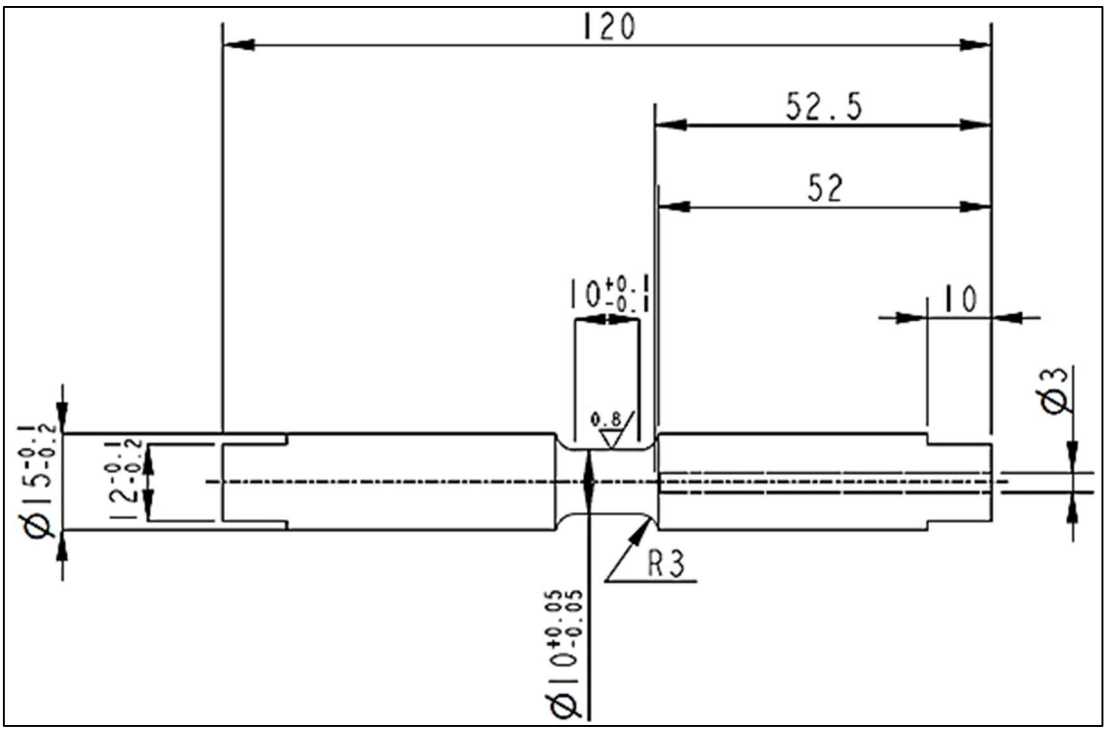

Fig. 3.8 Geometry of the solid bar specimen used for the aluminum hot torsion tests.

During the test, the temperature is measured by the thermocouple inserted inside the specimen in the 3mm-diameter hole, as shown in *Fig. 3.9*, and it is kept constant by the PID controller. The samples were heated at a rate of 1°C/s using a copper induction coil and maintained for 6 minutes at the testing temperature before torsion, to allow a

homogeneous temperature distribution throughout the gage length, as explained in section 3.1.3.

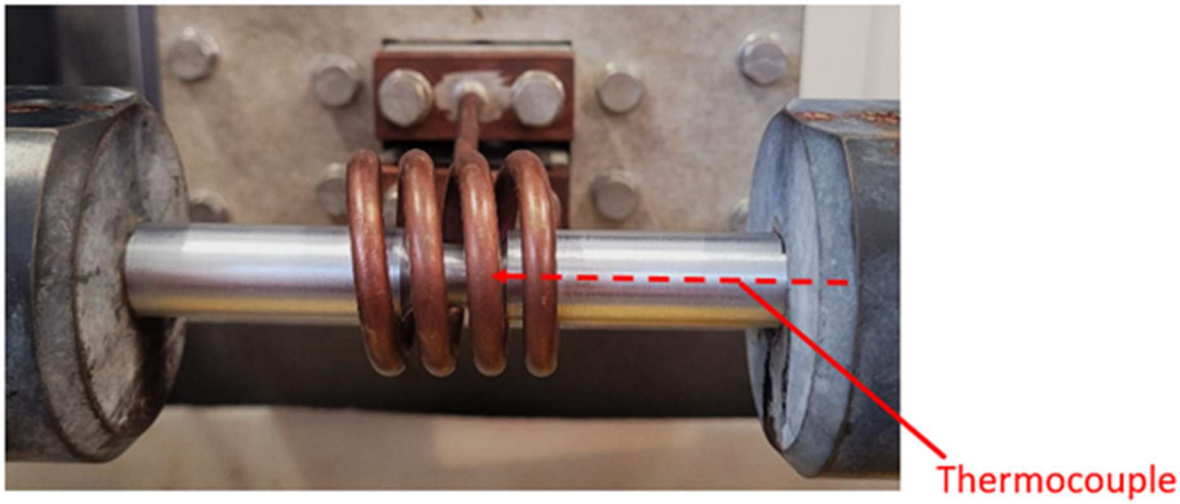

Fig. 3.9 Picture of an AA6082 sample during the hot torsion test performed at the DIN-Department of Industrial Engineering of the University of Bologna.

For processing the data from the hot torsion tests, to convert the torque-rotation angle values into equivalent stress-strain curves, the Fields-Backofen theory [10], extensively discussed in the previous sections, was applied. However, in this case, the strain hardening coefficient n and the strain rate sensitivity coefficient m were neglected. As a result, the equivalent stresses and strains, according to the von Mises criterion, take the form presented in Eqs. (3.5) and (3.6). This approach is supported by numerous studies in the literature, which have demonstrated that these coefficients assume very small values and do not significantly affect the aluminum material's behavior at high-temperature conditions [1,16–18,82,102].

Moreover, it is important to note that, when a material undergoes hot deformation, meaning it is worked at elevated temperatures, typically above its recrystallization temperature, the differences in its mechanical behavior under various loading conditions, such as tension and torsion, become so small that they can effectively be neglected. This is because, at higher temperatures, the material undergoes dynamic restorative processes, such as recrystallization and dynamic recovery, which reduce the influence of strain-hardening mechanisms. At cold working temperatures, these differences are more significant because of factors that affect the crystallographic texture and the microscopic slip processes governing macroscopic strain-hardening behavior. At high temperatures, the formation of crystallographic textures is inhibited

due to the ongoing restorative processes that prevent the accumulation of significant internal stresses. Therefore, the material exhibits a more uniform behavior under various deformation modes, contrasting with the marked differences observed in cold-working conditions, where texture development and slip systems play a more dominant role [1,4].

$$\bar{\sigma} = \frac{3M}{2\pi R^3}\sqrt{3} \tag{3.5}$$

$$\bar{\varepsilon} = \frac{R\theta}{L}\frac{1}{\sqrt{3}} \tag{3.6}$$

Extrusion Case Study

The case study considered for the experimental-numerical comparison was taken from the Extrusion Benchmark 2023 presented at the Aluminium2000 International Conference on Extrusion and Benchmark [103].

Fig. 3.10 Photo of the experimental trials from Extrusion case study of the Benchmark 2023 (Aluminium2000-International Conference on Extrusion and Benchmark ICEB 2023).

The process consists of the extrusion of three hollow tubes made of AA6082 alloy, as shown in *Fig. 3.10*. A porthole die with three tube-shaped openings was employed for the benchmark trials of hollow profile extrusion. The die assembly, made of AISI H-13 steel tempered to a hardness of 45-47 HRC, consisted of five components: the mandrel, the die, the die ring, the backer, and the bolster. *Fig. 3.11 a) and b).*

The final cold profile exhibited an external diameter of 40 mm and a wall thickness of 4 mm, resulting in a single profile surface area of 452.16 mm², which led to a total surface area for all profiles of 1356.48 mm². The material flow characteristics within the tooling varied among the three profiles, with the intention of generating significant velocity deviations at the exit, as shown in *Fig. 3.11c*:

- Exit No. 1: This configuration featured conical ports and cylindrical bearings. The bearings on the die surface had an inlet fillet radius of 1 mm and a length of 6 mm, whereas the bearings on the mandrel surface had the same length without the fillet radius.
- Exit No. 2: This setup utilized cylindrical ports and cylindrical bearings. The die surface bearings had an inlet fillet radius of 1 mm and a length of 7 mm, while the mandrel surface bearings were of the same length without a fillet radius.
- Exit No. 3: This configuration incorporated conical ports and tapered bearings. The die surface bearings had an inlet fillet radius of 1 mm, along with a choke featuring a 1° angle and a length of 4 mm, followed by a final cylindrical section measuring 1 mm in length. The mandrel surface bearings measured 5 mm in length.

The trials were performed on a 40MN press, setting a ram speed of 4.4mm/s; a ram stroke of 650mm was set over a billet length of 680mm (thus meaning 30mm discard length) and a puller tensile force of 350kg (3500N) was applied. The details of the process are listed in *Table 3.1*. The thermal field was monitored by means of a contactless pyrometer on a profile (profile 1), and several extrusion data were continuously acquired by the control system of the press, including the puller speed and the extrusion load.

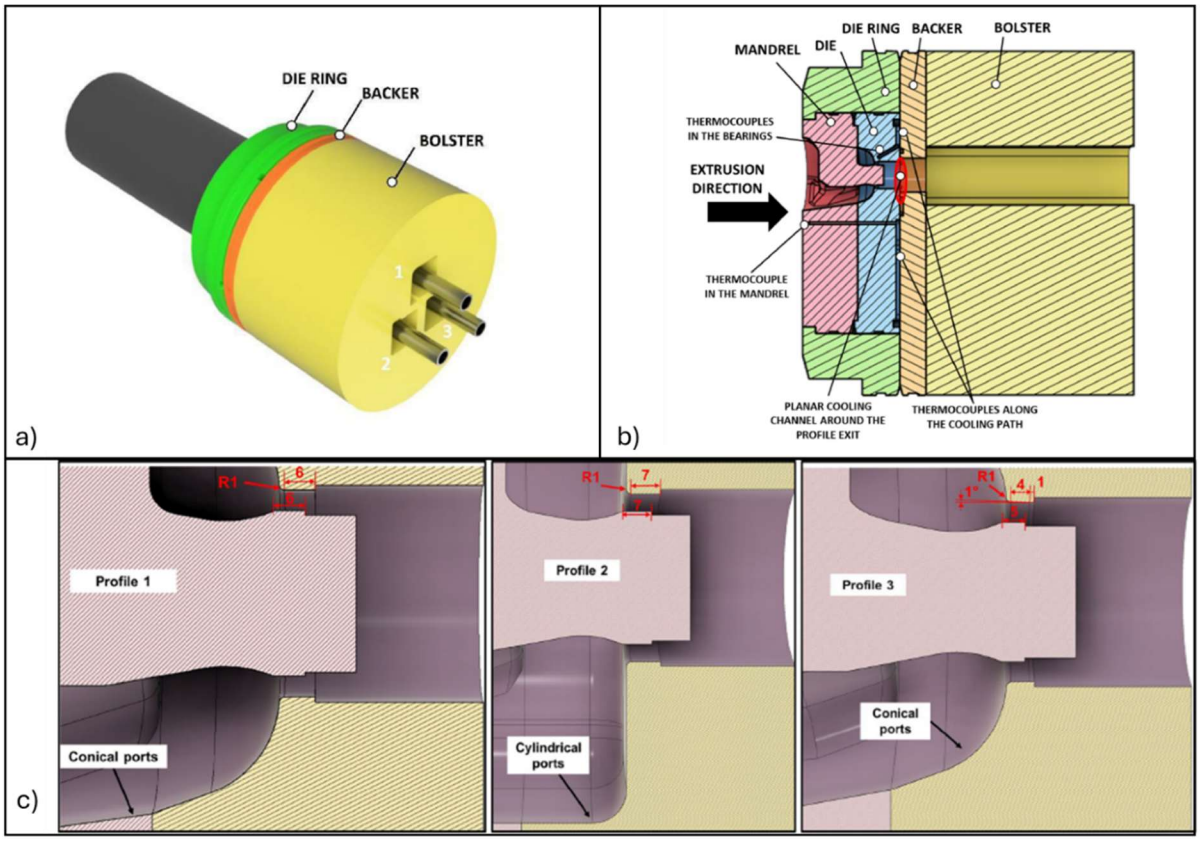

Fig. 3.11 a) 3D drawing of the billet and tools set-up; b) Die assembly; c) Dimensions of different types of die bearings. [103]

Table 3.1 Extrusion process parameters.

Process Parameter	**Value**
Profile alloy	AA6082
Billet diameter	279mm
Container diameter	286mm
Billet length	680mm
Billet rest	30mm
Skin layer thickness	0.3mm
Ram speed	4.4mm/s
Max press load	4000ton/40MN
Ram temperature	350°C
Container temperature	390°C-425°C (ram-die)
Pre-heating billet temperature	440°C (no taper)
Pre-heating die temperature	480°C

Numerical model

The simulation of the case study was performed using Qform Extrusion, an Arbitrarian-Lagrangian-Eulerian (ALE) tool optimized for simulating extrusion processes available in the commercial FE code Qform UK®, as shown in *Fig. 3.12*. The simulation was prepared following the guidelines obtained from prior validation studies that compared extrusion simulation outputs with experimental data [60,95,96,100,104].

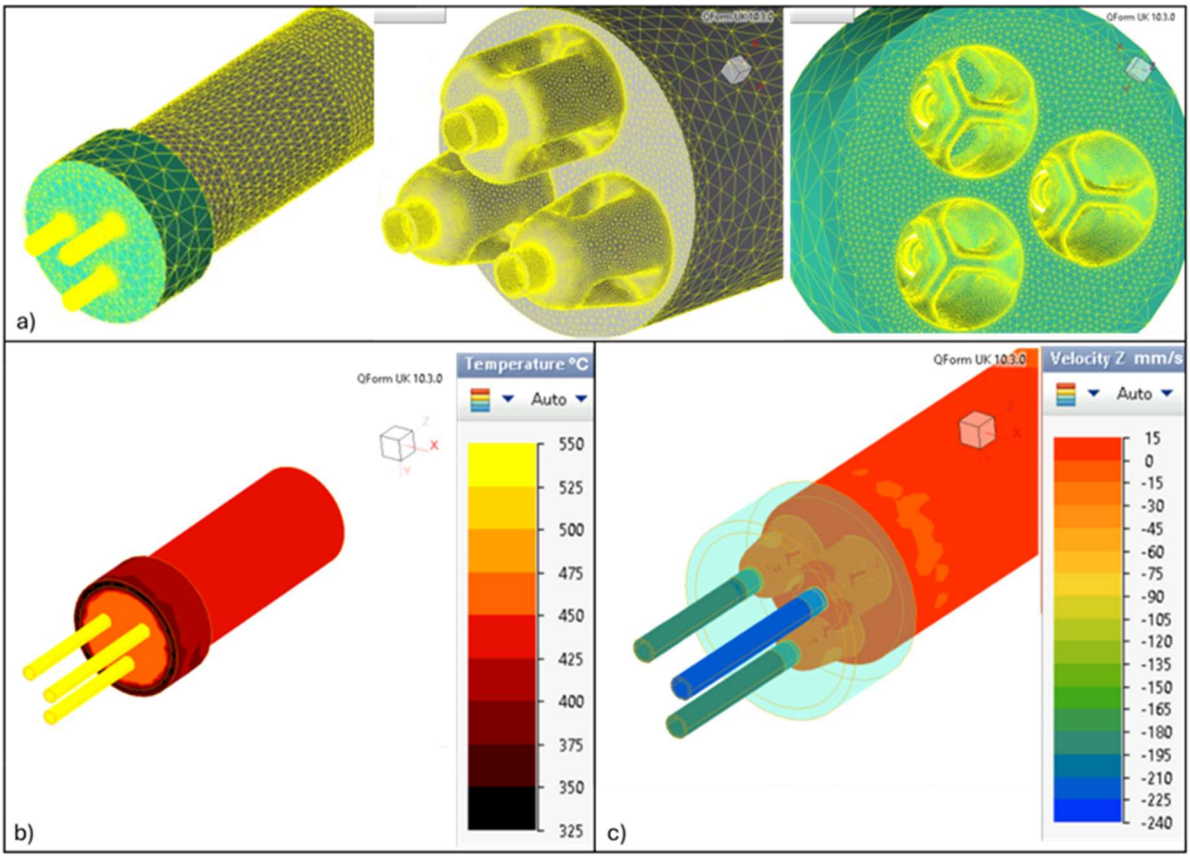

Fig. 3.12 FEM Simulation of the extrusion process using Qform Extrusion UK®: a) workpiece and tools mesh; b) temperature distribution [°C]; c) velocity in z-direction [mm/sec].

For the preparation of the 3-D geometries, QShape, a program internal to QForm to generate the volumetric meshes, was used and the mesh parameters are summarized in *Table 3.2*. The mechanical, physical, and thermal parameters of the tools (die, ram, and container) were set according to the default values of the H13 steel in the Qform® database. Concerning the workpiece, the modeling of the material flow stress was set in tabular form based on the results of the experimental torsion tests. The other physical and thermal properties of the workpiece were set according to the values of the Qform® database for the AA6082 alloy, as listed in *Table 3.3.* The friction conditions

between the workpiece and tools were set in the simulation according to the values presented in *Table 3.4,* which had been previously optimized for aluminum alloy extrusion, ensuring that the modeling accurately reflects the extrusion process characteristics [60].

Table 3.2 Mesh parameters.

Object	**Nodes on surface**	**Internal nodes**	**Total nodes**	**Surface elements**	**Volumetric elements**
Workpiece	45977	114651	160628	91986	843450
Die set	45772	133972	179744	91576	962155
Total	91749	248623	340372	183562	1805605

Table 3.3 Material parameters for the AA6082 alloy.

Material Properties	**AA6082**
Density [Kg/m^3]	2608
Specific heat [J/(kg·K)]	1017
Thermal conductivity [W/(m·K)]	217
Thermal expansion [1/°C]	2.73e-5
Young's modulus [MPa]	46000
Poisson's ratio	0.36

Table 3.4 Friction model parameters.

Levanov model	
Friction factor	1
Levanov coefficient	1.25
Heat transfer coefficient [W/(m^2·K)]	30000
Pause coefficient	0

3.2.3. Results and discussion

Hot Torsion Test Results: Comparison between Different AA6082 Alloys

Torsion tests were conducted on specimens extracted from four different billets, designated A, B, C, and D. All four billets were reported to be made of AA6082 alloy and nominally homogenized.

The graphs in *Fig. 3.13* present the experimental results of the tests performed on alloy A, showing equivalent stress versus equivalent strain. The tests were carried out at different equivalent strain rates of 0.1 s^{-1}, 1 s^{-1}, and 10 s^{-1}, under three temperature conditions: 450°C, 500°C, and 550°C. To ensure test repeatability, at least two trials were performed for each condition. In the graphs, the tests conducted at 450°C are represented by blue and light blue lines (the latter for the repeated test), those at 500°C are shown in green and light green, while tests at 550°C are depicted in red and pink. Regarding the strain rates, dashed curves correspond to tests at a strain rate of 0.1 s^{-1}, solid lines with circle markers represent tests at 1 s^{-1}, and lines with cross markers indicate tests conducted at 10 s^{-1}.

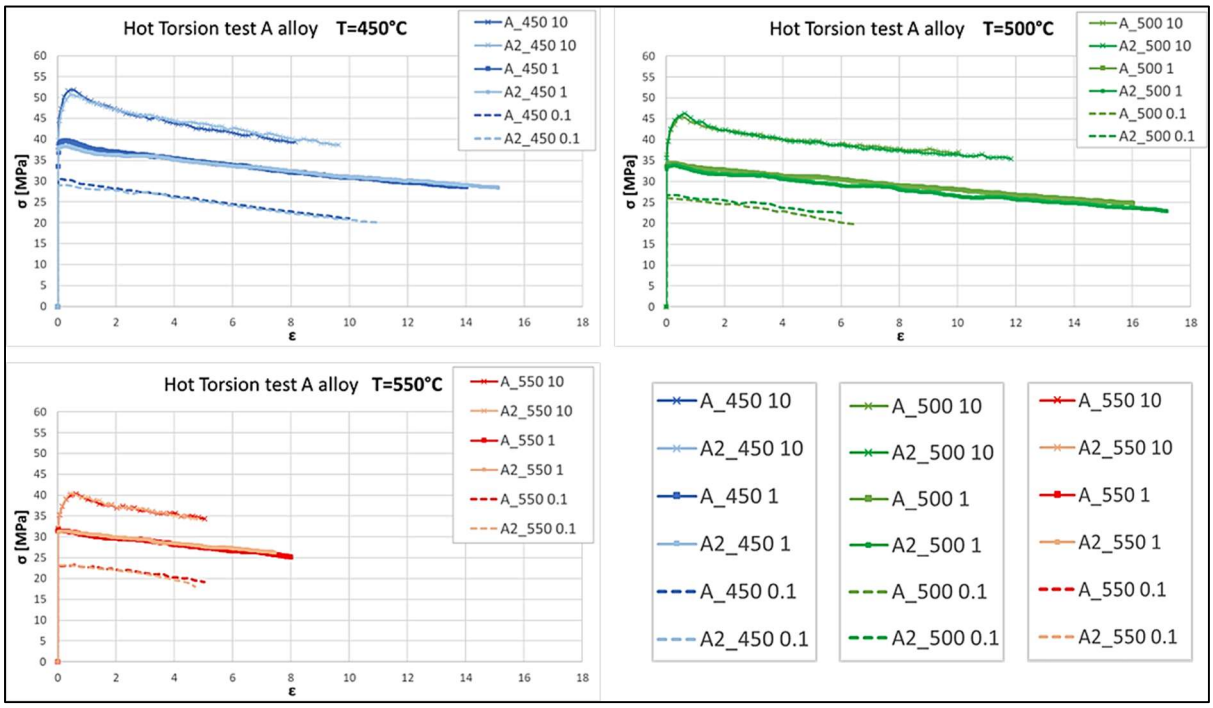

Fig. 3.13 Experimental σ-ε curves from hot torsion tests on A alloy. For each condition, two trials were carried out. [105]

The strain rate remains constant throughout the torsion tests as the torque is applied to the specimen at a constant speed, resulting in a constant twist rate $\dot{\theta}$ [rad/s], and the gage length geometry does not change during the test. Additionally, the temperature is precisely controlled by the machine's PID controller, which regulates the induction heating system. Despite the heat generated during the plastic deformation of the material and the thermal conduction into the grips, the temperature is kept stable within a narrow range of ±3°C, as illustrated in *Fig. 3.14*, where the trend of the temperature detected by the thermocouple into the specimen is reported for all the tests, indicating in green the tests at speed 0.1 s^{-1}, in orange those at 1 s^{-1}, and in blue at 10 s^{-1}.

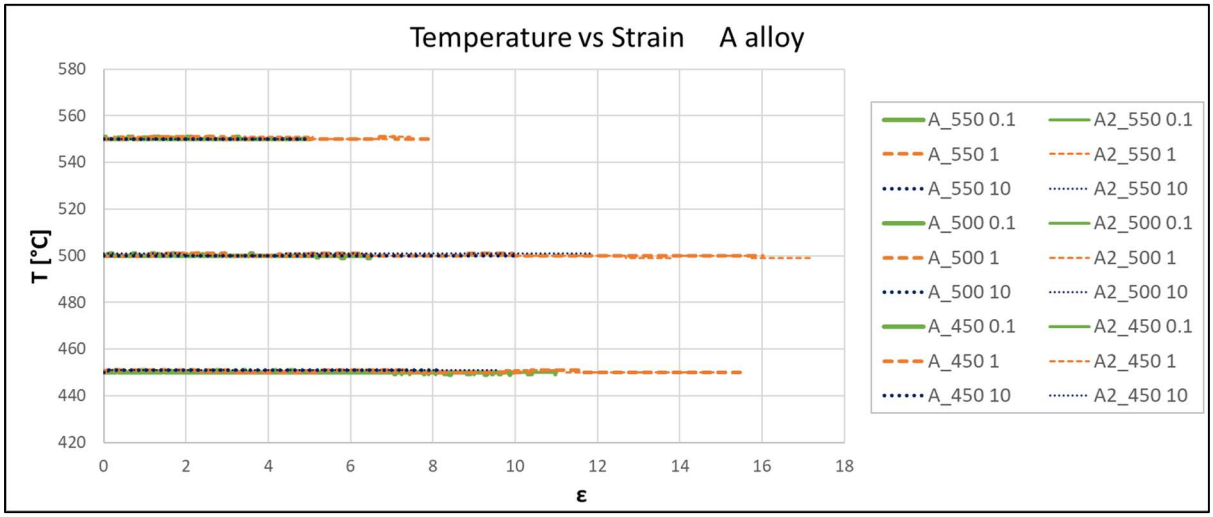

Fig. 3.14 Temperature control during the hot torsion tests on A alloy. [105]

Identical torsion tests under the same conditions were performed on alloys B, C, and D, and the results are presented in the following figures, from *Fig. 3.15* to *Fig. 3.18*. Each graph displays all tests conducted for each alloy, showing a single repetition for each condition maintaining the same legend. Additionally, *Fig. 3.19* provides a comparative overview, where all four graphs are shown together for a more direct and immediate comparison of the plastic behavior of the different alloys.

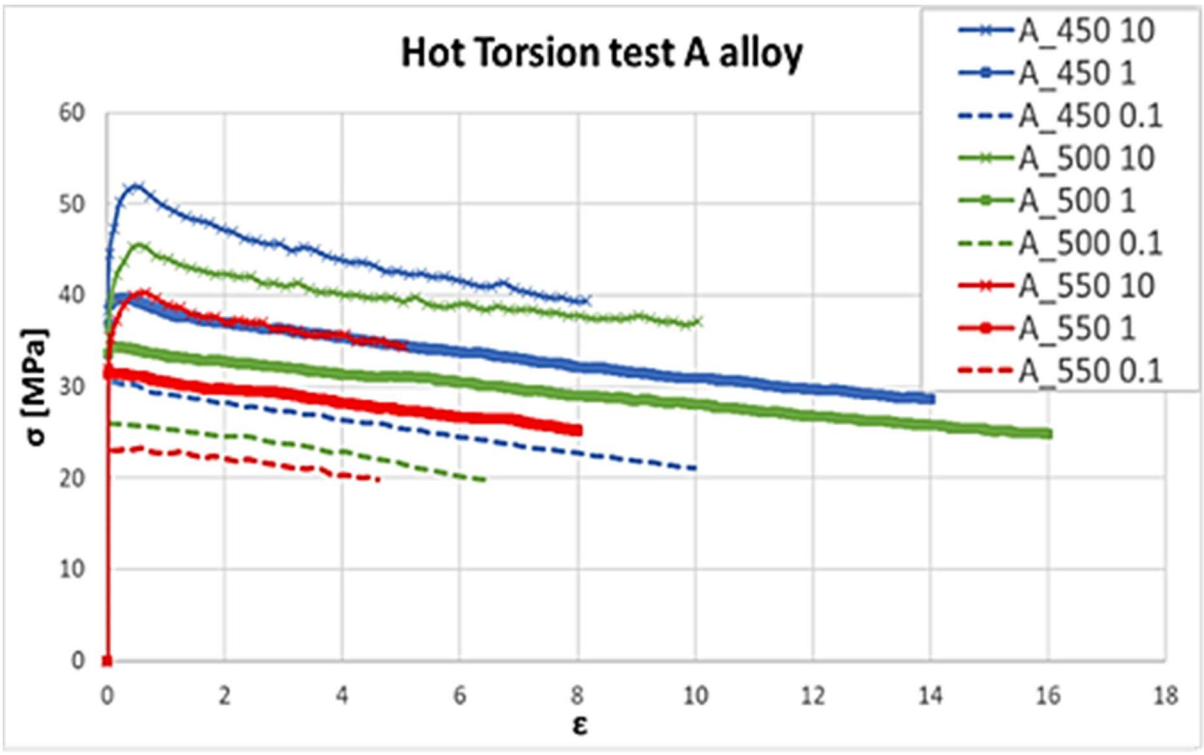

Fig. 3.15 Experimental σ-ε curves of A alloy. Blue lines represent tests at 450°C, green lines at 500°C, and red lines at 550°C, while different types of lines stile indicate the strain rates. [105]

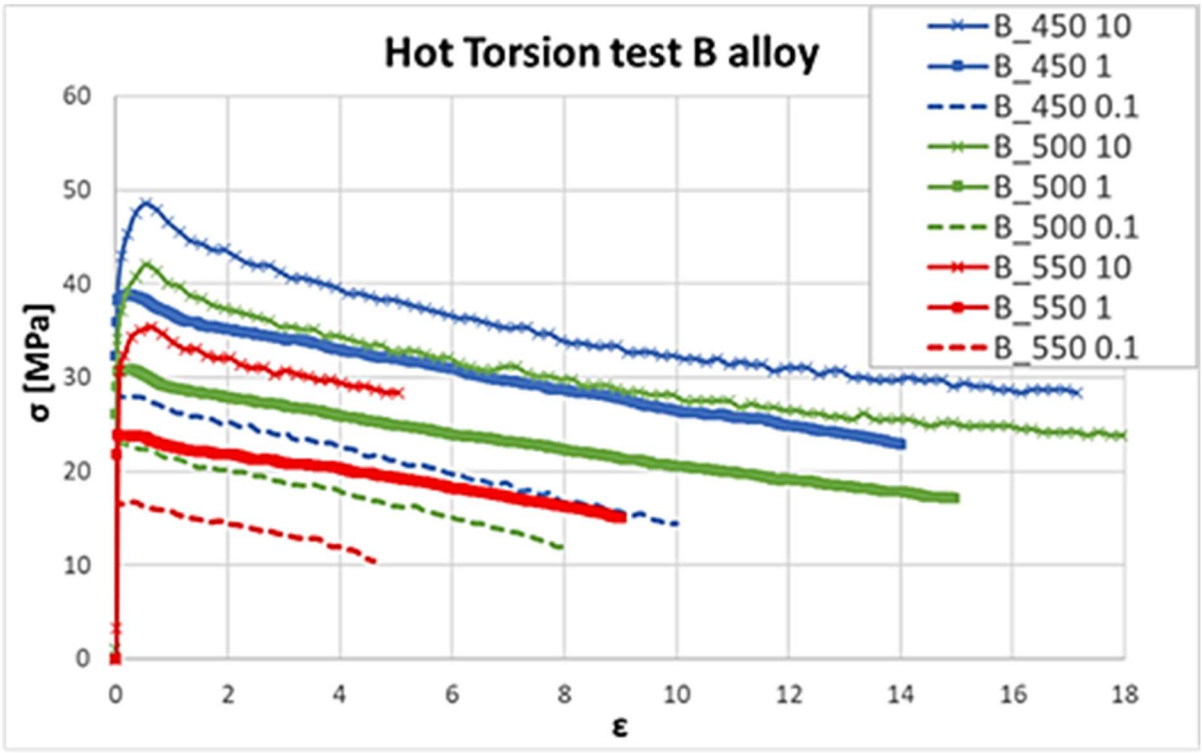

Fig. 3.16 Experimental σ-ε curves of B alloy. [105]

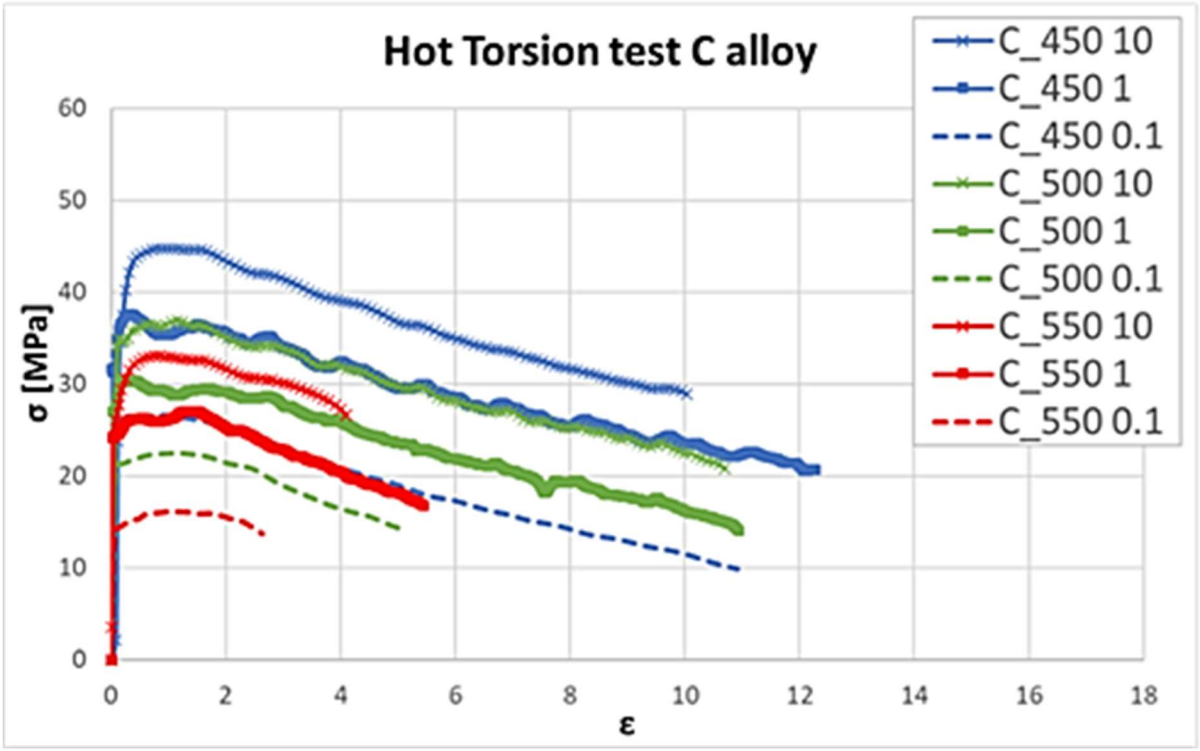

Fig. 3.17 Experimental σ-ε curves of C alloy. [105]

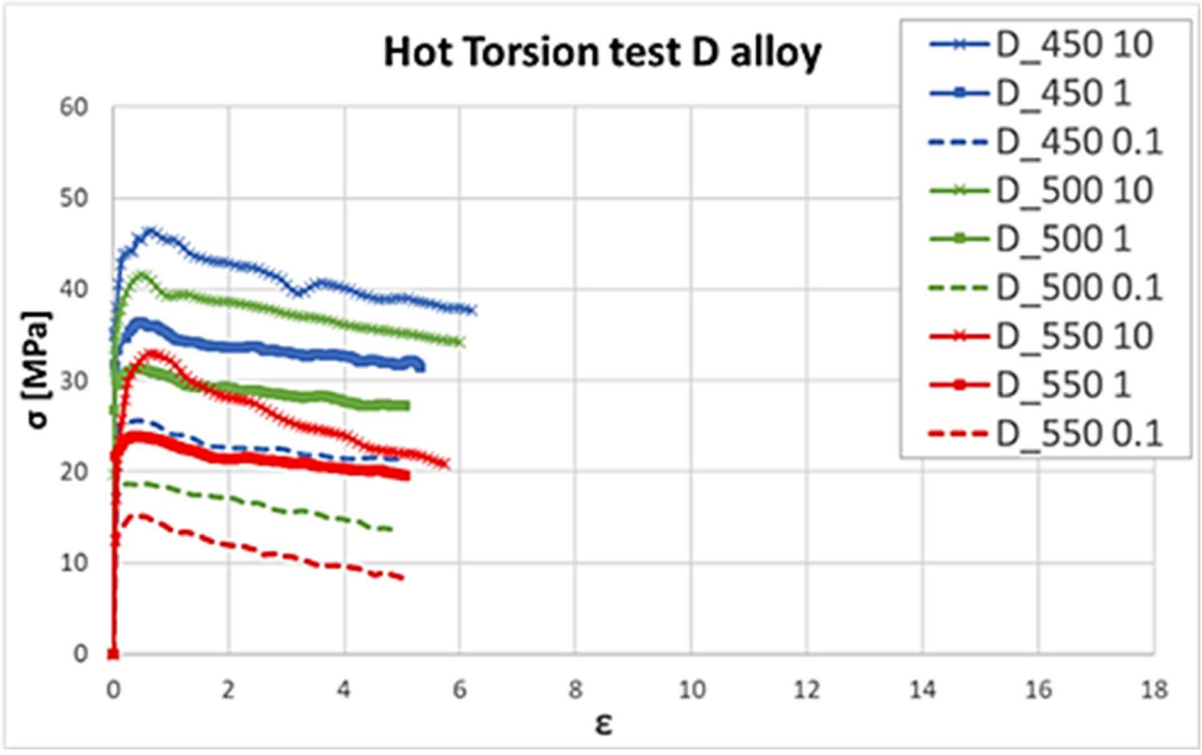

Fig. 3.18 Experimental σ-ε curves of D alloy. [105]

The curves obtained from the tests exhibit the typical shape of many aluminum alloys' behaviors, featuring an initial peak at low strains followed by a steady softening phase. The tests were terminated when the specimens fractured, providing insight into the ductility limits of each alloy.

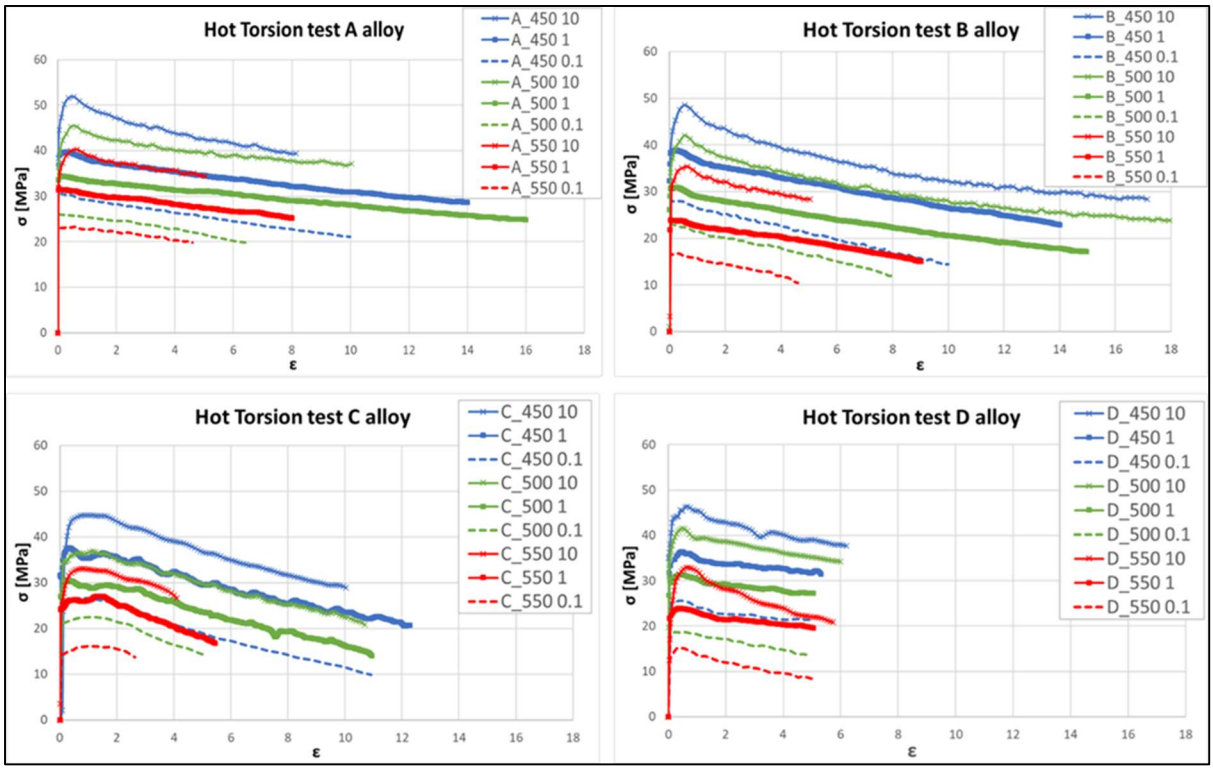

Fig. 3.19 Comparison of the experimental σ-ε curves of each alloy. [105]

Regarding alloy A, the specimens tested at 550°C reached strain values between 4.5 and 8, demonstrating moderate ductility at this elevated temperature. In contrast, at the lower temperatures of 450°C and 500°C, alloy A displayed significantly higher ductility, with strain values ranging from 14 to 16 for tests conducted at a strain rate of 1 s^{-1}. Alloy B exhibited similar ductility to alloy A, with strain values between 16 and 18 under the conditions of 450°C and 500°C at a strain rate of 10 s^{-1}. This suggests that alloy B is capable of maintaining high ductility even at higher strain rates, making it comparable to alloy A in terms of overall performance under these conditions. In contrast, alloy C demonstrated lower ductility compared to alloys A and B. The strain values ranged between 3 and 5.5 in the tests conducted at 550°C, indicating a sharp decline in plasticity at this higher temperature. At the lower temperatures of 450°C and 500°C, alloy C achieved strain values between 11 and 12, still falling short of the

performance exhibited by alloys A and B. Finally, alloy D consistently showed lower ductility across all testing conditions. The specimens failed at relatively low deformation values, with strain values between 5 and 6, suggesting that this alloy has a significantly reduced capacity for plastic deformation compared to the other alloys.

In summary, the comparative analysis of the four alloys reveals that alloys A and B exhibit superior ductility across a range of temperatures and strain rates, whereas alloys C and D show a more limited plastic deformation capacity, particularly under high-temperature conditions.

Moreover, *Fig. 3.20* presents a set of graphs where the tests have been grouped by temperature, allowing for the comparison of results for all the alloys in a single graph. The tests performed at a strain rate of 10 s^{-1} are represented by red lines, those at 1 s^{-1} by green lines, and those at 0.1 s^{-1} by blue lines, with different types of dashed lines used to distinguish between each alloy. It can be noted that, at a temperature of 450°C, all alloys exhibited relatively similar behavior, with a deviation of approximately ±5 MPa across the different strain rates. Alloy A exhibited marginally higher stress values compared to the other alloys under the same conditions, indicating slightly superior strength at this temperature. For tests conducted at 500°C, alloys B, C, and D demonstrated comparable stress values, except at the strain rate of 0.1 s-1, where alloy D displayed lower resistance than the others, and at 10 s-1, where alloy C showed reduced stress values compared to the others. At 550°C, all alloys displayed a marked reduction in ductility, with strain values ranging between 6 and 8 before the fracture occurred. Alloy A once again demonstrated higher resistance than the other alloys, achieving stress values of approximately 10 MPa greater for each strain rate condition. Additionally, alloy C exhibited a pronounced softening effect, with stress values decreasing significantly as the strain increased, indicating that the alloy loses strength more rapidly under these conditions. In contrast, alloy A demonstrated a less pronounced softening steady state, showing less variability in stress as deformation progressed.

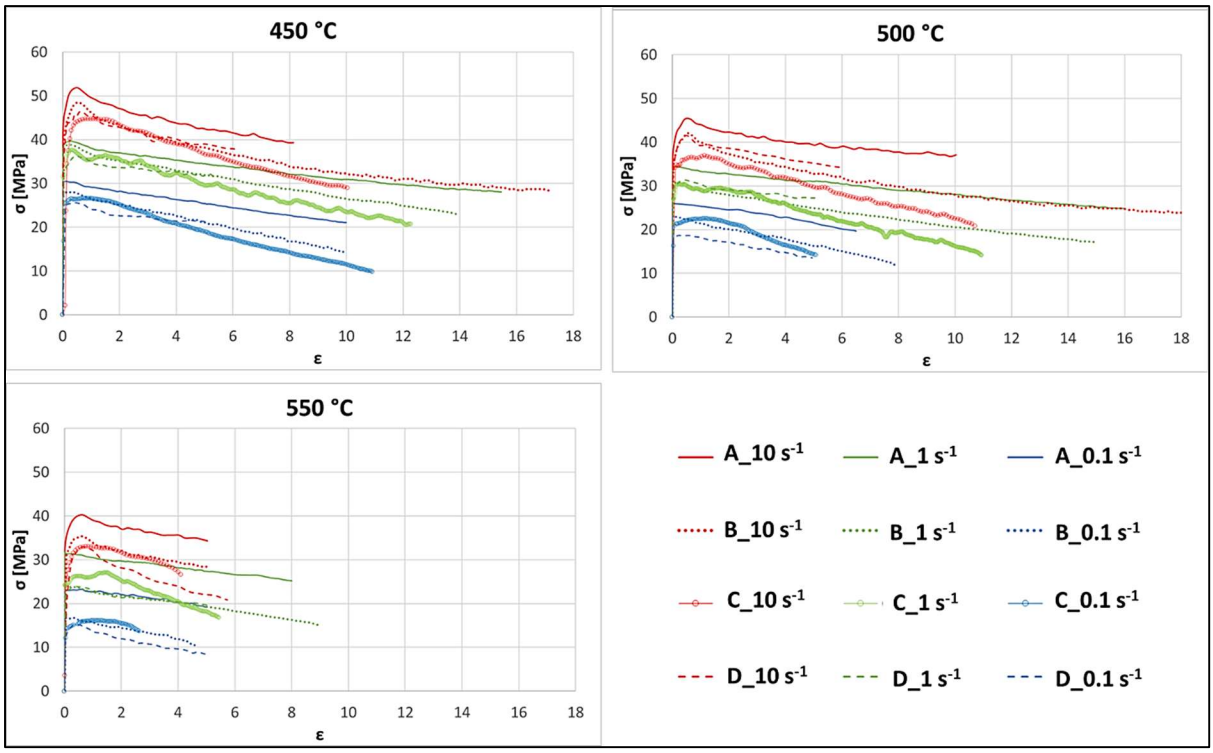

Fig. 3.20 Comparison of the experimental σ-ε curves of each alloy, grouped by temperature. Red lines represent the test at 10 s^{-1}, green lines at 1 s^{-1}, and blue lines at 0.1 s^{-1}. [105]

Extrusion process Numerical Results

For the extrusion case study, four different simulations were conducted by modifying only the flow stress input data, using the torsion test results from alloys A, B, C, and D, without changing any other parameters. These simulations aimed to investigate the variations in material behavior during the extrusion process. The numerical values for extrusion load, profile velocities, and profile exit temperatures were compared to the experimental data. The results are depicted in the subsequent graphs, from *Fig. 3.21* to *Fig. 3.23*, with red lines representing alloy A, green for alloy B, yellow for alloy C, and purple for alloy D. It is crucial to emphasize that all billets were specified as being composed of AA6082 alloy and nominally homogenized; however, only the alloy A was sourced from the same casting batch utilized during the experimental extrusion trials.

Fig. 3.21 presents the results for the extrusion load. The experimental peak value was measured at 36 MN, with a statistical distribution of 1.35%. In comparison, the numerical peak loads were calculated as 35 MN for alloy A, 32 MN for alloy B, 28 MN

for alloy C, and 30 MN for alloy D. Consequently, the numerical error in predicting the peak extrusion load was approximately 2% for alloy A when compared to the mean experimental value of 36 MN, while the error ranged between 10% and 21% for the other alloys. These results highlight the limited variability in flow stress outcomes across different casting batches (A vs. B vs. C vs. D) but also underscore the significant impact that minor differences in values can have on load-stroke predictions in FEM analyses.

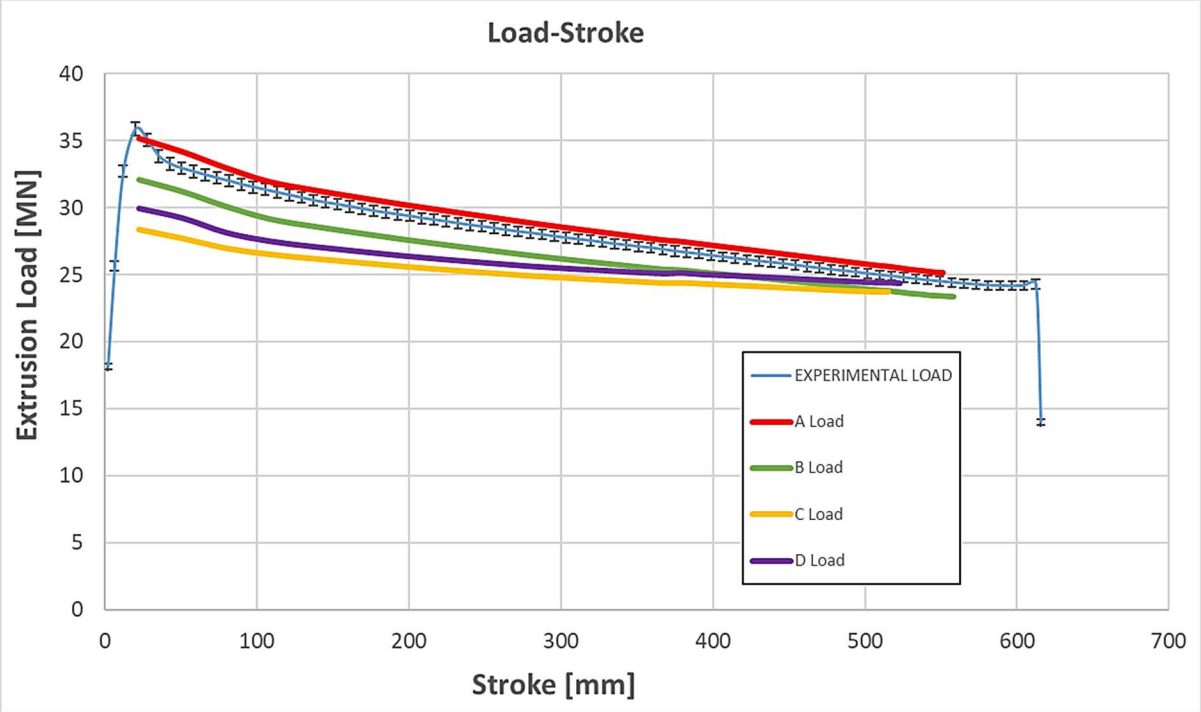

Fig. 3.21 Comparison between the experimental extrusion load and those obtained from numerical simulations using the flow stress data of alloys A, B, C, and D, respectively. [105]

In terms of profile speed during the initial extrusion process, prior to employing the puller, profile 2 exhibited a velocity approximately 50% greater than that of the other two profiles. Even after a tensile force of 3500 N was applied, profile 2 maintained a higher speed as it passed through the puller. As shown in *Fig. 3.22*, the velocities of profiles 1 and 3 were regulated by the puller, averaging around 195 mm/s, whereas the speed of profile 2, with an average of 225 mm/s, was determined by evaluating the differences in extrudate lengths at the conclusion of the extrusion process. These substantial variations in profile speed are attributed to differences in the geometries of the ports and bearings among the three profiles.

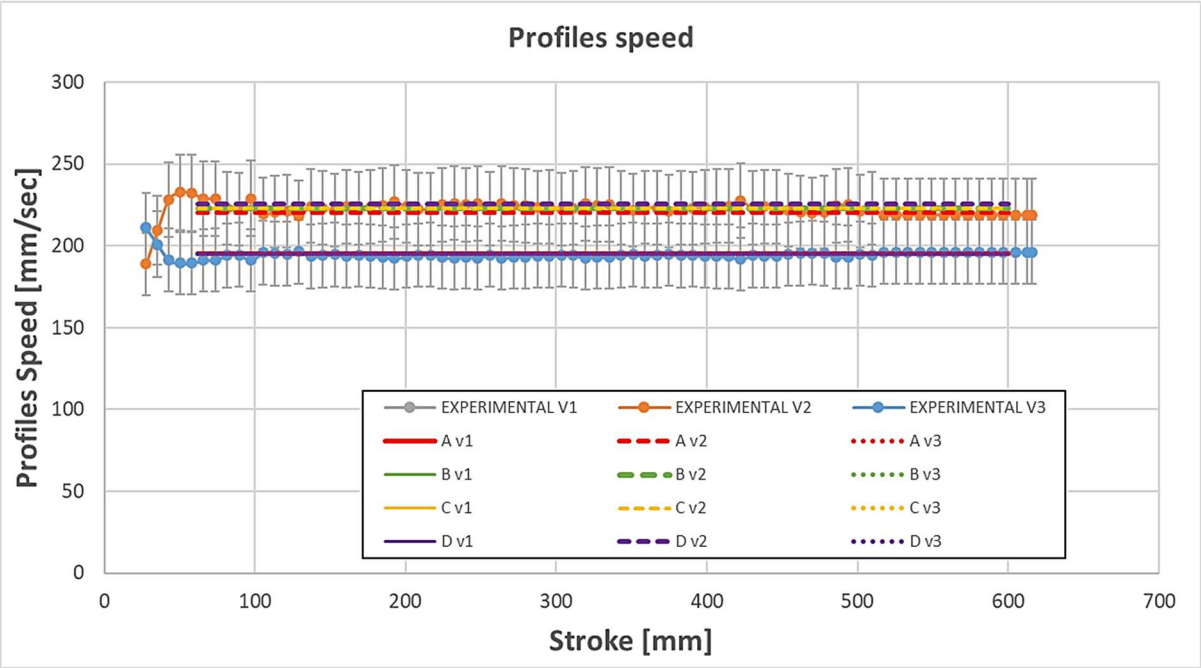

Fig. 3.22 Comparison between the experimental profiles' speed and those obtained from numerical simulations using the flow stress data of alloys A, B, C, and D, respectively. [105]

Consequently, even in the simulation, the speeds of profiles 1 and 3 were imposed by a puller, modeled as a velocity boundary condition on the profiles exiting the die, while profile 2 was left free to slide out of the die. *Fig. 3.22* provides a comparison between the experimental and simulated speeds of the profiles. It is evident that the flow stress of the alloys (A, B, C, and D) has minimal impact on the speed, as the simulated speed values demonstrate errors of less than 1% for all four alloys.

Regarding the measurement of the experimental profiles' temperatures, a non-contact pyrometer was used to monitor only the temperature of profile 1 at a distance of 1500 mm from the bolster surface. *Fig. 3.23* illustrates a comparison between the experimental temperature of profile 1 and the simulated temperatures for all profiles. The data reveals that, for all four alloys, profile 1 consistently reaches lower temperature values compared to the experimental measurement. The discrepancies are approximately 1.5% for alloy A, 3% for alloy B, 4% for alloy C, and 3.5% for alloy D, while there is an experimental standard deviation of 0.9% observed in the data acquisition. This indicates that while the simulation provides a reasonable approximation of the thermal behavior, slight variations reflect the inherent complexities in capturing precise thermal dynamics in experimental settings.

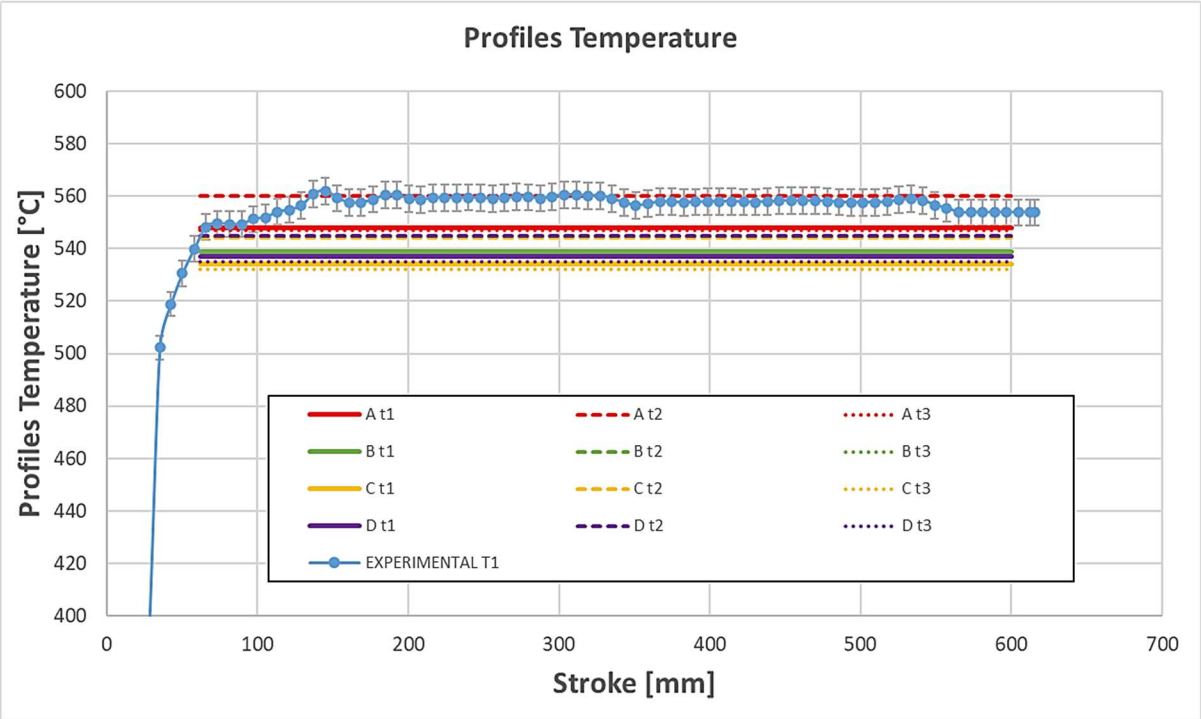

Fig. 3.23 Comparison between the experimental profiles' temperature and those obtained from numerical simulations using the flow stress data of alloys A, B, C, and D, respectively. [105]

3.3. CONCLUSIONS

In this chapter, the flow stress behavior of four aluminum alloy billets, assumed to belong to the class AA60282 and to be nominally homogenized, was examined through hot torsion testing. The tests were carried out using the torsion machine from the University of Bologna's Department of Industrial Engineering, under varying strain rates (0.1 s^{-1}, 1 s^{-1}, and 10 s^{-1}) and at three distinct temperatures: 450°C, 500°C, and 550°C.

The experimental data were represented as equivalent stress versus equivalent strain, showing notable differences in strength and ductility across the four samples, designated as A, B, C, and D.

The findings revealed that alloy A exhibited greater strength resistance compared to the others, consistently reaching higher stress values under all testing conditions. On the contrary, alloy C demonstrated significant softening, particularly in comparison to alloy A. Furthermore, alloys A and B displayed higher ductility, allowing for greater

strain accumulation during the tests, except at 550°C, where all alloys showed reduced ductility.

Subsequent to the torsion tests, the collected data served as input for a numerical simulation of an extrusion process, based on the experimental setup from the Extrusion Benchmark 2023 presented at the Aluminium2000 International Conference. [103] The experiment involved the extrusion of three hollow tubes made from AA6082 alloy, with alloy A used in the actual trial. Four separate simulations were conducted using Qform UK® software, each incorporating the flow stress data of alloys A, B, C, and D without altering any other parameters.

The accuracy of the simulations was assessed by comparing the numerical results with the experimental outcomes, particularly focusing on extrusion force, temperature, and speed of the profiles. For alloy A, the simulation results deviated by only 2% in extrusion force and 1.5% in temperature, whereas the other alloys presented larger errors, ranging from 10% to 21% in load and 3% to 4% in temperature. Predicted speed values across all alloys showed an impressive accuracy, with deviations lower than 1%. These results underscore the significance of detailed experimental characterization of flow stress for accurate numerical simulations, as the choice of flow stress data directly impacts the precision of the predictive model used in metal forming processes [105].

REFERENCES

[82] El Mehtedi M, Ryum N, Spigarelli S, Evangelista E, Ronning B. EVALUATION OF HOT FORMABILITY OF AN AL-4.6ZN-0.8MG ALLOY BY INCREASING-STRAIN-RATE TORSION TESTS n.d.

[83] Rudnev V, Cook R, Loveless D. Handbook of induction heating. Second edition. Boca Raton, FL: CRC Press, Taylor & Francis Group; 2017. https://doi.org/10.1201/9781315117485.

[84] Jones P, Taylor S, Nakai S, Jennings J. Electroheat and Materials Processing. Electrical Engineer's Reference Book, Elsevier; 2003, p. 9-1-9–38. https://doi.org/10.1016/B978-075064637-6/50009-5.

[85] Lucía Ó, Domínguez A, Sarnago H, Burdío JM. Induction Heating. Control of Power Electronic Converters and Systems, Elsevier; 2018, p. 265–87. https://doi.org/10.1016/B978-0-12-816136-4.00022-1.

[86] Induction Heating and Heat Treatment. ASM Handbook, vol. 4C, Dr. Valery Rudnev, Dr. George Totten, FASM; 2014.

[87] Kennedy MW. Magnetic fields and induced power in the induction heating of aluminium billets. Stockholm: KTH Royal Institute of Technology; 2013.

[88] Saha PK. Thermodynamics and tribology in aluminum extrusion. Wear 1998;218:179–90. https://doi.org/10.1016/S0043-1648(98)00210-5.

[89] Sheppard T. Extrusion of Aluminium Alloys. Boston, MA: Springer US; 1999. https://doi.org/10.1007/978-1-4757-3001-2.

[90] Saha PK. Aluminum extrusion technology. 1. print. Materials Park, Ohio: ASM International; 2000.

[91] AEC. Aluminum Extrusion Manual. 4.2. 2018.

[92] He Z, Wang H, Wang M, Li G. Simulation of extrusion process of complicated aluminium profile and die trial. Transactions of Nonferrous Metals Society of China 2012;22:1732–7. https://doi.org/10.1016/S1003-6326(11)61380-0.

[93] Eivani AR, Jafarian HR, Zhou J. Simulation of peripheral coarse grain structure during hot extrusion of AA7020 aluminum alloy. Journal of Manufacturing Processes 2020;57:881–92. https://doi.org/10.1016/j.jmapro.2020.07.011.

[94] Kniazkin I, Vlasov A. Quality prediction of longitudinal seam welds in aluminium profile extrusion based on simulation. Procedia Manufacturing 2020;50:433–8. https://doi.org/10.1016/j.promfg.2020.08.079.

[95] Negozio M, Pelaccia R, Donati L, Reggiani B, Pinter T, Tomesani L. Finite Element Model Prediction of Charge Weld Behaviour in AA6082 and AA6063 Extruded Profiles. J of Materi Eng and Perform 2021;30:4691–9. https://doi.org/10.1007/s11665-021-05752-x.

[96] Negozio M, Pelaccia R, Donati L, Reggiani B. FEM Analysis of the Skin Contamination Behavior in the Extrusion of a AA6082 Profile. KEM 2022;926:452–9. https://doi.org/10.4028/p-y37nm3.

[97] Negozio M, Donati L, Pelaccia R, Reggiani B, Di Donato S. Experimental analysis and modeling of the recrystallization behaviour of a AA6060 extruded profile, 2023, p. 477–86. https://doi.org/10.21741/9781644902479-52.

[98] Di Donato S, Pelaccia R, Negozio M. Phase Field Method for the Assessment of the New-Old Billet Material Interaction during Continuous Extrusion Using COMSOL Multiphysics. J of Materi Eng and Perform 2024. https://doi.org/10.1007/s11665-024-10013-8.

[99] Negozio M, Pelaccia R, Donati L, Reggiani B, Di Donato S. Microstructure Evolution and FEM Prediction on AA6XXX Alloys. Key Engineering Materials 2024;987:3–10. https://doi.org/doi:10.4028/p-qO8WAd.

[100] Pelaccia R, Negozio M, Di Donato S, Reggiani B, Donati L. Numerical simulation of the extrusion process with different FEM code approaches: analysis of thermal field, profile speed, defects evolution, and microstructure of hollow tubes, 2024, p. 771–80. https://doi.org/10.21741/9781644903131-85.

[101] Pelaccia R, Negozio M, Donato SD, Donati L, Reggiani B. Recent Trends in Nitrogen Cooling Modelling of Extrusion Dies. Key Engineering Materials 2024;987:11–22. https://doi.org/doi:10.4028/p-Q0NDkB.

[102] Verlinden B, Suhadi A, Delaey L. A generalized constitutive equation for an AA6060 aluminium alloy. Scripta Metallurgica et Materialia 1993;28:1441–6. https://doi.org/10.1016/0956-716X(93)90496-F.

[103] Pelaccia R, Negozio M, Di Donato S, Reggiani B, Donati L. Extrusion Benchmark 2023: Effect of Die Design on Profile Speed, Seam Weld Quality and Microstructure of Hollow Tubes. Key Engineering Materials 2024;988:47–62. https://doi.org/10.4028/p-gNXRC5.

[104] Negozio M, Pelaccia R, Donati L, Reggiani B, Di Donato S. Validation of charge welds and skin contamination FEM predictions in the extrusion of a AA6082 aluminum alloy, 2023, p. 86–93. https://doi.org/10.21741/9781644902714-11.

[105] Di Donato S, Donati L, Pelaccia R, Reggiani B, Negozio M. The Influence of Alloy Characterization Approaches on Extrusion Process FEM Simulation Reliability. Extrusion Technology for Aluminum Profiles Foundation (“ET Foundation”) in The Proceedings of the ET Seminar, Orlando, Florida: 2024.

SUMMARY, CONCLUSIONS AND FUTURE WORK

This PhD thesis was focused on the analysis of the torsion test as a method for characterizing the plastic behavior of materials, with the aim of advancing the accuracy and reliability of Finite Element Method (FEM) simulations for metal forming processes by improving the evaluation of material flow stress. The research addressed the limitations of traditional tensile and compression tests, while the torsion test was then presented as a viable alternative for obtaining precise flow stress data.

The initial chapters provided a comprehensive theoretical framework, detailing the fundamental principles of metal forming, the mechanisms of plastic deformation, and the critical role of material flow stress in determining process parameters and workability. Issues and limitations of traditional tensile and compression tests were examined. The torsion test presents a solution to avoid these issues, providing a methodology for material characterization at high levels of strain, strain rate, and temperature. The specimen in a torsion test undergoes deformation primarily in the form of shear, and its geometry remains relatively constant throughout the test. This characteristic allows for more accurate control of strain rates and provides reliable data on the material's flow stress. Moreover, the torsion test permits testing at controlled elevated temperatures, using induction heating techniques. A PID control system, integrated with a thermocouple positioned within the specimen's gauge section, enhances precise temperature regulation, minimizing thermal gradients.

The thesis explored the design and essential components of a custom-built torsion test machine, aimed at achieving accurate and reliable experimental data. However, the torsion test presented challenges in data processing and interpretation. Converting torque and twist angle data into stress-strain values required suitable mathematical models, each with specific assumptions and limitations. The study thoroughly examined several key models: the Saint-Venant model for elastic deformation, Nadai's model, which extends analysis into plastic deformation yet lacks sensitivity to strain rate, and the Fields-Backofen model, which incorporates strain-rate sensitivity but entails complex experimental requirements.

The second chapter presents a comparative experimental study of tensile, compression, and torsion tests performed on ETP copper, focusing on cold metal forming. The tensile test, while effective at moderate strains, showed limitations for

data processing beyond the onset of necking, at approximately 0.33 true strain. Application of the Bridgman correction partially mitigated this issue, still, uncertainties persisted due to the evolving triaxial stress state during necking. Compression testing, while achieving higher maximum strains, approximately 1.1, introduced complexities due to barreling and friction. A thorough analysis was conducted, varying lubrication conditions to identify optimal testing methodology minimizing measurement errors. From the comparison between experimental flow stress curves, it has emerged that equivalent stress values obtained from the torsion tests were lower than those from tensile and compression tests. This discrepancy has been attributed to factors such as crystallographic anisotropy and the development of different textures. Particularly, tension activates more slip systems than torsion, resulting in greater dislocation interaction and increased work-hardening. This difference in mechanical response is linked to the microstructural evolution of the material, where grain reorientation and texture development differ under various loading conditions. Torsional loading induces shear stresses that affect dislocation movement and crystallographic slip differently than tensile loading, leading to distinct hardening behaviors in the material. The discrepancy between the flow stress of the material obtained from tensile and torsional tests has already been observed in studies present in the literature. In particular, for the torsion of FCC materials, it was found that the Taylor factors evolve with strain from an initial value of 1.65, gradually decreasing to about 1.38, reflecting changes in texture. Simultaneously, the resolved critical shear stress increases due to work hardening. This evolution leads to a reduction in the Von Mises equivalent stress at large strains. In contrast, during tension, due to fiber texture development, the Taylor factor increases from 3.06 to 3.67, leading to an increase in equivalent stress.

Therefore, correction factors were calculated based on this approach to compare the flow stress curve obtained in the torsion test with that obtained in the tensile and compression tests. In the first attempt, a coefficient was calculated considering the Taylor values for tensile and torsion at low strains. However, by correcting the torsion test with this factor, the equivalent stress values in the torsion test remain lower than those in the compression test. In the second attempt, a correction factor was calculated, taking into account the Taylor values at large strains; however, this time, the corrected torsion stress values were higher than those from the compression test.

Additionally, it should be noted that it is difficult to define the specific strain values for which the different Taylor coefficients can be considered valid.

Consequently, from the comparison between the compression test and the torsion test, a new correction function was modeled by interpolating through a nonlinear regression the correction coefficient values as a function of deformation. The flow stress curve obtained according to the new modeling aligns precisely with the tensile test and with the compression test up to a deformation value of 1.1, while simultaneously allowing for material characterization up to higher deformation values. Since the new model was derived from the comparison between the same compression and torsion tests, a new test was designed to validate its accuracy. In the so-called hybrid compression test, the material is subjected to a triaxial deformation condition, ensuring perfect adherence between the plates and the specimen, allowing for an experimental-numerical comparison of the loads applied to the specimen while avoiding errors that could be introduced by modeling proper friction behavior.

Numerical simulations of the tests—tensile, torsion, and hybrid compression—were carried out using the QformUK® software. A comparative analysis between the different characterization tests was therefore performed, also through FEM modeling, varying the material flow stress each time according to the curves obtained in the various experimental tests. From this comparison, it emerged that in the simulation of the tensile test, the actual load values are well predicted by the simulation using the flow stress curves obtained from the tensile, compression, and torsion tests processed with the proposed model. In contrast, utilizing the flow stress obtained from the torsion test while applying the Fields-Backofen theory with the Von Mises criterion leads to an underestimation of the experimental load with errors around 20-25%. Regarding the torsion test, it was found that using the flow stress curves obtained from the tensile and compression tests leads to overestimated torque values obtained in the experimental test, with errors between 25-35%. In contrast, a perfect overlap between actual and experimental data was observed when using the flow stress from the torsion test. This discrepancy arises because the software does not account for the fact that the material exhibits different crystallographic behavior when subjected to tensile loading compared to torsional loading. Initially, the calculations of the Fields-Backofen model applied to process the torsion test data were consistent with the actual torque values; however, once the proposed model is applied, the simulation fails to account for the intrinsic

crystallographic differences of the material between tension and torsion, leading to an overestimation of the torque. This difference in mechanical response is linked to the microstructural evolution of the material, where grain reorientation and texture development differ under various loading conditions. Torsional loading induces shear stresses that influence dislocation motion and crystallographic slip differently than tensile loading, resulting in distinct hardening behaviors in the material. Consequently, without specific modeling to account for these behaviors, the simulation cannot accurately capture the material's response in all conditions. To determine the most suitable test for characterizing the material's plastic behavior under cold deformation, particularly when subjected to triaxial stress states and large strain values, the hybrid compression test was simulated.

From the results of the numerical-experimental comparison for the hybrid compression test, it emerges that using the flow stress derived from tensile and compression tests produces excellent agreement between experimental and simulated data. On the other hand, when the simulation is performed using the flow stress from torsion tests, an underestimation of the actual loading force is observed. However, when the torsion test data are processed using the proposed model, a perfect agreement between numerical and experimental results is achieved. This behavior aligns with the observation that, under cold working conditions, the effects of texture and dislocation interactions become more pronounced, affecting the macroscopic mechanical response. Conversely, under hot deformation conditions, where the material is processed above its recrystallization temperature, these crystallographic and work-hardening effects are significantly minimized. This is because elevated temperatures enable dynamic recovery and recrystallization processes, which inhibit texture formation and reduce internal stress accumulation. As a result, the material exhibits a more uniform response to varying loading conditions, without the marked discrepancies observed in cold working conditions, where texture development and slip systems play a more dominant role.

Subsequently, material characterization was performed using cold torsion tests on four different copper batches purchased by ICEL s.c.p.a. from four different suppliers. The torsion tests were conducted by varying three strain rates: 0.1, 1, and 5 s^{-1}, and the data were analyzed according to the proposed model for cold torsion tests. The resulting flow stress data were utilized for modeling the industrial wire drawing process

for the production of electrical cables. An analytical, numerical, and experimental analysis of the multi-pass wire drawing process was conducted to assess the material's behavior and optimize the operational parameters. Initially, a prediction model of the stresses acting on the material during the wire drawing process in multi-pass industrial machines was proposed and discussed. The drawing stresses acting on the material were investigated and compared step by step to the material yield stress when different processing conditions were applied. The study highlighted that among the process parameters, lubrication conditions and the effects of capstans significantly influence the stress behavior in wires. The friction coefficient between capstans and wire has an opposite effect on the stresses compared to the friction coefficient between the wire and die, and a significant influence of wire windings around the capstans on the wire stress behavior was noted. It is not feasible to adjust the wire reduction ratio at each step to reduce tensions because the mechanical elongation ratio of the machine remains lower than the elongation ratio of the wire. By adjusting the number of windings, it is possible to deform more homogeneously, thereby generating lower drawing stress values. Additionally, it was demonstrated that utilizing accurate material characterization in modeling can lead the wire into critical processing zones that may cause fractures, effects that typically do not lead to wire breaks under ideal modeling conditions.

However, for the multi-pass process modeling, theoretical values for the friction coefficient were still employed due to the challenges in estimating it accurately. In a subsequent analysis, a comparative study was conducted, evaluating the calculated drawing force values obtained from three different analytical models, the SLAB method, the Wistreich-Wright model, and the Avitzur theory, in conjunction with those from numerical simulations modeled using the QformUK® code. By comparing experimental data with the calculated values, a range of friction coefficient values for both lubricated and unlubricated conditions was established for each analytical model, considering a maximum calculation error of 2%. It was found that the analytical models tend to underestimate the value of the friction coefficient due to simplified assumptions regarding the average strain and strain rate of the material within the die. The analysis of deviations among the various methods highlights the importance of evaluating friction coefficient values in each model to prevent errors in estimating drawing forces. The aim of providing a reliable numerical model for predicting wire stress during the

multi-pass drawing process will be achieved by accurately characterizing material flow stress and appropriately assessing the friction model.

Finally, the last chapter investigated the thermomechanical behavior of AA6082 aluminum alloys during hot extrusion, focusing on the impact of material characterization on FEM simulation accuracy. A detailed methodology for hot torsion testing, including precise temperature control via induction heating (using a PID control system and embedded thermocouple), was established and validated through a systematic experimental investigation of heating cycles at varying rates. The 1°C/s heating rate, followed by a holding period of 6 minutes, was identified as optimal, balancing temperature uniformity and cycle time. However, future work will focus on developing a numerical model for solenoid design and induction heating optimization. This model aims to predict optimal heating parameters for various workpiece dimensions and materials, eliminating the need for repetitive experimental validation procedures for each new material and geometry.

Subsequently, torsion tests were carried out on specimens extracted from four different AA6082 casting batches. The trials were performed in the following conditions: three levels of strain rate 0.1, 1, and 10 s^{-1}, and three temperatures 450, 500, and 550 °C. The resulting flow stress data revealed differences in strength and ductility among the billets despite all being nominally declared of the AA6082 alloy class and homogenized to the O condition. This highlights also the torsion test's utility as a powerful tool for assessing the quality and consistency of incoming materials used in industrial processes.

The flow stress data then served as input for FEM simulations of the industrial extrusion process from the Extrusion Benchmark 2023. The process consists of the extrusion of three hollow tubes with the final cold profile exhibiting an external diameter of 40 mm and a wall thickness of 4 mm. The material flow characteristics within the tooling varied among the three profiles, with the intention of generating significant velocity deviations at the exit. The process simulation was run four times, keeping all parameters constant and changing only the material's flow stress, inputting the value from a different batch each time. The comparison between numerical and experimental results showed that the simulation using the flow stress data of the material actually used in the experimental extrusion trials yielded excellent agreement (2% deviation in extrusion force, 1.5% in temperature, <1% in speed). In contrast, simulations using

flow stress data from the other alloys exhibited larger deviations, underscoring the critical need for accurate material characterization in achieving precise FEM predictions.

Concluding, the validated torsion test methodology and associated data processing model proved highly effective in characterizing the flow stress behavior of various materials under high-strain conditions, even at elevated temperatures. This capability was then directly applied to optimizing industrial metal forming processes. The accuracy of FEM simulations was extensively compared against experimental data, highlighting the crucial impact of precise material characterization. Minor variations in flow stress data significantly affected the precision of simulations. These findings underscore the necessity of using appropriate characterization tests and data processing methods to accurately capture the complex interplay between stress, strain, strain rate, and temperature that characterize the industrial processes. Further works will focus on: 1) expanding the experimental database to include a broader range of materials and processing conditions; 2) developing more sophisticated constitutive models that can better account for the material's complex behavior at extreme conditions; and 3) integrating the refined torsion test methodology into FEM software.